Ultra-Low Noise Fiber Laser Systems For Advanced Multiphoton Microscopy

Dissertation

zur Erlangung des Doktorgrades

an der Fakultät für Mathematik, Informatik und Naturwissenschaften

Fachbereich Physik

der Universität Hamburg

vorgelegt von

M. Sc. Marvin Edelmann

Hamburg, 2026

Gutachter/innen der Dissertation:	Prof. Dr. Franz X. Kärtner Prof. Dr. Gerd Leuchs
Zusammensetzung der Prüfungskommission:	Prof. Dr. Roman Schnabel Prof. Dr. Franz X. Kärtner Prof. Dr. Gerd Leuchs Prof. Dr. Markus Glatzel Prof. Dr. Tobias Herr
Vorsitzende/r der Prüfungskommission:	Prof. Dr. Roman Schnabel
Datum der Disputation:	10.06.2026
Vorsitzender des Fach-Promotionsauschusses PHYSIK:	Prof. Dr. Johannes Haller
Leiter des Fachbereichs PHYSIK:	Prof. Dr. Markus Drescher
Dekan der Fakultät MIN:	Prof. Dr.-Ing. Norbert Ritter

Eidesstattliche Versicherung

Hiermit versichere ich an Eides statt, die vorliegende Dissertationsschrift selbst verfasst und keine anderen als die angegebenen Hilfsmittel und Quellen benutzt zu haben. Sofern im Zuge der Erstellung der vorliegenden Dissertationsschrift generative Künstliche Intelligenz (gKI) basierte elektronische Hilfsmittel verwendet wurden, versichere ich, dass meine eigene Leistung im Vordergrund stand und dass eine vollständige Dokumentation aller verwendeten Hilfsmittel gemäß der Guten wissenschaftlichen Praxis vorliegt. Ich trage die Verantwortung für eventuell durch die gKI generierte fehlerhafte oder verzerrte Inhalte, fehlerhafte Referenzen, Verstöße gegen das Datenschutz- und Urheberrecht oder Plagiate.

Hamburg, 06.02.2025 

Ort/Datum Unterschrift

Zusammenfassung

Die Multiphotonenmikroskopie (MPM) ist eine zentrale Methode der modernen Lebenswissenschaften und ermöglicht hochauflösende Bildgebung tief in streuendem biologischem Gewebe. Trotz ihres Erfolgs werden weitere Fortschritte und eine breitere Anwendung zunehmend durch Zielkonflikte zwischen Bildgebungstiefe, Gesichtsfeld, Signalstärke und Photodamage sowie durch laserinduzierte Fluktuationen, spektrales Übersprechen und begrenzte Multicolor-Abstimmbarkeit eingeschränkt. Diese Herausforderungen werden durch die hohe Empfindlichkeit nichtlinearer Anregungsprozesse gegenüber Umwelteinflüssen und die Komplexität bestehender ultraschneller Lichtquellen verstärkt. Ihre Überwindung erfordert einen integrierten photonischen Ansatz, in dem ultraschnelle Pulserzeugung, nichtlineare spektrale Kontrolle, Rausch-Engineering und gezielte Multiphotonenanregung als gekoppelte Elemente eines einheitlichen Systems behandelt werden.

Diese Dissertation etabliert ein solches plattformorientiertes Rahmenkonzept durch einen modularen Baukasten ultraschneller, ultra-rauscharmer Faserlasertechnologien und dessen Überführung in fortgeschrittene MPM-Anwendungen. Rauscharme Generation von Femtosekundenpulsen wird in interferometrischen, vollständig polarisationserhaltenden Faseroszillatoren realisiert und erreicht integriertes relatives Intensitätsrauschen bis 0,04% sowie Timing-Jitter von 14,5 fs. Darauf aufbauend werden MPM-taugliche Energieskalierung, spektrale Agilität und Multicolor-Anregung mittels eines simulationsgestützten Ytterbium-Faserlaser-Treibers in Kombination mit Large-Mode-Area-Fasertechnologie, deterministischer interferometrischer Wellenlängenkonversion und rauschtechnisch optimierter Superkontinuumerzeugung realisiert. Numerische Systemmodelle ermöglichen dabei die prädiktive Kontrolle nichtlinearer Dynamik und des Rauschtransfers.

Diese modularen Technologien werden in anwendungsgetriebene MPM-Plattformen überführt, darunter eine abstimmbare dispersive-Wellen-Quelle zur kontrastreichen Zwei-Photonen-Bildgebung neuronaler und vaskulärer Strukturen im Mausgehirn in Tiefen von über 600 µm sowie ein synchronisiertes Dreifarben-Anregungssystem für übersprechfreie, multiplexe Bildgebung von Gehirn- und viszeralem Gewebe. Zusammen vereinen diese Plattformen Bildgebungstiefe, spektrale Selektivität und Langzeitstabilität innerhalb einer einzelnen faseroptischen Architektur. Gegenüber konventionellen ultraschnellen Laser- und Mehrquellen-Anregungskonzepten stellen sie eine kompakte, justagefreie Alternative dar, die Multicolor-Fähigkeit und Anregungsflexibilität deutlich erweitert. Insgesamt etabliert diese Arbeit integrierte, rauschtechnisch optimierte ultraschnelle photonische Plattformen als neue Leistungsbasis für die Multiphotonenmikroskopie und verwandte nichtlineare optische Anwendungen.

Abstract

Multiphoton microscopy (MPM) is a cornerstone of modern life sciences, enabling high-resolution imaging deep within scattering biological tissue. Despite its success, further progress and broader adoption are increasingly constrained by trade-offs between imaging depth, field of view, signal strength, and photodamage, as well as by laser-induced fluctuations, spectral crosstalk, and limited multicolor tunability. These challenges are amplified by the sensitivity of nonlinear excitation to environmental perturbations and the complexity of existing ultrafast light sources. Addressing these limitations requires an integrated photonic approach in which ultrafast pulse generation, nonlinear spectral control, noise engineering, and targeted multiphoton excitation are treated as coupled elements of a unified system.

This dissertation establishes such a platform-level framework through a modular toolbox of ultrafast, ultra-low-noise fiber-laser technologies and their translation into advanced MPM applications. Low-noise femtosecond pulse generation is achieved in interferometric, all-polarization-maintaining fiber oscillators, reaching integrated relative intensity noise as low as 0.04 percent and timing jitter down to 14.5 fs. Building on this foundation, MPM-capable energy scaling, spectral agility, and multicolor excitation are realized using a simulation-guided Ytterbium fiber laser driver combined with large-mode-area fiber technology, deterministic interferometric wavelength conversion, and noise-engineered supercontinuum generation. Numerical system-level modeling provides predictive control over nonlinear dynamics and noise transfer.

These modular technologies are translated into application-driven MPM platforms, including a tunable dispersive-wave source for high-contrast two-photon imaging of neuronal and vascular structures in mouse brain tissue at depths exceeding 600 μm, and a synchronized three-color excitation system for crosstalk-free multiplexed brain and visceral imaging. Together, these platforms combine imaging depth, spectral selectivity, and long-term stability within a single fiber-optic architecture. Compared to conventional ultrafast laser and multi-source excitation schemes, they provide a compact, alignment-free alternative that substantially expands multicolor capability and excitation versatility. Overall, this work establishes integrated, noise-engineered ultrafast photonic platforms as a new performance baseline for multiphoton microscopy and related nonlinear optical applications.

Acknowledgements

This dissertation was carried out at the University of Hamburg and Deutsches Elektronen-Synchrotron (DESY) in the Ultrafast Optics & X-Rays (UFOX) Group, and it reflects the support of many people to whom I am deeply grateful.

First and foremost, I thank my doctoral advisor, Prof. Franz X. Kärtner, who has guided my scientific development since I joined his group as a bachelor's student. His mentorship, trust, scientific freedom, and encouragement to pursue ambitious, interdisciplinary research directions, together with his long-term vision in ultrafast optics, have been decisive for my development and have fundamentally shaped this dissertation. I am equally grateful to my second examiner, Prof. Gerd Leuchs, for the careful review of this thesis and valuable feedback.

I would also like to thank Uta Freydank for her invaluable support with logistical and administrative matters throughout my studies and doctoral work.

I thank my co-supervisor, Dr. Mikhail Pergament, for his continuous mentorship and support. His guidance brought structure and depth to my scientific work and, through the high-power laser division, significantly broadened my technical expertise. I further thank Martin Kellert, Alexey Yakovlev, and Jelto Thesinga for their ongoing support within this division.

I further am grateful to my colleagues in the UFOX group for the stimulating scientific environment and fruitful discussions, in particular Neetesh Singh, Milan Sinobad, and Christian Rentschler. I also thank Thomas Tilp and Andrej Berg for mechanical engineering support, and Kemal Shafaq, Erwin Cano Vargas, Anan Dai and Theia El Sharkawy from Cycle GmbH for technical discussions supporting synchronization and timing experiments. I further thank Prof. Tobias Herr for his support as my teaching supervisor and for valuable scientific discussions.

I thank the Institute of Neuropathology at University Medical Center Hamburg-Eppendorf (UKE) and the Institute of Biochemistry and Molecular Biology at the University of Hamburg for enabling the interdisciplinary multiphoton microscopy experiments presented in this work. At UKE, I am grateful to Prof. Markus Glatzel, Andreu Matamoros-Angles, Mohsin Shafaq, and Edda Thies for scientific guidance, collaboration, and support with sample preparation. At UHH, I thank Prof. Christian Betzel, Prince Prabhu, and Susanna Gevorgyan for collaboration, including joint work on the interdisciplinary grant on Alzheimer's research.

Finally, I would like to thank my parents, Frank and Anja Edelmann, and my brother, Marcel Edelmann, for their unconditional support, encouragement, and confidence in me throughout my studies and beyond. I am also deeply grateful to my partner, Yi Hua, for her constant support, patience, and understanding throughout this journey. Her encouragement and presence has been invaluable.

Table of Contents

List of Abbreviations

2PFM	*Two-Photon Fluorescence Microscopy*
2PM	*Two-Photon Microscopy*
3PM	*Three-Photon Microscopy*
AC	*Autocorrelation*
ASE	*Amplified Spontaneous Emission*
ATT	*Attenuator*
CA1	*Cornu Ammonis 1 (hippocampal subregion)*
CA3	*Cornu Ammonis 3 (hippocampal subregion)*
CW	*Continuous Wave*
CT	*Computer Tomography*
DM	*Dichroic Mirror*
DW	*Dispersive Wave*
EGFP	*Enhanced Green Fluorescent Protein*
FAD	*Flavin Adenine Dinucleotide*
FDOT	*Fluorescence Diffuse Optical Tomography*
FMT	*Fluorescence Molecular Tomography*
FOV	*Field of View*
FWHM	*Full Width at Half Maximum*
FTL	*Fourier Transform Limit*
FWM	*Four-Wave Mixing*
GDD	*Group-Delay Dispersion*
GFP	*Green Fluorescent Protein*
GNLSE	*Generalized Nonlinear Schrödinger Equation*
GP	*Grating Pair*
GVD	*Group-Velocity Dispersion*
LMA	*Large-Mode-Area*
LOT	*Laminar Optical Tomography*
MFMT	*Mesoscopic Fluorescence Molecular Tomography*

ML	*Mode-Locked / Mode-Locking*
MFD	*Mode-Field Diameter*
MPM	*Multiphoton Microscopy*
MRI	*Magnetic Resonance Imaging*
NADH	*Nicotinamide Adenine Dinucleotide*
NA	*Numerical Aperture*
NALM	*Nonlinear Amplifying Loop Mirror*
NIR	*Near-Infrared*
NLI	*Nonlinear Interferometer*
NLSE	*Nonlinear Schrödinger Equation*
NPE	*Nonlinear Polarization Evolution*
OCT	*Optical Coherence Tomography*
OPA	*Optical Parametric Amplifier*
OPO	*Optical Parametric Oscillator*
OPM	*Orthogonal Polarization Mode*
PAT	*Photoacoustic Tomography*
PBS	*Phosphate Buffered Saline*
PCF	*Photonic Crystal Fiber*
PCMA	*Pre-Chirp Managed Amplifier*
PET	*Positron Emission Tomography*
PM	*Polarization-Maintaining*
PMT	*Photomultiplier Tube*
PSF	*Point-Spread Function*
PSD	*Power Spectral Density*
QWP	*Quarter-Wave Plate*
RFP	*Red Fluorescent Protein*
RIN	*Relative Intensity Noise*
ROI	*Region of Interest*
SA	*Saturable Absorber*
SCG	*Supercontinuum Generation*

SHG	*Second-Harmonic Generation*
SLM	*Spatial Light Modulator*
SNR	*Signal-to-Noise Ratio*
SO	*SYTOX Orange*
SPM	*Self-Phase Modulation*
SQL	*Standard Quantum Limit*
SRS	*Stimulated Raman Scattering*
SSA	*Signal Source Analyzer*
STED	*Stimulated Emission Depletion*
THG	*Third-Harmonic Generation*
TOD	*Third-Order Dispersion*
US	*Ultrasound Imaging*
VIS	*Visible Spectrum*
Yb	*Ytterbium*
YDF	*Ytterbium-Doped Fiber*
YFL	*Ytterbium-Doped Fiber Laser*
YFP	*Yellow Fluorescent Protein*

List of Publications

First Author Publications

- **M. Edelmann**, A. Matamoros-Angles, M. Shafiq, M. Pergament, M. Glatzel & F. X. Kärtner, "Deep-tissue two-photon brain imaging enabled by a tunable fiber-optic dispersive wave generator," *Scientific Reports* (Nature Portfolio) **15**, 24404 (2025).
- **M. Edelmann**, A. Matamoros-Angles, M. Shafiq, M. Pergament, F. X. Kärtner & M. Glatzel, "Multiplexed brain and visceral two-photon imaging using a simulation-guided ultrafast three-color fiber laser," *bioRxiv*, DOI: 10.1101/2025.06.19.660526 (2025).
- **M. Edelmann**, Y. Hua, K. Şafak, Y. El Sharkawy, M. Pergament, and F. X. Kärtner, "Optimized Noise and Stability Regimes in XPM-Suppressed All-PM Linear Mode-Locked Fiber Lasers," *J. Lightwave Technol.* **43**, 8378-8385 (2025).
- **M. Edelmann**, M. Pergament, Y. Hua, M.M. Sedigheh & F.X. Kärtner, "Fiber-interferometric second harmonic generator with dual-color standard quantum-limited noise performance," *Optics Express* **32**, 10362–10372 (2024).
- **M. Edelmann**, Y. Hua, M. Pergament & F.X. Kärtner, "Performance enhancement via XPM suppression of a linear all-PM mode-locked fiber oscillator," *Optics Letters* **49**, 1237–1240 (2024).
- **M. Edelmann**, M.M. Sedigheh, Y. Hua, E.C. Vargas, M. Pergament & F.X. Kärtner, "Large-mode-area soliton fiber oscillator mode-locked using NPE in an all-PM self-stabilized interferometer," *Applied Optics* **62**, 1672–1676 (2023).
- **M. Edelmann**, Y. Hua, G. Kulcsar & F.X. Kärtner, "All-polarization-maintaining divided pulse fiber oscillator mode-locked with the optical Kerr effect," *Optics Letters* **46**, 6083–6086 (2021).
- **M. Edelmann**, Y. Hua, K. Şafak & F.X. Kärtner, "Nonlinear fiber system for shot-noise-limited intensity noise suppression and amplification," *Optics Letters* **46**, 3344–3347 (2021).
- **M. Edelmann**, Y. Hua, K. Şafak & F.X. Kärtner, "Intrinsic amplitude-noise suppression in fiber lasers mode-locked with nonlinear amplifying loop mirrors," *Optics Letters* **46**, 1752–1755 (2021).

Co-Author Publications

1. N. Singh, J. Lorenzen, K. Wang, M.A. Gaafar, M. Sinobad, H. Francis, **M. Edelmann**, M. Geiselmann, T. Herr, S.M. Garcia-Blanco & F.X. Kärtner, "Watt-class silicon photonics-based optical high-power amplifier," *Nature Photonics* **19**, 307–314 (2025).
2. S. Malekmohamadi, M. Pergament, G. Kulcsar, M. Seidel, Y. Liu, **M. Edelmann**, M. Kellert, J. Thesinga, C.M. Heyl & F.X. Kärtner, "44-fs, 1-MHz, 70-µJ Yb-doped fiber laser system for high harmonic generation," *Optics Express* **32**, 39460–39468 (2024).
3. S. Okuyucu, U. Demirbas, J. Thesinga, **M. Edelmann**, M. Pergament & F. Kärtner, "Diode-pumped passively mode-locked femtosecond Yb:YLF laser at 1.1 GHz," *Optics Express* **32**, 15555–15564 (2024).

4. K. Şafak, E.C. Vargas, A. Dai, **M. Edelmann**, F. Emaury, K. Balskus, B. Rudin, P. Battle, T.D. Roberts, B. Slezak, T. Hawthorne & F.X. Kärtner, "Photonically referenced extremely stable oscillator," *Optics Letters* **49**, 977–980 (2024).
5. N.H. Matlis, Z. Zhang, U. Demirbas, C. Rentschler, K. Ravi, M. Youssef, G. Cirmi, M. Pergament, **M. Edelmann**, S.M. Mohamadi, S. Reuter & F.X. Kärtner, "Precise parameter control of multicycle terahertz generation in PPLN using flexible pulse trains," *Optics Express* **31**, 44424–44443 (2023).

International Conference Contributions

1. **M. Edelmann**, S. Gevorgyan, M. Pergament, C. Betzel & F.X. Kärtner, "Structural Biomedical Two-Photon Microscopy using a sub-35 fs, High-Energy (>40 nJ), Pre-Chirp Managed Yb:Fiber Laser System," *CLEO Europe*, Munich, Germany (2025).
2. **M. Edelmann**, A. Matamoros-Angles, M. Shafiq, M. Pergament, F.X. Kärtner & M. Glatzel, "Versatile two-photon brain imaging using a wavelength-tunable, fiber-optic dispersive wave generator," *Optica Biophotonics Congress*, San Diego, USA (2025).
3. **M. Edelmann**, A. Matamoros-Angles, M. Shafiq, M. Pergament, M. Glatzel & F. X. Kärtner, "Deep-Tissue Neuronal Two-Photon Imaging Using Pre-Chirp Managed Dispersive Waves," *Conference on Lasers and Electro-Optics (CLEO)*, Long Beach, USA (2025).
4. **M. Edelmann**, Y. Hua, K. Şafak, Y.E. Sharkawy, M. Pergament & F.X. Kärtner, "Enhancement of Kerr-type, all-PM, linear mode-locked fiber lasers via suppression of cross-phase modulation," *Laser Congress (ASSL, LAC, LS&C)*, Osaka, Japan (2024).
5. S. Okuyucu, U. Demirbas, J. Thesinga, **M. Edelmann**, M. Pergament & F.X. Kärtner, "11-GHz SESAM-mode-locked femtosecond Yb:YLF laser," *Conference on Lasers and Electro-Optics (CLEO)*, Charlotte, USA (2024).
6. **M. Edelmann**, M. Pergament, Y. Hua, M.M. Sedigheh & F.X. Kärtner, "Fiber-interferometric second harmonic generator for dual-color standard quantum-limited noise suppression," Conference on Lasers and Electro-Optics (CLEO), Charlotte, USA (2024).
7. **M. Edelmann**, M. Pergament & F.X. Kärtner, "Intra-pulse intensity noise shaping in a mode-locked fiber oscillator," *Conference on Lasers and Electro-Optics Europe & European Quantum Electronics Conference (CLEO/Europe-EQEC)*, Munich, Germany (2023).
8. N. Singh, J. Lorenzen, M. Sinobad, K. Wang, M.A. Gaafar, H. Francis, **M. Edelmann**, T. Herr, S.M. Garcia-Blanco & F.X. Kärtner, "Watt-class CMOS-compatible power amplifier," *Conference on Lasers and Electro-Optics Europe & European Quantum Electronics Conference (CLEO/Europe-EQEC)*, Munich, Germany (2023).
9. E.C. Vargas, K. Şafak, A. Dai, **M. Edelmann**, F. Emaury, B. Rudin, P. Battle, T.D. Roberts, T. Hawthorne & F.X. Kärtner, "Photonic microwave oscillator based on fiber delay stabilization using a waveguide balanced cross-correlator," *Conference on Lasers and Electro-Optics (CLEO)*, San Jose, USA (2023).
10. **M. Edelmann**, M. Pergament & F.X. Kärtner, "Intra-pulse intensity noise shaping by saturable absorbers," *Conference on Lasers and Electro-Optics (CLEO)*, San Jose, USA (2023).

11. S. Malekmohamadi, M. Pergament, Y. Liu, M. Seidel, **M. Edelmann**, M. Kellert, C.M. Heyl & F.X. Kärtner, "70-W, 1-MHz, sub-50-fs Yb-doped fiber laser system for high harmonic generation," *Conference on Lasers and Electro-Optics Europe & European Quantum Electronics Conference (CLEO/Europe-EQEC)*, Munich, Germany (2023).
12. Y. Hua, **M. Edelmann**, F.X. Kärtner & I. Hartl, "Influence of XPM in all-PM fiber oscillators mode-locked using NPE in linear self-stabilized fiber interferometers," *Conference on Lasers and Electro-Optics Europe & European Quantum Electronics Conference (CLEO/Europe-EQEC)*, Munich, Germany (2023).
13. E.C. Vargas, K. Şafak, A. Dai, **M. Edelmann**, F. Emaury, B. Rudin, P. Battle, T.D. Roberts, T. Hawthorne & F.X. Kärtner, "Low-noise photonic microwave oscillator based on a novel repetition rate stabilization," *Joint Conference of the European Frequency and Time Forum & IEEE International Frequency Control Symposium (EFTF/IFCS)*, Toyama, Japan (2023).
14. **M. Edelmann,** M. Pergament & F.X. Kärtner, "Large-mode-area soliton fiber oscillator mode-locked with linear self-stabilized Sagnac interferometer," *International Conference on Ultrafast Phenomena (UP)*, Montréal, Canada (2022).
15. **M. Edelmann,** Y. Hua, K. Şafak & F.X. Kärtner, "All-optical nonlinear noise suppression in state-of-the-art fiber oscillators and amplifiers," *Conference on Lasers and Electro-Optics (CLEO)*, San Jose, USA (2022).
16. **M. Edelmann**, Y. Hua, K. Şafak & F.X. Kärtner, "Nonlinear fiber amplifier for intensity-noise reduction to the shot-noise limit," *Conference on Lasers and Electro-Optics (CLEO)*, San Jose, USA (2021).
17. **M. Edelmann**, Y. Hua, K. Şafak & F.X. Kärtner, "Amplitude-noise suppressing mechanism in fiber lasers mode-locked with nonlinear amplifying loop mirror," *Laser Congress (ASSL, LAC)*, Washington, D.C., USA (2020).
18. **M. Edelmann**, Y. Hua, A. Koch & F.X. Kärtner, "Generation of 64-fs, 10-kW peak-power, transform-limited pulses directly from an Yb-doped Figure-9 fiber laser," *Conference on Lasers and Electro-Optics (CLEO)*, Washington, D.C., USA (2020).

1 Introduction

1.1 Biomedical Imaging: Advances, Limitations and Emerging Demands

Over the past decades, modern life sciences have undergone a profound technological transformation driven by advances in photonics [1–3], computational capabilities [4–6], and molecular biology [7–9]. These developments are central to addressing the most pressing biomedical challenges of our time that continue to limit human longevity and lifelong functional independence, including neurodegenerative diseases, cancer, and cardiovascular conditions. Alzheimer's and Parkinson's disease alone are projected to affect over 150 million globally by the year 2050, posing not only a growing burden on the healthcare systems but also deeply affecting patients, families, and caregivers [10–12]. In parallel, cancer remains a primary cause of worldwide mortality, with more than 10 million deaths annually and globally rising incidence rates [13].

Gaining a mechanistic understanding of these complex diseases and their impact on tissue morphology and cellular dynamics critically depends on the ability to visualize biological systems *in situ*, in real time and with sub-cellular resolution [14,15]. Consequently, imaging technologies have become indispensable across nearly all domains of biomedical research and clinical diagnostics and their continued advancement represents a central focus within adjacent fields such as bioengineering, photonics and applied physics in general [16–18]. The fundamental importance of advanced imaging technologies is reflected in several recent Nobel Prizes at the intersections of Chemistry, Physics, and Medicine, which recognized transformative breakthroughs in terms of resolution, molecular contrast, and dynamic imaging capabilities. Notable examples include Stimulated Emission Depletion (STED) super-resolution microscopy, pioneered by Stefan W. Hell, Eric Betzig, and William E. Moerner (Nobel Prize in Chemistry 2014) [19], cryo-electron microscopy, developed by Jacques Dubochet, Joachim Frank, and Richard Henderson (Nobel Prize in Chemistry 2017) [20], and fluorescent protein-based live-cell and structural imaging, enabled through the discovery and application of green fluorescent protein (GFP) by Osamu Shimomura, Martin Chalfie, and Roger Y. Tsien (Nobel Prize in Chemistry 2008) [21,7,22].

Over the years, a broad spectrum of imaging modalities has emerged to meet the diverse demands of biomedical applications. Different imaging technologies are thereby characterized by specific trade-offs in spatial resolution, imaging depth, field-of-view (FOV), acquisition speed, and compatibility with biological tissue. Their selection is typically dictated by the specific biological question, the sample architecture, and the required temporal or spatial scale. For a few selected imaging modalities, Fig.1.1 illustrates the fundamental trade-offs encountered in

many biomedical applications. Fig.1.1 (a) compares spatial resolution and imaging depth across a range of modalities, while Fig.1.1 (b) highlights their FOV limitations as a function of resolution. As shown, magnetic resonance imaging (MRI), positron emission tomography (PET), and ultrasound (US) enable large FOVs and imaging depths but are limited in spatial resolution. MRI for instance, a standard imaging technique in both research and clinical diagnostics, that utilizes strong magnetic fields and radiofrequency pulses to generate soft tissue contrast, enables whole-body imaging with a typical spatial resolution on the order of 0.5 to 1 mm [23]. In contrast, optical imaging methods such as widefield fluorescence imaging, confocal and multiphoton microscopy, and optical coherence tomography (OCT) typically achieve significantly higher spatial resolution in the micrometer range within scattering tissue, at the cost of reduced imaging depth and FOV, typically limited to a few millimeters [14,24,25].

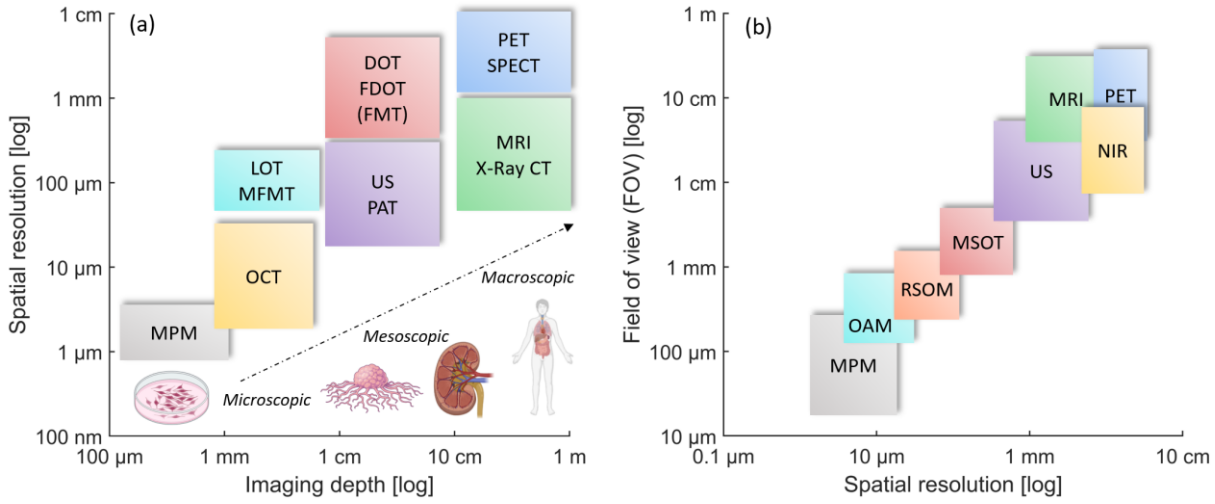

Figure 1.1: Performance comparison of biomedical imaging modalities. (a): Spatial resolution vs. imaging depth for representative biomedical imaging modalities, adapted based on data and layout from Ref. [26]. Created in part with BioRender.com. MPM: Multiphoton microscopy, LOT: laminar optical tomography, MFMT: mesoscopic fluorescence molecular tomography, OCT: optical coherence tomography, FDOT: fluorescent diffuse optical tomography, FMT: fluorescence molecular tomography, US: ultrasound imaging, PAT: photoacoustic tomography, PET: positron emission tomography, MRI: magnetic resonance tomography, CT: computed tomography. (b): Imaging modalities shown for the characteristic field of view vs. imaging depth, reproduced from Ref. [27]. OAM: opto-acoustic microscopy, MSOT: multispectral opto-acoustic microscopy, RSOM, raster-scan opto-acoustic microscopy, NIR: near infrared fluorescence imaging.

These contrasting performance regimes expose a fundamental limitation in biomedical imaging: no single modality simultaneously delivers the large FOVs and penetration depths required for macroscopic assessment while maintaining the sub-micrometer resolution necessary to resolve cellular and subcellular structures. Consequently, biological insight typically relies on the

combination of multiple, scale-specific imaging techniques, each optimized for a narrow operating regime. This intrinsic trade-off motivates the ongoing development of advanced technologies designed to further push imaging performance boundaries and enable more comprehensive interrogation of living systems.

1.2 Principles and Capabilities of Multiphoton Microscopy

Within the landscape of advanced imaging modalities, multiphoton microscopy (MPM) stands out as highly innovative and impactful technique in fields such as neuroscience [28], developmental biology [29], and cancer research [30]. As a unique characteristic, MPM relies on the nonlinear optical principle of multiphoton excitation, originally proposed in the year 1931 by Maria Goeppert-Mayer in her dissertation entitled *"Über Elementarakte mit zwei Quantensprüngen"* (Engl.: "Elementary processes with two quantum transitions") [31]. In her work, she described how the near-simultaneous absorption of two photons could drive a quantum transition equivalent to the absorption of a single photon at twice the energy. To illustrate the difference in signal generation between MPM and conventional fluorescence (one photon) microscopy (FM), Fig.1.2 (a) depicts the respective excitation schemes. In FM, excitation occurs through the absorption of individual photons with energy matching the electronic transition from the ground state S_0 to the first excited singlet state S_1 (excitation wavelength λ_{ex}) by fluorescent molecules labeling specific tissue structures or functional indicators. After rapid non-radiative relaxation, fluorescence emission occurs at a red-shifted wavelength λ_{em} as the electron returns to the ground state S_0 with a linear dependence on the excitation intensity. In contrast, MPM relies on the near-simultaneous absorption of two or more photons of excitation wavelength λ_{ex} to address the same energetic transition of the fluorophore, generating a fluorescence signal with λ_{em} that scales quadratically with the local excitation intensity for two-photon excitation, or cubically in the case of three-photon excitation.

The nonlinear excitation mechanism of MPM gives rise to several fundamental advantages over FM and other high-resolution imaging modalities. Most notably, as illustrated in Fig.1.2 (b), the fluorescent signal generation in MPM is inherently confined to a sub-femtoliter volume around the focal point, rather than being distributed along the entire excitation path as in FM. This confinement arises from the requirement of high photon densities for efficient multiphoton absorption, which naturally has its maximum close to the focal spot [28]. By scanning the tightly focused excitation volume through the specimen, MPM enables intrinsic optical sectioning and high-resolution three-dimensional reconstruction of complex tissue structures, while

simultaneously enhancing contrast and imaging depth by effectively suppressing out-of-focus fluorescence.

In addition, since most biomedically relevant fluorophores have absorption transitions in the visible spectrum (~300 - 600 nm) [25], multiphoton excitation enables their activation via multiple lower-energy near infrared (NIR) photons between 700 - 1700 nm [2,14]. This shift to longer excitation wavelengths offers several additional advantages. First, scattering losses are significantly reduced, as they scale approximately with λ^{-4}, which drastically improves the achievable imaging depth in highly scattering biological tissue such as brain or skin [32]. Second, NIR light experiences lower linear absorption by endogenous chromophores (e.g., hemoglobin and melanin), which minimizes photothermal effects, phototoxicity, and tissue damage [33,34]. These properties collectively enhance tissue viability and imaging depth, making MPM highly suitable for long-term imaging of live specimens, including *in vivo* studies or chronic experiments [29,35,36]. Unlike FM, which typically requires micrometer-scale thin tissue sections for high-resolution imaging [37], MPM routinely achieves subcellular-resolution imaging at depths exceeding 1 mm even in highly scattering brain and visceral tissues [38].

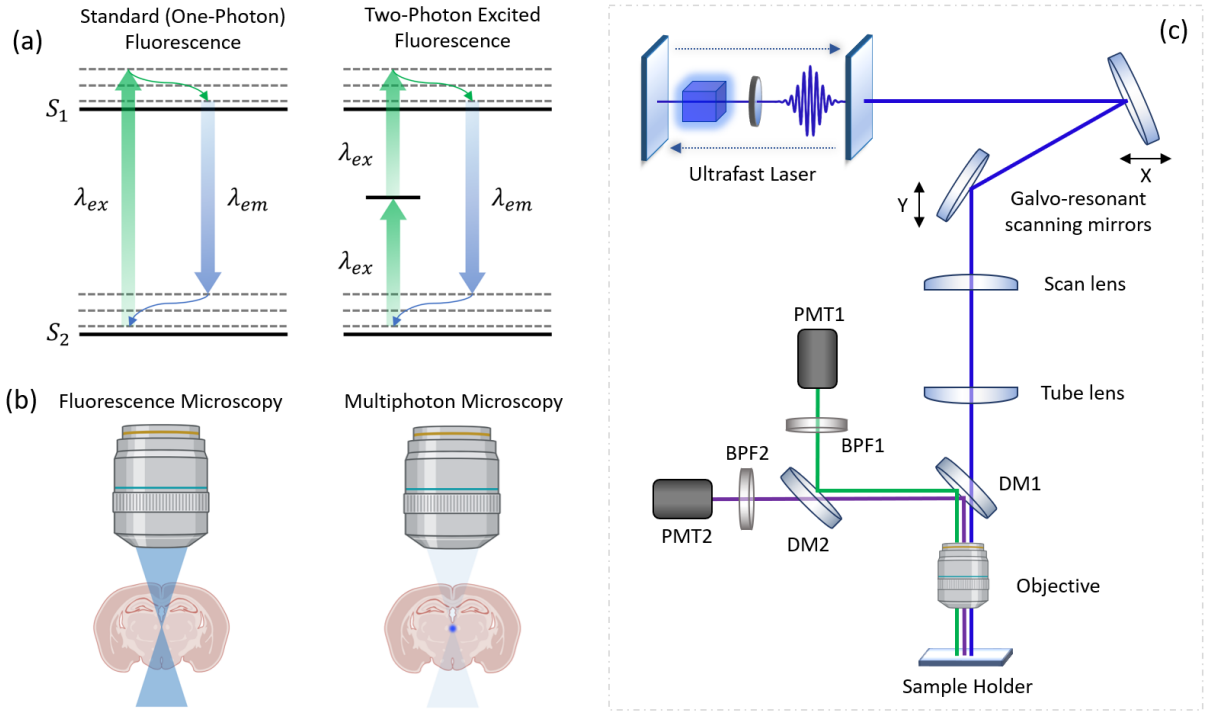

Figure 1.2: Working principle and optical configuration of multiphoton microscopy. (a): Excitation scheme for standard one-photon fluorescence and two-photon microscopy. (b): Corresponding fluorescent signal generation in the sample. (c): Typical experimental setup of a multiphoton scanning microscope. DM: dichroic mirror, BPF: bandpass filter, PMT: photo-multiplier tube. Created in part with BioRender.com

Another important advantage of MPM is its ability to generate parametric, label-free signals through second-harmonic generation (SHG) and third-harmonic generation (THG). These nonlinear processes provide intrinsic contrast based on molecular order, symmetry, and refractive-index variations, enabling the visualization of structural features such as collagen fibers, lipid-rich membranes, crystalline deposits, and tissue interfaces [39–41]. Because SHG and THG signals arise without the need for exogenous fluorophores, they can be detected in parallel with fluorescence emission, offering complementary information and mitigating the reliance of conventional FM on externally introduced labels or limited endogenous autofluorescence [25,42]. This multimodal capability combined with the aforementioned advantages has established MPM as a transformative tool for *in vivo* studies at substantial depths, driving breakthroughs such as large-scale neuronal network mapping to uncover principles of brain connectivity and function [43,44], the high-resolution analysis of tumor microenvironments to investigate cancer progression and therapeutic response [45], and the visualization of dynamic cellular interactions within developing embryos to study tissue morphogenesis and developmental processes [46].

A typical MPM setup, illustrated in Fig. 1.2 (c), consists of a femtosecond laser source, fast beam-scanning optics, a high-numerical-aperture objective, and highly sensitive detectors such as photomultiplier tubes (PMTs). Dichroic mirrors (DMs) and bandpass filters (BPFs) are used to spectrally separate excitation and emission channels. During imaging, the focused excitation spot is rapidly scanned across the sample in the x-y plane to cover the FOV, and the PMTs record the fluorescence signal at each pixel while a synchronized acquisition system reconstructs the image in real time.

A defining characteristic of MPM is the requirement for femtosecond pulses to enable the high peak intensities and photon densities in the focal spot required for efficient multiphoton excitation. To meet the demands of advanced MPM applications, the driving ultrashort-pulse laser systems must satisfy stringent requirements regarding wavelength coverage, pulse energy, pulse duration, and operational stability. For instance, two-photon fluorescence microscopy (2PFM) with exogenous fluorophores, which is extensively applied throughout this dissertation, requires broad tunability across roughly 700 to 1200 nm to match the absorption bands of common fluorophores and fluorescent proteins [47]. Efficient excitation further demands pulse energies in the tens of nanojoules at repetition rates of several tens of megahertz, with pulse durations below approximately 100 fs to generate the high peak intensities needed for nonlinear excitation while minimizing average power, thermal load, and phototoxicity [32].

In comparison, three-photon microscopy (3PM) excites the same fluorophores through the absorption of three photons in the 1300 to 1700 nm spectral window, which provides greater penetration depth because scattering and absorption in tissue decrease at longer wavelengths. However, 3PM requires substantially higher pulse energies, typically in the microjoule regime, together with pulse durations below ~50 fs to compensate for the inherently lower three-photon excitation probability [2,48,49].

1.3 Photonic Requirements and Limitations of Current Ultrafast Sources

The key enabling technology for generating energetic femtosecond pulses required for efficient multiphoton fluorescence excitation is the mode-locked laser. In contrast to the first continuous-wave laser demonstrated by Theodore Maiman in 1960 [50], which emitted a monochromatic and temporally continuous stream of coherent photons, mode-locked lasers operate by phase-locking multiple longitudinal cavity modes. This phase coherence compresses the optical field into a periodic train of ultrashort pulses with extremely high peak intensities. First demonstrated in the 1960s by DeMaria *et al.* using passive mode-locking in a Nd:Glass laser [51], this principle underlies all modern femtosecond laser systems and ultimately enabled the first 2PFM experiments by Denk *et al.* in 1990 [52]. Beyond biomedical imaging, mode-locked lasers play a central role in highly-advanced and transformative applications such as attosecond science and frequency-comb metrology, which were recognized through the Nobel Prizes in Physics 2023 and 2005, respectively [53–55].

For biomedical imaging and for MPM in particular, mode-locked titanium-doped sapphire (Ti:Sa) lasers have traditionally been used as the primary excitation source. These systems provide watt-level average power and broad tunability across 700 - 1000 nm, which is well suited for two-photon excitation of many established fluorophores [56,57]. While Ti:Sa lasers have been essential for advancing the field, their solid-state architecture introduces practical constraints, including relatively large footprint, alignment sensitivity, and the need for active thermal stabilization [58]. These factors can pose challenges for extended operation, clinical translation, and integration into compact or turnkey imaging systems.

At the same time, there has been a substantial trend toward novel red-shifted fluorophores with two-photon absorption peaks between 1000 and 1250 nm, which requires excitation wavelengths that extend beyond the intrinsic Ti:Sa gain bandwidth [59,60]. Nonlinear wavelength conversion using additional optical parametric oscillator (OPOs) or optical parametric amplifiers (OPAs) stages can access these longer wavelengths, but at the cost of increased system complexity, higher alignment demands, and greater maintenance overhead [61]. As a result,

many state-of-the-art MPM platforms remain predominantly located in specialized optics laboratories and are not yet widely deployed in broader biomedical or clinical environments [62–64].

These challenges have motivated strong interest in ultrafast fiber lasers, which offer compact system architectures, intrinsic mechanical stability, alignment-free operation, and straightforward energy scalability [65–67]. In fiber-based systems, the optical pulses propagate within a single-mode waveguide, typically composed of fused silica, which shields the beam path from environmental perturbations such as vibrations, thermal drift, and air currents. Their large surface-to-volume ratio enables efficient passive cooling and eliminates the need for water-cooled laser heads, while amplifier stages can be integrated with minimal additional complexity [68].

The strong confinement of the ultrashort and intense laser pulses in the fiber core, typically only a few micrometers in diameter, gives rise to a range of nonlinear light-matter interactions including self-phase modulation, self-steepening, and stimulated Raman scattering, together with dispersion profiles that can be tailored through the fiber design [69]. With modern numerical tools and established nonlinear theory, these effects can be precisely controlled and used for versatile spectral engineering of broadband supercontinua and tunable pulses far beyond the native fiber laser gain bandwidths [70–72]. They further enable the precise design of complex nonlinear systems such as mode-locked fiber oscillators and frequency-combs [73], fiber-optic interferometers for squeezed-light generation and precision metrology [74,75], or fiber-integrated parametric wavelength-conversion stages [76]. This combination of nonlinear flexibility, intrinsic stability, cost-effectiveness, and alignment-free operation makes fiber lasers a highly attractive technology platform for advanced MPM applications.

However, given these advantages of fiber lasers, there are several persistent technical constraints that currently limit their performance in the context of nonlinear biomedical imaging:

- **Spectral flexibility and tunability**
  Standard Yb-fiber gain is restricted to approximately 1020-1080 nm and does not directly cover important excitation bands in the 700-900 nm or 1100-1250 nm regions. As already mentioned, achieving broad or continuous tunability requires nonlinear spectral conversion with careful design of dispersion and nonlinear effects.

- **Energy-scaling and nonlinearity management**
  Scaling pulse energy beyond a few nanojoules in standard fibers can lead to excessive nonlinear phase accumulation, soliton breakup, Raman shifts, and associated pulse distortions. These nonlinearities impose strict constraints on power scaling unless tailored dispersive control or large-mode-area specialty fibers are used.

- **Noise and stability**
  Intensity noise from pump diodes, cavity fluctuations, and nonlinear phase noise can degrade fluorescence stability and limit functional imaging contrast. Timing jitter arises from guided ASE, dispersion fluctuations, and Kerr-induced phase variations, while environmental changes can affect polarization and long-term stability.

- **Multi-color and synchronized excitation**
  Many imaging applications require two or more synchronized wavelengths. Generating multiple femtosecond pulses with sufficient spectral coverage, high peak power and ultra-low noise from a single platform is challenging and typically requires additional nonlinear stages or complex system designs to ensure ideal performance.

- **Application-specific constraints in biological imaging**
  Deep-tissue 2PM benefits from tunable wavelengths, low noise, and high peak intensity, yet achieving all three simultaneously remains technically challenging due to the constraints outlined above. Additional general factors such as dispersion management, heat-load control, and compatibility with resonant scanning systems further influence the practical performance of fiber-laser-based excitation sources.

As outlined in the following section, these limitations define the central technological challenges addressed throughout this dissertation, where a combination of fiber-laser engineering, interferometric noise control, and nonlinear spectral design is used to push the capabilities of ultrafast fiber lasers toward compact, robust, and highly versatile excitation platforms to enable next-generation MPM applications.

1.4 Objectives and Structure of This Dissertation

State-of-the-art MPM applications increasingly rely on excitation sources that combine low noise, spectral agility, multi-color capability, and robust energy delivery within compact, alignment-stable and highly adaptable architectures. These requirements are driven by a broad range of emerging optical interrogation techniques for highly advanced visualization of biological structure and function across multiple spatial, temporal, and spectral scales. Prominent examples include ultrafast voltage and functional imaging of synaptic and circuit-level dynamics [77–79], widefield and mesoscopic *in vivo* recordings across large neuronal populations [80,81], and miniaturized or head-mounted two-photon systems enabling deep-tissue imaging in freely moving animals [82–84]. Similar performance demands also arise in advanced

multiphoton spectroscopy, nonlinear contrast microscopy, and multimodal optical readout schemes that combine imaging with stimulation or control.

As MPM applications continue to expand in capability and complexity, the limitations of conventional ultrafast laser technologies become increasingly apparent. Many state-of-the-art experiments depend on costly and complex multi-source configurations composed of synchronized lasers or multiple OPO/OPA stages. Such approaches inherently restrict spectral reach, scalability, and long-term stability, while posing significant challenges for synchronized multicolor and dynamically reconfigurable excitation schemes [85–87]. These constraints are further enhanced in demanding experimental environments, particularly in *in vivo* applications, where optical excitation, optogenetic stimulation, and electrophysiological readout are intrinsically noisy and highly sensitive to parameter fluctuations, environmental perturbations, and synchronization drifts between laser sources and the imaging system [78,88–90].

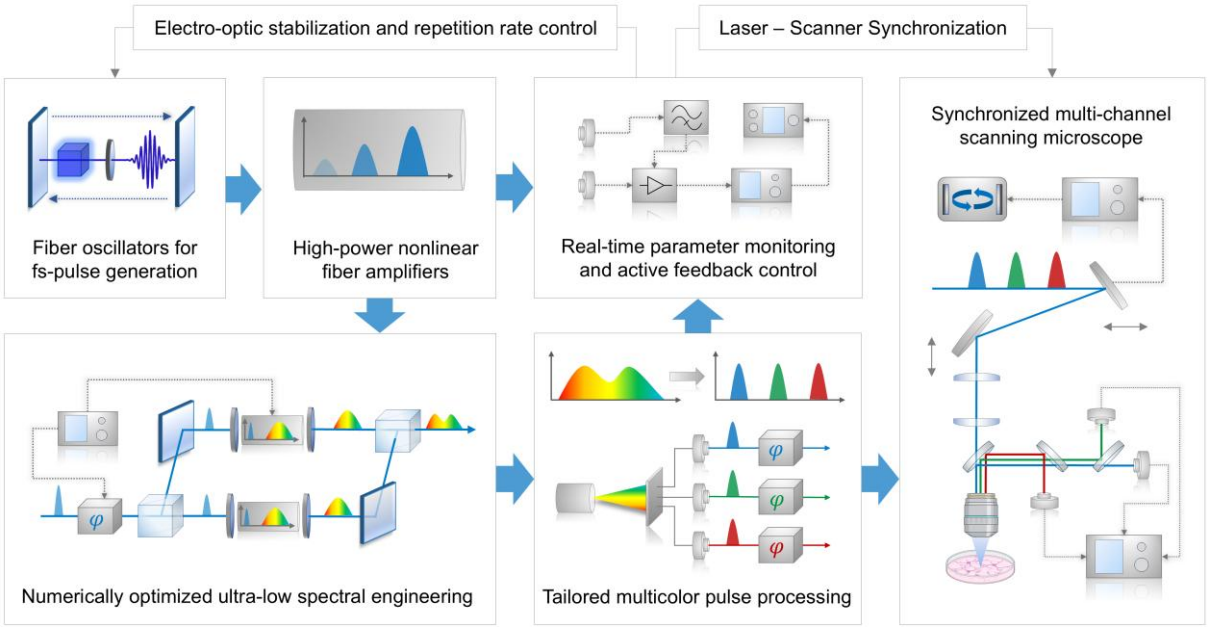

Figure 1.3: High-level overview of the fiber-optic photonic technologies developed in this dissertation, spanning robust femtosecond pulse generation, energy-scalable amplification, ultra-low-noise spectral engineering, multicolor wavelength conversion, and synchronized multi-channel two-photon microscopy. Created in part with BioRender.com

Meeting the performance demands of advanced MPM and related nonlinear optical techniques would therefore immensely benefit from a shift toward integrated, precisely engineered photonic platforms, in which ultrafast laser design, nonlinear pulse evolution and energy scaling, noise and drift management, wavelength conversion, and multiphoton excitation are treated as tightly interconnected elements of a unified, application-adaptable system. This system-level

perspective, treating novel photonic technologies as interdependent elements of a unified MPM platform, forms the conceptual foundation of this dissertation. While the primary motivation is rooted in biomedical imaging, the photonic strategies and design principles introduced here are equally relevant to precision spectroscopy, optical metrology, ultrafast quantum optics, nonlinear wavelength conversion, and coherent control, underscoring their broader applicability beyond a single application domain.

To illustrate the technological realization of such this unified imaging platform approach Fig. 1.3 presents a conceptual overview of an integrated fiber-optic MPM architecture, highlighting the complete pathway from highly-stable femtosecond pulse generation in performance-enhanced fiber oscillators, through energy-scalable and nonlinearity-managed amplification, interferometric noise stabilization with simulation-guided spectral engineering, and multi-color wavelength conversion, to high-performance two-photon imaging in a multi-channel resonant-scanning microscope. Guided by this framework, this dissertation is organized into the following complementary chapters:

- **Chapter 2** establishes the theoretical foundations of ultrafast nonlinear fiber photonics and multiphoton microscopy. It reviews fundamental noise mechanisms in femtosecond lasers, including amplitude noise, phase noise, and timing jitter, and formulates a hierarchy of nonlinear Schrödinger equations (NLSEs) ranging from gain-modified and coupled forms to the full generalized NLSE. The chapter further develops a semiclassical stochastic framework to include quantum and technical noise into generalized NLSE simulations, enabling quantitative modeling of coherence degradation and noise transfer in nonlinear fiber systems. Finally, it summarizes the governing principles of nonlinear contrast generation in MPM, including two-photon fluorescence and harmonic generation.
- **Chapter 3** presents fiber-optic modules for ultra-low-noise pulse-generation, wavelength-conversion, and noise-control that form the core of the photonic imaging platforms. The chapter introduces XPM-suppressed femtosecond fiber oscillators with Kerr-type interferometric saturable absorbers and quantitatively analyzes their noise performance and energy scalability across distinct mode-locking regimes. Building on this foundation, a fiber-interferometric dual-color source operating at the standard quantum-limited intensity noise floor is demonstrated, and the interferometric concept is extended to achieve ultra-low-noise supercontinuum generation in dispersion-engineered photonic crystal fibers (PCFs). In addition, an energetic ultrafast Ytterbium-fiber laser

system is developed to drive the subsequent two-photon imaging platforms. Collectively, these systems constitute a modular toolbox for low-noise, multi-color, and energy-scalable femtosecond pulse generation.

- **Chapter 4** translates the developed photonic toolbox into a tunable deep-tissue excitation platform driven by an all-PM Yb-fiber laser driver for ultrashort, energetic pulse generation. Using generalized NLSE simulations and dispersion-engineered photonic crystal fibers, the chapter realizes efficient, phase-matched dispersive-wave excitation between 880 and 950 nm, producing sub-100 fs, nanojoule-level pulses with high stability. Integrated into a resonant-scanning two-photon microscope, this platform enables deep-tissue imaging across multiple biological system, including EGFP-labeled mouse hippocampus and SYTOX-Orange-labeled cerebellum, resolving neuronal and vascular structures at depths beyond 600 μm. Chapter 4 thus demonstrates the platform-level deployment of the developed fiber-optic sub-systems for tunable deep-tissue MPM.
- **Chapter 5** extends the developed photonic framework and laser architecture into a multicolor excitation platform built on a ground-up developed nonlinear fiber laser combined with deterministic spectral-engineering for efficient multicolor two-photon excitation. Guided by numerical design tools developed in earlier chapters, the system generates three spectrally isolated and temporally synchronized excitation bands at approximately 940 nm, 1080 nm, and 1175 nm. This platform enables simultaneous multitarget excitation across a broad range of biological preparations, including triple-labeled mouse brain, kidney, and liver tissue, and is further validated through a preliminary *in vivo* assay in transgenic *C. elegans* for prospective Alzheimer-related screening. Comprehensive analyses of spectral separation, and multicolor imaging performance establish the resulting three-color architecture as a compact, scalable, and biologically versatile implementation of the unified photonic imaging platform for advanced multiplexed MPM.

2 Theoretical Fundamentals

To establish the theoretical foundation for the ultrafast photonic subsystems and multiphoton imaging platforms developed in this dissertation, this chapter introduces the core physical concepts of nonlinear pulse generation, fiber-optic propagation, supercontinuum generation, noise dynamics, and multiphoton contrast formation. To this end, Section 2.1 reviews the fundamental noise mechanisms of femtosecond lasers, covering the general principle of mode-locking influenced by quantum-limited and technical noise contributions, explaining how amplitude noise, phase noise, and timing jitter degrade the stability and coherence of optical pulse trains. Section 2.2 presents the nonlinear Schrödinger equation (NLSE) as the central framework for modeling ultrashort pulse evolution in passive and active fibers, discussing gain-modified, coupled, and generalized forms that enable accurate numerical descriptions of amplification, fiber-laser dynamics, multi-channel interactions, nonlinear interferometers, and supercontinuum generation in PCFs. Section 2.3 extends this numerical framework by including semi-classical stochastic noise, detailing how the one-photon-per-mode model of quantum noise and Gaussian technical noise provide a quantitative description to simulate quantum-initiated instabilities and noise transfer in generalized NLSE models. Finally, Section 2.4 outlines the principles of nonlinear contrast generation in MPM, including two-photon fluorescence and parametric harmonic generation, together with the spatial-resolution considerations relevant to the imaging applications addressed in later chapters.

2.1 Noise of Femtosecond Lasers

Mode-locked lasers generate femtosecond pulses through constructive interference of longitudinal resonator modes (υ_m), that (i) lay within the gain bandwidth, (ii) exceed the net loss per roundtrip; and (iii) fulfill the resonance condition $\nu = m\,c/2L$, where m is a positive integer, c the speed of light, and L the resonator length [91]. In continuous-wave (CW) lasers, longitudinal modes oscillate independently, resulting in a narrowband output laser field. In contrast, mode-locking enforces a fixed phase relationship between the modes via implementation of saturable absorbers (SA); nonlinear elements whose transmission increases with intensity, enabling ultrashort pulse formation from broadband constructive interference [92]. Common SAs include semiconductor devices [93], dyes [94], and mechanisms such as Kerr-lens mode locking [95] or nonlinear interferometers (NLIs) operating on the optical Kerr-effect [96].

The difference in CW and mode-locked laser operation is illustrated in Fig. 2.1. Panels (a) and (b) show simplified resonator configurations for CW and mode-locked lasers, respectively.

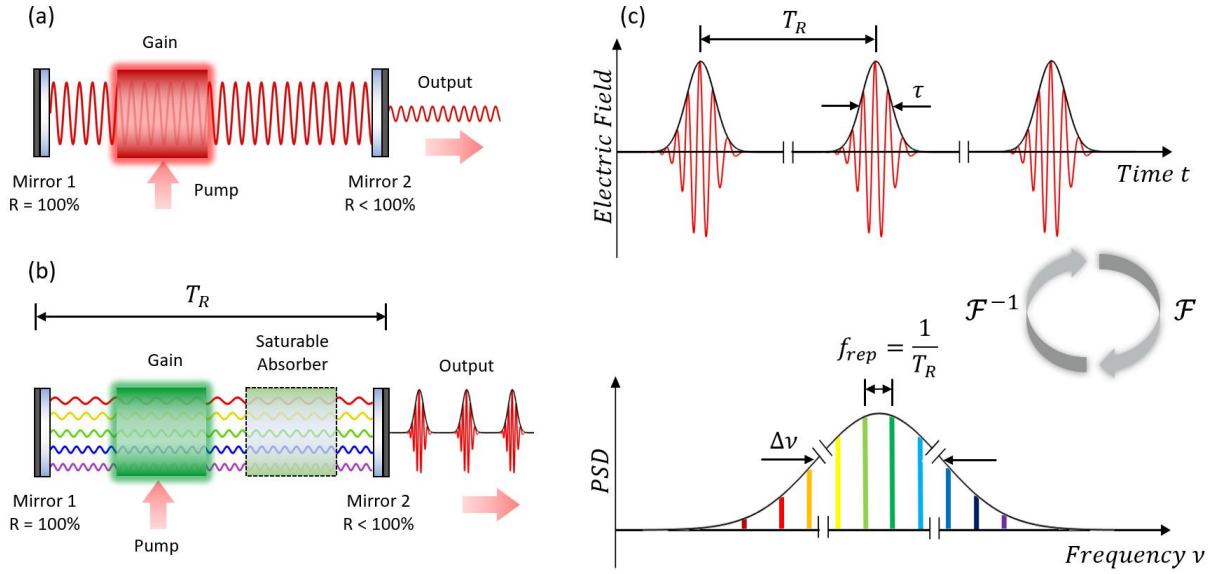

Figure 2.1: Comparison of continuous-wave and mode-locked laser operation**.** (a): CW laser cavity with gain medium and independent longitudinal modes. (b): Mode-locked cavity including a saturable absorber to lock the phases of multiple modes. (c): Temporal output of a mode-locked laser: a train of femtosecond pulses spaced by the roundtrip time T_R. (d) Frequency-domain output: a comb of phase-locked modes with spacing f_{rep} and bandwidth $\Delta\nu$. The bi-directional arrow highlights the Fourier relationship between time and frequency domains.

In the CW case, only a small number of uncorrelated modes contribute to a nearly monochromatic output field, whereas the inclusion of a saturable absorber in the mode-locked cavity results in a phase-locked, coherent addition of many modes. Fig.2.1 (c) shows the resulting output of the mode-locked laser in frequency and time domain together with its fundamental Fourier-relation. In time-domain, the constructive interference of many sinusoidal longitudinal laser modes results in a periodic train of optical pulses with spacing equal to the roundtrip time T_R. In frequency-domain, this corresponds to a discrete comb of equidistant optical frequencies with spacing $f_{rep} = 1/T_R$ and bandwidth $\Delta\nu$, governed by the number of locked modes.

The stability of such pulse trains is fundamentally limited by noise coupled into the intracavity field, originating from quantum vacuum fluctuations, amplified spontaneous emission (ASE), pump power instabilities, mechanical vibrations, and environmental drifts [97]. The complex field $A(t)$ of a noise-perturbed pulse train can be expressed as

$$A(t) = \big(A_0 + \delta A_0(t)\big) \sum_{m=-\infty}^{+\infty} a\big(t - mT_R + \delta T_R(t)\big)\ exp\big\{i\big(2\pi\nu_c t + m\phi_{CE} + \delta\theta(t)\big)\big\} \tag{2.1}$$

where, A_0 denotes the nominal pulse amplitude, $\delta A_0(t)$ the amplitude noise, δT_R the timing-jitter, ν_c the carrier-frequency, ϕ_{CE} the carrier-envelope phase-shift per roundtrip, and $\delta\theta(t)$

the residual phase-noise of the respective field [73]. Eq. (2.1) defines the three main noise categories discussed below in greater detail: amplitude noise, phase noise, and timing jitter.

2.1.1 Amplitude and Relative Intensity Noise

Amplitude noise refers to fluctuations in pulse amplitude, affecting instantaneous intensity, pulse energy, and average power. In nonlinear processes such as multiphoton excitation and supercontinuum generation, where signals scale nonlinearly with intensity, such fluctuations can directly degrade the signal-to-noise ratio (SNR), signal coherence, and reproducibility.

The relative intensity noise (RIN) spectrum is a practical means to quantify amplitude fluctuations. In logarithmic form, it is express in units dBc/Hz as

$$RIN_{dB}(f) = 10log_{10}\frac{S_{\delta P}(f)}{P_0^2} \tag{2.2}$$

were, P_0 is the average optical power on the photodetector, and $S_{\delta P}(f)$ the single-sided power spectral density (PSD) of the power fluctuations $\delta P(t)$ in units W^2/Hz. The PSD is defined via the Wiener-Khinchin theorem:

$$S_{\delta P}(f) = \int_{-\infty}^{+\infty} \langle \delta P(t)\delta P(t+\tau)\rangle e^{-i2\pi f\tau} d\tau \tag{2.3}$$

Integrating Eq. (2.2) in linear form yields the RMS RIN, often expressed in percentage, which is used as a normalized and comparable performance metric for ultrafast laser systems [98].

Even in the complete absence of technical or environmental noise, direct detection of an ideal coherent laser field is bounded by the shot-noise limit arising from Poissonian photon statistics [99]. In this case, the detected photocurrent shows a flat (“white”) noise floor, which corresponds to a shot-noise-limited RIN of

$$RIN_{SQL} = \frac{2h\nu}{P_0} \tag{2.4}$$

with h Planck’s constant and ν the optical frequency [97]. This limit represents the standard quantum limit for direct power measurements and should be distinguished from quantum noise sources that seed fluctuations inside the laser cavity, such as spontaneous emission and vacuum fluctuations coupled through loss, which can drive amplitude, phase, and timing instabilities of the emitted pulses.

2.1.2 Phase Noise and Timing-Jitter

Phase noise describes random fluctuations of the optical carrier phase and is modeled as a time-dependent phase perturbation $\delta\phi(t)$ on carrier. It is quantified by the PSD of $\delta\phi(t)$:

$$S_\phi(f) = \int_{-\infty}^{+\infty} \langle \delta\phi(t)\delta\phi(t+\tau)\rangle e^{-i2\pi f\tau} d\tau \tag{2.5}$$

Integrating Eq. (2.5) over a frequency range $[f_1, f_2]$ yields the total phase variance σ_ϕ^2 in rad^2, representing the accumulated phase fluctuations within that bandwidth [73,98,100]. In practice, phase noise is commonly measured via heterodyne detection, RF beat-note analysis, or signal-source analyzers (SSAs), and expressed as single-sideband (SSB) phase noise in dBc/Hz,

$$\mathcal{L}(f) = 10log_{10}\left(\frac{S_\phi(f)}{2}\right) \tag{2.6}$$

where the factor of two accounts for conversion from double-sided to single-sided PSD.

In contrast, timing jitter refers to random variations in pulse arrival time relative to an ideal, equidistant grid defined by the roundtrip time T_R. It is typically modeled as a stochastic perturbation $\delta T_R(t)$ added to the nominal emission times nT_R in Eq. (2.1) [100]. Timing jitter leads to autocorrelation and cross-correlation broadening in the time domain, and to phase noise on the repetition rate and its harmonics in the RF spectrum. As result, it is particularly critical for synchronization, optical sampling, frequency-comb stabilization, and time-resolved measurements [101–104]. The PSD of the temporal displacement fluctuations $\delta T_R(t)$ is described by:

$$S_T(f) = \int_{-\infty}^{+\infty} \langle \delta T_R(t)\delta T_R(t+\tau)\rangle e^{-i2\pi f\tau} d\tau \tag{2.7}$$

Integrating $S_T(f)$ over $[f_1, f_2]$ yields the total timing variance σ_T^2. The square root σ_T, typically expressed in femtoseconds, denotes the timing-jitter of the pulse train [73]. While phase noise and timing jitter describe different physical processes, they are often coupled in ultrafast laser systems through dispersion and nonlinear effects [83]: optical carrier-phase fluctuations can convert into timing errors via group delay dispersion, and timing jitter can induce phase fluctuations through stochastic pulse-carrier misalignment [89].

2.2 Nonlinear Schrödinger Equation (NLSE)

2.2.1 Standard NLSE and Gain Implementation

The NLSE is the fundamental mathematical framework for modeling ultrashort pulse propagation in optical fibers [69]. Starting from standard form, sufficient to describe most mode-locked fiber oscillators, amplifiers, and interferometric systems, including additional effects such as higher-order dispersion, Raman scattering, and self-steepening, lead to the generalized NLSE (GNLSE) used in advanced modeling of strongly nonlinear processes such as supercontinuum generation (SCG) and dispersive-wave conversion in PCFs [71].

First derived by Hasegawa and Tappert in 1973 to describe solitons in dielectric waveguides [105,106], the NLSE governs the evolution of the pulse envelope $A(z,t)$ along the propagation distance z and in a co-moving time frame t, accounting for group velocity dispersion (GVD) and the optical Kerr effect. It follows from Maxwell's equations under the slowly varying envelope approximation. Assuming negligible loss and higher-order effects, the NLSE takes the form:

$$\frac{\partial A}{\partial z} + \frac{\beta_2}{2}\frac{\partial^2 A}{\partial t^2} = i\gamma|A|^2 A \tag{2.8}$$

Here, β_2 is the GVD parameter and γ the nonlinear coefficient of the dielectric waveguide. The GVD originates from a Taylor expansion of the propagation constant $\beta(\omega)$ around the carrier frequency ω_0 [107]:

$$\begin{aligned}\beta(\omega) &= \sum_{k=0}^{\infty} \frac{1}{k!} \left.\frac{d^k \beta}{d\omega^k}\right|_{\omega_0} (\omega - \omega_0)^k \\ &= \beta_0 + \beta_1(\omega-\omega_0) + \frac{1}{2}\beta_2(\omega-\omega_0)^2 + \frac{1}{6}\beta_3(\omega-\omega_0)^3 + \cdots,\end{aligned} \tag{2.9}$$

Here, β_1 denotes the group velocity, β_2 the GVD, and β_3 the third-order dispersion (TOD). Higher-order dispersion terms become relevant for ultrashort pulses with broad bandwidths. The sign of β_2 determines whether the dispersion is normal ($\beta_2 > 0$; higher-frequency components travel more slowly) or anomalous ($\beta_2 < 0$; higher frequencies travel faster), thereby influencing instantaneous frequency ("chirp") and temporal broadening. The nonlinear coefficient γ arises from the Kerr-induced refractive index change:

$$n(I) = n_0 + n_2 I = n_0 + n_2|A|^2 \tag{2.10}$$

where n_0 is the linear and n_2 the nonlinear refractive index [92,107]. Here, $\gamma = n_2\omega_0/cA_{eff}$, with A_{eff} as the effective mode area. The underlaying optical Kerr effect, originating from the third-order susceptibility $\chi^{(3)}$, gives rise to important nonlinear effects such as self-phase modulation (SPM), cross-phase modulation (XPM), and four-wave mixing (FWM) [69].

SPM, central to many applications in this work, describes the nonlinear phase shift

$$\phi_{NL} = \gamma L|A(t)|^2 \tag{2.11}$$

accumulated in Kerr-media such as optical fibers over the propagation distance L [107]. Since ϕ_{NL} depends on the instantaneous intensity, it varies across the pulse envelope and induces an instantaneous frequency shift:

$$\delta\omega(t) = -\frac{d\phi_{NL}}{dt} = -\gamma L\frac{d|A(t)|^2}{dt} \tag{2.12}$$

This effect causes spectral broadening of the pulse, since rising and falling edges of the pulse generate new frequency-components. With normal dispersion SPM leads to temporal broadening, while anomalous dispersion regime enables pulse compression and soliton formation [69].

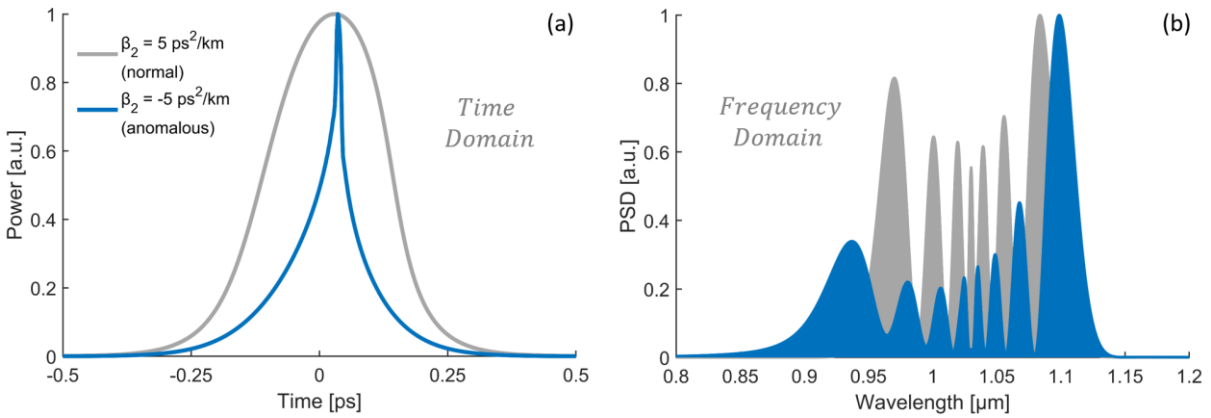

Figure 2.2: Effect of normal and anomalous GVD on pulse propagation in the time and frequency domains. (a): Simulated temporal pulse profiles (normalized) after propagation with SPM combined with normal (grey) and anomalous (blue) dispersion $\beta_2 = \pm 5\ ps^2/km$ in 33 mm fiber. (b): Corresponding normalized output spectra.

Both regimes are illustrated in Fig.2.2, where nonlinear propagation of a Fourier-limited pulse with duration $\tau_p = 200\ fs$ and pulse energy $E_p = 20\ nJ$ is simulated in a fiber with $\beta_2 = \pm 5\ ps^2/km$, $A_{eff} = 16\ \mu m^2$ and $L = 33\ mm$. To include optical gain and loss, the NLSE can be modified with an additional term, taking the form [108]:

$$\frac{\partial A}{\partial z} + \frac{\beta_2}{2}\frac{\partial^2 A}{\partial t^2} + \frac{(g-\alpha)}{2}A = i\gamma|A|^2 A \tag{2.13}$$

Here, g denotes the wavelength-dependent gain factor and α the attenuation coefficient of the optical waveguide. For doped fibers, g is modeled using rate equations for the population dynamics, which yield propagation equations for pump and signal power [109,110]:

$$\frac{dP_p}{dz} = \eta_p\left(\sigma_{21}^{(p)} n_2 - \sigma_{12}^{(p)} n_1\right) N_{tot} P_p \tag{2.14}$$

$$\frac{dP_s}{dz} = \eta_s\left(\sigma_{21}^{(s)} n_2 - \sigma_{12}^{(s)} n_1\right) N_{tot} P_s \tag{2.15}$$

where, $\eta_{p,s}$ are the overlap factors between pump/signal modes and the doped fiber core; $\sigma_{12}^{(p,s)}$ and $\sigma_{21}^{(p,s)}$ are the absorption/emission cross sections; $P_{p,s}$ the average pump/signal powers; $n_{1,2}$ the ground- and excited-state population densities; and N_{tot} the total dopant concentration.

2.2.2 Coupled NLSEs and Cross-Phase Modulation

In addition to SPM, another important nonlinear effect in this dissertation is cross-phase modulation (XPM), arising from Kerr-induced refractive index change caused by one optical field acting on another. This leads to mutually induced nonlinear phase shifts that is particularly relevant for the nonlinear propagation characteristics of co-propagating orthogonal polarization modes (OPMs) in standard, non-PM optical fibers. The nonlinear propagation of two such fields, here denoted $A_x(t)$ and $A_y(t)$, is described by two coupled NLSEs in the form [69]:

$$\frac{\partial A_x}{\partial z} = -\beta_{1,x}\frac{\partial A_x}{\partial t} - \frac{i\beta_2}{2}\frac{\partial^2 A_x}{\partial t^2} + \frac{g}{2}A_x + i\gamma\left(|A_x|^2 + \kappa\left|A_y\right|^2\right)A_x \tag{2.16}$$

$$\frac{\partial A_y}{\partial z} = -\beta_{1,y}\frac{\partial A_y}{\partial t} - \frac{i\beta_2}{2}\frac{\partial^2 A_y}{\partial t^2} + \frac{g}{2}A_y + i\gamma\left(\left|A_y\right|^2 + \kappa|A_x|^2\right)A_y \tag{2.17}$$

Here, $\beta_{1,x}$ and $\beta_{1,y}$ are the inverse group velocities of the respective OPM, accounting for linear phase-velocity differences and walk-off during propagation. The fields are nonlinearly coupled through the XPM terms $\kappa\left|A_{y,x}\right|^2$, which describe the intensity-dependent phase shifts induced by one mode onto the other. The total nonlinear phase shift experienced by each mode is:

$$\phi_{NL,x}(t) = \gamma L\left(|A_x(t)|^2 + \kappa\left|A_y(t)\right|^2\right) \tag{2.18}$$

The factor κ quantifies the nonlinear interaction strength between the OPM, with $\kappa = 2/3$ for orthogonally polarized fields and $\kappa = 2$ in the scalar, co-polarized case [69]. In non-PM fibers, XPM enables coupling of fluctuations between polarization states, which can lead to enhanced noise transfer between modes and degraded pulse stability in ultrafast fiber systems [111,112].

2.2.3 Generalized NLSE, Raman Scattering and Self-Steepening

The NLSE in Eq. (2.8) describes nonlinear pulse evolution in fiber systems with high accuracy for moderate pulse durations and limited spectral broadening. However, for ultrashort pulses and broadband propagation in more extreme nonlinear regimes, for example in fiber-based supercontinuum generation (SCG), a more comprehensive model is required to account for higher-order dispersive and nonlinear effects. This extended mathematical framework is provided by the generalized nonlinear Schrödinger equation (GNLSE) [71]:

$$\frac{\partial A}{\partial z} + \left(\sum_{n\geq 2} \frac{i^{n-1}}{n!}\beta_n \frac{\partial^n A}{\partial T^n}\right) = i\gamma\left(1 + \frac{i}{\omega_0}\frac{\partial}{\partial T}\right)\left(A(z,T)\int_{-\infty}^{+\infty} R(t')|A(z,T-t')|^2 dt'\right) \tag{2.19}$$

The left-hand side includes higher-order dispersion coefficients β_n obtained from the Taylor expansion of the propagation constant in Eq. (2.9). The right-hand side describes nonlinear effects including SPM, self-steepening, and stimulated Raman scattering (SRS). The Raman contribution is modeled through the nonlinear response function $R(t)$, which accounts for both the instantaneous electronic and delayed vibrational response of the medium:

$$R(t) = (1 - f_R)\delta(t - t_e) + f_R h_R(t) \tag{2.20}$$

Here f_R denotes the fractional Raman contribution ($f_R = 0.18$ for fused silica fibers [69]), t_e the sub-femtosecond electronic response delay, and $h_R(t)$ the vibrational Raman response that determines the temporal profile and strength of the delayed nonlinearity. An analytical approximation for fused silica is given by [69]:

$$h_R(t) = (\tau_1^{-2} + \tau_2^{-2})\tau_1 exp\left\{-\frac{t}{\tau_2}\right\} sin\left(\frac{t}{\tau_1}\right) \tag{2.21}$$

where $\tau_1 = 1/\Omega$, with $\Omega \equiv \omega_p - \omega_s$ denoting the frequency difference between pump and Stokes waves, and τ_2 is the vibration dampening time. Throughout this dissertation, $\tau_1 =$

12.2 fs and $\tau_2 = 32\ fs$ are used according to Ref. [69]. Through this delayed nonlinear response, SRS transfers energy from higher-frequency pump components to lower-frequency Stokes components via molecular vibrations. The efficiency of this process is governed by the Raman gain spectrum $g_R(\Omega)$, which is proportional to the imaginary part of the Fourier transform of $h_R(t)$.

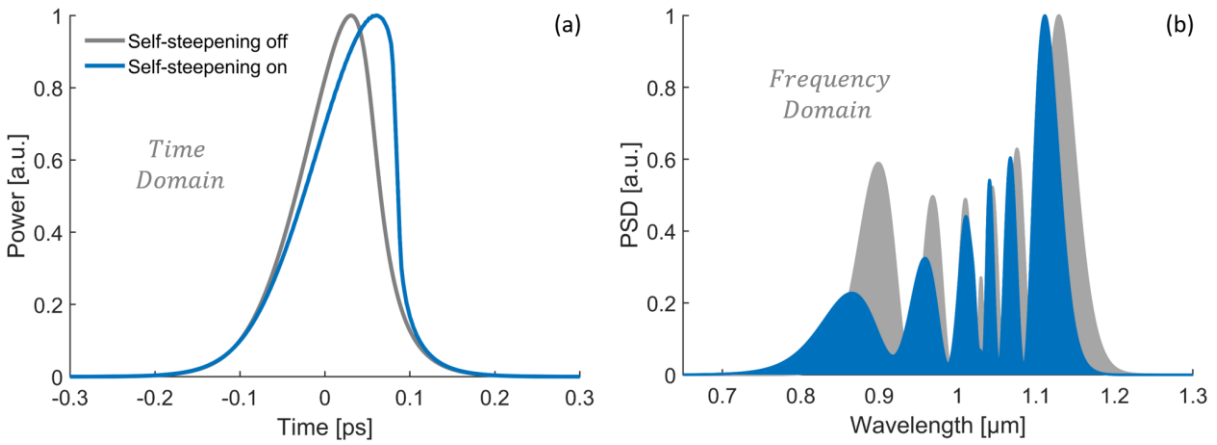

Figure 2.3: Effect of self-steepening on nonlinear pulse propagation in the time and frequency domains. (a): Simulated time-domain pulse profiles (normalized to peak power) at the fiber output with self-steepening disabled (gray) and enabled (blue). (b): Corresponding normalized output spectra.

Self-steepening describes an additional nonlinear effect that leads to asymmetric temporal distortion of the pulse envelope as a consequence of the intensity-dependent group velocity associated with the optical Kerr effect. Physically, higher-intensity regions of the pulse experience a slightly reduced group velocity, causing the trailing edge to compress while the leading edge stretches [113]. In the GNLSE introduced in Eq. (2.19), self-steepening is accounted for by the $(i/\omega_0)\,\partial/\partial T$ operator.

If only the instantaneous Kerr nonlinearity is considered and other effects such as dispersion and Raman scattering are neglected, the contribution of self-steepening can be isolated and written in the form of a shock term [69]:

$$\frac{\partial A}{\partial z} = i\gamma\tau_{shock}\frac{\partial}{\partial T}(|A|^2 A) \tag{2.22}$$

where the shock time constant $\tau_{shock} = 1/\omega_0$ defines the temporal scale over which steepening occurs (~0.4 fs at 1550 nm). The influence of time-domain shock formation and self-steepening is illustrated in Fig. 2.3, which presents numerical GNLSE simulations without dispersion for a transform-limited Gaussian pulse with $\tau_p = 100\ fs, E_p = 10\ nJ, A_{eff} = 16\ \mu m^2$ and a prop-

agation length of $L = 30\ mm$. The simulations show the development of an asymmetric temporal pulse profile and the corresponding asymmetric spectral broadening when self-steepening is included.

2.3 Stochastic Modelling of Semi-Classical Noise and Coherence

2.3.1 Classical Noise, Coherence and Quantum Fluctuations

An important aspect of nonlinear pulse propagation is the emergence and wavelength-dependent transfer of parameter fluctuations. In the form of Eq. (2.19), the GNLSE is deterministic and therefore does not capture the stochastic quantum and technical noise that is present in real ultrafast laser systems [97,98,100]. To realistically model the evolution and influence of such fluctuations, particularly in highly nonlinear regimes such as SCG, stochastic perturbations must be introduced to obtain a stochastic GNLSE framework [71].

In the semi-classical formulation of the stochastic GNLSE, quantum noise is implemented by adding random complex perturbations to the spectral field, corresponding to one photon of random phase per mode (that is, per frequency bin) of the discretized input spectrum $\tilde{A}(\omega)$ [71]. Numerically, this can be implemented as

$$\tilde{A}_{noisy}(\omega) = \tilde{A}(\omega) + \sqrt{\frac{\hbar\omega}{2}\Delta\omega}[X_\omega + iY_\omega] \tag{2.23}$$

where X_ω and Y_ω are independent Gaussian random variables with zero mean and unit variance, and $\Delta\omega$ is the size of the discretized frequency bins [71,114]. This normalized expression ensures that the added perturbation carries the correct physical noise energy per mode, independent of the chosen spectral resolution. Technical noise sources, including RIN (see Section 2.1.1), can be superimposed in either the time or frequency domain using Gaussian statistics matched to measured experimental values. For example, laser RIN can be modeled by drawing random values from a Gaussian distribution with a standard deviation equal to the measured RMS RIN and applying these fluctuations multiplicatively to the noiseless input pulse realizations to simulate shot-to-shot variations [115]. By running a large ensemble of noise realizations ($N \gg 1$), the stochastic GNLSE framework enables statistical evaluation of key performance metrics such as spectral and time-domain stability, wavelength-dependent RIN, and coherence.

Spectral coherence is a particularly important metric for assessing the quality and stability of supercontinua, as it quantifies the shot-to-shot reproducibility of both spectral amplitude and

phase. High coherence indicates that different realizations produce nearly identical spectral fields, whereas low coherence reflects strong noise amplification during nonlinear propagation [71]. The first order spectral coherence between two independent realizations is defined as

$$g_{12}^{(1)}(\lambda) = \frac{\langle E_1^*(\lambda) E_2(\lambda) \rangle}{\sqrt{\langle |E_1(\lambda)|^2 \rangle \langle |E_2(\lambda)|^2 \rangle}} \tag{2.24}$$

where $E(\lambda)$ denotes the complex spectral field at wavelength λ, and the brackets indicate averaging over all realization pairs. Values of $\left| g_{12}^{(1)} \right| = 1$ correspond to full spectral coherence, while values approaching zero indicate complete decoherence [115].

Beyond coherence, the stochastic ensemble framework further neables quantitative analysis of noise transfer through nonlinear propagation. To this end, a wavelength-resolved noise transfer function (NTF) can be defined as:

$$NTF(\lambda) = \frac{RIN_{out}(\lambda)}{RIN_{in}} \tag{2.25}$$

This ratio reveals whether a spectral component experiences net amplification ($NTF > 1$) or suppression ($NTF < 1$) of RIN during propagation, providing direct insight into the interplay of dispersion, nonlinearity, and noise-coupling mechanisms across the generated spectrum.

The stochastic GNLSE provides a powerful numerical framework for investigating intrinsic noise transfer, spectral coherence, and intra-spectral noise correlations in supercontinua generated in photonic crystal fibers (PCFs) and other highly nonlinear fibers (HNLFs). To illustrate the stochastic dynamics of SCG under different dispersion conditions and their impact on noise amplification and coherence, Fig. 2.4 compares numerical GNLSE simulations for a PCF operated near the zero-dispersion regime and in the all-normal-dispersion (ANDi) regime, each evaluated using an ensemble of 100 statistically independent pulse realizations with noise.The simulated pulses have a sech^2-shaped temporal profile and include both technical noise, modeled as 0.25% RIN, and quantum-noise implemented as described above. The pulses are centered at 1.04 µm with a Fourier-limited pulse duration of 100 fs and 13 nJ pulse energy.

Figure 2.4 (a) shows the dispersion profile of a PCF in the *zero-dispersion regime*, which has a MFD of 4.3 µm at a wavelength of 1.06 µm, a NA of 0.2 and $n_2 \approx 3.1 * 10^{-20}\ m^2/W$. In this case, the pump wavelength coincides with the fiber's zero-dispersion wavelength (ZDW) λ_{zwd}. In this regime, higher-order dispersion and self-phase modulation jointly initiate soliton dynamics that rapidly evolve during propagation.

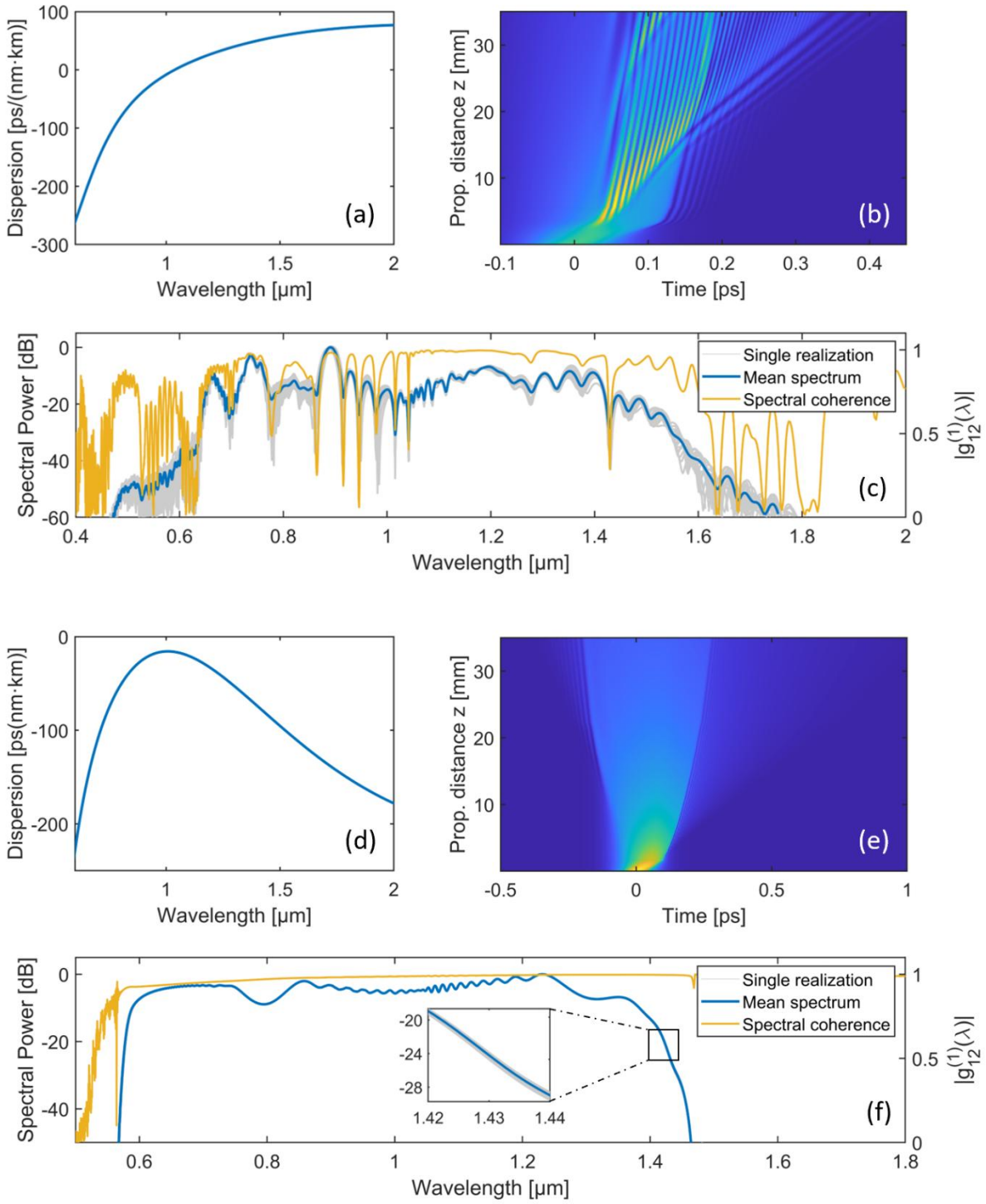

Figure 2.4: Numerical comparison of stochastic SCG noise and coherence in different dispersion regimes. (a-c): Anomalous-dispersion regime. (a): Dispersion profile of the PCF with $\lambda_{zdw} = 1.04\ \mu m$. (b): Simulated temporal evolution of the optical pulse along the propagation distance z. (c): Resulting output spectra for individual stochastic realizations (gray) together with the mean spectrum (blue) and the corresponding spectral coherence $| g_{12}^{(1)}(\lambda) |$ (yellow). (d-f): Simulated SCG in the normal-dispersion regime. (d): Corresponding ANDi-PCF dispersion profile. (e): Temporal pulse evolution along z. (f): Output spectra and spectral coherence analogous to (c). Inset: visualization of comparably low pulse-to-pulse spectral variance between 1.42-1.44 µm.

Fig.2.4 (b) shows the simulated temporal evolution in 35 mm of this PCF, illustrating the breakup of the initial pulse into multiple soliton components (soliton fission) accompanied by the emission of dispersive waves at longer wavelengths. These dynamics result in a strongly modulated spectral and temporal structure, characteristic of the high-nonlinearity ZDW regime.

The resulting output spectra, shown in Fig.2.4 (c), further reveal substantial shot-to-shot variation between individual realizations and the ensemble-averaged spectrum. The corresponding calculated spectral coherence $| g_{12}^{(1)}(\lambda) |$ displays pronounced modulation and rapid decay in regions associated with soliton fission, confirming noisy and low coherence SCG that is typical for this regime.

In contrast, Fig.2.4 (d) presents the dispersion profile of a PCF designed for ANDi operation, with a MFD of 2.6 µm at a wavelength of 1.06 µm, a NA of 0.2 and $n_2 \approx 2.9 * 10^{-20}\ m^2/W$. Here, the monotonic normal dispersion suppresses soliton formation and enables spectral broadening dominated by SPM and optical wave-breaking (OBW) [71]. The corresponding propagation map in Fig.2.4 (e) shows smooth temporal evolution without pulse breakup, indicating highly deterministic broadening behavior. The resulting output spectrum in Fig.2.4 (f) shows a nearly flat spectral envelope with minimal variations between single realizations and the ensemble-averaged spectrum, reflecting ultra-low noise performance due to the absence of the highly sensitive soliton dynamics and associated quantum noise amplification. In addition, the spectral coherence remains close to unity across the entire bandwidth confirming that the ANDi regime supports near-perfect reproducibility and shot-to-shot stability.

2.3.2 Intra-spectral Noise Distribution and Correlations

While the analysis so far enabled insight into the stability and coherence of the generated supercontinuum, it does not reveal how intensity fluctuations are distributed and correlated across the spectrum. To quantify the intra-spectral noise transfer during SCG [71,116], it is convenient to consider the energy within a narrow bandpass window centered at λ_0. For each of the n realizations, the corresponding band energy is then given by the relation

$$E_n(\lambda_0) = \sum_i w(\lambda_i; \lambda_0) I_n(\lambda_i) \Delta\lambda \tag{2.26}$$

where $w(\lambda_i; \lambda_0)$ is a normalized bandpass function (e.g., Gaussian) of bandwidth $\Delta\lambda_{BPF}$, $I_n(\lambda_i)$ the spectral intensity of the respective realization, and $\Delta\lambda$ the spectral sampling interval of the discrete wavelength grid. The wavelength-dependent RIN is then given by the coefficient

$$RIN_{band}(\lambda_0) = \frac{\sqrt{\langle E(\lambda_0)^2\rangle - \langle E(\lambda_0)\rangle^2}}{\langle E(\lambda_0)\rangle} \tag{2.27}$$

which is typically expressed as percentage [115]. By stepwise variation of the filter central wavelength λ_0, this approach yields a one-dimensional map of the local noise amplitude distribution across the supercontinuum.

To describe how fluctuations at different spectral components are statistically related, the intra-spectral noise correlation can be characterized using a Pearson correlation coefficient between the relative intensity deviations

$$\delta I_n(\lambda_i) = \frac{I_n(\lambda_i) - \langle I(\lambda_i)\rangle}{\langle I(\lambda_i)\rangle} \tag{2.28}$$

The corresponding correlation matrix

$$C(\lambda_i, \lambda_j) = \frac{\langle \delta I(\lambda_i)\delta I(\lambda_j)\rangle}{\sqrt{\langle \delta I(\lambda_i)^2\rangle \langle \delta I(\lambda_j)^2\rangle}} \tag{2.29}$$

quantifies the degree of correlated or anti-correlated power fluctuations between the spectral components λ_i and λ_j [117]. The coefficient $C(\lambda_i, \lambda_j)$ takes values in the range $-1 \leq C \leq 1$, where

- $C > 0$ indicates positive correlation, corresponding to synchronous intensity fluctuations (co-growth or co-depletion of power in the two bands),
- $C < 0$ denotes anti-correlation, implying an energy exchange or redistribution between the spectral components, and
- $C = 0$ represents statistical independence (no correlation).

Figure 2.5 provides a detailed analysis of the wavelength-resolved RIN and intra-spectral noise correlations of the simulated supercontinua for the ANDi and ZDW regimes introduced in Fig.2.4. For the ANDi case, Fig.2.5 (a) shows the simulated output spectrum together with the corresponding intra-spectral RIN distribution. The generated ANDi spectrum has a smooth, monotonic shape typical of SPM- and OBW-dominated broadening, accompanied by a low RIN level of only a few percent across large parts of the spectrum, with a steep increase towards the edges. The corresponding intra-spectral correlation map, shown in Fig.2.5 (b), reveals a high

degree of positive correlation along the diagonal, with minimal off-diagonal structure, indicating that noise fluctuations remain spectrally localized and weakly coupled between different wavelength components. This behavior reflects the deterministic and highly coherent character of SCG in the normal-dispersion regime [118].

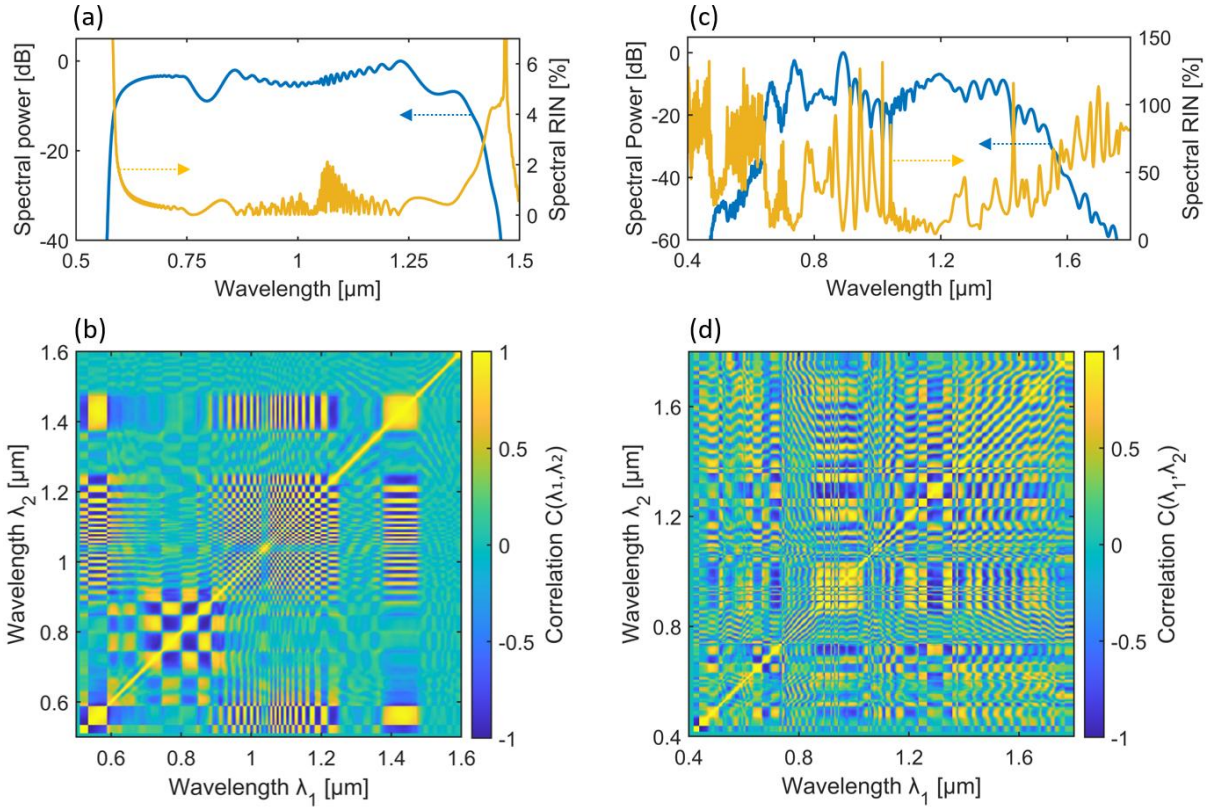

Figure 2.5: Simulated intra-spectral RIN and noise correlations in ANDi and zero-dispersion SCG regimes. (a): Mean spectrum (blue) and intra-spectral RIN trace (yellow) for the supercontinuum generated in the ANDi-PCF. (b): Corresponding intra-spectral Pearson noise correlation map $C(\lambda_1, \lambda_2)$. (c): Simulated mean spectrum (blue) with intra-spectral RIN distribution (yellow) and corresponding noise correlation map in (d).

The simulated output spectrum and corresponding wavelength-resolved RIN distribution for the ZDW case is shown in Fig.2.5 (c). In contrast to the smooth spectral shape of the ANDi case, the ZDW spectrum exhibits pronounced spectral modulation resulting from soliton fission as discussed earlier. The RIN strongly increases across most of the spectrum and exceeds 50 % in several spectral regions, particularly near the soliton and dispersive-wave components, reflecting the stochastic nature and efficient quantum-noise amplification of the underlying pulse dynamics. The corresponding intra-spectral correlation map, displayed in Fig. 2.5 (d), shows a complex oscillatory pattern with alternating regions of positive and negative correlation, validates strong cross-wavelength coupling of noise fluctuations due to nonlinear interactions between solitons and dispersive waves during propagation [71].

From the perspective of spectrally versatile MPM platforms, the contrasting noise and coherence properties of different SCG regimes have important practical implications. Supercontinuum generation in the ZDW regime provides access to highly nonlinear soliton-driven dynamics and efficient energy redistribution across widely separated spectral regions, but these mechanisms are intrinsically sensitive to quantum and technical noise and therefore require deliberate, often simulation-guided system design. When properly engineered, ZDW-based SCG enables targeted energy transfer into spectrally isolated components that are inaccessible by direct laser emission.

In contrast, ANDi-regime SCG offers smooth spectral broadening with high coherence and low wavelength-dependent noise, making it well suited for stable multi-color excitation schemes. As demonstrated in the following chapters, these complementary regimes form the basis of distinct, application-optimized ultrafast fiber-laser platforms for advanced multiphoton microscopy.

2.4 Principles of Multiphoton Microscopy

2.4.1 Mechanisms for Nonlinear Contrast Generation

As outlined in the introduction, MPM relies on femtosecond laser pulses to enable the large photon densities around the focal spot required to drive efficient multiphoton excitation. Signal generation in MPM arises either from multiphoton excitation of fluorescent molecules or from parametric wavelength conversion within the sample via second- and third-harmonic generation (SHG, THG) [41,57]. In the case of two-photon excitation (TPE) fluorescence, which will be extensively applied throughout this dissertation, the TPE rate of a given fluorescent molecule in Goeppert-Mayer units (GM) is given by:

$$R_{TPE} = \delta \frac{P_{avg}^2}{\tau_p f_{rep}^2 A_{eff}^2} \phi \tag{2.26}$$

where δ is the two-photon absorption cross-section, P_{avg} the average on-sample laser power, τ_p the pulse duration (FWHM), f_{rep} the laser repetition rate, A_{eff} the effective focal area, and $\phi = h\upsilon$ the photon energy [119]. As illustrated in Fig. 2.6, a wide range of fluorescent markers can be utilized for TPE, covering excitation cross-sections in a broad bandwidth between 700 – 1200 nm. These include endogenous fluorophores (e.g., NADH, FAD, elastin) that enable label-free imaging, and exogenous dyes or genetically encoded fluorescent proteins (e.g., fluorescein derivatives, Alexa Fluor series, GFP, YFP, mCherry) that provide targeted labeling of

specific cellular or subcellular structures [42,47,120,121]. The choice of marker depends on the available excitation wavelengths, required photostability, quantum yield, and compatibility with the biological system under investigation [52,57].

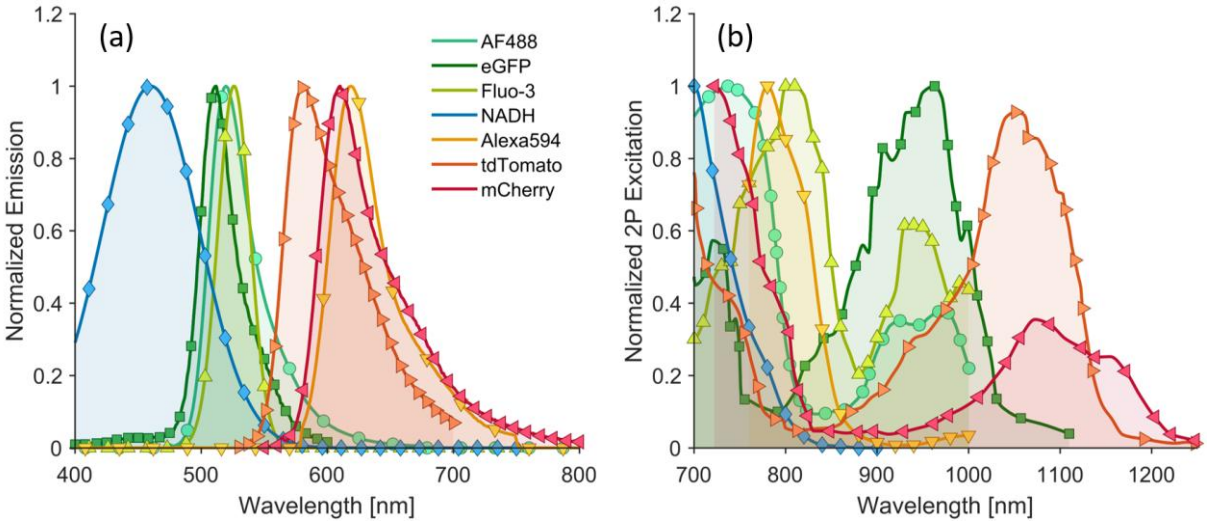

Figure 2.6: Spectral properties of common endogenous and exogenous fluorophores (AF488, eGFP, Fluo-3, NADH, Alexa594, tdTomato, and mCherry). (a): Normalized emission spectra. (b): Normalized two-photon excitation cross-sections versus excitation wavelength. Solid lines represent interpolations of tabulated data; markers indicate the underlying measured values. The shaded regions highlight the normalized envelopes (scaled to unity) to emphasize spectral placement instead of the absolute magnitude.

In contrast, SHG and THG contrast generation arises from coherent frequency conversion of the input pulses in non-centrosymmetric media $\chi^{(2)}$ or $\chi^{(3)}$ media, respectively [122]. With input power P_ω, the generated parametric second harmonic signal power $P_{2\omega}$ scales with:

$$P_{2\omega} \propto \frac{\omega^2 d_{eff}^2 L^2}{n_\omega^2 n_{2\omega} c^3 \epsilon_0} P_\omega^2 \tag{2.27}$$

where d_{eff} is the effective second-order coefficient, L the interaction length, n the refractive indices at the relevant frequencies, ϵ_0 the vacuum permittivity, c the speed of light.

The THG signal power $P_{3\omega}$ scales with:

$$P_{3\omega} \propto \frac{\omega^2 \chi^{(3)} L^2}{n_\omega^3 n_{3\omega} c^3 \epsilon_0} P_\omega^3 \tag{2.28}$$

In tissue, SHG originates from highly ordered structures such as collagen, while THG arises at refractive-index interfaces, both demonstrating directional emission and phase-matching sensitivity [119,122].

2.4.2 Spatial Resolution and Point-Spread-Function (PSF)

The spatial resolution of two-photon microscopy is fundamentally governed by diffraction and is fully characterized by the system's point-spread function (PSF). The PSF describes the three-dimensional intensity distribution produced by the microscope in response to an infinitesimally small emitter, and therefore sets the smallest spatial features that can be reliably resolved. In a high-NA objective, the lateral and axial extents of the PSF are primarily determined by the illumination wavelength and the focusing geometry [123].

As mentioned before, a key distinction from one-photon fluorescence microscopy lies in the nonlinear excitation mechanism: because the two-photon absorption probability scales quadratically with the local intensity, fluorescence is generated almost exclusively within the central high-intensity region of the focus. As a result, the effective two-photon PSF is narrower than its one-photon counterpart, providing intrinsic optical sectioning and improved background suppression without the need for a pinhole [32,57].

Under ideal diffraction-limited conditions, the lateral and axial resolutions can be approximated by $\Delta r \approx 0.7\,\lambda/NA$ and $\Delta z \approx 2.3\,\lambda n/NA^2$, respectively, where λ is the excitation wavelength, NA the numerical aperture of the objective and n the refractive index of the sample [124]. These relations highlight the main design trade-offs: shorter wavelengths and higher NA yield finer resolution, whereas longer wavelengths (commonly used in biological imaging to reduce scattering) broaden the PSF. In practice, refractive-index inhomogeneities, aberrations in the optical train, and sample-induced wavefront distortions further influence the PSF, especially at increasing imaging depths. Hence, the PSF provides a quantitative framework for analyzing spatial resolution, contrast formation, and the three-dimensional sectioning capability of MPM.

3 Ultra-low Noise Fiber-Optic Subsystems

This chapter presents the conceptual design, experimental realization, and systematic optimization of ultra-low-noise fiber-optic subsystems for femtosecond pulse generation and processing, forming the technological foundation for the advanced MPM platforms implemented in later chapters. The developments span a broad range of novel ultrafast fiber-optical technologies, including environmentally robust, all-polarization-maintaining mode-locked oscillators with enhanced performance metrics, interferometric schemes for quantum-limited multi-color intensity noise suppression, ultra-low-noise supercontinuum generation in dispersion-engineered photonic crystal fibers, and simulation-guided nonlinear fiber amplification stages enabling energetic ultrashort pulse generation.

All subsystems developed in this chapter follow the common guiding principle outlined in the introduction: the deliberate and predictive engineering of a fiber-optic technology toolbox to control amplitude and phase noise, timing stability, scalable pulse energy, and efficient, tunable multi-color wavelength conversion. Together, these capabilities enable the integration of advanced MPM platforms for deep-tissue and multicolor optical interrogation of complex biological systems.

Parts of this chapter are based on results previously published in the following peer-reviewed articles:

- M. Edelmann, *et al.*, "Optimized Noise and Stability Regimes in XPM-Suppressed All-PM Linear Mode-Locked Fiber Lasers," J. Lightwave Technol. 43, 8378-8385 (2025).
- M. Edelmann *et al.*, “Performance enhancement via XPM suppression of a linear all-PM mode-locked fiber oscillator,” *Opt. Lett.* 49, 1237 - 1240 (2024).
- M. Edelmann *et al.*, “Large-mode-area soliton fiber oscillator mode-locked using NPE in an all-PM self-stabilized interferometer,” *Appl. Opt.* 62, 1672 - 1676 (2023).
- M. Edelmann *et al.*, “Fiber-interferometric second-harmonic generator with dual-color standard quantum-limited noise performance,” *Opt. Express* 32, 10362-10372 (2024).

All sections have been revised, expanded, and reformatted to provide a unified presentation and additional discussion in the context of this dissertation.

3.1 XPM-Suppressed Ultra-low Noise Femtosecond Fiber Oscillators

Fiber oscillators are nonlinear optical systems that enable the generation of highly stable optical femtosecond pulse trains based on the mechanism of mode-locking (see Section 2.1). This

makes them a core technology of advanced ultrafast laser applications in fields such as nonlinear biomedical imaging [58], timing-and synchronization of large-scale facilities [125], photonic microwave generation [126] and frequency metrology [127]. In the context of MPM, fiber oscillators are widely applied both as near-infrared (NIR) stand-alone excitation sources, delivering intense MHz-rate, sub-100 fs pulses with low RIN and timing-jitter [128–130], and as robust master oscillators integrated in complex tunable laser platforms designed for tailored pulse generation (e.g., based on SCG and parametric wavelength conversion), to extend spectral reach and address a broader range of fluorophores and biomolecular markers [131–133].

Over the past few decades, a wide range of fiber-laser architectures and saturable-absorber (SA) mechanisms have been developed and successfully implemented. Within this landscape, all-PM fiber oscillators mode-locked using Kerr-type interferometers have emerged as a particularly powerful technology, enabling unprecedented noise performance while simultaneously offering state-of-the-art robustness, versatility, and broadband generation of ultrashort pulses [73,96]. This enhanced performance is enabled by all-PM fiber structures, which incorporate stress-rod elements that impose a large and well-defined birefringence. When the input polarization is aligned with a principal fiber axis, the polarization state is preserved and polarization crosstalk is strongly suppressed [134]. As a result, environmental perturbations such as temperature, vibration, or humidity that induce random birefringence fluctuations in non-PM fibers do not lead to polarization rotation or operating-point drift in all-PM cavities, thereby reducing intracavity noise transfer and improving long-term output stability [135].

Another important technical reason for the superior performance of Kerr-type all-PM mode-locked lasers is the application of NLIs which act as artificial SA mechanisms to initiate and stabilize mode-locked steady-states [136]. NLIs convert a differential nonlinear phase-shift $\Delta\varphi_{nl}$ between two interferometer arms into self-amplitude modulation via polarizing elements or direct interference [96]. Due to the instantaneous response of the Kerr effect, NLIs are exceptionally fast SAs which support broadband, sub-100 fs pulses while simultaneously avoiding the parameter degradation of material-based SAs (e.g., dyes, semiconductors, or topological insulators) [137,138] and the parameter drift and instability common in non-PM ring-cavities mode-locked via the mechanism of nonlinear polarization evolution (NPE) [139].

NLI-type SAs can be realized in a variety of different architectures, most prominently in form of nonlinear amplifying/optical loop mirrors (NALM/NOLM); asymmetric fiber loops where $\Delta\varphi_{nl}$ is accumulated between counter-propagating pulses [140,141]. Another NLI variant is the linear self-stabilized interferometer (LSI), where $\Delta\varphi_{nl}$ is accumulated between OPMs in a linear fiber segment [142]. In recent years, the ongoing development and optimization of

LSI oscillators has revealed a series of advantages such as simplified cavity structures [143] and novel adaptation pathways for power scaling and ultra-low noise performance, some of which are subject of this dissertation [111,144,145]. Despite their strong potential to define the next state-of-the-art in fiber-optic pulse generation, LSI oscillators remain constrained by distortions in the mode-locked state, manifesting as spectral modulations with corresponding time-domain pulse deformation, as well as self-starting difficulties, excess nonlinear loss of the SA and reduced noise performance and energy-scalability compared to NALM/NOLM lasers [111,112,146].

In this chapter, novel approaches and modifications are presented to overcome the limitations of LSI mode-locked fiber lasers, establishing them as distortion-free, energy-scalable, and ultra-low-noise femtosecond sources for advanced ultrafast applications. First, the working principle of NLIs as artificial SA is introduced, together with a representative experimental implementation of LSI oscillators. The NLI mechanism is described analytically by deriving the intensity-dependent transmission function $T(\Delta\varphi_{nl})$ using the Jones formalism for linear and nonlinear intra-cavity polarization evolution. On this basis, and supported by detailed numerical simulations, it is shown that the distortions previously observed in LSI oscillators originate from XPM-induced nonlinear cross-talk between OPMs in the cavity.

Building on this insight, a birefringent XPM-suppression concept using intra-cavity yttrium orthovanadate (YVO_4) crystals is introduced and analyzed numerically and experimentally. In the implemented configuration, a 10 mm YVO_4 crystal introduces a temporal pre-separation of approximately 6.5 ps between the circulating OPMs, thereby eliminating XPM-induced cross-talk. Experimentally, this suppresses the characteristic spectral ripple and pulse distortions, reduces nonlinear loss in the artificial saturable absorber, and lowers the mode-locking threshold by more than 45%. Stochastic simulations and comparative measurements further demonstrate a broadened stable operating window and improved noise performance: in stretched-pulse operation, the integrated RIN is reduced from approximately 0.07% to 0.04% and the RMS timing jitter from about 22 fs to 14.5 fs (3 kHz - 5 MHz), while in the soliton regime the RIN decreases from roughly 0.08% to 0.06% and the jitter from about 87 fs to 39 fs (9 kHz - 5 MHz).

Finally, a cavity architecture for efficient energy scaling based on specialty PM large-mode-area (LMA) fibers is developed and characterized. An all-PM LSI oscillator employing a 25 µm-core PLMA fiber at 17.3 MHz is demonstrated to deliver approximately 10 nJ total pulse energy (about 5.4 nJ at Port T and 4.3 nJ at Port R) and 170 mW average power, corresponding to a 36-fold energy increase over an otherwise matched 5.5 µm-core reference, together with

up to 5-8 dB lower high-frequency (>20 kHz) RIN, for example 0.027% versus 0.033% integrated from 20 kHz to 5 MHz at Port T.

Taken together, these results establish a new class of XPM-suppressed interferometric fiber oscillators as flexible and highly adaptable ultra-low-noise femtosecond pulse generators for advanced MPM laser drivers an dother ultrafast applications. Beyond providing a robust and energy-scalable master oscillator, the detailed investigation of the NLI mechanism reveals general design principles for controlling nonlinear noise coupling in fiber-based interferometric systems. As demonstrated in the subsequent chapters, this insight is crucial for enabling novel ultra-low-noise nonlinear wavelength-conversion technologies and supercontinuum-based spectral engineering into MPM-relevant excitation bands.

3.1.1 Phase-biased Nonlinear Fiber Interferometers as Saturable Absorbers

As an initial step, the fundamental operating principle of LSI fiber oscillators and their operation as artificial SA mechanism are outlined. To this end, Fig.3.1 (a) illustrates a representative cavity structure, consisting of an all-PM fiber segment attached to two free-space arms with end mirrors M1/2 which form a closed laser resonator. The fiber segment contains the active medium, in this case an Yb-doped fiber (YDF), pumped via a wavelength-division multiplexer (WDM) that couples 976-nm pump light from a diode laser into the YDF to ensure coherent optical amplification (see Section 2.2.1). Both ends of the PM fiber segments are terminated with fiber collimators C1/2, which collimate the divergent fiber output beam into the free-space arms. The side of C1 includes a Faraday-rotator (FR, 45° polarization rotation for each single-pass) combined with end mirror M1. The side of C2 includes a non-reciprocal phase bias consisting of a second FR (45° single-pass) combined with a tunable half-wave plate (HWP2) and quarter-wave plate (QWP1), a polarization beam-splitter (PBS), a transmission grating pair for dispersion compensation, and the second resonator end mirror M2. In addition, QWP2 allows tunable output coupling to one of the reflected output Port R, while an additional HWP1 aligns one of the PM fibers principal axes to the transmission axis of the PBS to ensure a consistent frame of reference for the subsequent derivation of the SA transmission characteristics.

To understand the mode-locking mechanism of LSI and other NLI-based fiber oscillators, both the linear and nonlinear intra-cavity polarization evolution must be considered [142,147]. Linear transformations arise from the intra-cavity polarization modulators (e.g., QWPs, HWPs and FRs) while nonlinear polarization modulation result from the Kerr-induced intensity-dependent differential phase $\Delta\varphi_{nl}$ between the two interferometer arms. The intra-cavity polarization evolution is modeled by cascading the Jones matrices of all elements over one round trip

with additionally inserted Kerr-induced phase operator [142,148]. The resulting round-trip polarization transfer matrix enables to compute the intensity-dependent transmission function $T(\Delta\varphi_{nl})$ at the PBS. The sinusoidal $T(\Delta\varphi_{nl})$ characterizes the artificial SA behavior as function of the tunable phase-bias waveplate angles θ_H and θ_Q, the accumulated $\Delta\varphi_{nl}$ and the energy splitting ε between the co-propagating OPMs in the LSI.

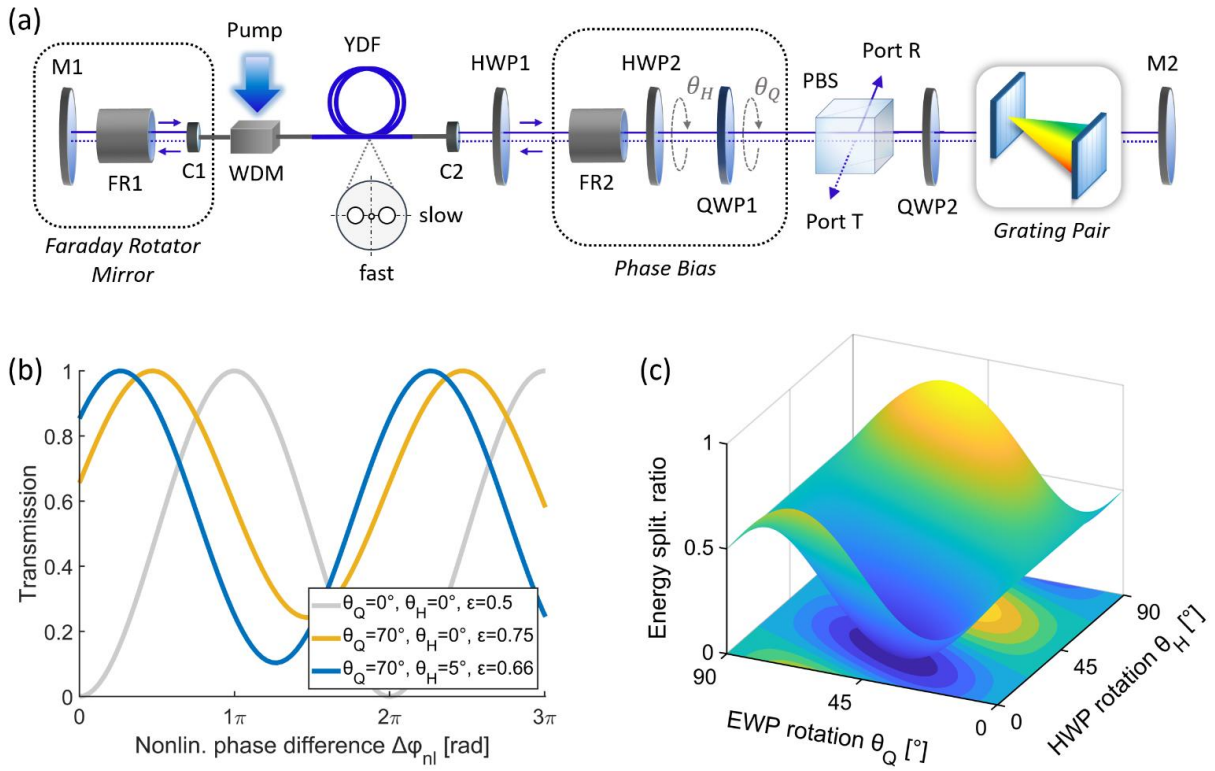

Figure 3.1: LSI oscillator architecture and NLI-based SA parameter tuning. (a): Typical experimental cavity schematic of an all-PM LSI mode-locked fiber oscillator. M: mirror, FR: Faraday-rotator, C: collimator, WDM: wavelength-division multiplexer, YDF: Yb-doped fiber, HWP: half-wave plate, QWP: quarter-wave plate, PBS: polarization beam-splitter. (b): Tunability of the intensity-dependent LSI transmission function $T(\Delta\varphi_{nl})$ for three different settings of the phase-bias waveplate rotation angles θ_H (HWP2) and θ_Q (QWP1), with corresponding energy splitting ratio ε. (c): Mapped energy splitting ratio $\varepsilon(\theta_Q, \theta_H)$ showing control of the power distribution between the OPM interferometer arms, corresponding to a control of accumulated $\Delta\varphi_{nl}$.

To apply Jones calculus on the cavity shown in Fig.3.1 (a), it is convenient to define the PBS transmission axis as parallel to the x-axis of the PM-fiber, and the reflection axis parallel to the y-axis. In this case, the orthonormal basis defined by $\{\boldsymbol{e}_x, \boldsymbol{e}_y\}$ corresponds to the PM-fiber axes, with the PBS transmitting $\boldsymbol{e}_x$, ensuring a consistent frame of reference. To describe the influence of the phase-bias (PB), one can define the rotation and retarder matrices:

$$R(\theta) = \begin{bmatrix} cos\theta & -sin\theta \\ sin\theta & cos\theta \end{bmatrix} \tag{3.1}$$

$$J(\delta, \theta) = R(-\theta) \begin{bmatrix} 1 & 0 \\ 0 & e^{i\delta} \end{bmatrix} R(\theta) \tag{3.2}$$

so that and ideal HWP and QWP at angles θ_H and θ_Q can be described with the jones matrices $J_H = J(\pi, \theta_H)$ and $J_Q = J(\pi/2\,, \theta_Q)$, respectively. Starting from the PBS in direction of the LSI fiber segment with $\boldsymbol{E}_{in} = \boldsymbol{e}_x = [1\ 0]^T$, the phase-bias in forward direction is described by:

$$B_f = J_H(\theta_H) J_Q(\theta_Q) R(\psi_{FR}) \tag{3.3}$$

where $R(\psi_{FR})$ with $\psi_{FR} = 45°$ accounts for a single-pass through the FR. The field launched into the PM axes can then be expressed as $\boldsymbol{L} = B_f \boldsymbol{E}_{in} = [L_x\ L_y]$, with energy splitting ratio:

$$\varepsilon = \frac{|L_x|^2}{|L_x|^2 + |L_y|^2} \tag{3.4}$$

and phase-bias $\varphi_{pb} = arg(L_y/L_x)$. This allows to define a normalized launch vector at the PM-fiber input:

$$\hat{\boldsymbol{L}} = \begin{pmatrix} \sqrt{\varepsilon} \\ \sqrt{1-\varepsilon} e^{i\varphi_{pb}} \end{pmatrix} \tag{3.5}$$

Due to the 90° of the Faraday-rotator mirror (FRM), linear phase shifts, and walk-off effects between the OPMs are compensated but they accumulate a Kerr-induced differential phase-shift $\Delta\varphi_{nl}$ according to Eq. (2.11), resulting in the modified launch vector:

$$\boldsymbol{L} \rightarrow \hat{\boldsymbol{L}} = \begin{pmatrix} \sqrt{\varepsilon} \\ \sqrt{1-\varepsilon} e^{i(\varphi_{pb} + \Delta\varphi_{nl})} \end{pmatrix} \tag{3.6}$$

On the return pass, the phase-bias section is traversed in reverse order, resulting in the backward operator:

$$B_f = R(\psi_{FR}) J_Q(\theta_Q) J_H(\theta_H) \tag{3.7}$$

Subsequent projection onto the PBS transmission axis (Port T) can be described by the analyzer row vector $\boldsymbol{A}^T = \boldsymbol{e}_x^T B_b = \begin{bmatrix} A_x & A_y \end{bmatrix}$, so that the transmitted field amplitude becomes:

$$E_T = \boldsymbol{A}^T \hat{\boldsymbol{L}}_{nl} = A_x\sqrt{\varepsilon} + A_y\sqrt{1-\varepsilon}e^{i(\varphi_{pb}+\Delta\varphi_{nl})} \tag{3.8}$$

The artificial SA transmission at Port T is then given by:

$$T(\Delta\varphi_{nl}) = |E_T|^2 = T_0 + Mcos(\Delta\varphi_{nl} + \varphi_0) \tag{3.9}$$

Here, $T_0 = |A_x|^2\varepsilon + \left|A_y\right|^2(1-\varepsilon)$ is an offset transmission, $M = 2\sqrt{\varepsilon(1-\varepsilon)}\left|A_x A_y^*\right|$ the modulation depth, and $\varphi_0 = \varphi_{pb} + arg\left(A_x A_y^*\right)$ is the effective phase-bias after double-pass through the LSI. These three quantities are jointly tunable via the phase-bias settings θ_H and θ_Q, which set ε, φ_{pb} and the analyzer coefficients A_x and A_y.

To quantify the responsiveness of the SA to small intra-cavity fluctuations, one can linearize $T(\Delta\varphi_{nl})$ around $\Delta\varphi_{nl} = 0$. Differentiation of Eq. (3.9) therefore gives the small-signal slope:

$$\left.\frac{dT}{d\Delta\phi_{nl}}\right|_{\Delta\phi_{nl}=0} = -Msin\varphi_0 \tag{3.10}$$

Using the derived model, Fig.3.1 (b) illustrates how different settings of θ_H and θ_Q translate to distinct $T(\Delta\varphi_{nl})$ curves with specific parameter set consisting of T_0, M,φ_0 and ε. Fig.3.1 (c) maps the parameter space $\varepsilon\left(\theta_H, \theta_Q\right)$, which is directly related to both modulation depth (via $M \propto \sqrt{\varepsilon(1-\varepsilon)}$) and the nonlinear working point (via $\Delta\varphi_{nl} \propto 2\varepsilon - 1$). In practice, reliable self-starting therefore requires a balance between high small-signal slope given by Eq. (3.10) with maximum simultaneous ε to efficiently accumulate $\Delta\varphi_{nl}$ in the LSI fiber segment.

3.1.2 XPM-induced Limitations in Standard LSI Oscillators

Although LSI oscillators share the all-PM architecture and Kerr-type artificial SA concept with state-of-the-art NALM/NOLM designs, their reported performance has been limited by elevated intensity and timing noise, a reduced stability window, and pronounced spectral rippling with degraded pulse quality over broad ranges of cavity parameters [111,112,146], drastically reducing their applicability for many high-performance applications.

To investigate the physical origin of these limitations, the pulse evolution in standard LSI oscillators is analyzed using numerical simulations. This analysis identifies nonlinear phase

distortions arising from XPM between OPMs in the PM fiber as the dominant mechanism underlying the observed performance degradation. Understanding this mechanism provides the foundation for the birefringent XPM-suppression concept introduced and analyzed in the following sections. The numerical model used to describe mode-locking in LSI oscillators combines computation of the phase-biased LSI transfer function $T(\Delta\varphi_{nl})$, derived in Section 3.1.1, with coupled NLSEs including gain (Section 2.2.2) iterated over successive cavity roundtrips.

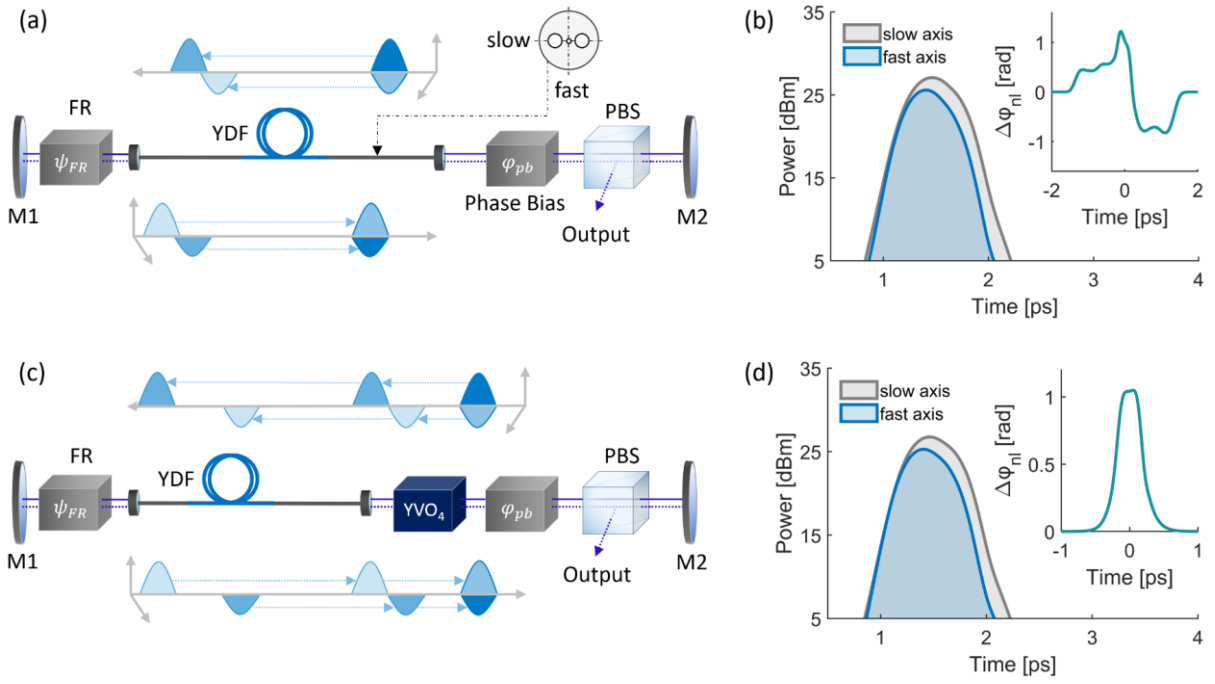

Figure 3.2: Influence of XPM on co-propagating OPMs in standard and XPM-suppressed LSI oscillators. (a): Simplified standard LSI cavity structure with indicated OPM propagation. M: mirror, FR: Faraday-rotator, YDF: Yb-doped fiber, PBS: polarization beam-splitter. (b): Simulated temporal pulse profile after isolated roundtrip parallel to the slow (grey) and fast (blue) fiber axis. Inset: corresponding accumulated $\Delta\varphi_{nl}$ with XPM-induced modulations and sing-changing waveform. (c): Simplified LSI cavity with implemented YVO_4-crystal for birefringent XPM-suppression (d): Corresponding simulation of the roundtrip pulse profiles on the respective fiber axes, together with the SPM-dominated, single-lobed, and positive accumulated $\Delta\varphi_{nl}$ (inset).

As an initial step, the origin and impact of XPM-induced distortions are investigated by simulating nonlinear pulse propagation in a representative LSI cavity operated in the standard configuration shown in Fig.3.2 (a). In this configuration, a linear polarized pulse leaves the PBS each roundtrip in the direction of the phase-bias and fiber segment. Two OPMs are generated based on the phase-bias settings, entering the PM fiber with full temporal overlap and subsequently walk off during propagation due to the group-velocity mismatch between the fast and slow PM-fiber axes (~1 ps/m for PM980 at 1030 nm). After the forward pass, the FRM rotates the polarization by 90°, ensuring that the OPMs recombine and re-overlap on the return path.

The overlap with progressive walk-off during propagation in the fiber segment enables strong nonlinear coupling via XPM; a key distinction e.g., from NALM/NOLM oscillators, where the OPMs counter-propagate in a Sagnac-type interferometric fiber loop with minimal overlap and inherently suppressed nonlinear cross-talk.

Simulation parameters, including fiber lengths, pump power and phase-bias settings, are set to ensure stable mode-locking convergence within 1000 roundtrips. Figure 3.2 (b) shows the simulated temporal pulse profiles of the OPMs along the fast and slow PM-fiber axes for the final roundtrip, together with the corresponding accumulated nonlinear phase difference $\Delta\varphi_{nl}(t)$ (inset). The fields are evaluated directly after double-pass through the fiber and phase-bias section, just before interaction with the PBS. As shown, the accumulated $\Delta\varphi_{nl}(t)$ is strongly modulated and with a sign-change close to $t = 0$, which distorts the SA transmission and pulse shaping characterized by its transmission function $T(\Delta\varphi_{nl})$. This distortion reduces modulation efficiency and introduces characteristic temporal and spectral artifacts as a direct consequence of XPM-induced nonlinear cross-talk.

To suppress these phase distortions, a birefringent XPM-suppression concept is introduced. As illustrated in Fig.3.2 (c), the approach utilizes a highly birefringent YVO_4 crystal inserted between the LSI fiber segment and the phase-bias. The crystal axes are aligned with the principal axes of the PM fiber, ensuring that the OPMs remain in a consistent reference frame while acquiring a relative group-delay offset $\Delta\tau \propto L_{YVO_4}$. The resulting temporal pre-separation prevents any direct overlap of the OPMs during nonlinear propagation in the LSI fiber segment, thereby effectively suppressing XPM-induced cross-talk. Upon double-pass propagation the pre-separation is fully compensated by the 90° polarization rotation of the Faraday-rotator mirror and therefore does not perturb the steady-state laser operation.

The impact of this mechanism is illustrated in Fig.3.2 (d), which shows the simulated OPM pulse profiles and the corresponding accumulated $\Delta\varphi_{nl}(t)$ obtained using identical simulation parameters as before but including YVO_4-induced pre-separation. In contrast to the standard configuration, the resulting $\Delta\varphi_{nl}(t)$ waveform is SPM-dominated, single-lobed, and strictly positive, closely following the pulse envelope. In the following sections, it is numerically and experimentally validated that this new technique for birefringent XPM suppression results significant performance enhancement of this laser structure across multiple domains, making them an ideal driver for complex MPM laser platforms and other ultrafast applications.

3.1.3 Impact of XPM Suppression on Spectral Quality and Mode-Locking Threshold

To experimentally investigate the influence of birefringent XPM suppression on the LSI laser operation, initially focused on the spectral output quality and general mode-locking performance, a setup is constructed as shown in Fig.3.3 (a). The modified setup is designed to allow switching between a standard configuration (SC) with XPM, and an enhanced configuration (EC) with XPM-suppression via implementation of a 20 mm long intra-cavity YVO_4-crystal.

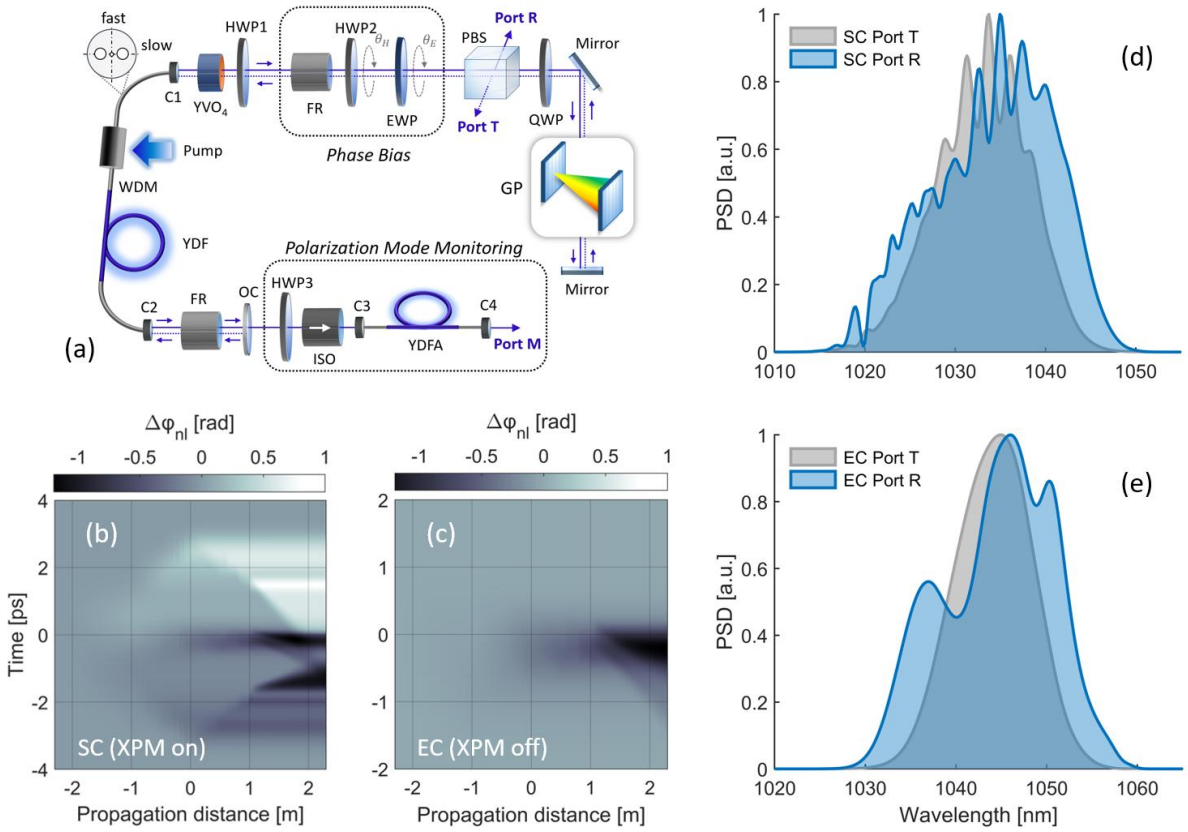

Figure 3.3: Experimental implementation and numerical analysis of birefringent XPM suppression in an LSI fiber oscillator. (a): Experimental setup including attached modification for OPM monitoring. GP: grating pair, QWP: quarter-wave plate, PBS, polarization beam-splitter, EWP: eight-wave plate, HWP: half-wave plate, FR: Faraday-rotator, C: collimator, WDM: wavelength-division multiplexer, YDF: Yb-doped fiber, OC: output coupler, ISO: isolator, YDFA: Yb-doped fiber amplifier. (b): Simulated evolution of $\Delta\varphi_{nl}(t)$ in SC with XPM as function of propagation distance in the LSI fiber segment with illustrated OPM time-delay. (c): Evolution of $\Delta\varphi_{nl}(t)$ in the EC with birefringent XPM-suppression. (d): Steady-state output spectra in SC at Port T (gray) and Port R (blue). (e): Corresponding Port T and R output spectra in EC.

The all-PM fiber segment includes 0.7 m of highly ytterbium-doped fiber (YDF, CorActive Yb401-PM), optically pumped by a 976 nm, 1 W laser diode coupled via a WDM. The free-space arm following collimator C1 contains the cavity end mirror, a 1000 lines/mm transmission grating pair (LightSmyth 1040-Series) for dispersion management, a PBS, and the non-

reciprocal phase-bias section composed of a 45° single-pass FR, a HWP, and an eight-wave plate (EWP) with adjustable rotation angles θ_H and θ_E, respectively. The usage of an EWP instead of a enables a reduced sensitivity of the phase-bias tuning, making it more practical to find a stable setting for reliable mode-locking initiation. The QWP between PBS and GP functions as a tunable output coupler, allowing access to the intra-cavity field at PBS Port T.

An additional half-wave plate (HWP1) is used to align the slow axis of the PM fiber with the transmission axis of the PBS. On the opposite side, a Faraday rotator mirror (FRM, 45° single-pass) is placed after collimator C2 to compensate linear phase shifts and ensure proper recombination of the OPMs in both SC and EC of the LSI oscillator. At the FRM side, an output coupler (OC) serves as second cavity end mirror, coupling out 20% of the intra-cavity field. After amplification by a Yb-doped fiber amplifier (YDFA), the output at Port M then enables polarization-resolved monitoring of the OPM time-delay, allowing direct verification of the temporal separation introduced when switching from SC to EC of the LSI oscillator.

To investigate the impact of XPM on the output pulse characteristics in a realistic cavity environment, numerical simulations are performed with parameters matched to this configuration, using the model described in Section 3.1.2. The phase-bias is set to $\theta_H = 52°$ and $\theta_E = 81°$, corresponding to a regime with high SA sensitivity and optimal starting behavior, i.e., a positive slope of the transmission function $T(\Delta\varphi_{nl})$ near $\Delta\varphi_{nl} = 0$. Figures 3.3 (b) and (c) show the simulated evolution of the accumulated $\Delta\varphi_{nl}(t)$ along the PM fiber segment in SC and ED, respectively, where the propagation distance of 0 m is referenced to the position of the FRM. As illustrated, the temporal waveform of $\Delta\varphi_{nl}$ in SC is strongly distorted due to XPM, leading to a temporally modulated SA transmission. In contrast, the birefringent XPM suppression introduced by the YVO_4 crystal in the EC ensures smooth temporal evolution of the nonlinear phase with strong suppression of temporal modulations. The corresponding output spectra in SC and EC are displayed in Figs.3.3 (d) and (e), respectively. In SC, the distorted nonlinear phase gives rise to pronounced spectral ripple and sidebands at both Ports T and R. By contrast, the EC spectra verify smooth spectral broadening and are essentially free of ripples, confirming that the artifacts observed in SC originate from XPM-induced phase distortions. These results therefore numerically demonstrate the effectiveness of the proposed suppression scheme under experimentally realistic conditions.

For experimental validation, comparative measurements are performed for the SC and EC of the LSI oscillator shown in Fig.3.3 (a). To enable a clear comparison of both laser configurations, the oscillators are operated in a stretched-pulse regime with a net intracavity dispersion of approximately $-5 * 10^3$ fs^2, where the material dispersion of the 20 mm YVO_4-crystal

(203.58 fs^2/mm GVD at 1030 nm) is compensated with a corresponding adjustment in the grating distance when switching from Sc to EC. The lasing threshold is measured at ~60 mW in both SC and EC, confirming that insertion of the antireflective (AR) coated YVO_4-crystal does not introduce any significant linear loss or misalignment.

To evaluate the influence of XPM suppression on the onset of mode-locking, Fig.3.4 (a) presents the measured slope efficiency dP_{out}/dP_p at Port T for both SC and EC, where P_{out} denotes the average Port T output power P_p the average pump power, along with the corresponding P_{out} versus P_p curves (inset). During this measurement, the pump power is increased in 25 mW steps up to 1.5 W. A distinct increase in slope efficiency marks the transition from cw to pulsed operation, which occurs more abruptly and at lower pump powers in the EC, highlighting improved self-starting behavior enabled by birefringent XPM suppression.

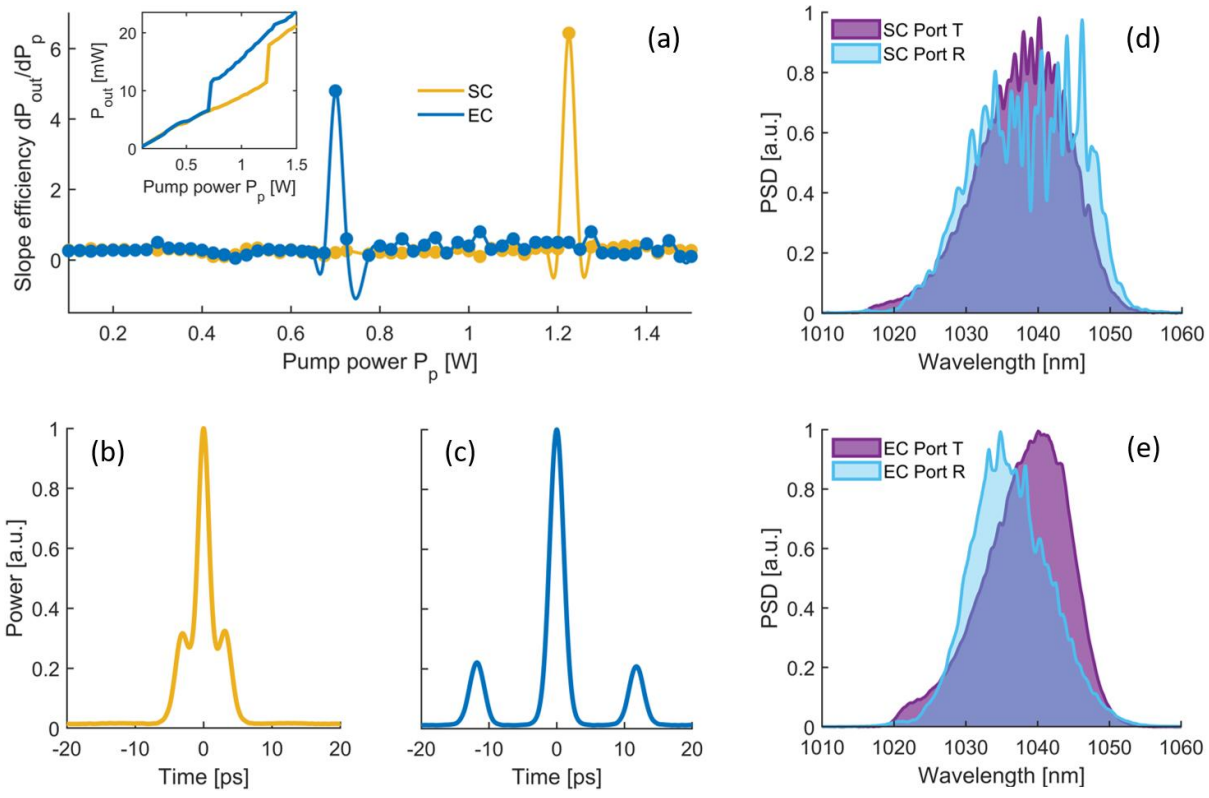

Figure 3.4: Experimental comparison of LSI laser operation in SC and EC with birefringent XPM suppression. (a): Measured slope efficiency dP_{out}/dP_p as function of the pump power P_p at Port T of the LSI oscillator in SC (yellow) and EC (blue). Inset: Corresponding output versus pump power characteristics. (b): Corresponding AC trace of the OPMs measured at Port M for the SC. (c): Corresponding AC trace of the OPMs in EC. (d): Measured output spectra in SC at Port T (purple) and Port R (cyan). (e): Corresponding output spectra in EC measured at Port T and R.

The transition from cw to the energetically more efficient mode-locked state is clearly visible in Fig.3.4 (a) as a sharp increase in slope efficiency. Compared to the SC, which demonstrates a measured mode-locking threshold at 1.23 W pump power, the EC enables a significantly reduced threshold of 0.7 W, corresponding to a ~45% lower pump power requirement. This improvement is attributed to the suppression of XPM-induced phase distortions in the EC, which reduces nonlinear losses in the artificial SA mechanism, as will be further verified below.

Once mode-locking is initiated, both configurations support stable single-pulse operation at pump powers far below the mode-locking threshold; approximately 50 mW for the SC and 55 mW for the EC. Figures 3.4 (b) and (c) show the measured autocorrelation (AC) traces of the OPMs at Port M for both configurations. In the SC, a temporal walk-off of ~3 ps is observed, consistent with the birefringence of the PM fiber alone. In contrast, the EC demonstrates a larger walk-off of ~13 ps, resulting from the additional pre-separation induced by the 20 mm YVO_4 crystal, whose fast axis is aligned parallel to the slow axis of the birefringent PM fiber.

In LSI mode-locked oscillators, the output power at Port T is proportional to the intra-cavity power, while the power at Port R reflects loss through the artificial SA [142]. Comparing their ratio thus provides insight into the nonlinear loss characteristics, independent of pump power. In the SC, the measured output power at Port T and R is 0.6 mW and 2.0 mW, corresponding to pulse energies of 16.7 pJ and 55.6 pJ, respectively. In contrast, the EC yields 1.4 mW at Port T and 0.9 mW at Port R, with corresponding pulse energies of 38.9 pJ and 25.0 pJ. Notably, the power ratio between Port T and R is inverted between the two configurations. Given the previously confirmed identical linear losses in SC and EC, this inversion clearly indicates that XPM suppression not only improves the mode-locking threshold and starting behavior but also enhances the nonlinear transmission efficiency of the artificial SA mechanism.

To further assess the overall output pulse quality in both configurations, Figs.3.4 (d) and (e) present the measured output spectra at Ports T and R for the SC and EC, respectively. To verify the periodic spectral perturbations predicted by simulation, the output spectra are recorded using a high-resolution optical spectrum analyzer (ANDO AQ6315A) at 0.02 nm resolution. As shown in Fig.3.4 (d), the SC spectra at Ports T and R demonstrates pronounced modulations, with a spectral FWHM of 13.8 nm and 18.1 nm, respectively. In excellent agreement with the numerical predictions, the EC spectra in Fig.3.4 (e) verify significantly reduced spectral modulation, with FWHM values of 13.4 nm at Port T and 12.2 nm at Port R. Interestingly, the influence of XPM suppression appears more pronounced in the spectral shape at Port R, potentially due to a phase-bias-dependent redistribution of XPM-distorted components, as recently discussed in Ref. [146].

These results clearly confirm that XPM suppression is a critical requirement for achieving high spectral output quality in LSI oscillators, comparable to established platforms such as NALM/NOLM or NPE-based designs. The successful suppression of XPM in all-PM LSI mode-locked fiber oscillators evidently enhances output pulse quality and reduces the mode-locking threshold by over 45%, as confirmed through experiment and simulation. These results establish birefringent XPM suppression as a key enabling technology for high-performance LSI designs, positioning them as competitive alternatives to NALM/NOLM-based systems.

3.1.4 Enhanced Noise Performance Across Mode-Locking Regimes

The noise performance and parameter stability of mode-locked lasers are crucial performance metrics for many state-of-the-art applications. For ultra-low noise fiber oscillators, the achievable noise performance is largely determined by intrinsic nonlinear dynamics and the technical architecture, including the cavity design, environmental isolation, SA type and the dispersion map [97,98,100]. A powerful lever to control RIN, timing-jitter and phase noise performance is the mode-locking regime, determined primarily by the net cavity dispersion. These include the stretched-pulse (SP), soliton, and self-similar (similariton) operation, each characterized by distinct pulse-shaping mechanisms and noise responses [73].

The SP regime, accessed at near-zero to slightly anomalous net dispersion by balancing the normal dispersion of the fiber with anomalous dispersion elements such as grating pairs or chirped mirrors, features strong pulse breathing, the broadest output spectra, and reduced nonlinear phase accumulation per roundtrip [149]. When carefully optimized, this regime yields some of the lowest reported levels of intensity noise and timing jitter [73]. In contrast, the soliton regime, operating at net anomalous dispersion, supports nearly transform-limited pulses which are, however, energy-limited by the soliton area theorem, often trading bandwidth and pulse energy for enhanced robustness [150]. Finally, the similariton regime, realized in all-normal-dispersion cavities with spectral filtering and gain shaping, supports large stretch factors and self-similar, highly chirped pulse evolution with substantially higher pulse energies directly from the oscillator, at the expense of increased intracavity nonlinear phase accumulation and reduced noise performance and stability [151].

The preceding section demonstrated that cross-phase modulation (XPM) in standard LSI oscillators induces nonlinear phase distortions, which manifest as spectral modulations and degraded pulse quality. It further introduced birefringent XPM suppression based on intra-cavity YVO_4 crystals as an effective strategy to eliminate this limitation. Building on these findings, two key questions naturally emerge. First, does birefringent XPM suppression translate into measurable improvements in noise performance, specifically in RIN and timing jitter, thereby

enhancing the suitability of LSI oscillators for ultra-low-noise applications such as frequency metrology, optical synchronization, and nonlinear biomedical imaging? Second, are the performance gains preserved across distinct mode-locking regimes, which would establish birefringent XPM suppression as a broadly applicable tool for extending the versatility of performance-enhanced LSI oscillators to the level of state-of-the-art NALM/NOLM oscillators?

To address these questions, stochastic numerical simulations of intracavity noise dynamics are combined with an extended experimental setup enabling detailed comparative noise measurements between the LSI oscillator in both configurations (i.e., SC with XPM and EC with birefringent XPM-suppression). As initial step of this numerical evaluation, the influence of XPM on steady-state stability and RIN is investigated by varying the net cavity dispersion and pump power. Classical noise is introduced stochastically as described in Section 2.3, by adding energy fluctuations at the LSI fiber input, sampled from a Gaussian distribution with a standard deviation of 0.1% of the instantaneous pulse energy. For each parameter set, 800 cavity roundtrips are simulated, and the output RIN is calculated at Port T as $RIN = \delta P/\bar{P}$, with δP denoting the standard deviation and $\bar{P}$ the mean of the peak power calculated over the last 75 roundtrips. The coupled output fraction at Port T is fixed to 20%. Phase-bias settings are set to $\theta_H = 6°$ and $\theta_E = 71°$ with $\varepsilon = 0.66$ and positive slope of $T(\Delta\varphi_{nl})$ at $\Delta\varphi_{nl} = 0$.

Figure 3.5 (a) and (b) show the simulated RIN values in SC and EC with and without XPM-induced distortions, respectively, as function of the oscillator pump power and grating pair GDD. As shown, the absence of XPM markedly broadens the parameter space for stable steady-state mode-locking with low RIN output over the simulated 800 roundtrips. To further analyze the origin of the observed performance degradation of the LSI oscillator in SC, Fig.3.5 (c) shows the evolution of the accumulated roundtrip phase shift $\Delta\varphi_{nl}$ for a selected working point (WP, indicated in Fig.3.5 (a) and (b)) at a grating GDD of $-17 * 10^{-3}\ ps^2$ and a pump power of $77.5\ mW$. At this WP, the simulated oscillator operates in a low-RIN state when XPM is suppressed in EC, but transitions into a high-RIN state when XPM is active in SC. In EC, $\Delta\varphi_{nl}$ stabilizes after ~340 roundtrips at a steady value of $\sim 0.6\pi$ rad per roundtrip, corresponding to stable mode-locking. In contrast, in SC, $\Delta\varphi_{nl}$ converges to the same mean value but demonstrates pronounced random fluctuations. Since $\Delta\varphi_{nl}$ directly determines the SA transmission via $T(\Delta\varphi_{nl})$, these fluctuations perturb both PBS transmission (and hence the effective cavity loss, leading to temporal instabilities as illustrated in Fig.3.5 (d)) and the spectral shaping of the artificial SA mechanism.

To further investigate the connection between XPM-induced stability degradation and output pulse quality, Figs. 3.5 (d) and (e) present the simulated Port T output pulses at the selected

working point with XPM in SC and EC, respectively, in both the spectral and temporal domains. The displayed traces correspond to averages over the final 75 of the total 800 simulated roundtrips. Consistent with the results of the preceding sections, XPM-driven fluctuations of the accumulated roundtrip nonlinear phase $\Delta\varphi_{nl}$ give rise to pronounced spectral modulations and a clear degradation of the temporal pulse shape. Beyond confirming the presence of XPM-induced pulse distortions, these results establish a direct correlation with reduced laser stability and elevated RIN, indicating that effective XPM suppression can systematically improve the output noise performance of LSI oscillator architectures.

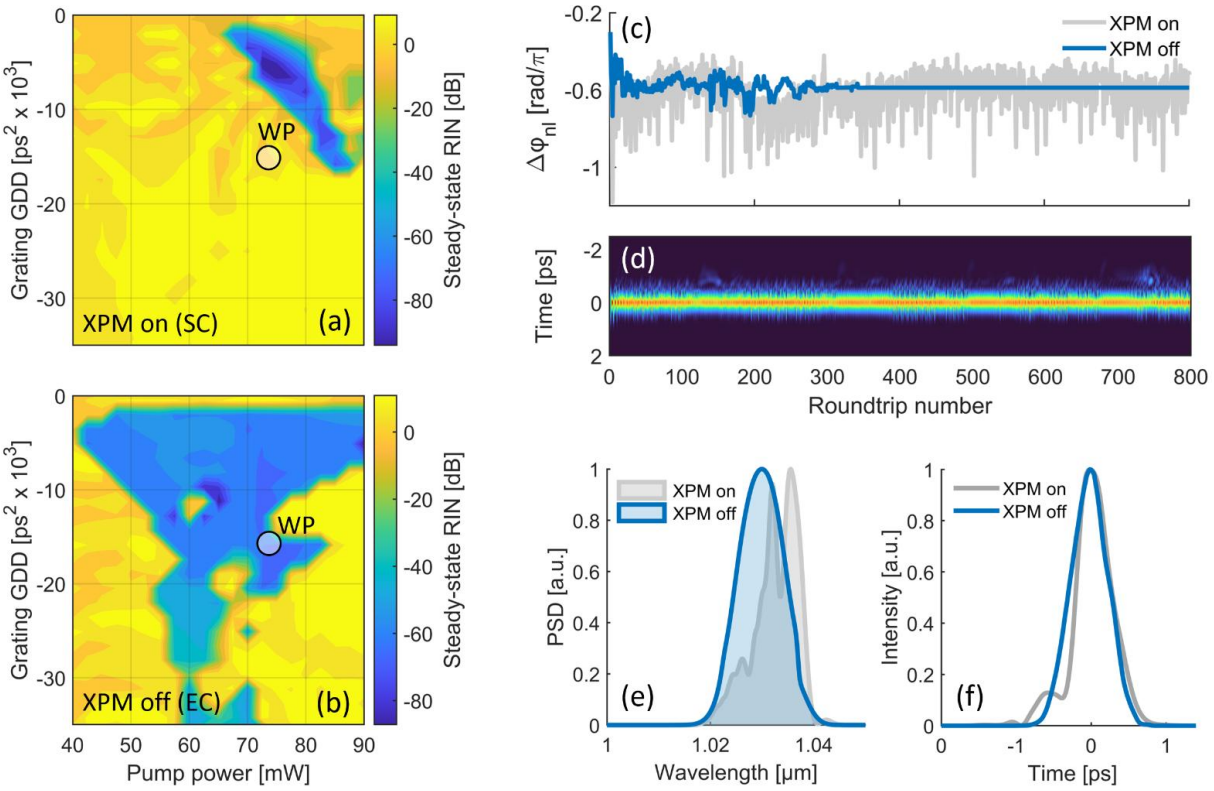

Figure 3.5: Numerical simulations of stability and RIN in the modeled LSI mode-locked fiber laser with and without XPM suppression. (a): Steady-state RIN as a function of intracavity grating-pair GDD and pump power at Port T of the SC with XPM. (b): Corresponding RIN of the EC with XPM suppression. (c): Evolution of the accumulated nonlinear phase shift $\Delta\varphi_{nl}$ over 800 roundtrips at the marked working point (WP) with XPM on/off in SC/EC (gray/blue). (d): Corresponding output pulses at Port T. (e): Simulated output spectra at Port T at WP with XPM on (SC, gray) and off (EC, blue), averaged over the last 75 roundtrips. (f) Output pulses corresponding to the spectra in (e).

To experimentally validate the numerically predicted improvements in noise and stability arising from suppression of XPM, an experimental setup is constructed as shown in Fig.3.6. The configuration allows direct RIN and timing-jitter measurements on a modified LSI oscillator, hereafter referred to as the laser under test (LUT). The LUT can be operated either SC,

where XPM is present, or in EC, where XPM is suppressed via optional implementation of a YVO_4-crystal. Its design closely follows the simulated system in Fig.3.1 (a), consisting of an all-PM fiber section with 0.5 m of highly Yb-doped fiber (YDF, CorActive Yb401-PM) and a total fiber length of 2.5 m. The YDF is pumped by a 976 nm, 1 W laser diode via a WDM. Free-space coupling is realized through collimators C1 and C2. On the C1 side, the free-space arm is built as a Faraday-mirror arrangement with a 45° single-pass FR and end mirror M1. On the C2 side, the arm contains the second end mirror M2, a transmission grating pair for dispersion compensation (LightSmyth T-Series, 1000 lines/mm), a PBS serving as output coupler, and the non-reciprocal phase-bias section.

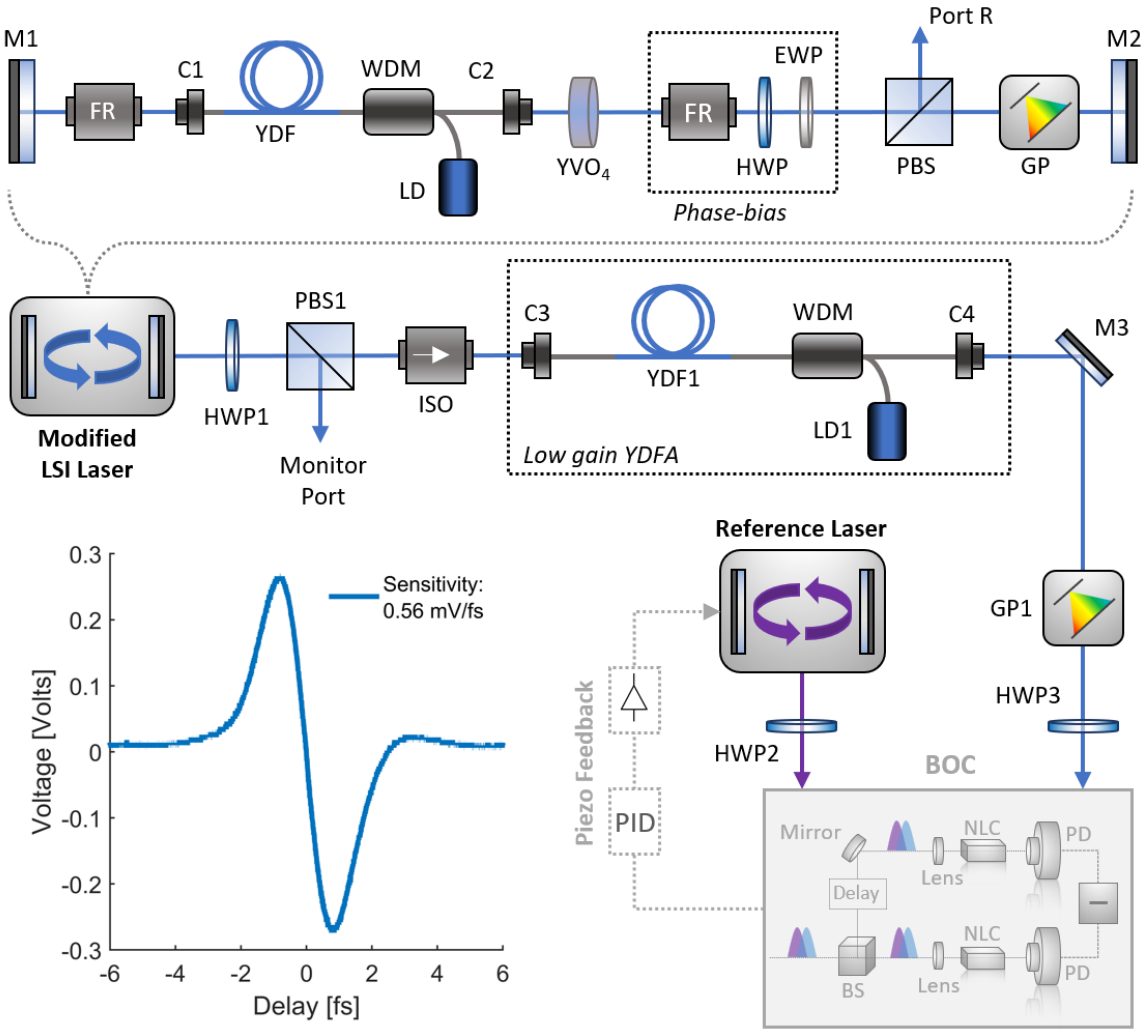

Figure 3.6: Experimental setup of the modified LSI oscillator with optional birefringent XPM suppression, together with the setup for comparative measurements of time- and frequency domain pulse characteristics, RIN, and timing-jitter performance. The inset shows a representative BPC sensitivity trace with 0.56 mV/fs. M: mirror, FR: Faraday rotator, C: collimator, PBS: polarization beam splitter, WDM: wavelength-division multiplexer, LD: laser diode, YVO_4: yttrium ortho-vanadate, HWP: half-wave plate, QWP: quarter-wave plate, GP: grating pair, BOC: balanced optical cross-correlator, BS: beam splitter, NLC: nonlinear crystal, PD: photodetector.

Switching between SC and EC is achieved by inserting a 10 mm YVO_4-crystal, which introduces a ~6.5 ps walk-off between the OPMs, thereby preventing nonlinear cross-talk in the fiber. The laser operates at a repetition rate of ~54 MHz. To provide a consistent reference for the orientation of the birefringent crystal and phase-bias wave plates, the slow axis of the PM fiber is aligned with the PBS transmission axis. Similar to the numerically simulated setup with results summarized in Fig.3.5, the phase bias of the experimental setup is realized with a 45° FR, a half-wave plate (HWP2), and an EWP with adjustable rotation angles θ_H and θ_E.

To characterize the RIN in both configurations, the output from Port R of PBS1 is detected using a low-noise InGaAs photodiode (Coherent ET3010). The fifth harmonic of the detected RF signal (270 MHz) is isolated by a bandpass filter and amplified with a low-noise RF amplifier (MiniCircuits ZX60-33LN-S+) powered by a stabilized supply (Toellner TOE8721). The resulting signal is analyzed with a signal-source analyzer (SSA, Keysight E5052B) to obtain both frequency-resolved single-sideband RIN spectra and integrated RIN values.

Timing-jitter measurements are performed using balanced optical cross-correlation (BOC) against a low-noise reference oscillator (RL) [152]. The RL is a highly optimized LSI laser with a piezo-actuated end mirror (Thorlabs PA25LEW), providing low-bandwidth synchronization to the LUT. It runs at 54 MHz with ~20 mW output and ~200 fs pulse duration. A commercial BOC unit (Cycle GmbH, BOC-MD-10) is employed. Because the LUT output power is insufficient for direct BOC operation, it is first amplified in a low-gain YDFA (<12 dB) and subsequently recompressed by a grating pair (LightSmyth T-Series, 1000 lines/mm). For consistency, the YDFA gain and input power are fixed throughout all measurements.

The BOC sensitivity is calibrated by slightly detuning the repetition rates of LUT and RL via a piezo offset, recording the frequency difference Δf_{rep}, and extracting the zero-crossing slope [153], which is ~0.56 mV/fs at 5 MHz bandwidth in the experiment (Fig.3.6 inset). This calibration is repeated for each LUT configuration to ensure a stable electronic noise floor. The timing-jitter spectral density is derived from the baseband noise of the BOC error signal, measured using a SSA. Synchronization between RL and LUT pulse trains is maintained by a feedback loop with <9 kHz bandwidth, using the RL's piezo-actuator, a high-speed servo controller (NewFocus LB1005), and a piezo driver (Thorlabs MDT694B). The measured timing-jitter spectrum above the locking bandwidth thus reflects the LUT's intrinsic noise response and enables direct comparison between SC and EC operation.

Using this setup, the influence of XPM on the RIN performance and output pulse characteristics is investigated in both the SP and the soliton regime, to confirm the numerical results.

In both regimes, the RIN is first characterized at a stable working point in SC with XPM influence. Subsequently, the YVO_4-crystal is inserted with its fast axis aligned to the fast axis of the PM fiber, and the RIN of the EC is measured and compared together with the corresponding pulse quality in time and frequency domain. The AR coating on the crystal surfaces ensures a negligible variation in cavity loss between SC and EC, which is further verified through a comparison of the respective cw-lasing threshold. To further avoid distortions in the RIN comparison caused by differences in net dispersion [73], the normal dispersion of the YVO_4 crystal (203.58 fs^2/mm group-velocity dispersion at 1030 nm) is compensated by an appropriate adjustment of the grating distance when switching between SC and EC. The LUT is operated at identical pump power in both configurations, and the RIN at output Port R is compared in the soliton and SP regimes. In both cases, mode-locking is established by tuning the phase bias, followed by a pump-power increase and subsequent reduction to the single-pulse threshold.

In the SP regime with a net dispersion of ~0.05 ps^2, mode-locking is obtained at a pump power of ~600 mW in both SC and EC, while the single-pulse threshold is ~100 mW in both cases, yielding output powers of 1.1 mW and 3.5 mW at Port R, respectively. The corresponding optical spectra and autocorrelation (AC) traces are shown in Fig.3.7 (a) and (b). Consistent with earlier studies (e.g., Refs. [111,146]) and the numerical results in Fig.3.5, suppression of XPM in EC leads to an improved spectral profile with significantly reduced modulation compared to SC. The compressed pulse durations are ~140 fs in both configurations, which is slightly longer than the respective Fourier limits of 110 fs (SC) and 91 fs (EC). Nonetheless, the measured AC traces confirm an improved temporal pulse quality in EC with strongly suppressed pedestals. To exclude multi-pulse operation as the origin of the spectral modulations observed in SC, the broadband RF spectrum is analyzed (inset of Fig.3.7 (b), here shown for the EC output at Port R). The absence of amplitude modulations in higher RF harmonics verifies single-pulse operation. In addition, the full 150-ps dynamic range of the autocorrelator is monitored to rule out signatures of multi-pulsing.

In the soliton regime of the LUT with a net dispersion of -0.17 ps^2, self-starting mode-locking is initiated at 700 mW and 540 mW pump power in SC and EC, with a corresponding single-pulse threshold at 92 mW and 80 mW, respectively. The Port R output power is 0.4 mW in SC and 1.2 mW in EC. Fig.3.7 (c) shows the corresponding output spectra, with a FWHM of ~9.6 nm in both LUT configurations. Spectral measurements and AC traces, shown in Fig.3.7 (c) and (d) respectively, confirm similar suppression of spectral and pulse distortions as in the SP regime. Single-pulse operation is again confirmed via the RF spectrum shown in the inset of Fig.3.7 (d) for the EC, and by large dynamic-range AC measurements.

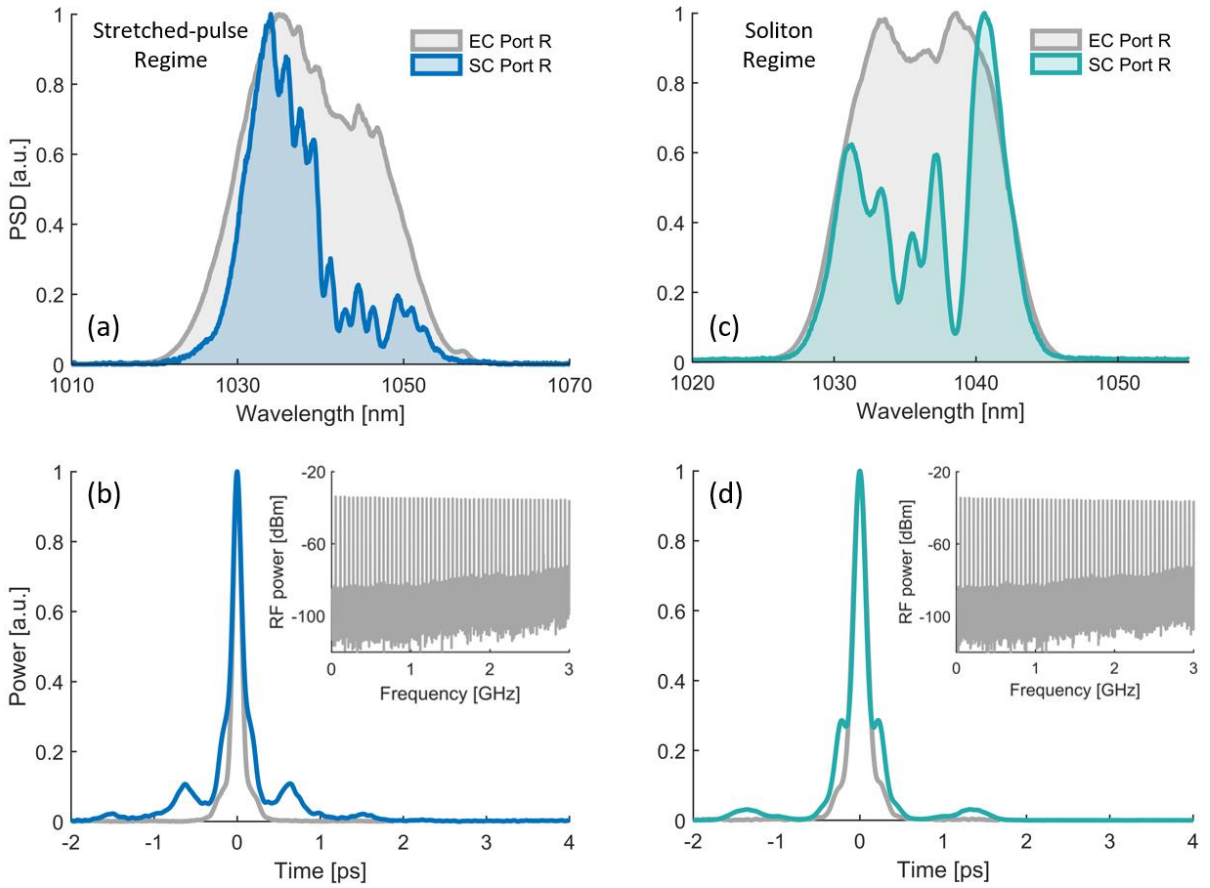

Figure 3.7: Time- and frequency-domain soliton and stretched-pulse regime output of the modified LSI oscillator in SC and EC. (a): Measured Port R spectra in the stretched-pulse regime for SC (blue) and EC (gray), with FWHMs of 9.6 nm and ~20 nm, respectively. (b): Corresponding compressed autocorrelation (AC) traces (FWHM ~140 fs in both cases). The inset shows the broadband RF spectrum of the EC output pulse train. (c): Port R spectra in the soliton regime for SC (cyan) and EC (gray). (d): Compressed AC traces in the soliton regime (FWHM ~190 fs in both cases). The inset shows again the corresponding RF spectrum of the EC soliton pulse train.

The RIN spectra of SC and EC operation in the SP regime are shown in Fig.3.8 (a), together with the RIN of the reference laser (RL), which is later used for timing-jitter measurements. As shown, suppression of XPM in the EC leads to up to 10 dB lower RIN in the high-frequency range above ~10 kHz, approaching the noise level of the RL beyond ~200 kHz. The corresponding integrated RIN, shown in Fig.3.8 (b), confirms a reduction from 0.062% in SC to 0.040% in EC when integrated over the full measurement bandwidth.

The frequency-dependent character of the RIN suppression can be attributed to the distinct response of XPM and the intracavity gain medium. XPM acts on a sub-femtosecond timescale and inherently exhibits a high-pass response, as previously demonstrated and analytically described by Hui *et al.* in the context of WDM systems [154]. In this regime, XPM generates stronger phase fluctuations $\Delta\varphi_{nl}$ at higher modulation frequencies, which are converted into amplitude noise by the artificial saturable absorber mechanism, thereby enhancing the high-

frequency RIN contributions. In contrast, the saturation dynamics of the Yb-doped gain medium act as a low-pass filter with a bandwidth set by the upper-state lifetime (typically ~1 ms). As discussed by Washburn *et al.* in Ref. [155], the gain medium is therefore unable to respond effectively to fast intracavity power fluctuations, which further increases the contrast between low- and high-frequency noise suppression once XPM is eliminated.

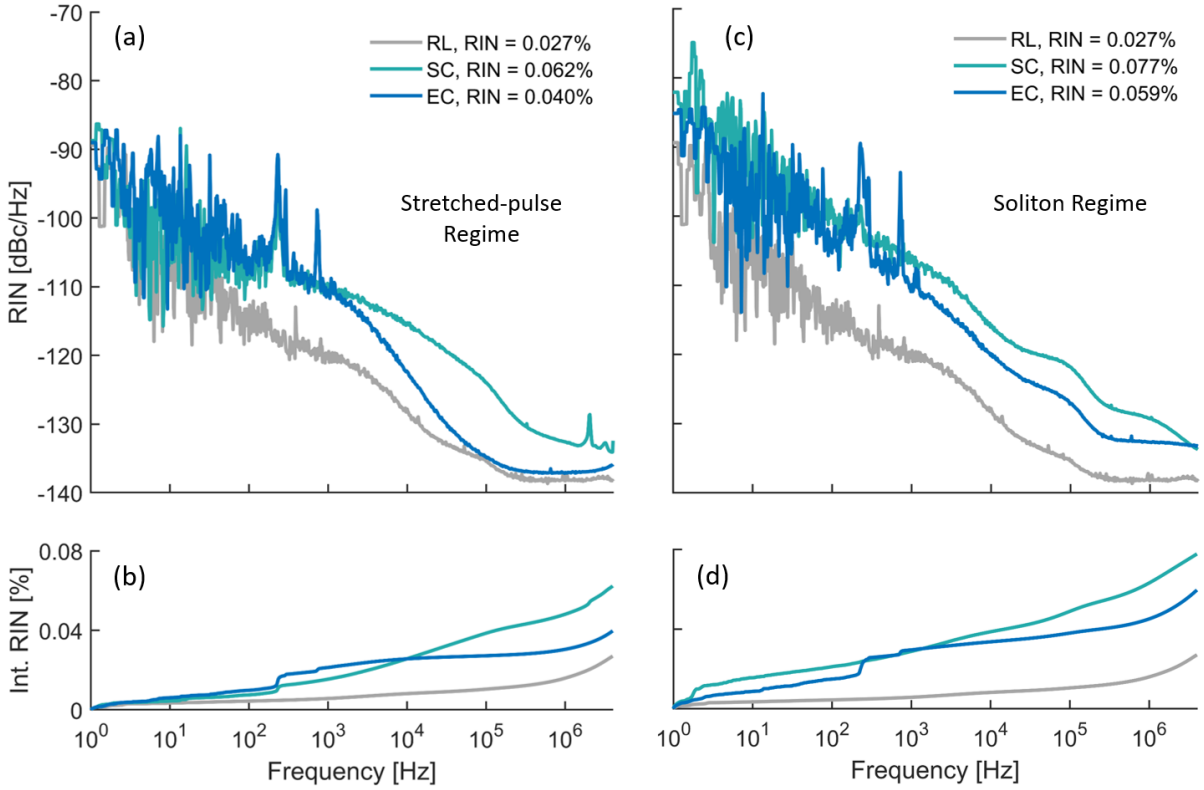

Figure 3.8: RIN performance of the modified LSI oscillator in SC and EC under stretched-pulse and soliton operation. (a): Measured RIN spectral density from 1 Hz to 5 MHz for the LUT in stretched-pulse regime, comparing SC (cyan) and EC (blue) to the reference laser RL (gray). (b): Corresponding integrated RIN traces. (c): RIN spectral density for the LUT operated in the soliton regime, again comparing SC and EC to the RL. (d): Corresponding integrated RIN traces.

The measured RIN spectra in the soliton regime, together with the RIN of the RL, are shown in Fig.3.8 (c) for both SC and EC. Similar to the SP regime, suppression of XPM results in broadband reduction of the RIN spectral density. In the high-frequency range above 10 kHz, the RIN suppression remains nearly constant at ~5 dB. The corresponding integrated RIN, shown in Fig.3.8 (d), confirms a reduction from ~0.08% in SC to ~0.06% in EC as a direct consequence of XPM suppression. In comparison to both soliton configurations, the SP regime exhibits overall lower RIN, consistent with theoretical predictions and earlier reports on the

dependence of noise performance on net cavity dispersion [73,156]. The RL maintains the lowest integrated RIN of 0.03%, verifying its suitability as a low-noise reference in the subsequent timing-jitter characterization. The experimentally observed improvements in pulse quality and RIN performance in both regimes further demonstrate excellent agreement with the numerical predictions.

To investigate the influence of XPM suppression on the timing-jitter performance of the LUT, comparative measurements relative to the low-noise RL are carried out in both the stretched-pulse and soliton regimes. To exclude any influence of varying pulse energy or duration on the results, both parameters are kept constant for all measurements [100,157].

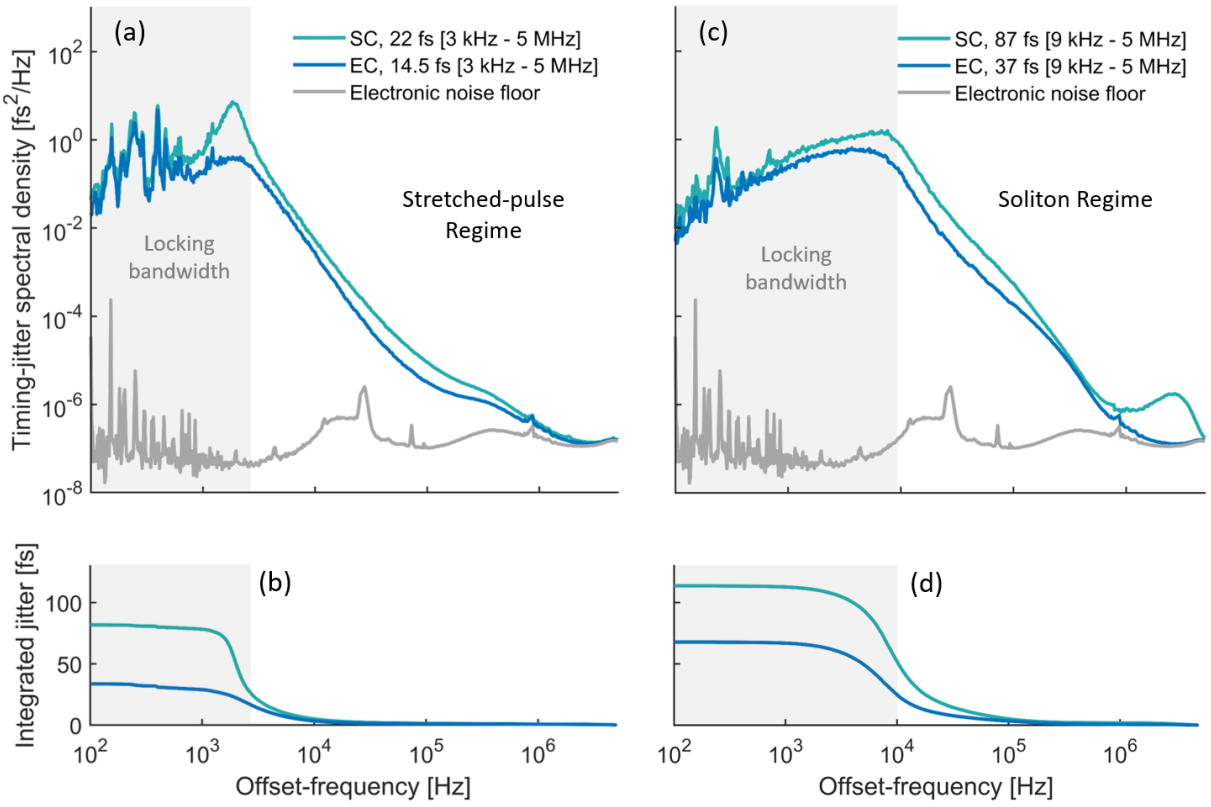

Figure 3.9: Influence of XPM suppression on the relative timing jitter in SP and soliton operation. (a) Measured timing-jitter spectral density of the LUT operated in the SP regime for SC (dark gray) and EC (blue) with a locking bandwidth of ~3 kHz. (b): Corresponding integrated timing-jitter traces (100 Hz - 5 MHz). (c): Timing-jitter spectral density of the LUT operated in the soliton regime for SC (dark gray) and EC (green) with a locking bandwidth of ~9 kHz. (d): Corresponding integrated timing-jitter traces (100 Hz - 5 MHz).

Figure 3.9 (a) shows the measured timing-jitter spectral densities for SC and EC operation in the stretched-pulse regime, recorded relative to the RL. Beyond the locking bandwidth of ~3 kHz, i.e., in the offset-frequency range from 3 kHz to 5 MHz, implementation of XPM suppression in the EC leads to a broadband reduction of the timing-jitter spectral density up to ~700

kHz. Above ~2 MHz, the spectra approach the electronic noise floor set by the BOC sensitivity (0.56 mV/fs). The corresponding RMS integrated jitter, shown in Fig. 3.9 (b), decreases from 22 fs in SC to ~14.5 fs in EC, confirming a clear improvement due to XPM suppression.

In the soliton regime, stable jitter measurements require a slightly higher locking bandwidth of ~9 kHz, reflecting the intrinsically higher noise level of this regime, as also evident from the RIN results. The timing-jitter spectral densities for soliton operation are presented in Fig.3.9 (c). As in the stretched-pulse case, XPM suppression in the EC enables broadband timing-jitter reduction across nearly the entire measured offset-frequency range from 3 kHz to 5 MHz. The corresponding integrated jitter, shown in Fig.3.9 (d), decreases from 87 fs in SC to 37 fs in EC, corresponding to a relative noise suppression of ~3.5 dB.

Consistent with the RIN analysis, the SP regime exhibits overall lower timing-jitter in both configurations compared to the soliton regime, despite the larger integration range. The slightly stronger relative suppression observed in the soliton regime can be attributed to its higher nonlinear phase shift per roundtrip, which enhances the coupling of RIN to timing-jitter via nonlinear effects, as discussed in Refs. [100,155,157].

Overall, the implementation of YVO_4-based XPM suppression in the LUT not only improves the temporal and spectral pulse quality but also yields a substantial reduction of both RIN and timing-jitter in the soliton and stretched-pulse regimes.

3.1.5 Energy-Scaling with Large-Mode-Area Fiber Technology

While the preceding sections focused on noise optimization and stability enhancement through XPM suppression, an equally important objective in the development of high-performance fiber oscillators, particularly as driving sources for complex MPM platforms, is the scaling of pulse energy without compromising environmental stability, output pulse quality or noise characteristics [65,68]. The achievable pulse energy in LSI oscillators is fundamentally constrained by the accumulated nonlinear phase shift per cavity roundtrip, which increases with mode confinement and fiber length [69]. Excessive nonlinear phase accumulation can lead to multi-pulsing or continuous-wave breakthrough, ultimately degrading the overall laser performance [158,159]. Consequently, the limited pulse energies available directly from the oscillator often necessitate additional amplifier stages, increasing overall system complexity and susceptibility to additional noise accumulation [160].

To address these intrinsic limitations, several energy-scaling strategies have been explored, including advanced dispersion management [161,162], intra-cavity divided-pulse operation [144,163], and the use of LMA fibers to reduce nonlinear phase accumulation by expanding the guided mode field [164]. However, the implementation of LMA fibers in All-PM LSI

oscillators has not been successfully demonstrated so far, owing to challenges related to higher-order mode excitation, mode-locking stability, thermal management, and noise control.

This section presents the first demonstration of energy scaling in an all-PM LSI mode-locked oscillator using Yb-doped LMA fiber technology to drastically enhance achievable output power and pulse energy. By integrating 25 µm core diameter PM LMA fibers into an adapted high-power LSI cavity design with dedicated higher-order mode suppression, stable soliton-like mode-locking is achieved at pulse energies of up to 10 nJ distributed between two output ports. This corresponds to a 36-fold energy increase compared to a reference LSI oscillator based on standard single-mode fibers, while simultaneously yielding improved high-frequency RIN. Together with the birefringent performance enhancement strategies developed in the preceding sections, these results establish a viable pathway toward unifying energy scalable femtosecond pulse generation and ultra-low-noise performance in a new class of environmentally stable, all-PM LSI-based fiber laser platforms.

The experimental setup of the LMA-adapted LSI oscillator is shown in Fig.3.10 (a). The active fiber segment includes a pump-beam combiner that couples pump light from an 18 W wavelength-stabilized multimode laser diode operating at 976 nm into the cladding of 2 m Yb-doped polarization-maintaining large-mode-area (Yb-PLMA) fiber. The Yb-PLMA fiber (Liekki Yb1200 25/250DC-PM) features a 25 µm core diameter, a numerical aperture of 0.065, and a peak cladding absorption of 10.6 dB/m at 976 nm. Since the Yb-PLMA supports multiple higher-order modes (HOMs), special measures are required to ensure clean single-mode operation without distortions of the intra-cavity pulse evolution. Following numerical simulations performed with the commercial software *RP Photonics*, the fiber is therefore coiled on a 30 mm radius aluminum cylinder, which introduces estimated propagation losses of ~2 dB and ~20 dB for the LP_{01} and LP_{11} modes, respectively. To further suppress residual HOM content, the LMA segment is spliced to mode-field adapters (MFA1/2) at both ends, tapering to 0.25 m sections of 5.5 µm core-diameter single-mode PM fiber (SMF1/2, Coherent PM980-XP).

In the experiment, self-starting mode-locking of the LSI-LMA oscillator is achieved for a configuration of the SA transmission function $T(\Delta\varphi_{nl})$ with the QWP angle set to $\theta_Q = 70°$ and the HWP angle tuned between $\theta_H = 5°$ and 0°. These settings correspond to an intracavity energy splitting ratio ε of 0.75 and 0.66, respectively. With a net cavity dispersion of -0.121 ps^2, the laser self-starts into a multi-pulse soliton regime at a pump power of approximately 6 W. Stable single-pulse operation is then obtained by reducing the pump power by about 63% to ~2.2 W. As mentioned before, this behavior is well known from NALM/NOLM Kerr-type mode-locked oscillators, and is generally associated with the limited accumulation of small-

signal nonlinear phase shift $\Delta\varphi_{nl}$ below a critical pump threshold [28,29]. The continuous-wave lasing threshold is measured at 1.5 W pump power, and the round-trip cavity loss, excluding the non-saturable contribution of the saturable absorber, is estimated to be ~65%.

Figure 3.10 (b) shows the measured output spectra in the single-pulse regime at Ports T and R; both centered near 1058 nm. The maximum pulse energy at Port T reaches 5.4 nJ with an average power of 92 mW, adjustable via the output coupling ratio controlled by QWP1. At the same working point, the Port R output provides up to 4.3 nJ with 72 mW average power.

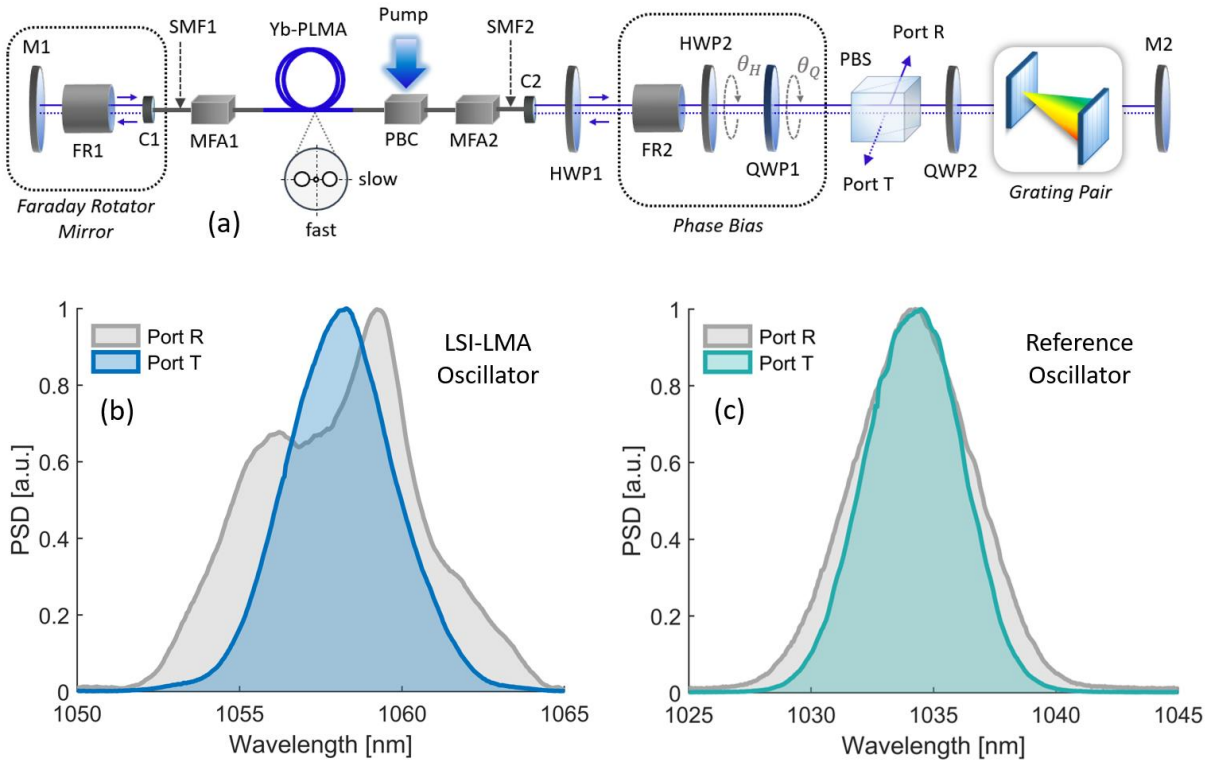

Figure 3.10: Setup and output comparison of the LSI mode-locked LMA fiber laser to a standard fiber reference laser. (a): Experimental setup of the LSI-LMA oscillator. M: mirror, FR: Faraday-rotator, C: collimator, SMF: single-mode fiber, MFA: mode-field adapter, Yb-PLMA: Ytterbium-doped polarization maintaining large-mode-area fiber, PBC: pump-beam combiner, HWP: half-wave plate, QWP: quarter-wave plate, PBS: polarization beam-splitter. (b): Measured output spectrum at Port T (blue) and Port R (gray) of the LSI-LMA oscillator in soliton-regime with a FWHM of ~6 nm and ~4 nm, respectively. Inset: Corresponding measured port T AC trace compared to the FTL. (c): Measured Port T (cyan) and Port R (gray) spectra of the reference oscillator with a FWHM of 6 nm and 5 nm, respectively. The inset shows again the corresponding Port T AC trace compared to its FTL.

Mode-locked steady states in the dissipative or dispersion-managed soliton regime are observed at pump powers between 7.5 and 8 W when the net dispersion is reduced by decreasing the grating separation. However, stable operation for durations longer than a few seconds is

prevented by damage occurring at the SMF facets or he MFAs, indicating the need for additional high-power measures such as anti-reflective coatings, fiber end-caps, or active and passive cooling strategies.

To evaluate the impact of the large-mode-area (LMA) fiber configuration on key laser parameters, the LSI-LMA oscillator is compared to a reference oscillator (RO) with a structure as shown Fig.3.1 (a). In contrast to the 25 µm core LMA fibers used in the LSI-LMA design, the fiber segment of the RO is constructed entirely from standard polarization-maintaining fibers with a 5.5 µm core diameter (Nufern PM980-XP). The cavity is pumped by a 1 W single-mode laser diode at 976 nm, coupled into a 0.5 m highly Yb-doped gain fiber (CorActive Yb401-PM) via a wavelength-division multiplexer. The free-space section of the RO is identical to that of the LSI-LMA oscillator, and both systems are matched in repetition rate (17.3 MHz) and net dispersion (-0.121 ps^2) by adjusting the passive fiber length. With a total fiber length of approximately 5.5 m, the close parameter matching between both oscillators ensures that any differences in mode-locked operation can be attributed directly to the transition from a standard PM to a PLMA fiber configuration.

Self-starting mode-locking of the RO occurs at a pump power of 0.75 W in a multi-pulse soliton regime. The corresponding phase-bias settings and transmission state of the artificial SA function $T(\Delta\varphi_{nl})$ are obtained for $\theta_Q = 70° \pm 2°$ and θ_H between 5° and 0°, similar to those of the LSI-LMA oscillator. Transition to stable single-pulse operation requires reducing the pump power by approximately 70% to ~0.14 W. The output pulse energies in the single-pulse regime, corresponding to the spectra in Fig.3.10 (c), are 0.15 nJ and 0.12 nJ at Ports T and R, respectively. Consequently, increasing the core diameter from 5.5 µm to 25 µm results in a 36-fold enhancement in output pulse energy for the LSI-LMA oscillator.

Compared to the RO, the LSI-LMA oscillator generates a slightly distorted Port R spectrum, likely caused by changes in the accumulated differential nonlinear phase shift $\Delta\varphi_{nl}$ due to multimode interactions and altered gain dynamics, leading to spectral reshaping through the SA mechanism. Furthermore, both output spectra of the LSI-LMA oscillator are red-shifted by approximately 20 nm, from ~1034 nm in the RO to ~1058 nm. This shift can be attributed to stronger reabsorption near 1030 nm, resulting from the higher Yb^{3+} doping concentration (~1.4 × 10^{21} cm^{-3}) in the Yb-PLMA fiber compared to ~2.7 × 10^{20} cm^{-3} in the RO's Yb-SMF. The increased doping is required to compensate for the reduced pump–core overlap factor (η_p) associated with the multimode pump beam in the LMA fiber.

The measured AC traces of the LSI-LMA oscillator at Ports T and R are shown in Figs.3.11 (a) and (b), respectively, together with the corresponding Fourier-transform-limited (FTL) profiles. Assuming a sech² pulse shape and applying a deconvolution factor of 1.54, the pulse duration (FWHM) at Port T is measured to be 1.2 ps, while the calculated FTL duration is ~0.6 ps. The temporal shapes and widths of the FTL pulses are derived numerically from the measured spectra in Fig.3.10 (b) using fast Fourier transform (FFT) analysis. The Port T output pulse therefore shows a slight negative chirp, characteristic of an average soliton as described by the laser master equation [165,166], in accordance with the cavity configuration shown in Fig.3.10 (a). The pulse emitted from Port R, in contrast, is positively chirped with a duration of 1.3 ps compared to a calculated FTL of 0.36 ps. For the RO, the output pulse energy is insufficient for reliable AC measurements. However, based on the output spectra, the corresponding FTL pulse durations at Ports T and R are estimated to be 0.61 ps and 0.54 ps, respectively. Figure 3.11 (c) further shows the RF spectrum of the fundamental repetition frequency at ~17.3 MHz for the LSI-LMA oscillator output pulse train at Port T, with a SNR of 75 dB, which confirms stable, low-noise mode-locked operation.

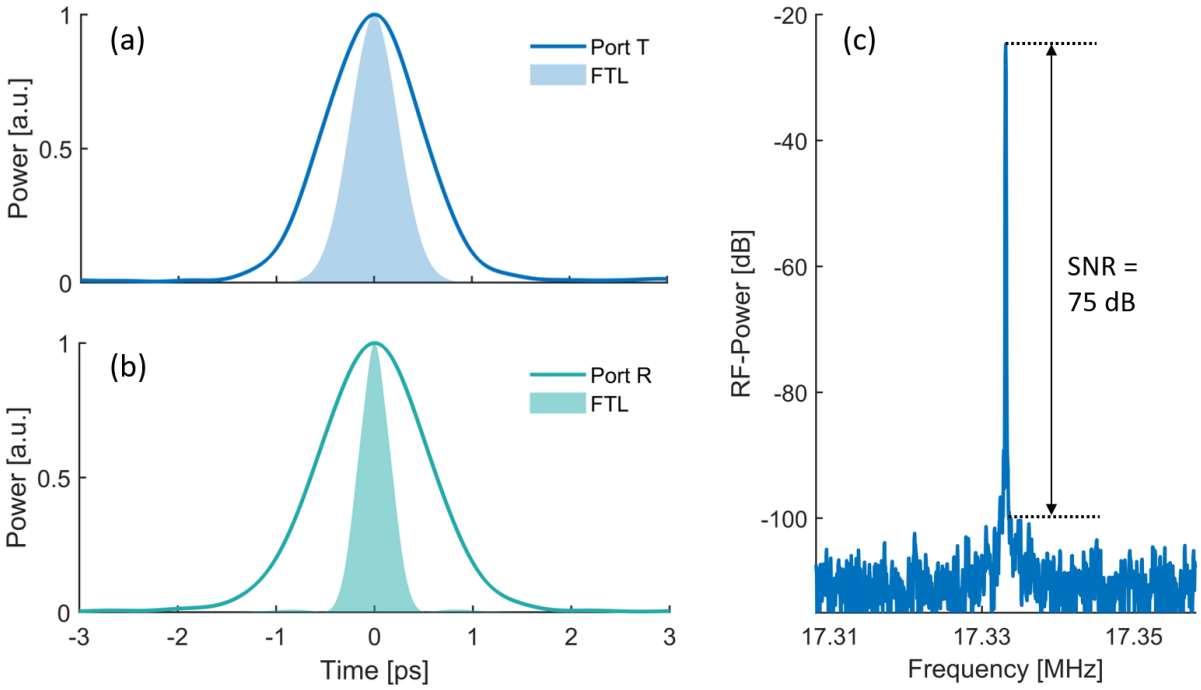

Figure 3.11: Characterization of the output pulse duration and RF spectrum of the LSI-LMA oscillator. (a): Measured output pulse (Port T, blue) AC trace and corresponding Fourier transform-limited (FTL) pulse (shaded) of the LSI-LMA oscillator, with FWHM of 1.2 ps and 0.6 ps, respectively. (b): Measured pulse (Port R, cyan) and calculated FTL pulse (shaded) with FWHM values of 1.3 ps and 0.36 ps, respectively. (c): RF spectrum of the LSI-LMA oscillator (Port T) recorded at the fundamental repetition rate of ~17.33 MHz, showing a signal-to-noise ratio (SNR) of approximately 75 dB.

An important characteristic of the energy-scaled LSI-LMA oscillator is to what extend the noise and stability is affected by the different cavity configuration, and in particular also by the usage of a high-power multimode pump. The frequency-resolved relative intensity noise (RIN) is therefore characterized and compared between the LSI-LMA oscillator and the RO.

Similar to the previous chapter, the RIN is characterized via detection of the pulse train from the respective output port using a fast, low-noise InGaAs photodetector (Thorlabs DET08CFC). The eighth harmonic of the detected RF signal at 139.2 MHz is isolated with a tunable bandpass filter and subsequently amplified by a 10 dB low-noise transimpedance amplifier (MiniCircuits ZX60-33LN-S+), resulting in an RF power level of -6.5 dBm. This corresponds to a consistent shot-noise floor of -142.3 dBc. The AM function of a SSA (Keysight E552B) is then employed to record the single-sideband, frequency-resolved RIN spectral density. The resulting RIN spectra for the LSI-LMA oscillator and the RO at Ports T and R are shown in Figs.3.12 (a) and (b), respectively.

Compared to the RO, the RIN magnitude measured at Port T of the LSI-LMA oscillator exhibits similar behavior in the low-frequency range below 50 Hz, which reflects the identical environmental conditions of both systems in the laboratory. Between 50 Hz and approximately 20 kHz, however, the LSI-LMA oscillator shows a noticeably higher noise level, with a difference of up to 12 dB. A characteristic feature of the LMA oscillator's RIN spectrum in this range is a series of resonant peaks at the 50 Hz utility frequency and its higher harmonics. This indicates that the increased RIN is not of optical origin, but rather results from power-supply interference due to insufficient electronic filtering and shielding, rather than from intrinsic properties of the LSI-LMA cavity or the multimode pump diode.

When integrated over the full measurement bandwidth (10 Hz - 5 MHz), the total RIN reaches up to 0.063% for the LSI-LMA oscillator and 0.038% for the RO, as shown in Fig.3.12 (c). In the high-frequency region above 20 kHz, dominated by the fast intracavity optical dynamics, the LSI-LMA oscillator exhibits a reduced RIN magnitude, improved by up to 5 dB compared to the RO. The corresponding integrated RIN over the 20 kHz – 5 MHz range is 0.027% for the LSI-LMA and 0.033% for the RO, confirming the superior high-frequency noise performance of the LMA configuration.

An almost identical trend is observed in the RIN spectra and corresponding integrated RIN measured at Port R, as shown in Figs.3.12 (b) and (c). Between 50 Hz and 20 kHz, the LSI-LMA oscillator exhibits higher RIN levels compared to the reference oscillator (RO), whereas at frequencies above 20 kHz, the LMA configuration demonstrates a clear improvement with noise reduction of up to 8 dB. When integrated over the full measurement bandwidth (10 Hz–

5 MHz), the total RIN at Port R amounts to 0.148% for the LSI-LMA oscillator and 0.071% for the RO. In the high-frequency range (>20 kHz), the integrated RIN decreases to 0.045% for the LSI-LMA oscillator compared to 0.050% for the RO, confirming the enhanced high-frequency noise performance of the LMA design.

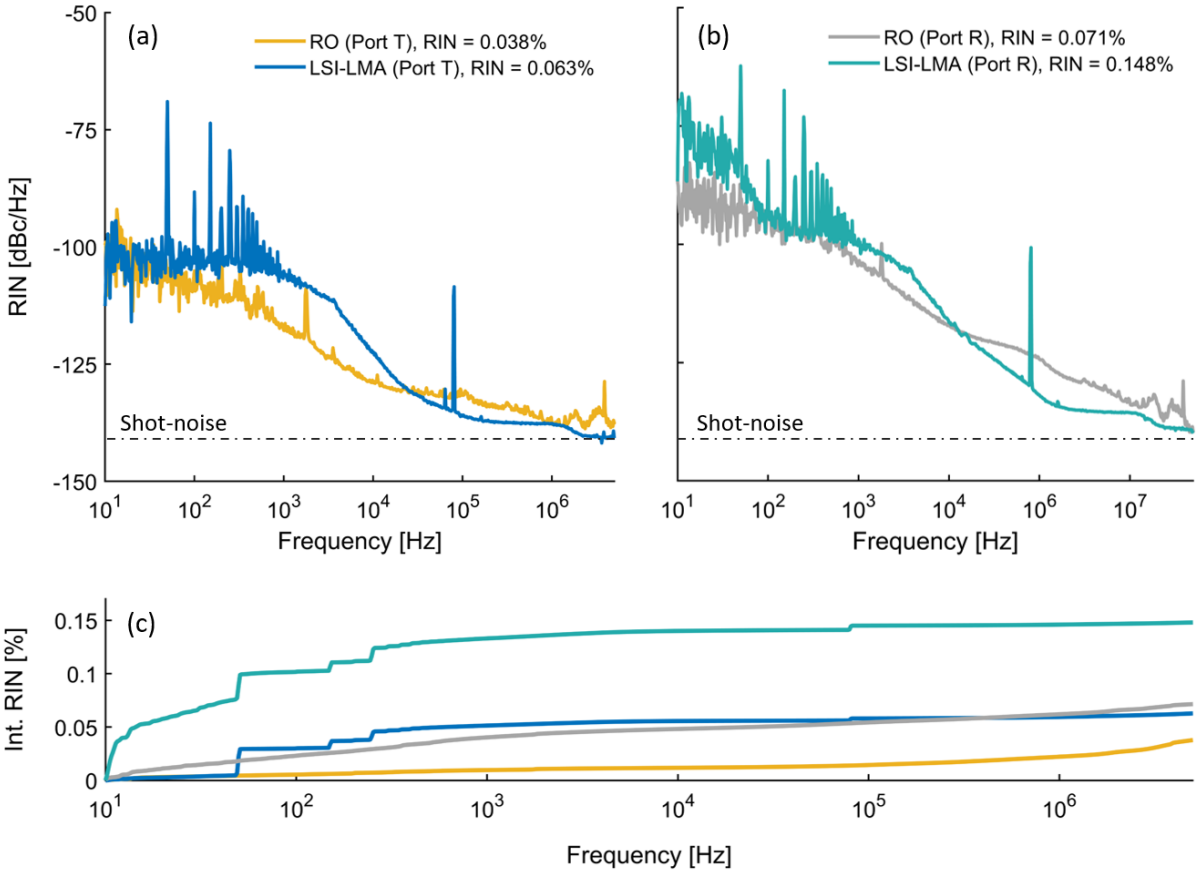

Figure 3.12: Frequency-resolved RIN performance of the LSI-LMA oscillator compared to the RO. (a): RIN spectral densities measured at Port T for the RO (yellow) and LSI-LMA oscillator (blue). (b): RIN spectral densities measured at Port R for the RO (gray) and LSI-LMA oscillator (cyan). (c): Corresponding integrated RIN values over the 10 Hz–5 MHz range: 0.063% (LSI-LMA) and 0.038% (RO) at Port T, and 0.148% (LSI-LMA) and 0.071% (RO) at Port R.

A comparison between the fluctuations measured at Ports T and R reveals that in both laser systems, the RIN spectral density at Port T is consistently lower than at Port R. This results in a difference of approximately 3.7 dB between the output ports in the LSI-LMA oscillator and about 2.7 dB in the RO. As we have shown in Ref. [167], this characteristic asymmetry is typical for fiber oscillators mode-locked with NLIs and originates from the dynamic response of the SA transmission function $T(\Delta\varphi_{nl})$ to intracavity intensity fluctuations. In the case of the LSI-LMA oscillator, additional RIN amplification of the reflected field at Port R, combined

with enhanced noise coupling from the multimode pump diode, likely contributes to the increased low-frequency (<100 Hz) RIN observed in the measurement.

In summary, the integration of 25 µm core-diameter large-mode-area (LMA) fibers into an all-polarization-maintaining linear self-stabilized interferometer enables efficient pulse-energy scaling while preserving stable mode-locked operation. The resulting LSI–LMA oscillator supports robust, self-starting soliton-like mode-locking with pulse energies of up to 10 nJ and an average output power of 170 mW distributed between two output ports, corresponding to a 36-fold energy increase compared to an otherwise matched 5.5 µm-core reference oscillator. Importantly, despite the substantially enlarged mode area, the system exhibits improved high-frequency noise performance, with relative intensity noise suppressed by up to 8 dB above 20 kHz. Together with the XPM-suppression concepts developed in the preceding sections, these results demonstrate that LMA fiber integration in LSI-based oscillators enables substantial energy scaling without sacrificing intrinsic stability or noise performance, marking a decisive step toward robust, high-power, and ultra-low-noise all-PM fiber laser platforms.

3.2 Fiber-Interferometric Dual-Color Source with Standard Quantum-Limited Intensity Noise

Derived from the insights of the LSI oscillator dynamics, this chapter introduces a fiber-interferometric dual-color laser system capable of generating simultaneous femtosecond pulse trains at the fundamental and second-harmonic wavelengths with standard quantum-limited (SQL) intensity noise in both channels. The system leverages intrinsic nonlinear dynamics of the LSI oscillator architecture introduced above to coherently integrate Kerr-type nonlinear polarization rotation with type-I phase-matched second-harmonic generation within a common interferometric topology. Precise phase-bias tuning and dispersion engineering enable simultaneous gain, frequency conversion, and interferometric noise suppression, yielding SQL-limited high-frequency RIN performance for both the fundamental and second-harmonic optical pulse trains.

The underlying concept and its experimental realization were developed and demonstrated as part of this doctoral work and reported in the peer-reviewed article:

- M. Edelmann *et al.*, “Fiber-interferometric second-harmonic generator with dual-color standard quantum-limited noise performance,” *Opt. Express* 32, 10362-10372 (2024).

The demonstrated system delivers dual-color pulse trains at a repetition rate of 42 MHz, with sub-150 fs pulse durations at 1030 nm and 515 nm, and achieves up to 14 dB simultaneous RIN suppression relative to the input, reaching the SQL beyond offset frequencies of 100 kHz. The

combination of interferometric robustness, coherent nonlinear coupling, and flexible phase-bias tunability establishes a versatile platform for ultra-low-noise wavelength conversion, directly relevant to multicolor MPM, nonlinear spectroscopy, and quantum-optical seeding schemes.

3.2.1 Experimental Setup and Physical Mechanism

As first step, the experimental layout and the underlaying physical mechanisms are introduced. The setup is illustrated in Fig.3.13. A home-built Yb-doped ultrafast fiber laser serves as the driving light source, delivering linearly polarized pulses at a repetition rate of 42 MHz with a maximum average power of 150 mW, corresponding to a pulse energy of approximately 3.5 nJ. The inset in Fig.3.13 shows the measured optical spectrum and AC trace at full output power.

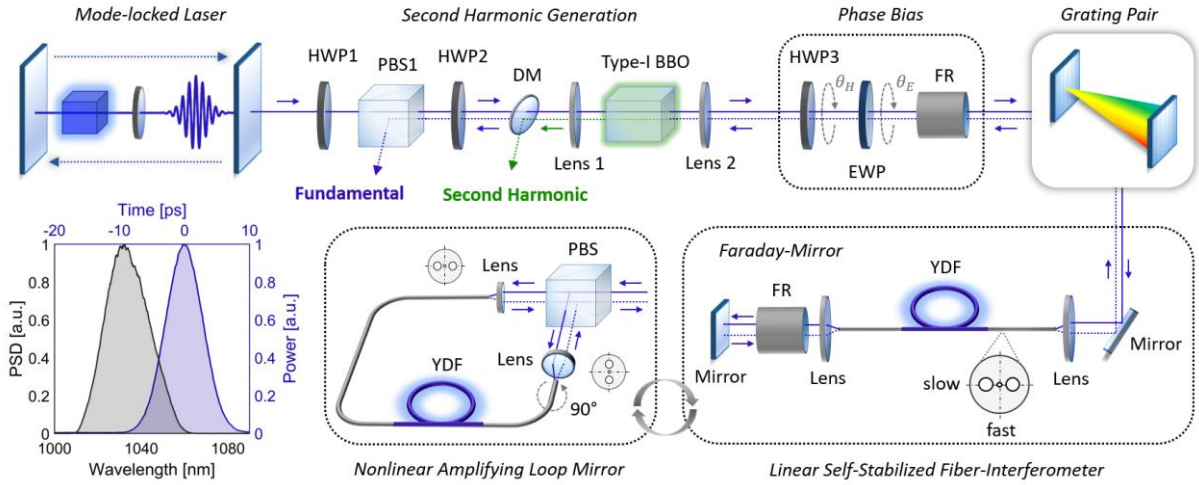

Figure 3.13: Experimental setup of the fiber-interferometric second-harmonic generator enabling the simultaneous generation of compressed pulse trains at 1030 nm and 515 nm with quantum-limited intensity noise. Inset: Measured optical spectrum (black) and AC trace (blue) of the mode-locked Yb-fiber laser source, showing FWHM values of ~17 nm and 4.6 ps, respectively. HWP: half-wave plate, PBS: polarizing beam splitter, DM: dichroic mirror, EWP: eight-wave plate; FR, Faraday rotator, YDF: Yb-doped fiber.

The emitted spectrum has a FWHM of ~17.2 nm centered at 1032 nm. Assuming a Gaussian temporal profile, the positively chirped output pulse features an estimated FWHM duration of ~4.6 ps. HWP1 is adjusted to maximize transmission through the PBS1. The resulting pulse train is directed into a module for type-I phase-matched SHG, consisting of a 3 mm-long BBO crystal (cut angle 24.3°), a dichroic mirror (DM), and two broadband AR-coated focusing lenses (Lens 1/2) with 19 mm focal length each.

In the forward propagation direction, HWP2 is rotated such that the linear polarization is orthogonal to the phase-matching axis of the BBO crystal, thereby suppressing SHG at this

stage and allowing the fundamental pulse train to pass through the module unaffected. Subsequently, the beam passes through a tunable phase-bias section consisting of an eight-wave plate (EWP, rotation angle θ_E) and HWP3 (rotation angle θ_H) combined with a 45° single-pass FR. The pulse train then enters a parallel transmission grating pair (GP, LightSmyth T-1000-1040 Series, 1000 lines/mm) arranged in a double-pass configuration, which provides adjustable dispersion management. Finally, the pulse train is coupled into a nonlinear and reflective fiber NLI. The NLI can be implemented either as an LSI or a NALM, both of which are widely used as artificial SAs in ultra-low-noise mode-locked fiber lasers as mentioned in the previous sections. In both configurations, the NLI simultaneously amplifies the incoming pulse and introduces a nonlinear phase difference $\Delta\varphi_{nl}$ between two orthogonally polarized components propagating in separate interferometer arms, leading to an intensity-dependent nonlinear polarization rotation (NPR). Here, and LSI configuration is implemented due to its straightforward alignment, well-understood dynamics, and seamless integration with the SHG stage.

The LSI consists of an all-PM fiber segment terminated with a fiber-coupled Faraday rotator mirror (FRM). The 8 m fiber section includes 5 m of Yb-doped active fiber (YDF, Coherent PM-YSF-LO-HP), which is optically pumped by a 1 W laser diode at 976 nm via a WDM, thereby operating as a double-pass fiber amplifier. The slow axis of the PM fiber is aligned with both the reflection axis of PBS1 and the phase-matching axis of the BBO crystal.

The system utilizes the identical working principle of the LSI which enables mode-locked steady-states in the oscillator designs; by adjusting the phase-bias angles θ_E and θ_H, two orthogonal polarization components are generated from the linearly polarized input field exiting PBS1. These components couple into the fast and slow axes of the PM fiber inside the LSI. During propagation, the birefringence of the fiber causes the two polarization modes to evolve independently with different group velocities, leading to the accumulation of a differential nonlinear phase shift $\Delta\varphi_{nl}$ through the optical Kerr effect, while both components are simultaneously amplified in the YDF.

After a single pass, the FRM rotates the polarization state by 90°, thereby compensating for birefringence-induced walk-off and ensuring that the two amplified polarization modes recombine upon double-pass propagation through the LSI. A comprehensive description of the operating principles of both the LSI and NALM configurations can be found in chapter 3.1.1. The amplified and nonlinearly modulated output from the LSI then retraces its path back toward the SHG module, passing again through both the GP and phase-bias section. However, in contrast to the forward propagation through the SHG module, the pulses emerging from the LSI now contain a polarization component parallel to the phase-matching axis of the BBO crystal [122].

This component arises from the combined effect of the linear phase bias (set by the angles θ_E and θ_Q) and the nonlinear, intensity-dependent phase shift induced by the magnitude of nonlinear polarization rotation within the LSI.

Due to the intrinsic working principle of the LSI, any peak power fluctuations in the input field E_{in}, expressed as $P_{in}(t) = \bar{P}_{in}(t) + \delta P_{in}(t)$, where $\bar{P}_{in}(t)$ denotes the average instantaneous power and $\delta P_{in}(t)$ a time-variant noise term, are directly mapped onto fluctuations of the differential nonlinear phase shift $\Delta\varphi_{nl}$ according to the relation:

$$\Delta\varphi_{nl}(t) = \overline{\Delta\varphi_{nl}}(t) + \delta\Delta\varphi_{nl}(t) = L_{LSI} n_2 g \frac{\pi}{\lambda_s A_{eff}} (\bar{P}_{in}(t) + \delta P_{in}(t))(2\varepsilon - 1) \qquad (3.2.1)$$

Here, λ_s denotes the center wavelength of E_{in}, A_{eff} the effective mode-field area of the LSI fiber segment, g the lumped gain factor of the LSI, n_2 the nonlinear refractive index, ε the energy splitting ratio between the OPMs, and L_{LSI} the length of the LSI fiber [69,167].

To evaluate how these fluctuations influence the noise transfer at both the BBO crystal and PBS1, it is essential to relate $\Delta\varphi_{nl}$ to the polarization state of the LSI output field E_{out}. To do so, the output field arriving at the BBO can be expressed as a Jones vector in the form

$$\boldsymbol{E}_{out}(t) = \begin{pmatrix} E_{fast} exp\left\{-i\frac{\left(\Delta\varphi_{nl}(t) + \varphi_{pb}\right)}{2}\right\} \\ E_{slow} exp\left\{i\frac{\left(\Delta\varphi_{nl}(t) + \varphi_{pb}\right)}{2}\right\} \end{pmatrix} \qquad (3.2.2)$$

where $E_{fast} \approx \sqrt{(1-\varepsilon)g}E_{in}$ approximates the output electric field amplitude parallel to the fast axis of the LSI, $E_{slow} \approx \sqrt{\varepsilon g}E_{in}$ the amplitude parallel to the slow axis, $\Delta\varphi_{nl}$ the differential nonlinear phase shift, and φ_{pb} the generalized phase shift from the phase-bias.

To describe $\boldsymbol{E}_{out}(t)$ in terms of the experimentally adjustable phase-bias parameters (θ_E and θ_H in the setup shown in Fig. 3.13), the Jones formalism can be applied to the system as outlined in detail in chapter 3.1.1. Since both the phase-matching axis of the BBO crystal and the reflection axis of PBS1 are aligned parallel to the slow axis of the LSI, the instantaneous rotation angle $\xi(t)$ can be obtained by evaluating the angle between $\boldsymbol{E}_{out}(t)$ and a unit vector $\boldsymbol{e}_{SHG,R} = \binom{0}{1}$ parallel to the respective axes, which defines the relevant reference direction for SHG and reflection. By further considering the transfer of input power fluctuations to fluctuations of $\Delta\varphi_{nl}$ in the LSI, as described by Eq. (3.2.1), one arrives at the relation

$$\xi(t) = \bar{\xi}(t) + \delta\xi(t) = cos^{-1}\left(\sqrt{\varepsilon}cos\left[\frac{\Delta\varphi_{nl}(t) + \delta\Delta\varphi_{nl}(t) + \varphi_{pb}}{2}\right]\right)$$
$$= cos^{-1}\left(\sqrt{\varepsilon}cos\left[\frac{\pi}{2\lambda_s A_{eff}} L_{LSI} n_2 g(\bar{P}_{in}(t) + \delta P_{in}(t))(2\varepsilon - 1)\right.\right. \quad (3.2.3)$$
$$\left.\left. + \frac{\varphi_{pb}}{2}\right]\right)$$

which provides an analytical expression to describe how fluctuations in the input peak power of the LSI translate into fluctuations of the instantaneous polarization rotation angle $\xi(t)$ at its output. This angle determines the conversion efficiency and power distribution at both the BBO crystal and PBS1.

Neglecting potential distortions in the SHG process arising from birefringent walk-off, dispersion, or other crystal effects, the generated second-harmonic power can be expressed as

$$P_{SHG}(t) \propto \vartheta_{\Delta} sin^2(\xi(t)) \quad (3.2.4)$$

where ϑ_{Δ} denotes the maximum achievable SHG efficiency [122]. The reflected power at PBS1, which is influenced by the preceding SHG process (see Fig.3.13), scales as

$$P_R(t) \propto \sin(\xi(t)) - \vartheta_{\Delta} sin^2(\xi(t)) \quad (3.2.5)$$

By substituting Eq. (3.2.3) into these relation, the corresponding noise transfer functions for the second harmonic and fundamental outputs can be obtained through evaluating the derivatives dP_{SHG}/dP_{in} and dP_R/dP_{in}, respectively. For generalization, it is convenient to express both the power and noise transfer in terms of the differential nonlinear phase shift $\Delta\varphi_{nl}$ rather than the input power P_{in}. While the two quantities are directly proportional, $\Delta\varphi_{nl}$ inherently considers all system-specific parameters of the LSI, including the fiber amplifier gain factor, as defined in Eq. (3.2.1).

Consequently, the noise transfer behavior for the second-harmonic and fundamental reflected output modes can be characterized by the derivatives $dP_{SHG}/d\Delta\varphi_{nl}$ and $dP_R/d\Delta\varphi_{nl}$, respectively. At system operating points where $dP_{SHG,R}/d\Delta\varphi_{nl} \approx 0$ near the peak of the LSI output pulse, strong dual-channel suppression of input power fluctuations can be achieved. Figure 3.14 (a) illustrates the numerically computed power transfer characteristics for both operational modes in an exemplary LSI configuration with $\varepsilon = 0.22$ and $\varphi_{pb} = 0.8\pi$, plotted as a

function of the power-dependent nonlinear phase difference $\Delta\varphi_{nl}$. Here, the output powers P_R and P_{SHG} are normalized to the input power P_{in}, scaled by the lumped LSI gain factor g. The corresponding noise transfer functions are shown in Fig.3.14 (b). As shown, the purely sin^2-dependent nature of the second-harmonic signal leads to a comparatively larger modulation depth in its noise transfer response.

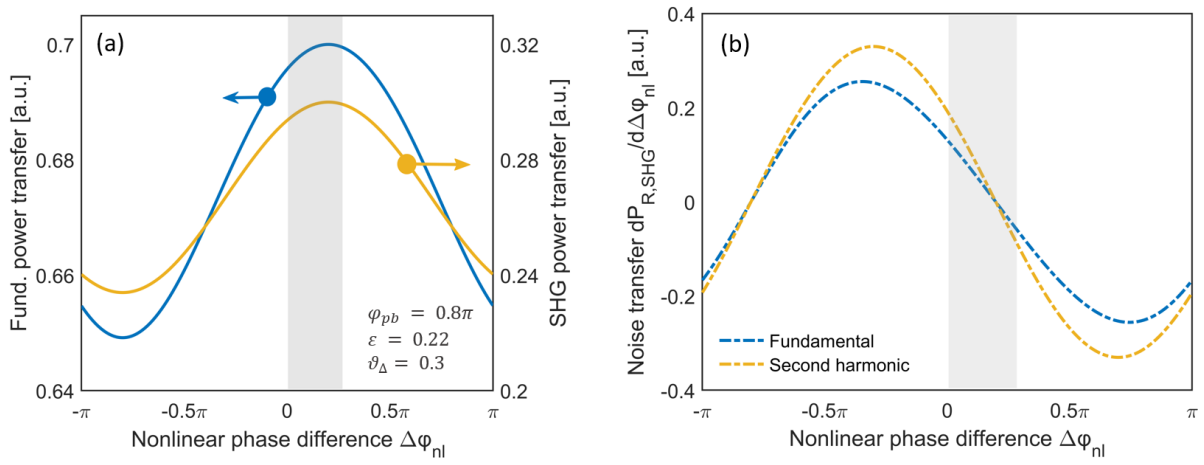

Figure 3.14: Simulated power and noise transfer characteristics of the linear self-stabilized interferometer (LSI). (a): Normalized power transfer functions of the amplified LSI output, $P_R/(gP_{in})$ and $P_{SHG}/(gP_{in})$, for $\varepsilon = 0.22$, $\varphi_{pb} = 0.8\pi$, and $\vartheta_\Delta = 0.3$, plotted as a function of the accumulated $\Delta\varphi_{nl}$ for the fundamental (blue) and second-harmonic (yellow) outputs, respectively. (b): Corresponding absolute noise transfer functions, $dP_R/d\Delta\varphi_{nl}$ and $dP_{SHG}/d\Delta\varphi_{nl}$. The shaded region indicates the operation range $0 \leq \Delta\varphi_{nl}(t) \leq 0.3\pi$, where $dP_{SHG,R}/d\Delta\varphi_{nl} \approx 0$ enables effective dual-channel noise suppression near the LSI pulse peak.

For an exemplary LSI output pulse in which the intensity-dependent $\Delta\varphi_{nl}(t)$ varies within the gray-shaded region between $0 \leq \Delta\varphi_{nl}(t) \leq 0.3\pi$, an appropriate choice of ε and φ_{pb} through the phase-bias control enables strong suppression of noise around the pulse peak, where $\Delta\varphi_{nl}(t) \approx 0.3\pi$, while maintaining nearly maximum power transfer in both output channels. For smaller phase shifts, $\Delta\varphi_{nl}(t) \approx 0.2\pi$, corresponding to the lower-intensity wings of the pulse, Fig.3.14 (b) shows an increase in the noise transfer function.

3.2.2 Experimental Results and Discussion

To validate this mechanism experimentally, the dual-color noise transfer of the setup is systematically characterized to verify the theoretically predicted operating points that enable simultaneous noise suppression and efficient power conversion in both the fundamental mode (FM) at 1030 nm and the second-harmonic mode (SHM) at 515 nm. Starting with measurements of the dual-color power transfer, Fig.3.15 (a) and (b) present the measured average output powers in the FM and SHM channels, respectively, as a function of the tunable phase-bias angle θ_E with

$\theta_H = 160°$. The corresponding output spectra are shown in Fig.3.15 (c) and (d). All rotation angles are defined relative to the PBS reflection axis according to the standard mathematical convention. For precise phase-bias control, θ_E is electro-mechanically adjusted using a digitally controlled rotation mount. In the experiment, the input pulse train is then launched into the system with a pulse energy of approximately 0.75 nJ. The total linear loss of the system, including the SHG module, GP, and LSI, is estimated to be about 42%. To compensate for this loss and simultaneously increase the pulse energy while avoiding nonlinear spectral distortions, the YDF within the LSI is optically pumped with 500 mW of average power from a 976 nm laser diode. The separation between the gratings in the GP is set to approximately 42 mm to pre-compensate the chirp of the input pulse and the dispersion of the LSI fiber segment, thereby ensuring a compressed pulse with maximum peak power incident on the SHG module.

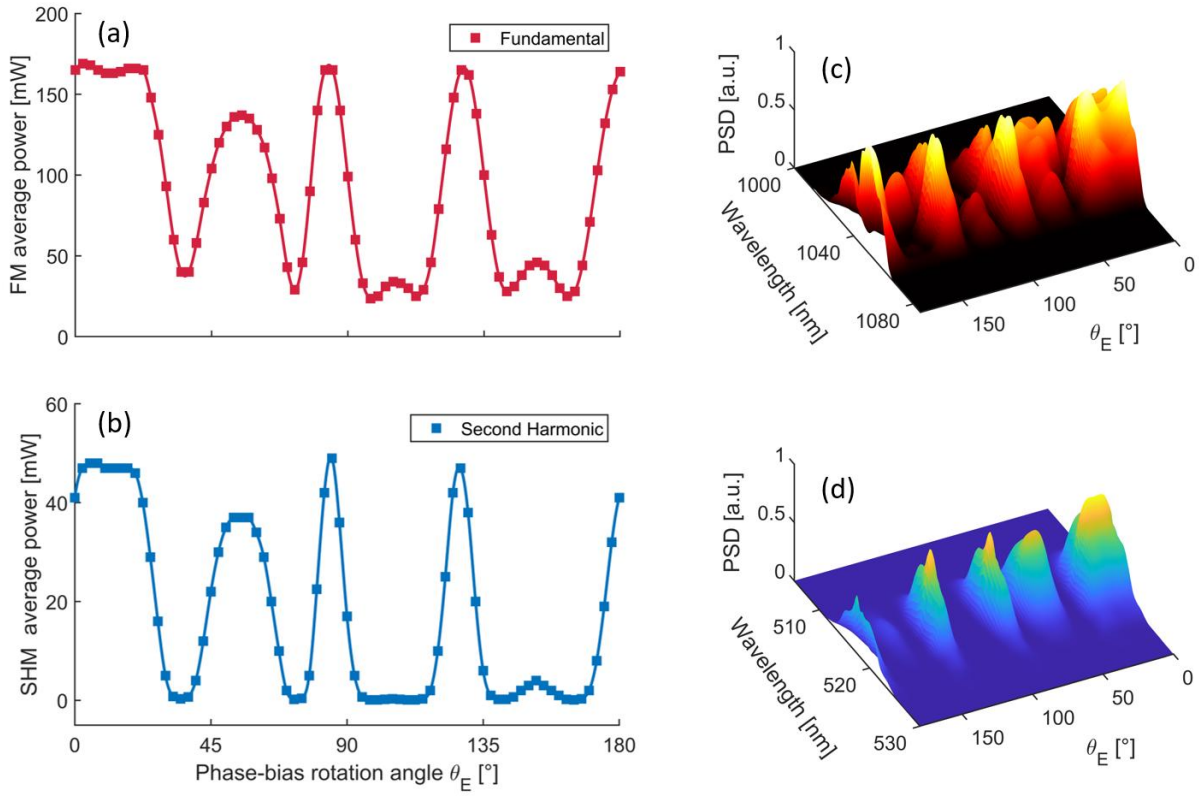

Figure 3.15: Experimental characterization of the dual-color power transfer and spectral behavior of the LSI-based SHG system. (a): Measured average output power of the 1030 nm fundamental mode (FM) at the reflected PBS1 output port as a function of the phase-bias rotation angle θ_E. (b): Corresponding average power of the 515 nm second-harmonic mode (SHM) measured after the dichroic mirror (DM). (c): Measured output spectra of the FM as a function of θ_E. (d): Corresponding SHM spectra recorded under identical conditions.

In agreement with theoretical predictions, the measured power transfer between the fundamental (FM) and second-harmonic modes (SHM) exhibits a directly correlated trend, which

arises from the parallel alignment of the PBS1 reflection axis and the phase-matching axis of the BBO crystal. At a phase-bias angle of $\theta_E = 85°$, the output powers of the FM and SHM reach their simultaneous maxima of approximately 165 mW and 50 mW, corresponding to pulse energies of 3.8 nJ and 1.2 nJ, respectively. The complex interplay between the energy splitting ratio ε between the PM-fiber axes in the LSI and the phase-bias φ_{pb}, both of which depend on the settings of θ_E and θ_H, leads to the appearance of multiple local maxima in the measured power transfer characteristics.

In the next step, the correlation between the dual-color power transfer and the corresponding noise transfer is investigated. For this purpose, the RIN spectra of both operational modes are measured as a function of θ_E using the same LSI parameters as before, and compared to the RIN spectrum of the laser source feeding the LSI.

For the FM and the laser source, the optical pulse train is detected with a fast, low-noise InGaAs photodiode (Coherent ET-3010). The third harmonic of the resulting radio-frequency (RF) signal at approximately 126 MHz is isolated using a suitable bandpass filter and amplified with a low-noise transimpedance amplifier (Mini-Circuits ZX60-33LN-S+), powered by a highly stable supply (Toellner TOE8721). The frequency-resolved RIN spectrum of the amplified signal is then recorded with a signal source analyzer (SSA, Keysight E5052B) over the 1 kHz-20 MHz range. The lower limit is chosen to exclude environmental low-frequency noise, while the upper limit was determined by the bandwidth of the RF components.

The measurement procedure for the SHM is identical in principle, except that a biased silicon photodiode (Coherent ET-2030) is used for efficient detection at the 515 nm center wavelength. The use of different detector types results in distinct standard quantum limits (SQLs) for the RIN in the two modes. For the FM and the laser source, an RMS voltage of 5 mV at a 100 Ω termination with a detector responsivity of 0.75 A/W yields an SQL of −142 dBc/Hz. For the SHM, the measurements are performed with an RMS voltage of 11 mV, a 50 Ω termination, and a responsivity of 0.25 A/W, corresponding to an SQL of −137.7 dBc/Hz. These SQL reference levels are kept constant across all subsequent RIN measurements to ensure consistency between both detection schemes.

Figures 3.16 (a) and (b) show the measured the integrated RIN values, obtained by integrating the measured RIN spectral densities over the full 1 kHz - 20 MHz bandwidth, for both FM and SHM as a function of the phase-bias angle θ_E. All other system parameters were identical to the previous measurements. As shown, the regions around $\theta_H = 85°$ and within $0° \leq \theta_E \leq 35°$, where local maxima in average power occur for both FM and SHM, correlate with local

minima of the integrated RIN in both modes, confirming the predicted operating points of simultaneous noise suppression and high conversion efficiency. The integrated RIN reaches minimum values of 0.04% for the FM and 0.07% for the SHM. Consistent with the theoretical predictions, the modulation depth of the RIN is significantly higher for the SHM than for the FM, which can be attributed to the inherent sin^2-dependence of its noise transfer function. Moreover, the overall structure of the RIN traces in both modes show strong correlation, further confirming the theoretically expected behavior.

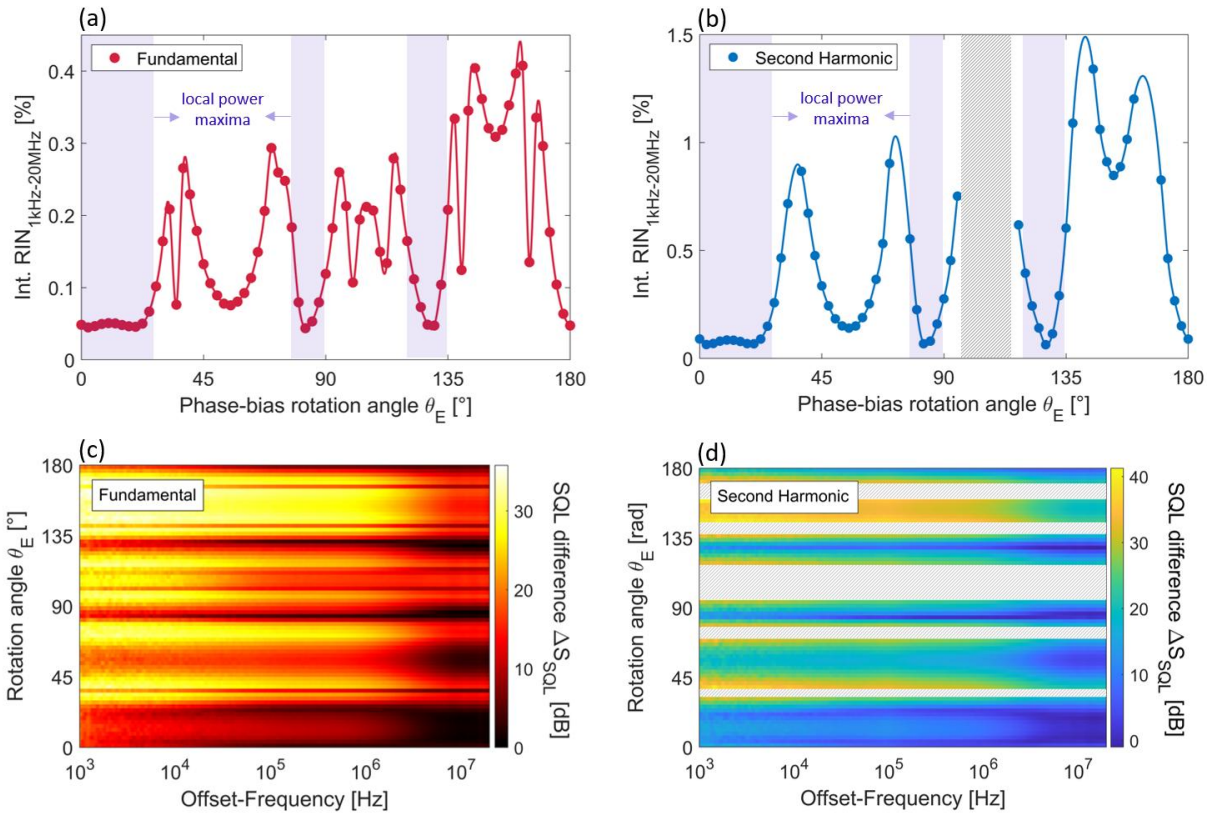

Figure 3.16: Experimental characterization of the RIN transfer in the dual-color LSI system. (a): Measured integrated RIN of the 1030 nm FM over the 1 kHz-20 MHz frequency range as a function of the phase-bias rotation angle θ_E. The blue-shaded regions indicate local maxima in average output power. (b): Simultaneously measured integrated RIN of the 515 nm second-harmonic mode (SHM) as a function of θ_E. (c): Frequency-resolved RIN spectra of the FM for different θ_E settings. (d): Corresponding frequency-resolved RIN spectra of the SHM. The gray-shaded areas mark regions of insufficient output power where RIN measurements could not be performed reliably.

Figures 3.16 (c) and (d) show the corresponding measured frequency-resolved RIN spectra for the FM and SHM, respectively. To enable direct comparison, the RIN spectral density is expressed as the deviation from the SQL, defined as $\Delta S_{SQL,dB}(f) = S_{FM,SHM}(f) - S_{SQL(FM,SHM)}$, where f denotes the offset frequency, S_{SQL} the frequency-independent SQL of

the respective mode as calculated previously, and $S_{FM,SHM}(f)$ the frequency-dependent RIN spectral density measured with the SSA. As shown, the range $0° \leq \theta_E \leq 35°$ corresponds to a broad plateau of high average power and low noise for both output modes, whereas the region around $\theta_E = 85°$ indicates lower $\Delta S_{SQL}(f)$-values, particularly at lower offset frequencies $f \leq 10^5\ Hz$, indicating enhanced noise suppression performance in around this working point.

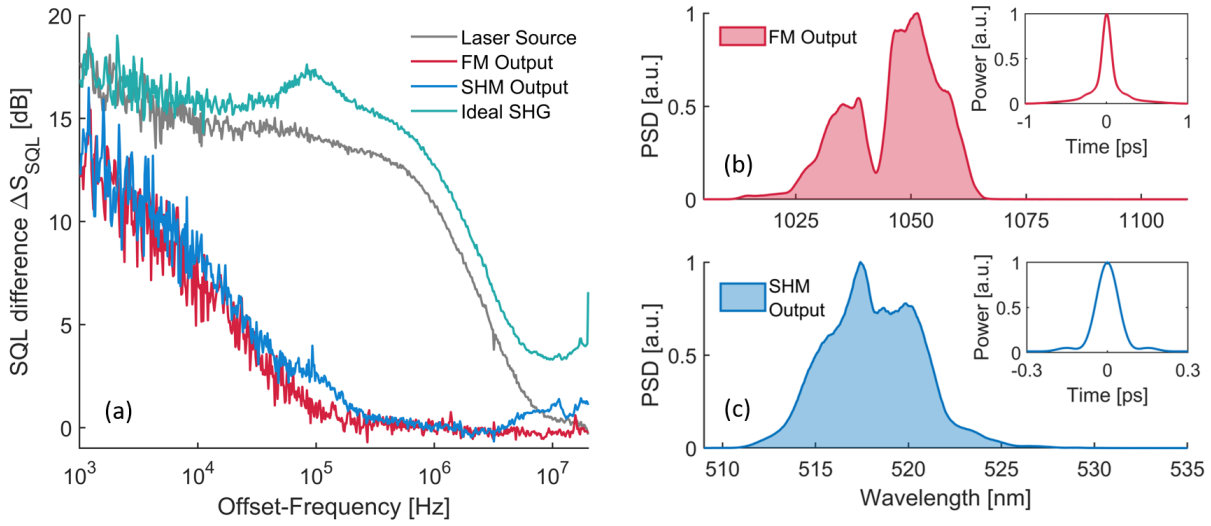

Figure 3.17: Experimental characterization of FM and SHM output at working point with dual-channel standard quantum-limited RIN suppression (a): Measured RIN spectral densities in the 1 kHz–20 MHz range, plotted as the SQL difference ΔS_{SQL}, for the laser source/LSI input (gray) compared to the fundamental mode (FM, red) and second-harmonic mode (SHM, blue) outputs at $\theta_E = 85°$ and $\theta_H = 160°$. The cyan trace represents the RIN spectrum of a regular SHG process under ideal phase-matching conditions ($\theta_E = \theta_H = 0°$). (b): Optical spectrum and AC trace (inset) of the FM at the operating point of maximum noise suppression ($\theta_E = 85°$). (c): Corresponding SHM spectrum together with the FTL pulse shape (inset).

Since the LSI operating point at $\theta_E = 85°$ and $\theta_H = 160°$ provides highly promising conditions for generating dual-color pulse trains with both maximum average power and simultaneous noise suppression in the FM and SHM, a closer examination of the corresponding output characteristics is justified. Figure 3.17 (a) compares the measured RIN spectra of the laser source/LSI input with those of the FM and SHM system outputs. As an additional verification of the underlying mechanism, Fig. 3.17 (a) also includes the RIN trace of the SHM obtained without any applied phase bias ($\theta_E = \theta_H = 0°$) and thus without NPR and LSI-based noise transfer, representing a conventional phase-matched SHG process under otherwise identical system parameters. As shown, the RIN spectral density of the laser source is strongly suppressed over a broad frequency range in both output modes, reaching up to 14 dB reduction between 100 kHz and 1 MHz. Above 100 kHz, both modes exhibit near–quantum-limited noise

performance, with only minor deviations in the SHM. At lower frequencies (< 100 kHz), the suppression becomes less effective. In contrast, the conventional phase-matched SHG without NPR, using linearly polarized light aligned with the BBO phase-matching axis, leads to an overall amplification of the RIN compared to the laser source, particularly at higher frequencies (> 10 kHz). Such RIN amplification is a well-known effect in standard SHG processes, originates in the fundamental square dependence on the input power, and has been reported in multiple experimental studies [168–170].

The comparison between the two cases; conventional type-I phase-matched SHG and NPR-enhanced SHG, clearly demonstrates the strong influence of NPR in the fiber-optic LSI as a novel underlying mechanism enabling ultra-low-noise second-harmonic generation. Figure 3.17 (b) shows the FM output spectrum and the corresponding AC trace at the operating point of maximum noise suppression identified in Fig.3.17 (a). Compared to the input spectrum of the laser source in the inset of Fig.3.13, the FM spectrum slightly broadens from 17 nm to approximately 24 nm due to nonlinear propagation within the LSI. The spectral dip near 1042 nm results from the combined effects of nonlinear broadening and NPR-induced polarization interaction with both the BBO and PBS1. Assuming a Gaussian pulse shape, the measured AC corresponds to a pulse duration of approximately 130 fs, yielding a peak power of around 23 kW at the FM output.

The corresponding SHM spectrum is shown in Fig.3.17 (c), with a FWHM bandwidth of ∼6 nm centered at 518 nm. Due to experimental constraints, direct AC measurements of the SHM are not available; instead, the inset displays the Fourier-transform-limited pulse derived from the measured spectrum, with a FWHM of ∼100 fs, representing the ideal temporal profile of the SHM output. Under these conditions, the corresponding SHM peak power is estimated to be approximately 11 kW.

In summary, the presented experiments demonstrate a novel approach to achieving ultra-low-noise SHG-based dual-color output pulse trains by exploiting Kerr-type NPR in combination with type-I phase-matched frequency conversion inside a nonlinear fiber interferometer. The experimentally verified theoretical framework enables the generation of dual-color, sub-150 fs optical pulse trains at 1030 nm and 515 nm with simultaneous intensity-noise suppression and efficient power transfer. Frequency-resolved RIN measurements confirm a noise reduction exceeding 14 dB in both operational modes, reaching SQL performance at average powers of up to 165 mW and 50 mW, respectively. Beyond establishing a new regime of noise-controlled SHG, the developed dual-wavelength fiber system provides a robust and scalable

platform for precision applications, including multimodal two-photon microscopy, ultra-stable frequency conversion, and low-noise seeding of nonlinear and quantum optical processes.

3.3 Fiber-Interferometric Ultra-Low Noise Supercontinuum Generation

Phase-biased NLIs implemented in LSI or NALM/NOLM configurations provide an effective mechanism for suppressing intensity fluctuations in ultrashort pulse trains, act as stabilizing saturable-absorber elements in advanced fiber oscillators, and can generate optical squeezing under well-defined operating conditions [74,75]. As shown in the preceding sections, this stabilization technology can be extended to the dual-color regime, enabling simultaneous noise suppression in two independently addressable spectral bands. Having demonstrated wavelength-selective interferometric conditioning, a natural question follows: can this approach be generalized to the highly nonlinear, broadband dynamics of SCG to achieve improved stability at wavelengths relevant for biomedical two-photon microscopy?

As discussed in Chapter 2, SCG produces ultra-broadband spectra through a cascade of nonlinear interactions, including the Kerr effect, modulation instability, soliton dynamics, Raman scattering, and dispersive-wave emission. These processes are intrinsically sensitive to small input fluctuations and strongly amplify both technical and quantum noise in the pump field [71,116] (see Section 2.3). As a result, standard SCG without precise optimization typically results in substantial shot-to-shot variability in spectral shape, bandwidth, coherence, and temporal structure [117]. Overcoming these noise limitations using NLI-based all-optical stabilization would open new capabilities in applications that require stable broadband sources, including deep-tissue nonlinear microscopy, label-free spectroscopy, frequency metrology, ultrafast imaging, and coherent waveform synthesis [171–175]. This motivates the investigations presented in this section, which combines numerical modeling and experimental validation to evaluate whether the phase-biased, interferometric noise suppression can effectively overcome longstanding noise limitations of SCG across a bandwidth relevant for 2PM applications.

3.3.1 Working Mechanism and Numerical Simulations

As an initial step, a numerical model is developed to describe the noise transfer of interferometric SCG, following the schematic shown in Fig.3.18 (a). In this implemented configuration, an ensemble of input pulses with stochastic noise contributions (see Section 2.3) enters a phase-biased NLI in Sagnac-geometry through PBS1 and passes a nonreciprocal phase-bias unit consisting of an achromatic HWP, a QWP, and a wavelength-dependent FR, which together impose a tunable phase bias φ and splitting ratio ε. The polarization rotation introduced by the phase-

bias is numerically implemented using the Jones formalism outlined in Section 3.1. The modulated field is then divided at PBS2 into two counter-propagating pulses that propagate through the PCF inside the Sagnac loop, acquiring distinct nonlinear phase shifts and correlated spectral broadening modeled by the stochastic GNLSE framework introduced in Sections 2.2 and 2.3. After completing their propagation in the nonlinear loop, the two fields recombine at PBS2 with a differential nonlinear phase shift $\Delta\varphi_{nl}(t)$, propagate back through the phase-bias unit in reverse, and are finally separated at PBS1 into Port T and Port R. Analogous to the LSI oscillator and ultra-low noise dual-color NLI concepts introduced earlier, the transmission at PBS1 becomes a direct function of $\Delta\varphi_{nl}(t)$, giving rise to the characteristic sinusoidal power-transfer functions $T(\Delta\varphi_{nl})$ and $R(\Delta\varphi_{nl})$ that can be tuned via the phase-bias settings.

The full numerical pipeline is repeated for an ensemble of 500 pulses; each seeded with randomized one-photon-per-mode quantum noise and technical RIN sampled from a Gaussian distribution with a standard deviation corresponding to 0.3 % of the mean pulse energy. The mean input pulse is a transform-limited, sech-shaped pulse with 80 fs temporal FWHM and 40 nJ pulse energy at 1.05 µm center wavelength. The PCF inside the NLI has a length of 50 mm, a zero-dispersion wavelength near 1.3 µm (positive dispersion below this wavelength), an effective mode-field diameter of $d_{eff} = 8.5\,\mu m$, a NA of 0.12 at 1064 nm, and a nonlinear parameter $\gamma = 3.5\,W^{-1}\,m^{-1}$. A complete set of simulation parameters is listed in Appendix Section 8.4.

To assess the effect of interferometric SCG conditioning, two operating states of the NLI are considered. The first serves as a reference working point (WP), defined by $\theta_{HWP} = 0°$ and $\theta_{QWP} = 45°$, which results in an energy splitting ratio of $\varepsilon = 0.5$ and an accumulated nonlinear phase difference $\Delta\varphi_{nl} = 0$. Under these conditions, the two counter-propagating fields acquire identical nonlinear phase, and their recombination at PBS2 is fully constructive toward Port R.

The NLI therefore acts as a passive bypass without intensity-dependent interference, and the output RIN is expected to simply follow the input fluctuations. This state (reference WP) thus provides the baseline against which all subsequent performance metrics are evaluated. A second, slightly detuned operating point is introduced by setting $\theta_{QWP} = 43.5°$ and $\theta_{HWP} \approx 2°$, yielding $\varepsilon \approx 0.53$ and a finite $\Delta\varphi_{nl}$ that shifts the recombination toward a noise-suppressing working point (optimized WP). As shown in Fig.3.18 (b), the mean output spectra corresponding to these two states show highly similar broadband characteristics, confirming that any observed differences in noise performance arise from interferometric conditioning rather than trivial spectral reshaping.

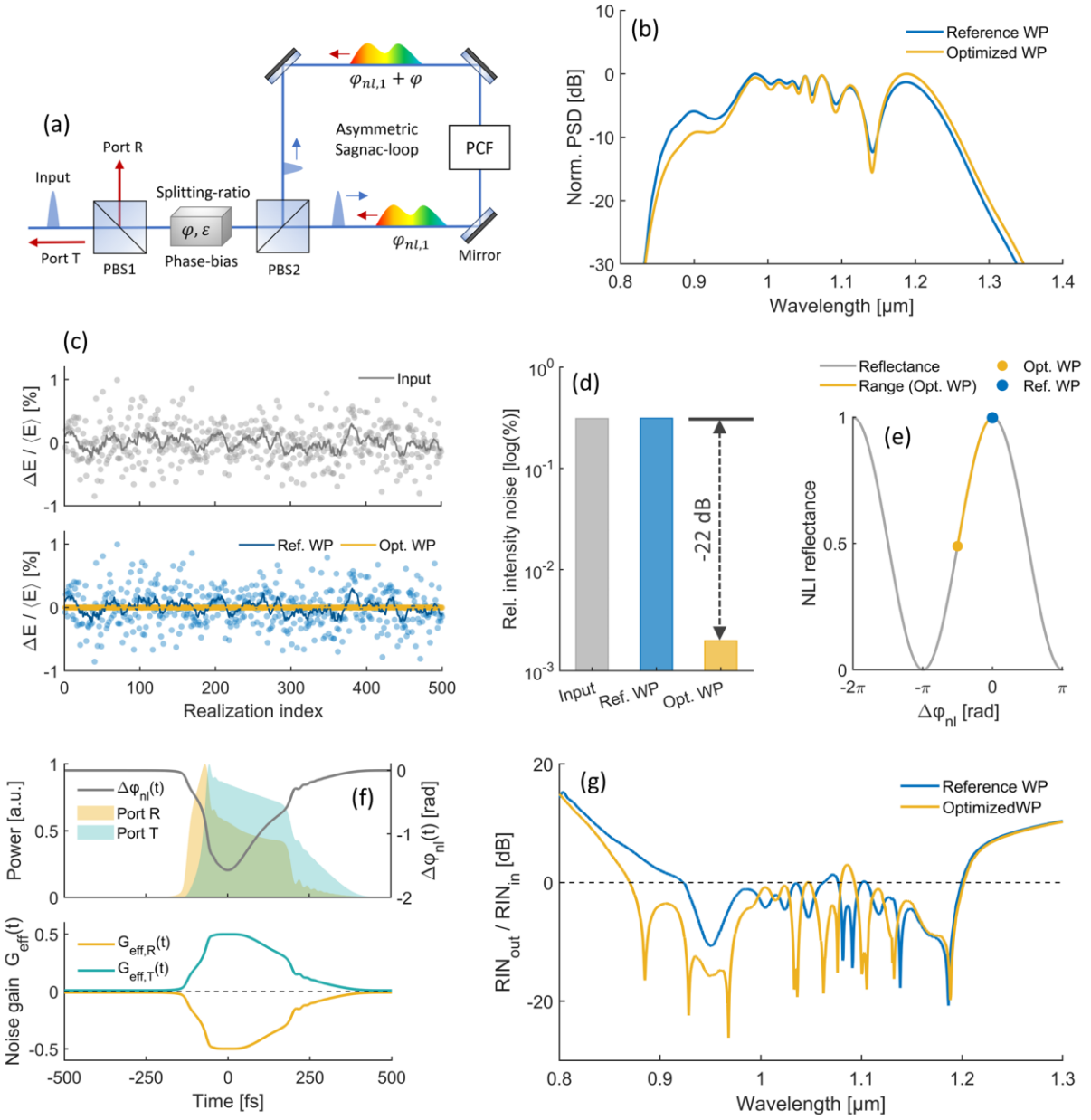

Figure 3.18: Numerical modeling of noise-suppressed nonlinear interferometric SCG. (a): Schematic of the asymmetric Sagnac NLI with adjustable splitting ratio and phase bias(φ, ε). (b): Simulated Port-R spectra for the reference (Ref. WP) and optimized noise-suppressed working point (Opt. WP). (c): Pulse-to-pulse energy fluctuations from 500 Monte-Carlo realizations (RIN_{in} = 0.3 %); points show individual shots, lines the moving-average trend. (d): Integrated RIN for input, Ref. WP, and Opt. WP, revealing ~22 dB noise suppression at Port R for the optimized configuration. (e) Reflectance curve $R(\Delta\varphi_{nl})$ with both WPs mapped onto the optimized R-curve; the Opt. WP lies on a high-slope region enabling efficient noise-to-amplitude conversion. (f): Instantaneous $\Delta\varphi_{nl}(t)$ together with the normalized Port T/R pulse envelopes for the optimized WP (top), and the corresponding instantaneous noise-gain functions $G_{eff,R/T}(t)$ (bottom), illustrating how different temporal portions of the pulse experience noise-amplifying or noise-suppressing interferometric response. (g) Wavelength-resolved noise transfer $10log_{10}(RIN_{out}/RIN_{in})$, showing broadband noise suppression across the full supercontinuum band.

Figure 3.18 (c) compares the relative pulse-energy fluctuations obtained for the reference and optimized WP at Port R. As expected, the reference WP reproduces the input noise level with no relevant modification, consistent with the absence of an interferometric response at $\Delta\varphi_{nl} = 0$. This trend is quantified in Fig.3.18 (d), where the RIN integrated over the full SCG spectrum is extracted from the ensemble and illustrated for both output states alongside the input. While the reference WP preserves the input noise (the ~0.2 dB deviation reflects numerical variability), the optimized WP yields a RIN suppression of more than 22 dB, demonstrating that even a slight detuning of the splitting ratio and the associated $\Delta\varphi_{nl}$-accumulation is sufficient to drive the NLI-generated SCG into an ultra-low noise regime.

The contrasting behavior of the two working points can be understood by considering their respective locations on the NLI reflectance curve $R(\Delta\varphi_{nl})$, shown in Fig.3.18 (e). The reference WP sits at $\Delta\varphi_{nl} = 0$, where the reflectance function exhibits an extremum with $dR/d\Delta\varphi_{nl} = 0$. In this regime, the NLI is effectively insensitive to fluctuations of $\Delta\varphi_{nl}$ (see Section 3.2.1), and the Port R output RIN follows the input noise level, as observed in Fig.3.18 (c-d). The optimized WP, by contrast, covers a sloped region of the curve, where fluctuations in the intensity-dependent $\Delta\varphi_{nl}(t)$ couple the input RIN to changes in the NLI reflectance and thereby enable dynamic noise transfer. For this operating point, an increase in input pulse intensity generates a more negative $\Delta\varphi_{nl}$, which shifts the effective working point toward lower reflectance and thus counteracts the underlying amplitude variation. From this mechanism, a more general condition for noise suppression follows, which can be expressed as

$$sign\left(\frac{dR}{d\Delta\varphi_{nl}}\right) \cdot Cov\big(I(t), \Delta\varphi_{nl}(t)\big) < 0 \tag{3.3.1}$$

and identifies the criterion under which the NLI converts SCG-induced amplitude–phase conversion into net noise suppression.

To illustrate how this condition manifests in the time domain, Fig. 3.18 (f) shows the temporal evolution of $\Delta\varphi_{nl}(t)$ together with the Port T and Port R pulse envelopes and the corresponding instantaneous noise-gain functions $G_{eff}(t) = \delta I_R(t)/\delta I_{in}(t)$. The optimized WP places the dominant temporal portion of the Port-R field in a regime of $R(t)$ where $G_{eff}(t)$ becomes negative (yellow marked range in Fig.3.18 (e)), meaning that an increase in input intensity produces a compensating reduction in reflected power. This directly fulfills the inequality in Eq. (3.3.1) across the full pulse width and explains the strong integrated RIN suppression observed in Fig.3.18 (c-d).

The spectral characteristics of the noise transfer are shown in Fig.3.18 (g), where the wavelength-resolved RIN is evaluated using a sliding 50 nm window. The reference WP produces a RIN trace fluctuating around 0 dB, consistent with the absence of interferometric conditioning. The optimized WP, by contrast, exhibits a clear broadband reduction in RIN, with suppression extending from roughly 0.85 μm to 1.18 μm and multiple regions exceeding 10-20 dB. While the fine spectral structure remains characteristic of SCG, the optimized WP thus introduces a pronounced net decrease of noise across the continuum. This broadband suppression reflects the time-domain mechanism discussed above, where large portions of the pulse satisfy Eq. (3.3.1) and yield reduced fluctuations after temporal-to-spectral mapping.

3.3.2 Experimental Validation

To assess the experimental feasibility of the interferometrically controlled SCG concept introduced in the previous section, a proof-of-principle experiment is implemented guided by the numerical results. To this end, a broadband NLI is constructed in close analogy to the simulated configuration shown in Fig.3.18 (a), including a non-reciprocal phase-bias stage (QWP, HWP, and Faraday rotator), a nonlinear fiber section incorporating a PCF, and PBS separating the output supercontinuum into Port T and Port R. The system is driven by a homebuilt Yb-fiber laser operating at 30 MHz repetition rate, delivering pulse energies up to 40 nJ with ~50 fs pulse duration (see Section 3.4).

To enable a direct comparison between numerical predictions and experimental observations, a two-dimensional scan of the interferometric RIN transfer at Port R is performed by systematically varying the rotation angles of the phase-bias HWP (θ_{HWP}) and QWP (θ_{QWP}). For each angular setting, the RIN transfer from the input laser to the generated supercontinuum is measured by detecting the respective pulse trains with a broadband InGaAs photodetector (Coherent ET-2030) and then measuring the RIN spectral density and integrated RIN (100 Hz – 5 MHz) using a SSA (Keysight E5052B). The scan over θ_{HWP} and $\theta_{QWP}$is fully automated using resonant piezoelectric rotation mounts for the waveplates (Thorlabs ELL14K) in combination with custom Python-based control software, enabling the acquisition of a two-dimensional RIN transfer map that directly corresponds to the simulated parameter space.

Figure 3.19 (a) shows the simulated RIN transfer map obtained from the stochastic GNLSE-based model described in Section 3.3 with experimental input parameters, while Fig.3.19 (b) presents the corresponding experimental measurement. Despite the reduced angular resolution and increased measurement noise inherent to the experimental scan, a clear qualitative agreement can be observed between simulation and experiment. This agreement confirms that the

dominant features of the noise-transfer is originated in the NLI dynamics captured by the numerical model, rather than by implementation-specific artifacts.

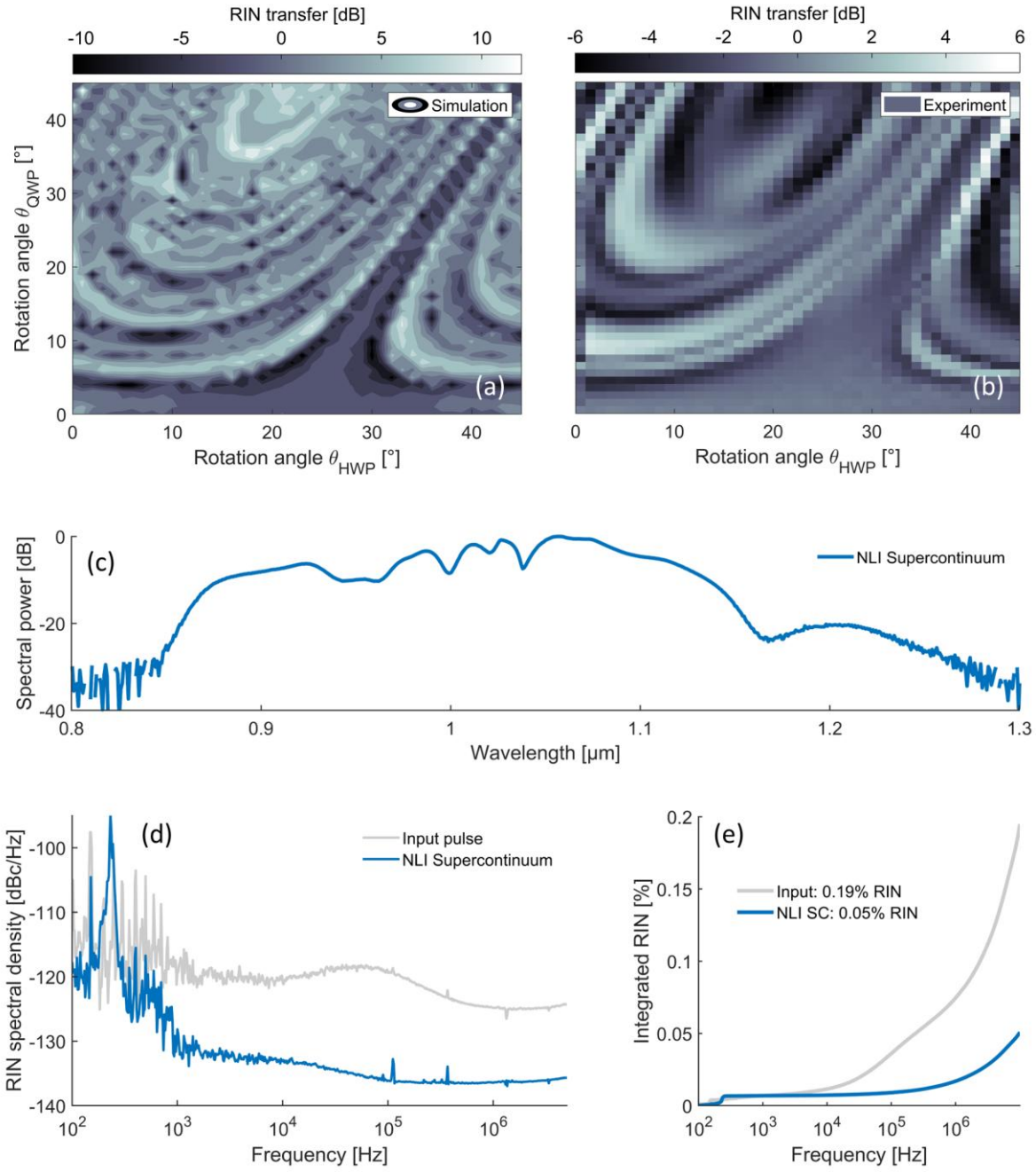

Figure 3.19: Experimental validation of interferometric ultra-low noise SCG. (a): Simulated two-dimensional contour map of RIN transfer as a function of phase-bias HWP and QWP rotation angles $(\theta_{HWP}, \theta_{QWP})$, obtained from stochastic GNLSE simulations. (b): Corresponding experimentally measured RIN transfer map acquired under comparable operating conditions. (c) Output spectrum of the interferometrically generated supercontinuum at a representative noise-suppressed working point. (d) Measured RIN spectral density (100 Hz – 5 MHz) of the input pulse train (gray) and the interferometrically generated supercontinuum (blue). (e): Corresponding integrated RIN with 0.19% at the input and 0.05% RIN of the output supercontinuum.

A representative operating point with ~6 dB RIN suppression is selected from the 2D map for further characterization. The corresponding output spectrum of the Port R supercontinuum output is shown in Fig.3.19 (c), verifying a strongly broadened bandwidth spanning from approximately 0.9 μm to 1.15 μm (FWHM). The corresponding frequency-resolved RIN transfer is quantified in Fig.3.19 (d), which compares the measured RIN spectral density of the input pulse train with that of the generated supercontinuum between 100 Hz to 5 MHz offset-frequency. A pronounced reduction in supercontinuum RIN of up to 15 dB relative to the input can be observed across a broad bandwidth >~500 Hz, demonstrating that the NLI mechanisms can effectively suppress input intensity fluctuations for correct phase-bias settings. Integration of the RIN spectra over the measurement bandwidth yields an integrated RIN reduction from 0.19% at the input to ~0.05% for the Port R supercontinuum output, corresponding to the observed suppression of ~6 dB.

All measurements were performed without active phase stabilization, confirming that the observed RIN suppression arises from the intrinsic interferometric transfer function rather than external feedback. Despite the absence of long-term drift analysis, the results provide direct experimental validation of ultra-low-noise interferometric SCG in quantitative agreement with the simulations of Section 3.3.1. These findings establish interferometric noise conditioning as a viable strategy for stabilizing broadband nonlinear wavelength conversion and directly motivate its application to low-noise, multi-wavelength light sources for two-photon microscopy in the green to red spectral window.

3.4 Fiber-Optic Ultrafast Ytterbium Laser Driver

Efficient fiber-based wavelength conversion in MPM platforms relies on ultrashort femtosecond pulses with sufficient pulse energy, well-defined temporal structure, and high coherence, as outlined in Section 2. Due to the strong noise sensitivity of SCG processes, stringent constraints are further imposed on the stability and noise performance of the driving laser source [71,116]. Consequently, a robust, low-noise, high-energy femtosecond laser system is a fundamental prerequisite to drive the advanced, wavelength-flexible MPM systems discussed in the following sections.

In this seciton, an all-PM Yb-doped fiber laser (YFL) system is designed for stable, high-energy pulse delivery around 1.05 μm. Guided by numerical modeling of pulse propagation and precise nonlinearity management, the laser architecture is optimized to provide sub-50 fs pulses with watt-level average power at a repetition rate of 30 MHz, while maintaining environmental

robustness and reproducible operation. These pulse characteristics enable efficient nonlinear wavelength-conversion to efficiently drive multiphoton excitation in complex biological tissue.

3.4.1 Experimental Setup and Numerical Simulations

Figure 3.20 summarizes the experimental architecture and input pulse characterization of the Yb:fiber laser system used as the driving source for the dispersive-wave (DW) generator. The system configuration is designed via subsequent numerical simulations to deliver stable, linearly chirped femtosecond pulses with adjustable dispersion and peak power for efficient nonlinear broadening in the following PCF stage. As shown in Fig.3.20 (a), a passively mode-locked Yb:fiber oscillator with attached pre-amplifier initially generates an optical pulse train centered at 1028 nm with 30 MHz repetition rate and up to 120 mW average power. The optical spectrum at the PCMA input, shown in Fig.3.20 (b), is centered at 1028 nm with ~8 nm FWHM, corresponding to positively chirped pulses of 0.7 ps FWHM as confirmed by the AC trace in Fig.3.20 (c), shown in comparison to the FTL pulse calculated from the spectrum.

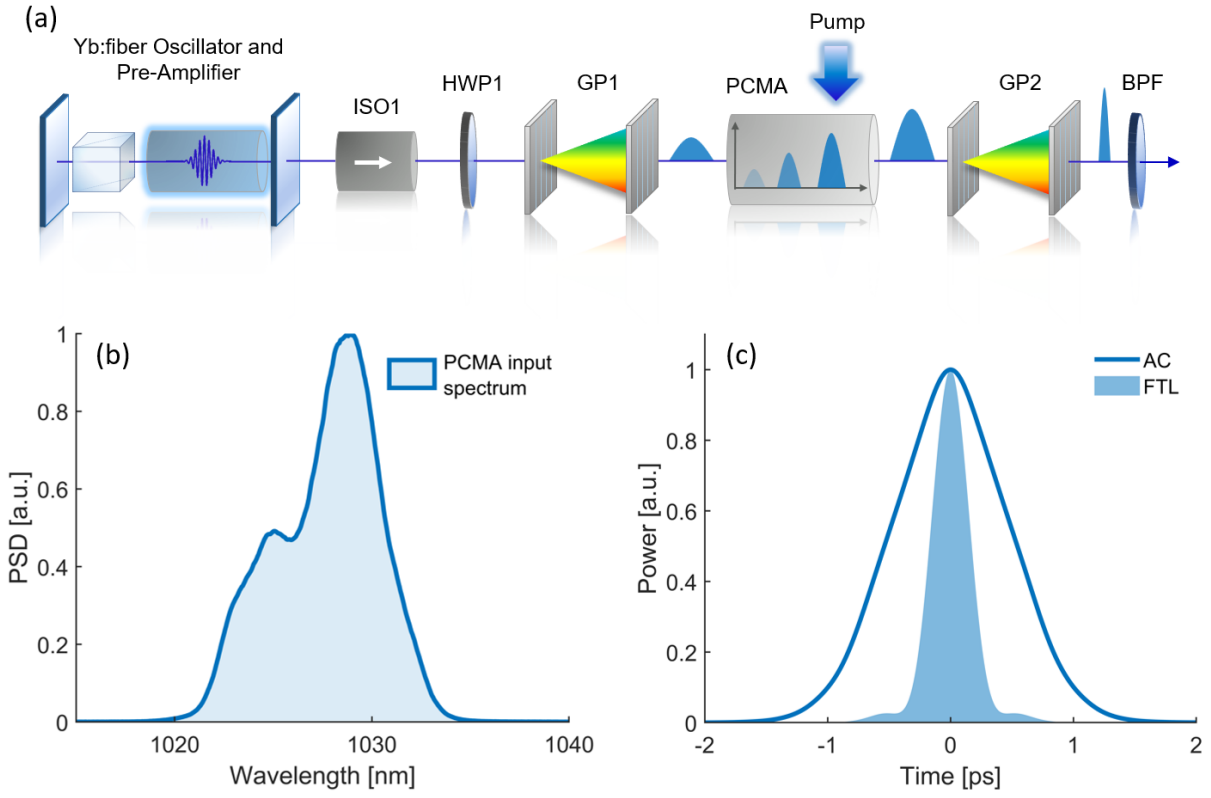

Figure 3.20: Schematic of the PCMA Yb:fiber laser. (a): Experimental setup consisting of an oscillator with pre-amplifier attached to a PCMA-stage. ISO: isolator, HWP: half-wave plate, PCMA: pre-chirp managed amplifier, BPF: bandpass filter. (b): PCMA input spectrum generated by the Yb:fiber oscillator with pre-amplifier. (c): Corresponding positively chirped output pulse AC trace before GP1 with calculated Fourier-transform limit (FTL)

The pulse train is then isolated (ISO1) and polarization-aligned via HWP1 before passing through a transmission grating pair (GP1) with 1000 lines/mm grating constant (Coherent Lightsmyth 1040), which enables fine control of the input group-delay dispersion. The pre-chirped pulses are then launched into a Yb-doped, pre-chirp-managed amplifier (PCMA), which consists of a 10 μm core LMA fiber segment with ~2 m highly-doped gain fiber (Coherent PLMA-YSF-10/125) that is optically pumped in backward direction using a pump-beam combiner (PBC) and an 18-W multimode diode (BWT K976AA2RN-18.00W). The PCMA-stage provides efficient amplification up to Watt-level average power while maintaining near-parabolic pulse evolution. After amplification, a second grating pair (GP2) compensates residual dispersion and compresses the output pulses to the sub-100 fs regime. To suppress weak spectral sidebands and ensure a smooth spectral phase, a 1050 ± 30 nm bandpass filter (BPF) is at the PCMA output applied prior to nonlinear wavelength conversion.

To achieve broadband, energetic, and compressible femtosecond pulses at the PCMA output, it is essential to maintain pulse evolution within the parabolic amplification regime. For the fixed experimental configuration shown in Fig.3.20 (a), this regime is accessed by tuning the input pulse energy E_0 and the applied group-delay dispersion GDD_0, implemented experimentally through the grating pair GP1. The nonlinear propagation inside the Yb-doped fiber is modeled using the NLSE as described in Section 2.1.1 of this dissertation, which includes GVD and TOD, SPM, and optical gain via rate equations.

To identify the optimal input conditions for efficient compression, E_0 and GDD_0 are systematically varied, and the resulting output pulses are numerically compressed to evaluate their Strehl ratio, defined as the ratio between the peak power of the compressed pulse and the FTL peak power. Figures 3.21 (a) and (b) show the simulated Strehl-ratio maps for the PCMA output with and without the implemented BPF (see Fig.3.20 (a), Unfiltered/Filtered), respectively. Without filtering (Fig. 3.21 (a)), the maximum Strehl ratio reaches approximately 0.7 at an input average power of ~40 mW ($E_0 \approx 1.3\ nJ$) and a pre-chirp of $GDD_0 = -0.5\ ps^2$. Introducing the 1050 ± 30 nm BPF, modeled as a 4th-order super-Gaussian transmission function, substantially enhances the temporal quality of the output (Fig. 3.21 (b)), yielding Strehl ratios above 0.9 at the optimized working point ($E_0 \approx 1.3\ nJ, GDD_0 = -0.02\ ps^2$).

The NLE is solved numerically using experimental parameters corresponding to the PCMA fiber and pumping scheme (5.8 W pump power at 976 nm) with a gain fiber length of ~2 m. A complete set of simulation parameters is listed in Appendix Section 8.1. The temporal and spectral pulse characteristics at the optimized working point are illustrated in Fig.3.21 (c-f). Figure

3.21 (c) shows the amplified pulse in the time domain before spectral filtering, together with its instantaneous frequency (chirp).

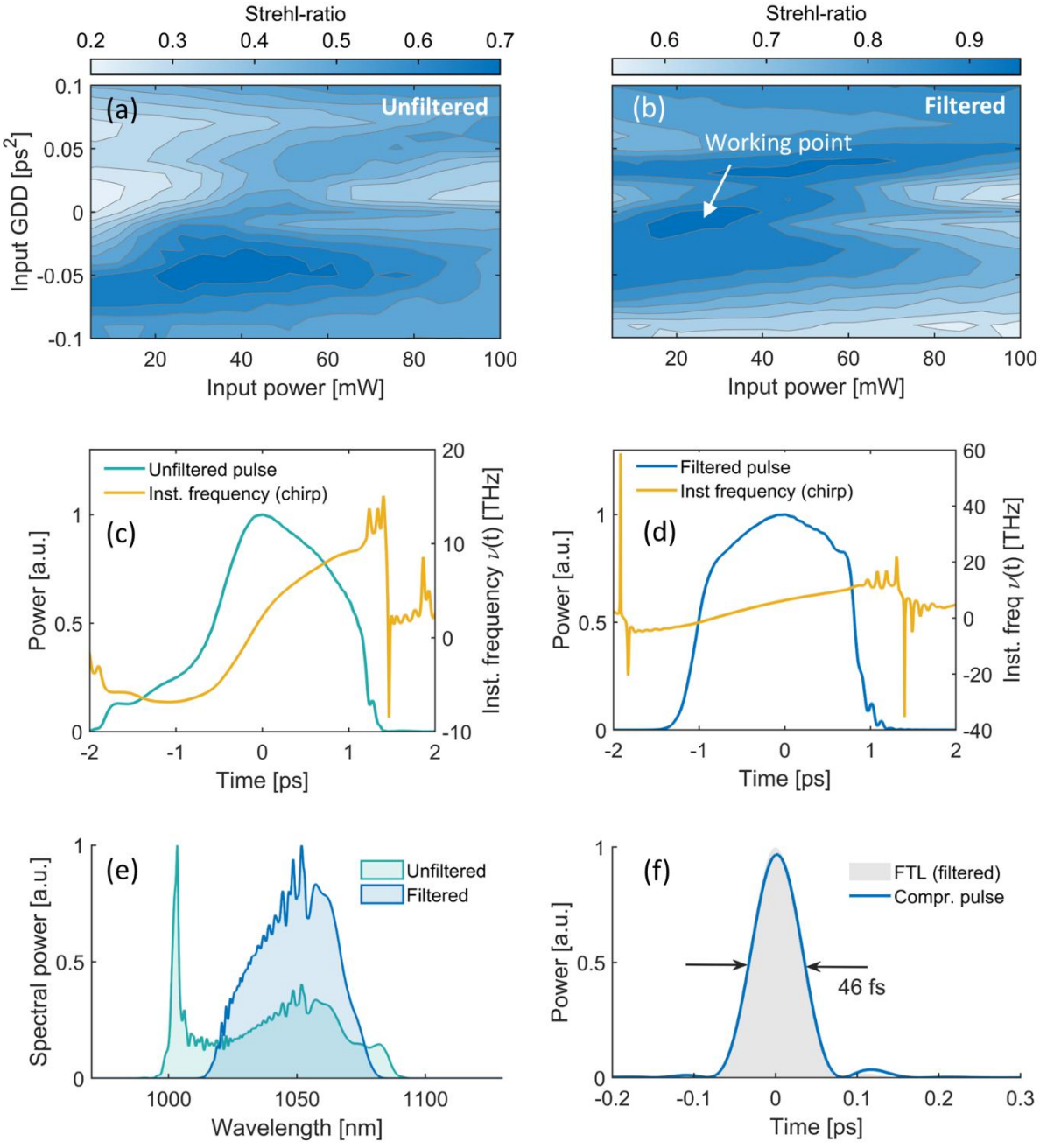

Figure 3.21: Numerical optimization and output characteristics of the PCMA stage. (a): Simulated Strehl-ratio map as a function of input average power and applied GDD for the unfiltered PCMA output. (b): Strehl-ratio map after applying a 1050 ± 30 nm super-Gaussian BPF, with marked working point. (c): Temporal intensity and instantaneous frequency (chirp) of the amplified pulse before spectral filtering. (d): Temporal intensity and linearized chirp of the filtered pulse at the optimized working point. (e): Corresponding spectra of the unfiltered and filtered pulses. (f): Compressed temporal intensity profile of the filtered pulse (blue) compared to its FTL counterpart (gray), demonstrating a clean pulse shape with 46 fs FWHM duration.

As shown, the unfiltered pulse has distinct higher order phase components with an asymmetric temporal shape, originating from TOD and nonlinear phase accumulation within the PCMA. In contrast, Fig.3.21 (d) shows the corresponding result after applying the numerical 1050 ± 30 nm band-pass filter. In this case, the temporal profile becomes smooth and symmetric, and the instantaneous frequency reveals a nearly linear chirp, confirming the suppression of higher-order phase distortions with an approximately parabolic output pulse shape.

Figure 3.21 (e) compares the simulated output spectra before and after filtering. As shown, the spectral wings and fine structure visible in the unfiltered spectrum are effectively removed, resulting in a clean, single-lobed spectral envelope centered at 1050 nm. The compressed temporal pulse after filtering is shown in Fig.3.21 (f), in comparison to the FTL pulse calculated form the corresponding spectrum. The compressed pulse duration reaches 46 fs (FWHM), in excellent agreement with the calculated FTL value and without residual pedestals.

These results numerically confirm that the combination of parabolic amplification and moderate spectral filtering enables the generation of broadband, high-quality pulses with sub-50 fs duration, and simultaneously provide guidelines for an experimental parameter space to achieve ideal laser performance to drive efficient PCF-based spectral broadening.

3.4.2 Experimental Laser Characterization

Building on the results of the numerical optimization, the experimental PCMA setup shown in Fig.3.20 (a) is implemented to match the identified parameter space. Figure 3.22 (a) compares the measured unfiltered output spectrum with the numerically simulated spectrum at an input average power of approximately 40 mW and an input pulse duration of 0.4 ps. Both spectra show similar bandwidth and spectral shape, validating the accuracy of the numerical model and confirming that parabolic pulse amplification is achieved under the chosen operating conditions.

The measured average output power of the PCMA, shown in Fig. 3.22 (b), reaches up to 1.2 W at maximum pump current, corresponding to pulse energies exceeding 40 nJ at the 30 MHz repetition rate. After applying the 1050 ± 30 nm BPF, the measured spectrum shown in Fig.3.22 (c) closely matches the simulated output, demonstrating effective suppression of residual sidebands and higher-order spectral components. The corresponding temporal characterization, summarized in Fig.3.22 (d), reveals a clean, transform-limited pulse shape with a FWHM duration of 48 fs, in excellent agreement with the calculated 46 fs from the simulation.

The strong correspondence between experimental and numerical results confirms the predictive reliability of the NLSE simulation framework and an undistorted operation of the amplifier design. The successful generation of energetic, sub-50 fs pulses establishes optimal driving conditions for the subsequently developed advanced 2PM platforms.

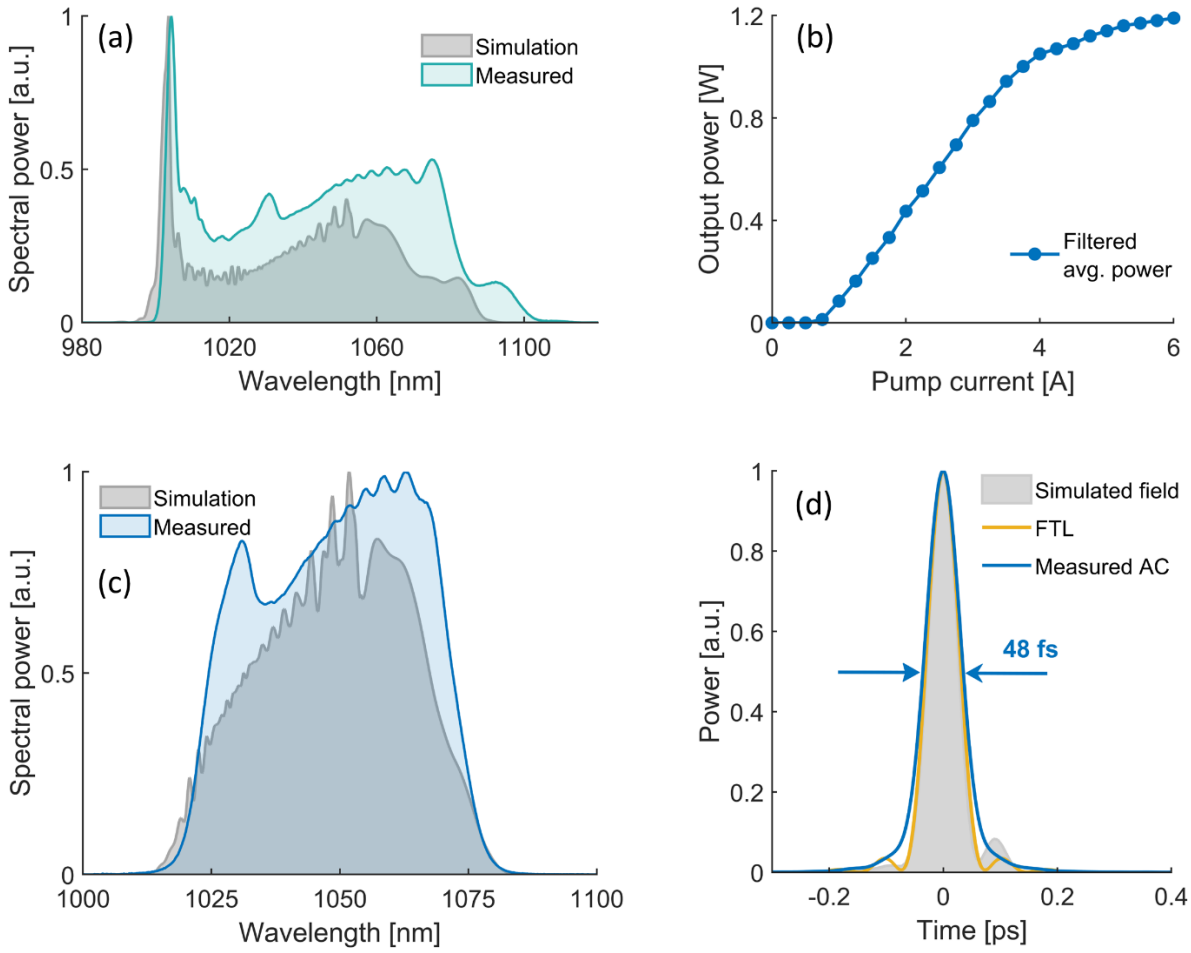

Figure 3.22: Experimental characterization of the PCMA stage and comparison with numerical simulations. (a): Measured (cyan) and simulated (gray) unfiltered output spectra of the PCMA at 40 mW input power and input 0.4 ps pulse duration. (b): Measured output power as a function of pump current for the filtered output, reaching up to 1.2 W average power at 6 A pump current. (c): Comparison between simulated (gray) and measured (blue) spectra after applying a 1050 ± 30 nm BPF. (d): Measured AC trace of the filtered and compressed output pulse (blue) compared to the FTL pulse (yellow) and simulated electric field (gray), with an experimental pulse duration of 48 fs FWHM in excellent agreement with the simulation.

4 Tunable Deep-Tissue Two-Photon Imaging Platform Based on Dispersive-Wave Excitation

As described in the introduction of this dissertation, 2PM represents one of the most powerful tools for sub-cellular resolution, three-dimensional imaging in scattering biological tissue making it an essential tool for numerous biomedical disciplines such as embryology [176], oncology [177], and neuroscience [28]. The performance of 2PM critically depends on the properties of the driving ultrafast laser source, in particular its ability to deliver energetic, spectrally matched, and temporally stable femtosecond pulses that efficiently excite application-specific fluorophores and biomolecular markers [32,57,124]. In neuroscience, for instance, visualizing neuronal morphology and activity relies heavily on pulsed laser excitation within the spectral window between approximately 800 and 1000 nm, which coincides with the two-photon excitation peaks of many key fluorescent proteins and calcium indicators [178]. Prominent neuronal markers include derivatives of green fluorescent protein (GFP) with two-photon excitation maxima near 920 nm, widely used for example in GFP-expressing transgenic mouse models, to investigate neuronal connectivity, synaptic plasticity, and activity dynamics in both healthy and pathological brain states [179–182]. Likewise, calcium indicators such as the GCaMP family or the chemical dye Fluo-4 AM have excitation peaks between 900 nm and 950 nm, allowing a direct observation of intracellular Ca^{2+} transients associated with neuronal action potentials and signaling [81,183–185]. Additional fluorophores such as Alexa Fluor and Fluorescein derivatives (e.g., AF488 with a peak near 950 nm) are extensively applied for visualizing structural or vascular components of brain tissue [186–188].

Precise spectral matching between the excitation wavelength and the fluorophore absorption maximum provides multiple benefits, including enhanced fluorescence signal and contrast, improved penetration depth, and reduced risk of photodamage due to lower required average power. Traditionally, Ti:Sa-based femtosecond lasers have been the standard solution for these tasks, offering watt-level average power and sub-100 fs pulse durations over a broad tuning range of 700-1000 nm. However, as mentioned in the introduction, these systems are characterized by high cost, large physical footprint, complex alignment, and the need for active cooling and regular maintenance. In contrast, fiber-based ultrafast laser systems have gained increasing attention as compact, cost-efficient, and alignment-stable alternatives. In particular, Neodymium-doped, and frequency-doubled Thulium-doped fiber lasers have demonstrated high-power, sub-150 fs operation in the 900-920 nm range, enabling reliable excitation in the green spectral window relevant for fluorophores such as GFP and GCaMP6. However, their inherently limited gain bandwidth and the reliance on narrowly defined, highly optimized

mode-locking conditions typically confine these systems to a single, fixed center wavelength. This constraint fundamentally limits their applicability to advanced two-photon microscopy modalities that require tunable or multi-target excitation.

To extend the accessible wavelength range beyond the laser gain bandwidth, nonlinear spectral broadening in PCFs offers a flexible and compact route for versatile wavelength conversion. Approaches such as SPM-enabled spectral selection (SESS) have demonstrated broad tunability across several hundred nanometers, but at the expense of low conversion efficiency (typically 10-20 %) and limited pulse energy in the biologically relevant 800 - 1000 nm range [132,189–191]. Such energy constraints are particularly critical for deep-tissue brain imaging, where pulse energies above a few nanojoules are typically required to achieve sufficient signal strength through scattering media [32].

In this context, phase-matched dispersive-wave (DW) generation provides a highly efficient and controllable nonlinear mechanism for producing tunable ultrashort pulses within the desired spectral window [192]. DW generation relies on resonant energy transfer from a soliton propagating in the anomalous dispersion regime to a phase-matched frequency component in the normal dispersion regime, enabling the formation of isolated, spectrally narrow output bands with high conversion efficiency and excellent temporal coherence [71]. Building on this mechanism, this section presents a fiber-optic DW generator designed for high-efficiency, wavelength-tunable pulse generation between 880 nm and 950 nm, specifically tailored to the requirements of deep-tissue neuronal two-photon imaging. The system is driven by the compact Yb-fiber laser driver described in Section 3.4 and delivers tunable sub-100 fs pulses with energies exceeding 6.7 nJ at optical conversion efficiencies of up to 65 %. The output enables selective excitation of neuronal and vascular architectures across the green-to-yellow spectral window in mouse hippocampal and cerebellar brain tissue at imaging depths up to 650 µm. The developed DW generator thus provides a compact, robust, and alignment-free alternative to conventional Ti:Sa systems, establishing this platform as a versatile excitation source for advanced application-specific two-photon microscopy and related biomedical imaging modalities.

Parts of this chapter are based on results previously published by the author in the following peer-reviewed articles and preprints:

- M. Edelmann *et al*., “Deep-tissue two-photon brain imaging enabled by a tunable fiber-optic dispersive wave generator,” *Scientific Reports* (Nature Portfolio) **15**, 24404 (2025).
- M. Edelmann *et al*., “Multiplexed brain and visceral two-photon imaging using a simulation-guided ultrafast three-color fiber laser,” *bioRxiv*, DOI: 10.1101/2025.06.19.660526 (2025).

All sections have been revised, expanded, and reformatted to provide a unified presentation and additional discussion in the context of this dissertation.

4.1 Dispersive Wave Generation: Physical Mechanism and Simulations

To numerically demonstrate the conditions required for wavelength-tunable DW generation and the underlaying physical mechanisms, comprehensive numerical simulations are applied in the ZDW regime with the GNLSE-based numerical framework described in Section 2.2.3. Figures 4.4 (a, b) present the simulated pulse evolution in the frequency and time domain, respectively, for a 40 mm long segment of PCF (NKT LMA-PM-5) with an effective mode area $A_{eff} = 4.4\ \mu m^2$, nonlinear coefficient $\gamma = 10\ W^{-1}cm^{-1}$ at 1064 nm, and a zero-dispersion wavelength λ_{ZDW} near 1060 nm. The input pulse is Fourier-transform-limited with a $sech^2$-shaped temporal profile, a duration of 100 fs, a center wavelength of 1050 nm, a pulse energy of 12 nJ, and a corresponding peak power of 105 kW. A complete set of simulation parameters is listed in Appendix Section 8.2.

As shown, SPM dominates the initial propagation stage, leading to the characteristics symmetric spectral broadening up to approximately 20 mm. As the spectrum expands toward longer wavelengths and enters the PCFs anomalous-dispersion regime, soliton self-compression and subsequent soliton fission take place, resulting in the breakup of higher-order solitons into fundamental solitons. This evolution drives an efficient transfer of energy toward shorter wavelengths, giving rise to a distinct spectral peak around 940 nm that progressively blue-shifts to approximately 880 nm between 20 mm and 32 mm of propagation, as indicated in Fig.4.4 (a,b) and denoted as the *DW generation regime*.

To gain further insight into the underlying mechanism of this energy transfer, Fig.4.4 (c) presents simulated supercontinuum (SC) spectra at selected propagation distances (21–26 mm). The results show that the blue-shifting spectral peak near 930 nm, located in the normal-dispersion regime of the PCF, is accompanied by a concurrent depletion and red-shift of spectral power between 1.1 μm and 1.2 μm in the anomalous-dispersion region.

The corresponding spectrogram at a propagation distance of 26 mm, shown in Fig.4.4 (d), reveals that the power spectral density (PSD) maximum near 930 nm originates partly from temporally self-compressing solitons at the pulse center and partly from a weak, dispersed pedestal at the leading edge of the pulse. These observations confirm that the observed energy transfer to shorter wavelengths arises from highly efficient DW generation that occurs through resonant energy transfer from a soliton (centered near 1.15 μm) to a phase-matched DW in the

normal-dispersion regime (around 930 nm in this case) mediated by higher-order dispersion [72].

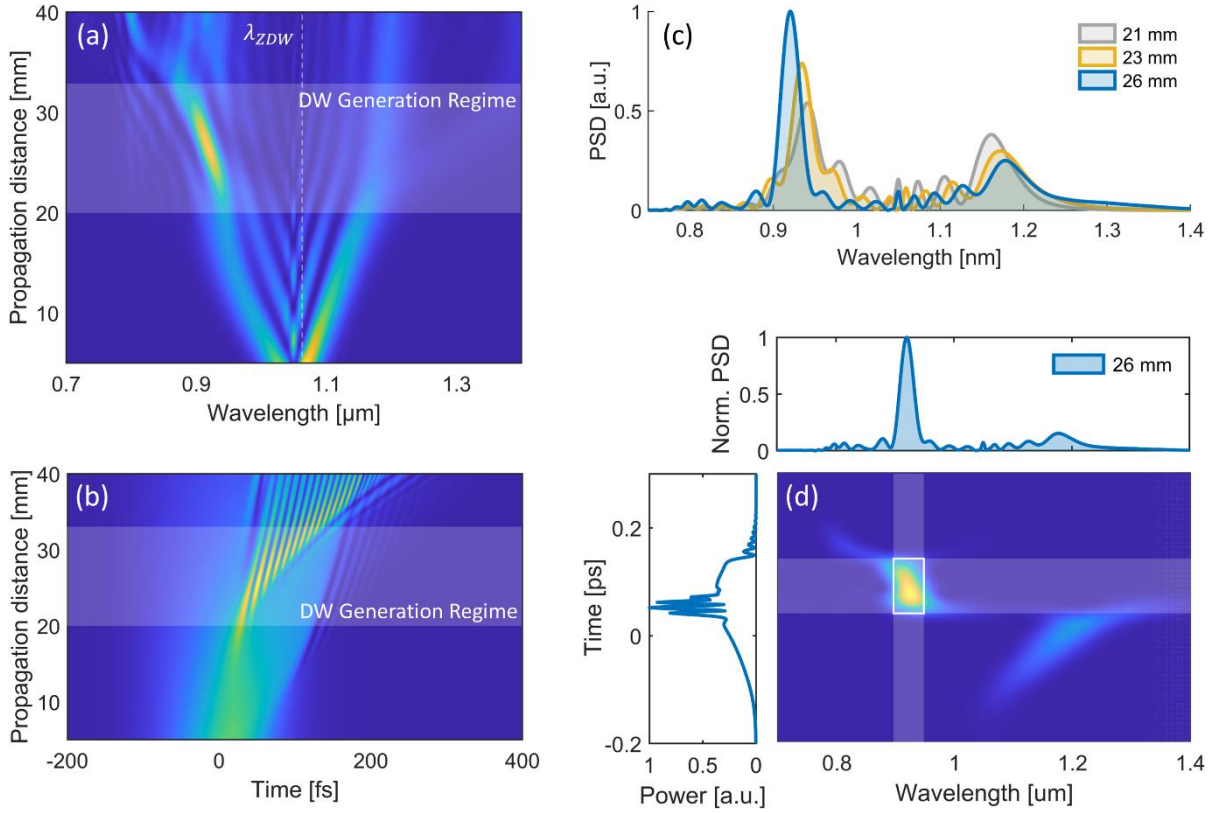

Figure 4.4: Numerical simulation of DW generation in a PCF. (a): Simulated spectral evolution of the pulse along the fiber propagation distance, highlighting the DW generation regime. (b): Corresponding temporal evolution of the pulse. (c): SC spectra at selected propagation distances. (d): Spectrogram of the simulated SC at a propagation distance of 26 mm, illustrating the temporal and spectral localization of the generated DW.

Mathematical verification and analytical physical insight into the mechanism enabling wavelength-tunable DW generation can be obtained from the DW phase-matching condition, which is defined by the relation

$$\sum_{n\geq 2} \frac{(\omega_{DW} - \omega_S)^2}{n!} \beta_n(\omega_S) = \frac{\gamma P_S}{2} \tag{4.1}$$

where ω_S and ω_{DW} denote the angular center frequencies of the soliton and the generated DW, respectively; $\beta_n(\omega_S)$ represents the n^{th}-order dispersion coefficient at the soliton frequency; γ is the nonlinear coefficient; and P_S is the soliton peak power [193]. According to Eq. (4.1), phase-matched DW generation at ω_{DW} therefore occurs when the linear phase shift of the DW equals the combined linear and nonlinear phase shift of the soliton centered at ω_S.

Using the numerical parameters described previously, Fig.4.5 (a) shows the calculated phase-matched DW wavelength as a function of the corresponding soliton wavelength for varying P_S, obtained by solving Eq. (4.1) with the dispersion properties of the PCF. As illustrated, a red-shift of the soliton results in a corresponding blue-shift of the phase-matched DW wavelength, consistent with the numerical observations presented in Fig.4.4 (c). While a decrease in P_S (as observed, for example, near 1.15 μm in Fig.4.4 (c)) leads to a minor additional blue-shift, its effect on the overall phase-matched DW position remains small compared to the soliton-induced red-shift, resulting in a net blue-shifting DW.

These results confirm that wavelength-tunable DW generation can be achieved by exploiting the soliton-DW phase-matching condition, where the continuous red-shift of the soliton dynamically controls the ejection wavelength of the DW. In practical implementation, this tunability can be realized by adjusting the input pre-chirp and peak power while maintaining a fixed fiber length and input energy. To illustrate this numerically, Fig.4.5 (b) presents the simulated output spectra after 35 mm of propagation for varying input GDD, using the same parameters as before but with a slightly increased input pulse energy of 13 nJ (corresponding to a peak power of ~114 kW). As shown, tuning the input GDD from $12.5 * 10^2\ fs^2$ to $22.5 * 10^2\ fs^2$ enables a shift of the ejected DW peak from approximately 880 nm to 940 nm. The conversion efficiency from the 1050 nm input to a 50 nm spectral band around the DW center wavelength remains above 40% throughout the tuning range and exceeds 50% near 920 nm, corresponding to a pulse energy of 6.8 nJ. It is thereby important to note, that for a fixed PCF length, the DW generation efficiency also depends on the input pulse energy and central wavelength. This dependency provides a practical means for optimizing and fine-tuning the DW conversion efficiency at a targeted center wavelength in the subsequent experimental investigations.

In addition to the available pulse energy within the tuning range, a key performance factor of the generated DW output, particularly for 2PM applications, is the achievable pulse quality and duration, as these parameters directly determine the peak power delivered to the sample. Figure 4.5 (c) shows the simulated output SC for an input group delay dispersion (GDD) of approximately $20 * 10^2\ fs^2$, yielding a DW peak centered around 920 nm.

Applying a 920/50 nm BPF isolates the ultrashort DW pulse shown in Fig.4.5 (d, e) in the spectral and temporal domains, respectively. The filtered DW exhibits a spectral FWHM of about 22 nm and a corresponding pulse duration of ~70 fs with a clean temporal profile free of pedestals or satellite features. This value is close to the Fourier-transform-limited pulse duration of 64 fs, also shown in Fig.4.5 (e). The small residual chirp originates from DW propagation in the normal-dispersion regime, which induces a slight positive chirp visible in the spectrogram

of Fig.4.4 (d). Comparable pulse durations and spectral quality are obtained across the entire DW tuning range, as later confirmed experimentally. The simulated parameter space of wavelength-tunable DWs with sub-100 fs pulse durations, clean temporal profiles, and pulse energies exceeding 5 nJ thus appears well-suited for deep-tissue 2PM applications.

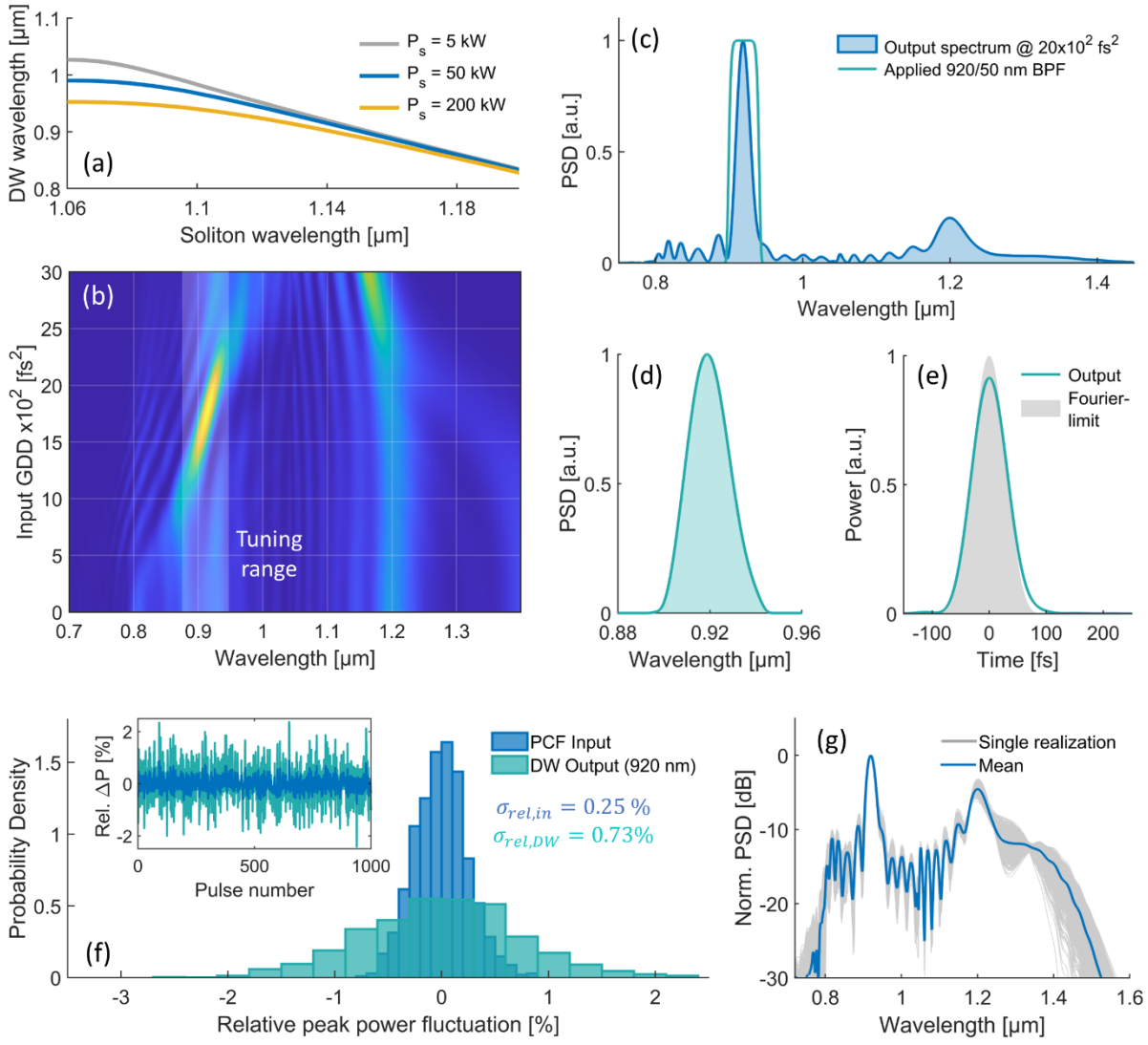

Figure 4.5: Simulation of DW phase-matching, wavelength-tunability and output pulse quality. (a): Calculated phase-matched DW wavelength as function of the soliton wavelength for varying soliton peak power. (b): Simulated PCF output spectra as function of the input pre-chirp with highlighted wavelength-tunable DW range. (c): Output SC spectrum with indicated 920/50 nm BPF to isolate the DW. (d): Spectrum of the filtered DW with a FWHM of ~ 22 nm. (e): Corresponding filtered DW pulse in time-domain with a FWHM of 76 fs, compared to the Fourier-limited pulse calculated from the filtered spectrum. (f): Probability density of relative peak power fluctuations at the PCF input (blue) and the filtered 920 nm DW output (cyan), derived from the stochastic simulation of 1000 pulses. Inset corresponding pulse-to-pulse peak power fluctuations. (g): Corresponding normalized PCF output spectra from the individual noise realizations (gray) compared to the mean spectrum (blue).

A crucial requirement for biomedical two-photon imaging is the stability of the generated DW pulse train, as fluctuations in pulse energy or spectral shape directly affect fluorescence intensity, image contrast, and signal-to-noise ratio (SNR). To numerically evaluate the robustness of the DW generation process under realistic input noise conditions, stochastic GNLSE simulations are performed for an ensemble of 1000 pulses, following the numerical approach outlined in Section 2.3 of this dissertation. Technical input RIN is implemented by randomly sampling Gaussian-distributed peak power fluctuations with a standard deviation corresponding to the measured RIN of the laser source used in subsequent experiments (0.25%, see Section 4.3). Quantum noise was modeled using the one-photon-per-mode model, adding a single photon of random phase (uniformly distributed between 0 and 2π) per spectral bin.

Figure 4.5 (f) presents the normalized probability density functions of the relative peak power fluctuations at the PCF input and at the filtered 920 nm DW output (as characterized in Fig.4.5 (c–e)). The inset shows the corresponding pulse-to-pulse fluctuation traces. As expected, the DW output has a broader fluctuation distribution, with the relative standard deviation σ_{rel} increasing from 0.25% at the input to approximately 0.73% at the output, indicating nonlinear noise amplification by a factor of about three. This amplification arises from the exponential sensitivity of soliton dynamics and phase-matched DW emission to initial conditions, as discussed in Ref. [71]. Figure 4.5 (g) illustrates the spectral variability across the simulated ensemble, where the normalized PSD of individual realizations (gray) are compared to the ensemble-averaged mean spectrum (blue). The grey shaded area thus indicates the range of spectral fluctuations, revealing the regions most affected by noise-induced variability. The DW peak at 920 nm shows a relative center-wavelength RMS fluctuation of 0.5% and a bandwidth RMS fluctuation of approximately 1.5%. In the context of 2PM, this stability analysis confirms that while moderate noise amplification occurs during DW generation, it remains well within a manageable range and can be effectively mitigated through the use of low-noise input pulses and a mechanically robust experimental setup.

4.2 Technical Implementation and Experimental Characterization

4.2.1 Experimental Laser and Imaging Setup

Guided by the numerical optimization results, an experimental setup was developed to realize wavelength-tunable DW generation for multicolor deep-tissue two-photon brain imaging. The overall configuration, illustrated in Fig.4.6 (a), consists of a laser source and a two-photon-capable scanning microscope. The laser source is the 30 MHz home-built ultrafast YFL described in Section 4.1, however, operated at a different working point with further optimized,

almost 2 W average power and 67 nJ output pulse energy. Figure 4.6 (b) shows the resulting laser output spectrum together with the filtered PCF input spectrum when the TBPF is positioned at its default center wavelength of 1050 nm (FWHM ≈ 42 nm). A rotation of the TBPF enables a fine wavelength tuning of ±4 nm, providing an effective means to optimize both the DW conversion efficiency and the spectral position for a given pre-chirp, as discussed previously. Under these conditions, the filtered pulses exhibit an average power of 1.3 W, corresponding to pulse energies of approximately 43 nJ. The YFL output is directed through a tunable bandpass filter (TBPF, 50 nm FWHM) and a transmission-grating pair (1000 lines/mm, Coherent T-1000-1040 series), which allow independent control of the center wavelength and the pre-chirp, respectively. The temporal characteristics of the filtered pulses were verified by AC measurements, as shown in Fig.4.6 (c), verifying a compressed pulse duration of 38 fs (FWHM, Gaussian fit), in excellent agreement with the corresponding FTL of 36 fs.

Following pre-chirp adjustment by the GP, the filtered pulse train passes a HWP that aligns the polarization with the fast axis of a 30 mm long polarization-maintaining PCF (NKT LMA-PM-5) used for DW generation. The beam, with a diameter of approximately 1.5 mm, is mode-matched to the PCF using a 4 mm focal-length aspheric lens (FL; Thorlabs C340TME-B), achieving a coupling efficiency of roughly 75%. After propagation through the fiber, the output is collimated with a 4.5 mm lens (CL; Thorlabs C230TMD-B), resulting in a beam diameter of about 0.9 mm. A subsequent beam-expander assembly (L1: 75 mm, L2: 200 mm; 2.7× magnification) enlarges the beam to approximately 2.4 mm before entering the scanning microscope. Finally, a reflective variable neutral-density attenuator (Thorlabs NDC-25C-4M-B) is placed before the microscope input to enable continuous power control during imaging. This allows the average power on the sample to be dynamically adjusted, ensuring a stable fluorescence signal during deep-tissue imaging experiments.

Two-photon brain imaging experiments are performed using a commercial scanning microscope (Thorlabs MPM-2PKIT) equipped with an 8 kHz resonant scanner and a ~30 Hz galvanometric mirror for rapid FOV acquisition. The imaging objective was a 25× water-immersion lens (Olympus XLPLN25XWMP2) with a NA of 1.05, a working distance of 2 mm, and a free back-aperture diameter of approximately 12.5 mm. With a 5× magnification between the scan and tube lenses, the input beam diameter of ~2.4 mm was well matched to the objective's back aperture, ensuring optimal spatial resolution. The total insertion loss from the microscope input to the sample plane was measured to be approximately 40%.

A dichroic mirror (DM; Semrock FF665-Di02-25×36) separated the excitation beam from the epi-collected two-photon fluorescence. The emitted signal is further spectrally filtered by a

bandpass filter (BPF) matched to the fluorophore's emission band before detection with an amplified photomultiplier tube (PMT; Thorlabs PMT2101), which provides maximum sensitivity around 580 nm. The sample was mounted on a motorized XY translation stage, while the z-position was adjusted via a precision translation mount driven by a software-controlled stepper motor actuator (Thorlabs Z825B). To maintain a compact and technically streamlined system design, no additional dispersion pre-compensation are implemented in the optical path. Nevertheless, the available pulse parameters provided sufficient peak power for high-quality structural imaging, as demonstrated in the following Sections.

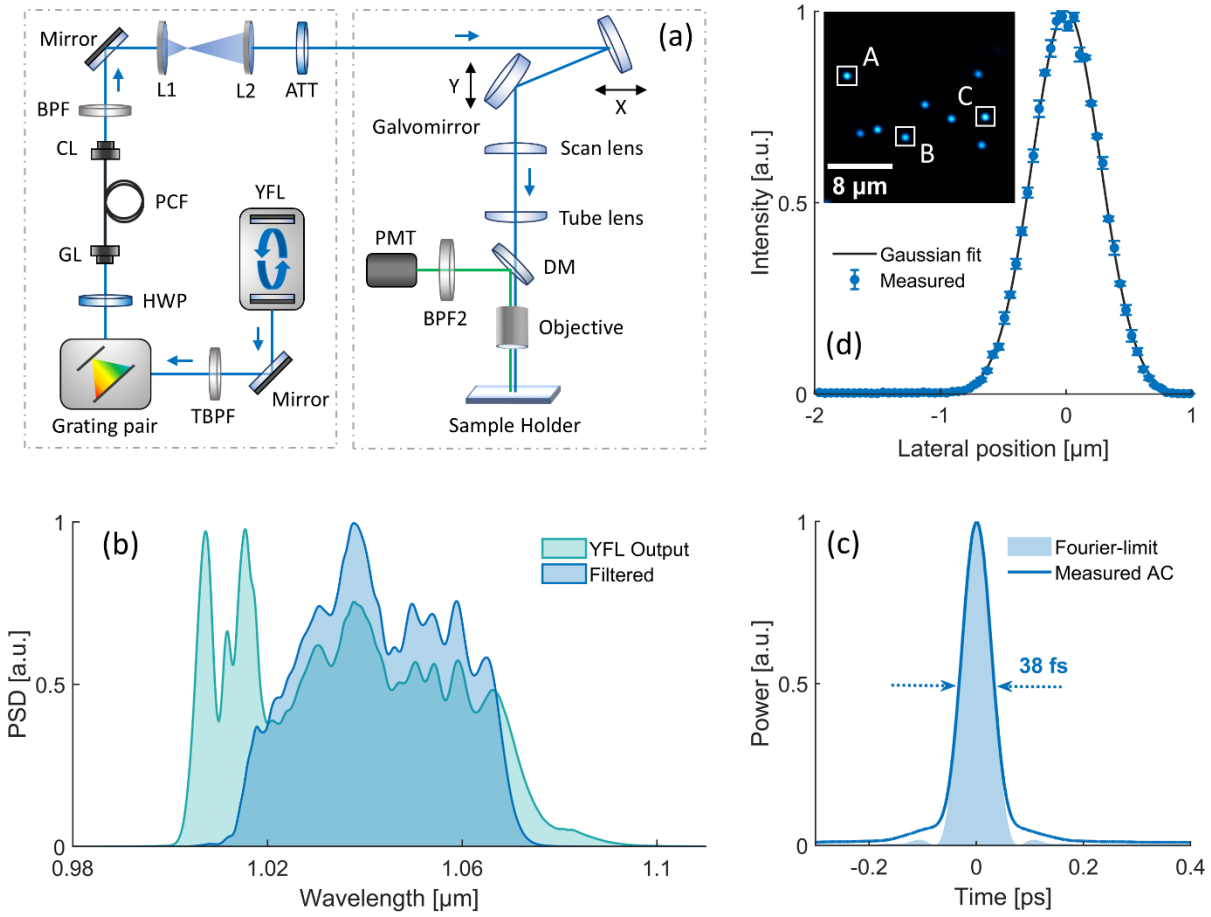

Figure 4.6: Experimental realization of the wavelength-tunable DW source and its integration into the two-photon imaging system. (a): Experimental setup used for wavelength-tunable DW generation and two-photon deep-tissue neuronal imaging. TBPF: tunable bandpass filter, HWP: half-wave plate, FL: focusing lens, CL: collimation lens, BPF: bandpass filter, L: lens, ATT: attenuator, DM: dichroic mirror, PMT: photomultiplier tube. (b): Output spectrum of the YFL (cyan) together with the 1050/60 nm filtered spectrum used as input to the PCF (blue). (c): Measured autocorrelation trace of the filtered PCF input pulse compared to the calculated FTL pulse (gray). (d) Measured lateral PSF obtained from three sub-resolution fluorescent microspheres, as highlighted in the inset.

Data and image acquisition were carried out using the commercial control software (Thorlabs ThorImageLS) and its integrated data acquisition card (DAQ, AlazarTech ATS9440). The acquisition timing was internally synchronized to the 8 kHz resonant scanner but not phase-locked to the 30 MHz repetition rate of the YFL. Consequently, each pixel integrated fluorescence signals from approximately three to four excitation pulses, depending on the relative timing between the scanner-derived pixel clock and the laser pulse train. This asynchronous excitation scheme is typical for resonant-scanning two-photon microscopy systems operating with high-repetition-rate lasers, where direct synchronization is often impractical due to hardware limitations. To mitigate pixel-to-pixel intensity variations arising from this effect, a ten-frame averaging protocol was applied in all subsequent structural imaging experiments, ensuring effective suppression of temporal noise and high signal consistency, as confirmed in the next Section.

The spatial resolution of the two-photon microscope was quantified by measuring the PSF using sub-resolution fluorescent microspheres (Invitrogen PS-Speck Green) with a nominal diameter of 175 nm. The beads were embedded in 2% agarose (1:100 dilution) and imaged at an excitation wavelength of 920 nm. A representative image of the fluorescent beads is shown in the inset of Fig.4.6 (d), corresponding to a 23.5 × 23.5 μm field of view with a pixel size of 0.046 μm. The normalized fluorescence intensity profiles of three beads (A, B, and C) were analyzed to determine the averaged lateral PSF, as displayed in Fig.4.6 (d). The extracted FWHM yielded a lateral resolution of 639 ± 21 nm (SEM), which is close to the theoretical diffraction limit of approximately 438 nm. The remaining deviation can be attributed to slight optical misalignments and chromatic aberrations within the microscope and scanning optics.

4.2.2 Experimental Results and Discussion

The described laser system was employed to generate energetic DWs with tunable center wavelengths by adjusting the pre-chirped pulse duration, the average input power P_{in} (including the 75% coupling efficiency), and the center wavelength λ_c of the pulse launched into the PCF. As shown in Fig.4.7 (a), together with the corresponding input parameters, this approach enables SCG within the PCF featuring a continuously tunable DW peak spanning from 880 nm to 950 nm. The pulse duration at the PCF input corresponds to the FWHM of the measured AC trace, assuming a Gaussian pulse shape, while the center wavelength is determined from the 10 dB spectral bandwidth. Although the generated SCs extend over more than an octave for each working point, a pronounced and efficient energy transfer occurs toward the phase-matched DW wavelength region predicted by the numerical simulations. To spectrally isolate the DW

peaks, BPFs with 25 nm FWHM and suitable center wavelengths are applied to the PCF output. The resulting filtered spectra, shown in Fig.4.7 (b) in 10 nm increments, confirm the broad wavelength tunability of the system across the 880-950 nm range.

The measured output average power and corresponding optical conversion efficiency of the filtered DWs are presented in Fig.4.7 (c) as a function of the coupled PCF input power. Throughout the full tuning range, the system produced pulses with average powers exceeding 200 mW, corresponding to pulse energies of approximately 6.7 nJ. At a center wavelength of 930 nm, the DW output reached a maximum average power of 380 mW (12.7 nJ), with an optical conversion efficiency exceeding 45% across the entire tuning range and peaking at 66% near 920 nm. Fig.4.7 (d) shows the measured temporal FWHM as function for the filtered DWs across the full tuning range, again in 10 nm steps. Across all center wavelengths, the pulse durations, extracted from the measured AC traces assuming Gaussian profiles, remained below 100 fs, reaching as short as 60 fs at 890 nm. Representative AC traces for selected DW wavelengths are shown in Fig.4.7 (e), confirming clean pulse shapes without pedestals or satellite features.

To assess the stability of the DW generator, frequency-resolved single-sideband relative intensity noise (RIN) measurements were performed using the SSA setup described in the previous chapters. In short, the optical pulse trains were detected with a fast, low-noise InGaAs photodiode (Coherent ET-3000), and the resulting RF signal at ~64 MHz was filtered and amplified before analysis with the AM-noise function of the SSA. All measurements were conducted at a constant RF power of -10 dBm to maintain a fixed shot-noise floor and ensure comparability across all data sets. Figure 4.8 (a) shows the measured single-sideband RIN spectra of the YFL compare to the output DWs at selected center wavelengths (880 nm, 920 nm, and 950 nm), together with the corresponding integrated RIN (inset) between 1 Hz to 15 MHz offset-frequency. The YFL, with an integrated RIN of approximately 0.25% across the full measurement bandwidth, served as a low-noise reference for comparison.

In contrast, the DW outputs showed increased RIN levels as a result of nonlinear noise transfer and quantum noise amplification during soliton fission and DW emission (see Section 2.3 of this dissertation), accompanied by broadband amplification of the RIN spectral density at frequencies above roughly 90 Hz. Among the characterized DW wavelengths, the 920 nm output showed the lowest integrated RIN of about 1.1%, while the 880 nm and 950 nm outputs showed slightly higher values of approximately 2.1% and 2.2%, respectively.

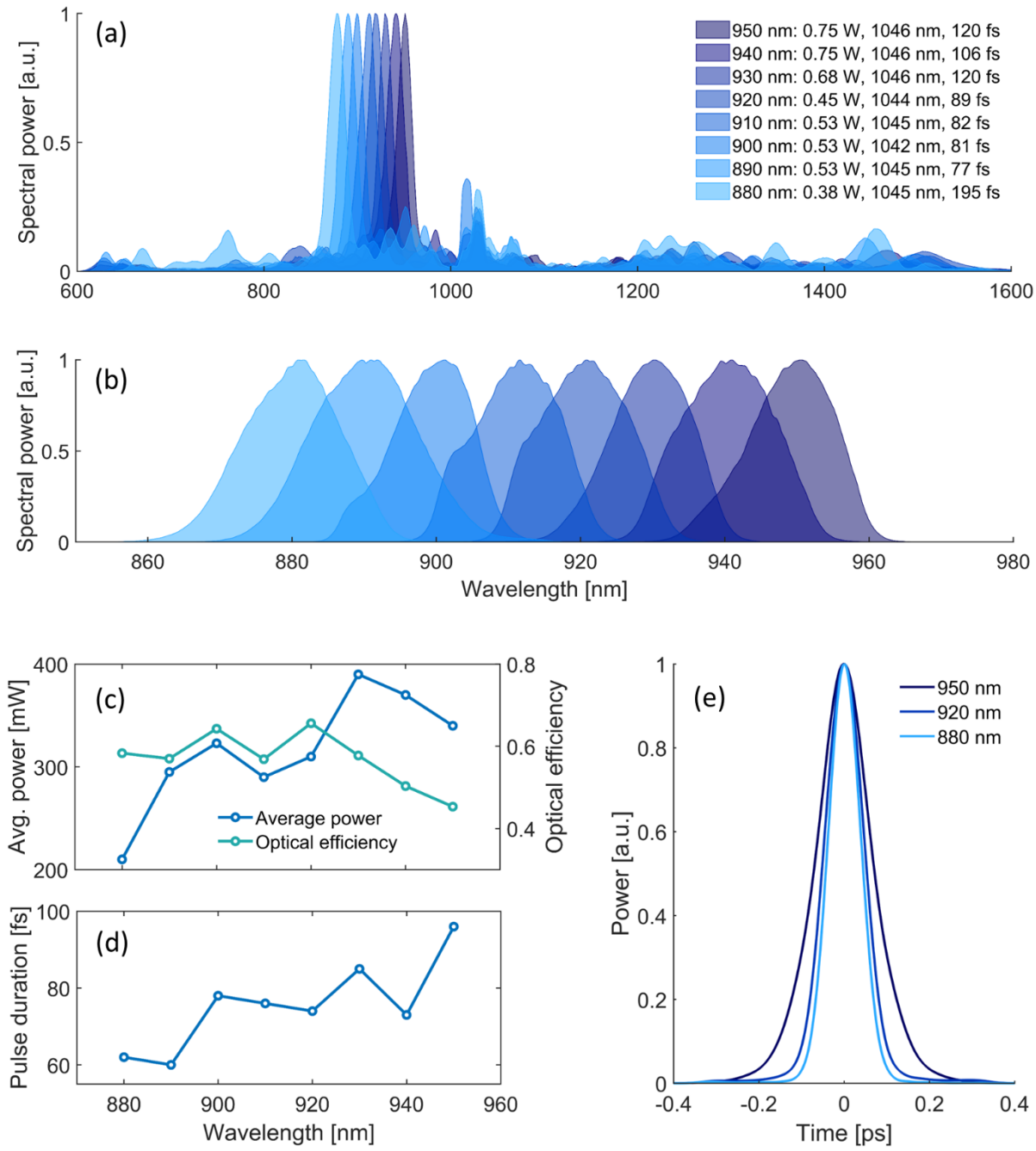

Figure 4.7: Experimental characterization of wavelength tunable DW generation. (a) Measured supercontinuum spectra generated in the PCF for varying input parameters including coupled average power (with 75% coupling efficiency), center wavelength, and pulse duration (FWHM assuming a Gaussian pulse shape), showing DW peaks tunable from 880 to 950 nm in 10 nm steps. (b): Spectra of the filtered DW components extracted from the corresponding SC outputs. (c): Measured DW output average power and optical conversion efficiency as a function of the coupled PCF input power. (d): Corresponding temporal FWHM of the measured AC traces assuming Gaussian pulse profiles. (e) Representative AC traces of the filtered DWs at selected center wavelengths.

These experimental results align well with the numerical simulations, which predicted a relative peak-power fluctuation of ~0.73% for the 920 nm DW (see Fig.4.5 (f)). The slightly higher RIN observed experimentally can be attributed to additional technical noise sources not

included in the simulation, such as amplified spontaneous emission from the YFL, which can increase the effective input noise beyond the shot-noise-limited quantum fluctuations assumed in the model.

To further assess the pulse-to-pulse intensity stability of the DW generator under realistic operating conditions, the SHG signal produced in a 3 mm-long, type-I phase-matched BBO crystal ($\theta = 23°$) was characterized using the 950 nm DW output. Owing to its nonlinear dependence on peak power, the SHG signal serves as a sensitive probe of pulse energy fluctuations and provides a direct measure of temporal frame-to-frame stability relevant to two-photon imaging performance.

For comparison, the SHG stability of the driving YFL was also evaluated as a low-noise reference. At both wavelengths, SHG was performed with an average input power of 50 mW, focused into the BBO crystal using a 19 mm focal-length lens (Thorlabs AC-127-019-B), yielding approximately 20% conversion efficiency. The relative noise of both sources was quantified by recording the root-mean-square (RMS) voltage fluctuations ($\Delta V/V$) of the photo-detected pulse trains at a 0.1 Hz sampling rate over a 600 s interval using a digital oscilloscope (Rohde & Schwarz HMO722). The YFL fundamental near 1030 nm was monitored with a fast InGaAs photodetector (Coherent ET-3010), while the YFL SHG at 515 nm, the DW fundamental at 950 nm, and the corresponding DW SHG at 475 nm were detected using a Si-based photodetector (Thorlabs PDA10A2).

As shown in Fig.4.8 (b), the SHG spectrum of the YFL reveals a clean and symmetric peak centered at approximately 515 nm, confirming efficient frequency doubling of the fundamental emission near 1050 nm. The corresponding temporal stability traces in Fig.4.8 (c) reveal relative RMS $\Delta V/V$ fluctuations of about 1.0% in the SHG signal and 0.68% in the fundamental, demonstrating the excellent stability of the driving laser. In comparison, the SHG spectrum of the 950 nm DW, shown in Fig.4.8 (d), is centered around 475 nm and maintains a similarly clean spectral shape. However, as illustrated by the corresponding $\Delta V/V$ traces in Fig.4.8 (e), the DW output has higher pulse-to-pulse fluctuations, with RMS noise levels of approximately 5% in the SHG signal and 1.8% in the fundamental.

These results indicate that while the DW generation process introduces moderate additional intensity noise, the overall stability remains sufficient for robust two-photon imaging applications. Overall, the demonstrated performance with sub-100 fs pulse durations and multi-nJ energies across a tunable 880-950 nm range highlights the suitability of the developed system as a versatile source for deep-tissue, wavelength-multiplexed two-photon neural imaging which will be verified experimentally on multiple samples in the next section.

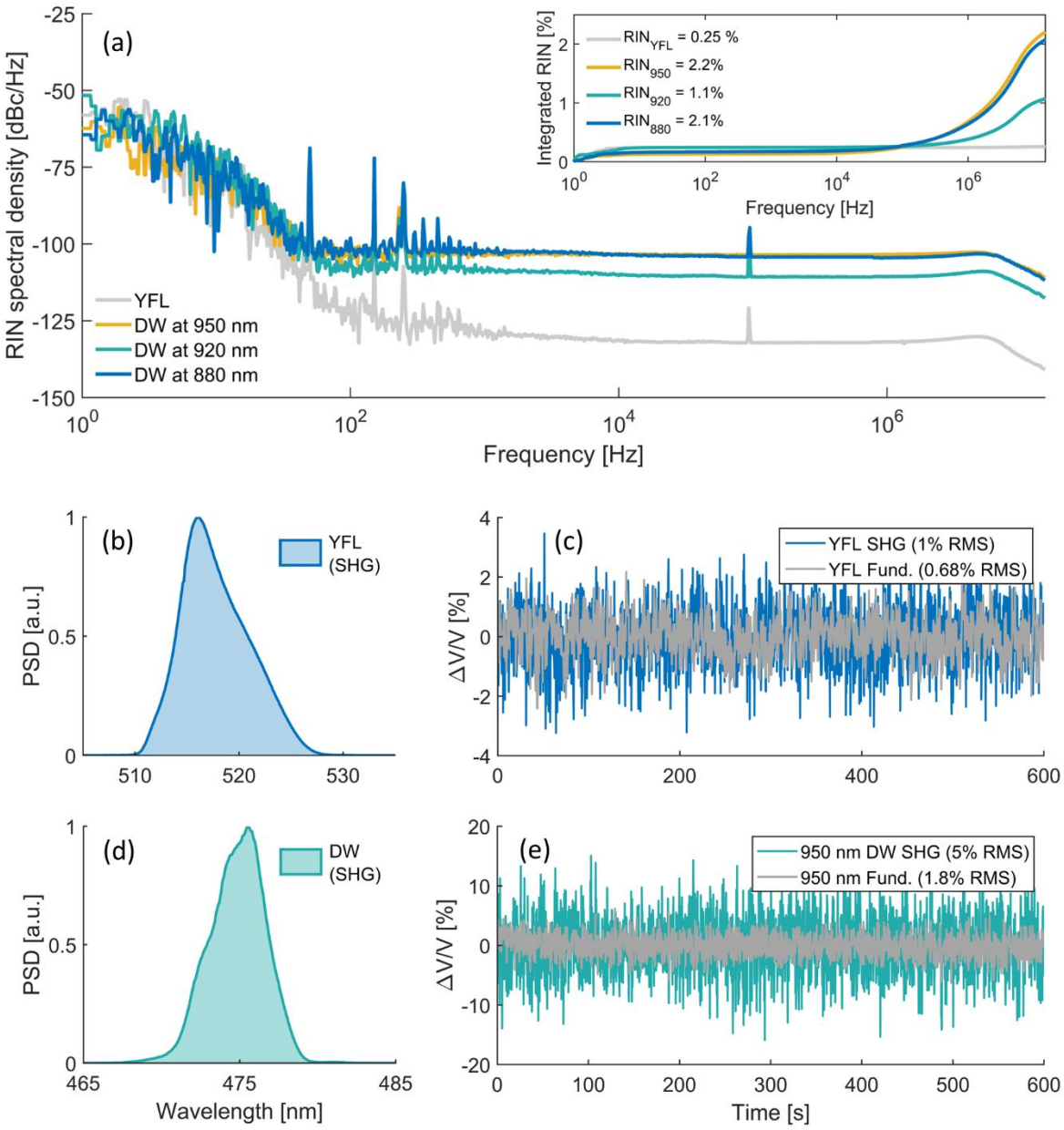

Figure 4.8: Frequency- and time-domain stability characterization of the tunable DW generator. (a): Single-sideband RIN spectra (1 Hz to 15 MHz) of the driving YFL (gray) and the DW outputs centered at 880 nm (blue), 920 nm (green), and 950 nm (yellow). The inset shows the corresponding integrated RIN values of 0.25 % (YFL), 2.1 % (880 nm), 1.1 % (920 nm), and 2.2 % (950 nm). (b): Measured SHG spectrum of the YFL output (~1050 nm fundamental) centered at 515 nm. (c): Corresponding time traces of the normalized SHG (blue) and fundamental (gray) signals showing RMS fluctuations of 1.0 % and 0.68 %, respectively. (d): SHG spectrum of the 950 nm DW output centered at 475 nm. (e): Corresponding time traces of the DW SHG (cyan) and fundamental (gray) signals, revealing higher RMS fluctuations of ~5 % and 1.8 %, respectively.

4.3 Application for Advanced Deep-Tissue Two-Photon Microscopy

4.3.1 Neurovascular Deep-Tissue Imaging in GFP-labeled Mouse Hippocampus

As an initial demonstration of the system's flexible deep-tissue two-photon imaging capabilities, the wavelength-tunable DW generator was applied to visualize neuronal and vascular structures in the hippocampus of a transgenic mouse model ubiquitously expressing EGFP, which has an excitation peak near 920 nm [47]. To match the EGFP excitation maximum, the DW source was tuned to a center wavelength of 920 nm and adjusted for optimal excitation efficiency while minimizing photobleaching and photodamage.

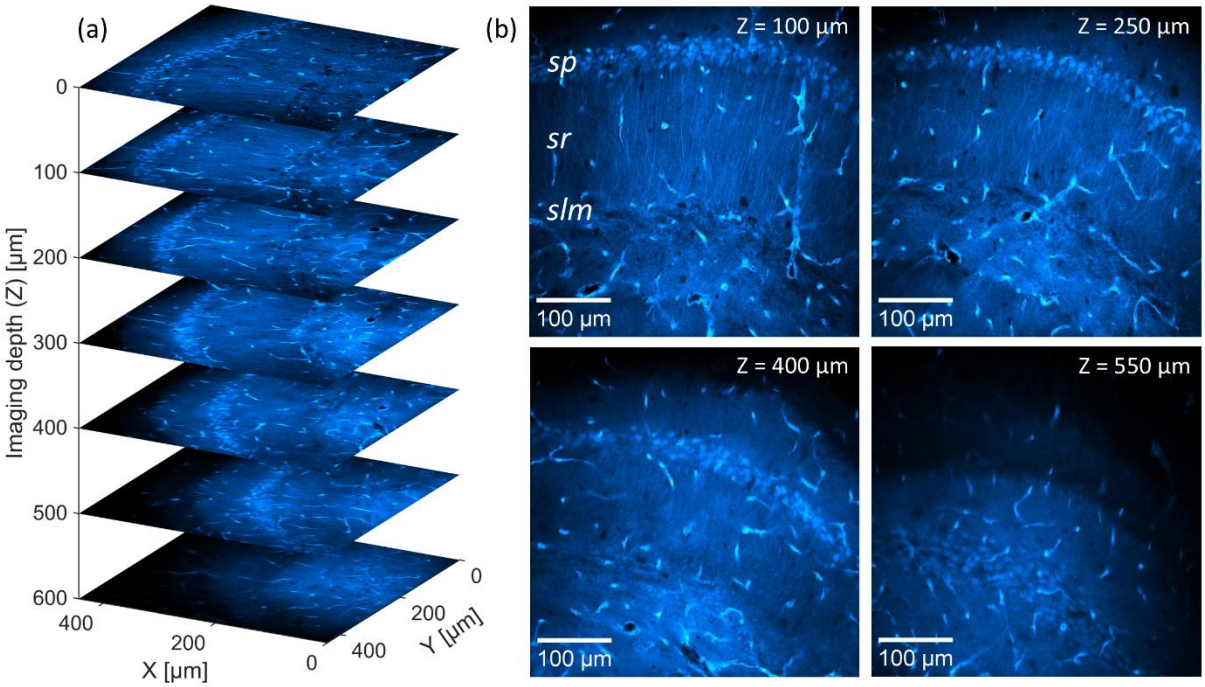

Figure 4.9: Deep-tissue two-photon imaging of EGFP-labeled mouse hippocampus using the DW generator tuned to a 920 nm center wavelength. (a): Depth-resolved imaging of the CA1 (*cornu ammonis 1*) hippocampal region in 100 µm steps up to a maximum depth of 600 µm, within a 443 × 443 µm field of view (1024 × 1024 pixels). Soma of pyramidal neurons located in the *stratum pyramidale* (sp) and their dendritic projections in the *stratum radiatum* (sr) and stratum *lacunosum-moleculare* (slm) are clearly resolved together with vascular structures. (b): Representative images at selected imaging depths, shown in the same FOV.

Under these conditions, the system delivered an average power of 310 mW (corresponding to ~10 nJ pulse energy) and a pulse duration of ~74 fs, as shown in Fig.4.7. A 520/36 nm bandpass filter (EO #67-030) was positioned in front of the PMT (see Fig.4.6 (a)) to isolate the EGFP fluorescence. Detailed information on the animal handling and sample preparation is provided in the Appendix of this dissertation, Section 8.3.1.

Figure 4.9 (a) presents a depth-resolved image stack of the mouse hippocampus acquired up to an imaging depth of 600 µm in steps of 100 µm. Each frame covers a 443.3 × 443.3 µm field of view (1024 × 1024 pixels) with a pixel size of 0.433 µm and a dwell time of 0.122 µs. To suppress background noise, each image represents the average of ten consecutive frames acquired at ~10 frames per second, corresponding to an effective acquisition time of approximately five seconds per depth. To maintain a constant fluorescence level during deeper imaging, the average power on the sample was gradually increased using the attenuator (ATT) from 8 mW at the surface (28 mW at the system input) to 59 mW at the maximum imaging depth of 600 µm (168 mW at the input).

To further illustrate the system's imaging performance, Fig.4.9 (b) shows representative frames extracted from the depth scan at selected imaging depths. Up to approximately 250 µm, distinct layers of pyramidal neurons in the CA1 region, together with their projections in the *stratum radiatum* (sr) and stratum *lacunosum-moleculare* (slm), are clearly resolved along with several blood vessels. At larger depths (e.g., z = 400 µm), the neuronal projections gradually lose contrast, while the somata remain discernible. This characteristic degradation in fine-structure visibility is typical for two-photon microscopy and arises from increased background emission and scattering-induced blurring at higher excitation powers, particularly near the sample surface [32,38].

4.3.2 Resolving Neuronal Nuclei in Deep SO-labeled Mouse Cerebellum

To further demonstrate the wavelength-tunable deep-tissue two-photon imaging capability of the developed system, the DW generator was applied to visualize and distinguish individual neuronal nuclei within a stained mouse brain cerebellum. The sample consisted of a prepared slide (SunJin Lab FluoTissue) containing a 550 µm-thick mouse brain section, multi-labeled with Alexa Fluor 488 for blood vessels, SYTOX Orange (SO) for neuronal nuclei, and Alexa Fluor 647 for dopaminergic neurons. The tissue was mounted using an optical clearing reagent (SunJin Lab RapiClear 1.52) and sealed between a microscopy slide and a glass cover slip. Two-photon imaging was performed with the DW generator tuned to a center wavelength of 950 nm, providing efficient excitation of SO-labeled neuronal nuclei [133]. At this working point, the source delivered a maximum average power of 340 mW (corresponding to ~11 nJ pulse energy) and a pulse duration of approximately 96 fs, as shown in Fig.4.7. To isolate the SO fluorescence, a 572/28 nm bandpass filter (EO #84-100) was placed in front of the PMT, as indicated in Fig.4.6 (a).

To evaluate deep-tissue imaging performance using the 950 nm DW excitation, Fig.4.10 (a) presents a depth scan of the mouse cerebellum down to 450 µm in steps of 100 µm. Each frame

was acquired within a 595 × 594 µm field of view (1024 × 1024 pixels) with a pixel size of 0.581 µm and a dwell time of ~0.2 µs, corresponding to the average of ten consecutive frames (~10 frames/s, ~5 s total acquisition time). To maintain a consistent fluorescence level on the detector with increasing imaging depth, the average power on the sample was gradually increased using the ATT, from 23 mW (57 mW at the system input) at the surface (z = 0 µm) to 76 mW (190 mW at the input) at the maximum depth (z = 450 µm). As shown, the resulting depth stack clearly resolves neuronal nuclei and blood vessels in both the molecular and granular layers of the cerebellum throughout the full sample thickness of 450 µm.

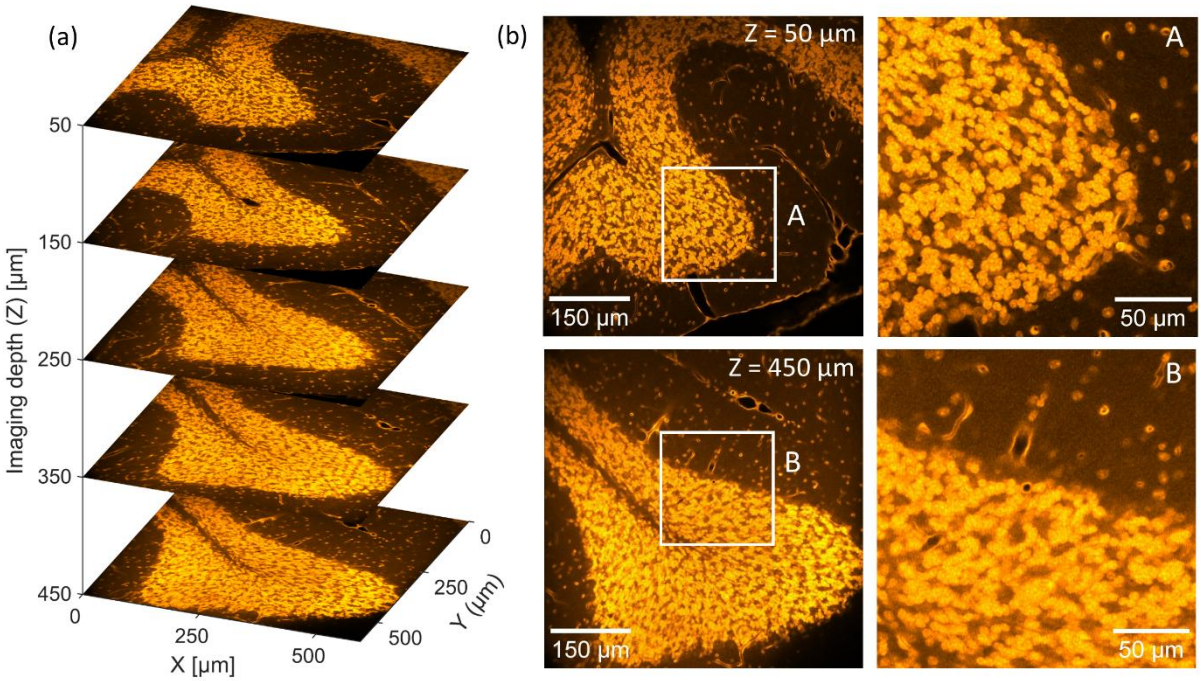

Figure 4.10: Deep-tissue two-photon imaging of SYTOX Orange-labeled mouse cerebellum using the 950 nm output of the DW generator. (a): Depth-resolved imaging of a SYTOX Orange–stained cerebellar slice acquired in 100 µm steps down to a maximum depth of 450 µm, within a 595 × 595 µm field of view (1024 × 1024 pixels). (b): Representative images at imaging depths of 50 µm and 450 µm acquired in the same field of view, with marked regions of interest (ROIs A and B) magnified by approximately 2.9× to a 208 × 208 µm field of view (358 × 358 pixels). The magnified ROIs illustrate the system's ability to resolve individual cerebellar granule-cell nuclei across the full imaging depth.

Cerebellar granule-cell nuclei typically have diameters of ~5 µm, well above the lateral resolution of the two-photon system [194], and thus provide suitable structural references for assessing imaging performance. Figure 4.10 (b) displays representative images obtained at z = 50 µm and z = 450 µm, including marked regions of interest (ROIs A and B). These ROIs are shown with 2.9× magnification, corresponding to a 208 × 208 µm field of view (358 × 358

pixels). ROI A, acquired near the surface (z = 50 µm), reveals clearly resolved individual neuronal nuclei within the granular layer. In contrast, ROI B, imaged at the maximum depth of 450 µm, exhibits reduced contrast due to increased background and scattering-induced noise. Nevertheless, the granular nuclei remain distinguishable, confirming that the 950 nm DW excitation enables stable, high-resolution imaging across the entire accessible depth range.

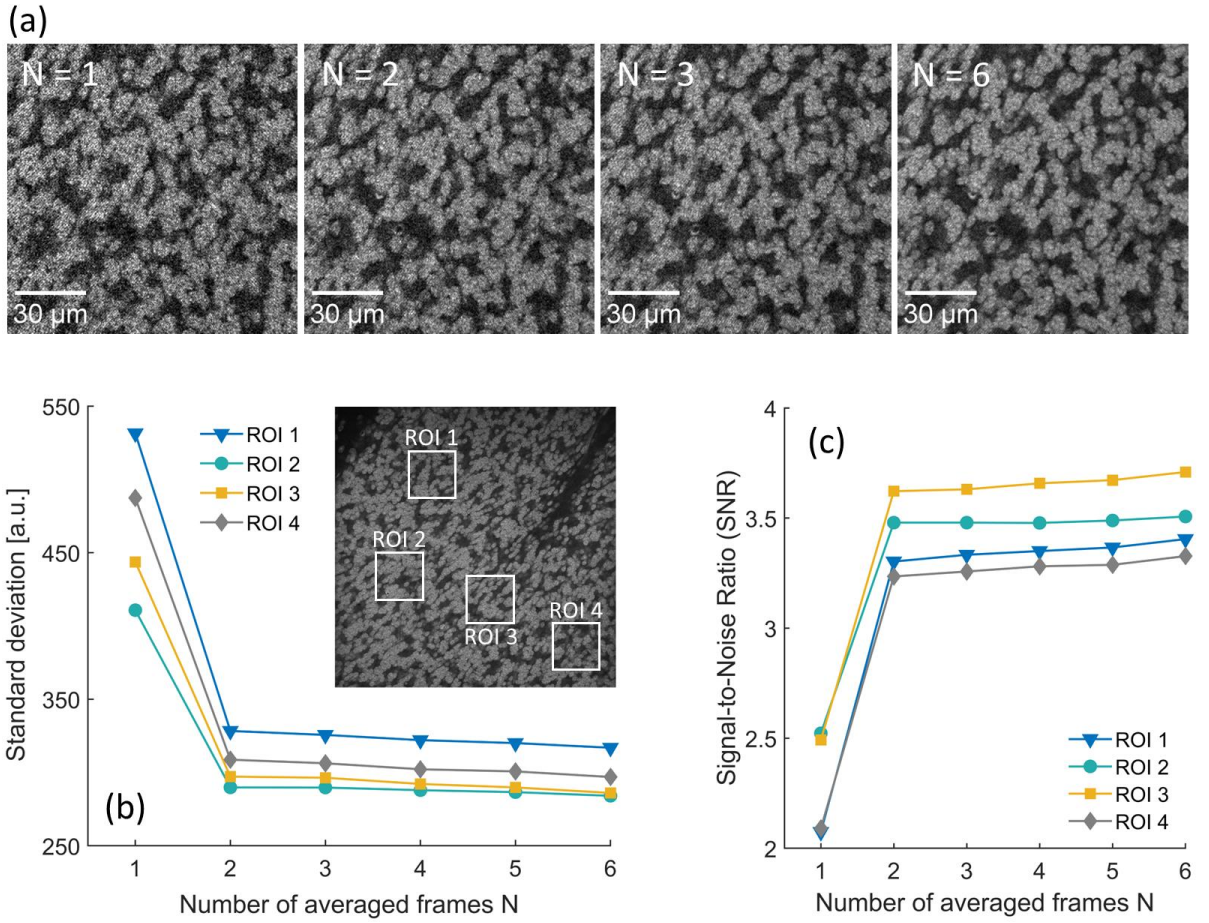

Figure 4.11: Effect of frame averaging on image quality and quantitative noise suppression in two-photon fluorescence imaging. (a) Two-photon images of SYTOX Orange–labeled neuronal nuclei in fixed mouse cerebellum acquired at 950 nm excitation for different numbers of averaged frames (N = 0, 3, 6, 10, 12, 15). All images were obtained under identical excitation and acquisition conditions. (b): Quantitative analysis of the standard deviation of pixel intensities within four representative regions of interest (ROIs 1-4, shown in the inset). (c): Corresponding SNR for the same ROIs.

Overall, this experiment highlights the strong deep-tissue imaging performance of the DW-based excitation source. Compared to the EGFP-labeled hippocampal images shown in Fig.4.9, the SO-stained sample exhibits noticeably enhanced contrast and overall image quality. This improvement is attributed to both the optical clearing process and the highly specific labeling of neuronal nuclei by SO, resulting in a substantially improved signal-to-background ratio.

To evaluate the influence of temporal noise and frame averaging on image quality, two-photon fluorescence imaging was performed on fixed mouse cerebellum tissue labeled with SO to visualize neuronal nuclei, using the DW output centered at 950 nm (corresponding to the stability characterization in Fig. 4.8). Image stacks were repeatedly acquired at an imaging depth of 200 µm over a 461 × 461 µm field of view (1024 × 1024 pixels, 0.45 µm pixel size) while systematically varying the number of averaged frames (N = 0, 3, 6, 10, 12, 15). The average excitation power on the sample was kept constant at approximately 25 mW for all measurements.

Magnified ROIs of the acquired images (272x271 pixels, 0.45 µm pixel size) for varying N are shown in Fig.4.11 (a). Without averaging (N = 0), minor frame-to-frame brightness fluctuations, and reduced contrast can be observed. Increasing the number of averaged frames progressively suppresses temporal noise and enhances image uniformity, with pronounced improvement already observed at N = 3. Quantitative analysis of the pixel intensity statistics within four representative ROIs, shown in Fig. 4.11 (b) and (c), confirms this trend: the standard deviation decreases steeply for the first few averages and approaches a stable baseline beyond $N \approx 3$, while the corresponding SNR rises sharply before saturating at higher averaging levels. These results demonstrate that the DW-based imaging system maintains excellent temporal stability and achieves high image consistency even under short integration times. Overall, the noise transfer analysis confirms the suitability of the 950 nm DW source for high-speed and time-resolved two-photon imaging, particularly when additionally combined with standard noise-suppression techniques such as active feedback or passive pulse stabilization.

4.4 High-Resolution Structural Imaging Across Diverse Biological Systems

To demonstrate the versatility of the DW-generator for 2PM application beyond the deep-tissue imaging experiments described previously, a diverse set of biological, crystalline, and synthetic samples were imaged at excitation wavelengths centered between 920-960 nm (Fig.4.12). Together, these datasets highlight the system's ability to generate high-resolution structural contrast across immunolabeled tissue, genetically encoded fluorescence, coherent nonlinear materials, and strongly scattering polymer particles.

Imaging parameters (FOV, pixel size, illumination power, etc.) were individually optimized for each sample to avoid saturation and photodamage while maximizing SNR. Because fluorescence brightness, scattering strength, emission spectra, and nonlinear response differ strongly between specimens, imaging settings are not identical across the different panels in Fig.4.12. Typical ranges include FOVs between 700-150 μm^2, pixel sizes of 0.72-0.3 µm/pixel,

excitation powers of 8-20 mW at the sample, and frame rates of 15-20 Hz. All images shown in Fig. 4.12 represent the optimal acquisition conditions for their respective specimens.

The first set of images (Fig.4.12 (b) and (c)) shows 2P fluorescence in AF488-labeled cortical tissue. As illustrated in Fig.4.12 (a), sections of adult mouse cortex were stained using a MAP2 primary antibody followed by an AF488-conjugated secondary antibody, resulting in strong cytoskeletal labeling of neuronal somata and dendritic processes. Under DW excitation at 920 nm with a spectral FWHM of 20 nm, the system resolves densely packed neuronal cell bodies, axonal projections, and fine structural detail across FOVs up to ~700 μm^2. A zoomed-in region (A, 5X magnification) reveals individual soma boundaries, axon fibers, and subcellular features at near-diffraction-limited resolution, consistent with the measured PSF described in Section 4.2.

A second fluorescence dataset (Fig.4.12 (d-f)) is obtained in GFP-expressing mouse retina from the same mouse model that provided the hippocampal brain tissue in Fig.4.9. Despite the inherently high scattering of retinal tissue, the DW generator provides uniform excitation and high-contrast structural detail across multiple FOVs. Retinal layers, fiber tracts, blood-vessels, and densely packed photoreceptors are clearly visible in all regions imaged. A high-magnification inset (B, 5X magnification) resolves individual photoreceptor somata and fine fiber structures, demonstrating that the resolution achieved in cortical tissue is preserved across different biological preparations with substantially different optical properties. The ability to maintain structural fidelity in retina further underscores the robustness of the excitation pulses and the stability of the microscope alignment.

To test coherent nonlinear contrast under the same excitation architecture, SHG imaging was performed on Thaumatin protein crystals (Fig.4.12 (g) and (h)). Thaumatin forms strongly non-centrosymmetric crystalline arrangements that generate pronounced second-harmonic signals. The SHG images reveal planar facets, internal crystalline domains, and localized precipitation features. Differences in morphology and crystal orientation across the two FOVs confirm consistent SHG performance and demonstrate that DW excitation maintains sufficient coherence and peak power for efficient SHG imaging.

Finally, two types of environmental microplastic fragments, polyethylene terephthalate (PET) and polypropylene (PP), were imaged without fluorescent staining (Fig.4.12 (i) and (j)). Nonlinear contrast in these materials is achieved through a combination of autofluorescence, nonlinear luminescence, and structural scattering. The PET fragment displays sharp edges, internal stress features, and layered morphology, whereas PP shows coarse fragmentation and

amorphous surface texture. Despite their strong scattering and heterogeneous nature, both materials are resolved with high contrast and structural clarity. The ability to image non-biological materials with significantly different nonlinear response demonstrates that the DW source is not limited to fluorescent tissue and performs reliably in synthetic and environmental samples.

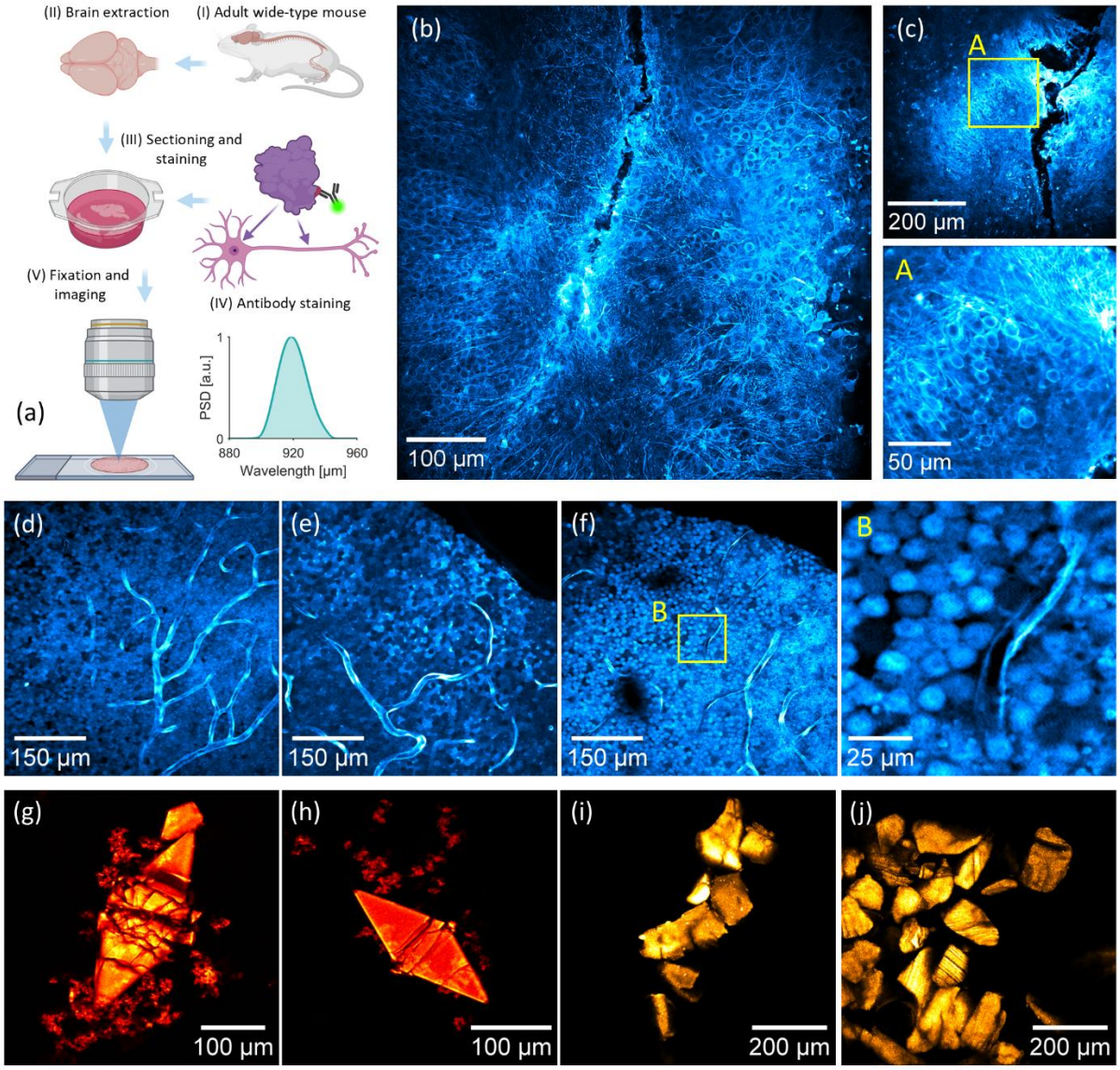

Figure 4.12: High-resolution and multimodal two-photon imaging enabled by the tunable DW generator. (a): Workflow of mouse brain sample preparation and MAP2 immunolabeling, together with the excitation DW (~920 nm) used for imaging. Created in part BioRender.com (b) Two-photon fluorescence (2PEF) image of AF488-labeled cortical neurons showing densely packed somata and axonal processes. (c) Second cortical region with zoomed view (A, 5X) highlighting individual neuronal cell bodies. (d–f) Three distinct fields of view of GFP-expressing mouse retina acquired under identical conditions; high-magnification inset (B, 5X) from panel (f) reveals the clearly resolved photoreceptor mosaic and fine fiber structure. (g,h): SHG imaging of Thaumatin protein crystals, illustrating strong coherent structural contrast and variation in crystalline morphology. (i,j): 2P structural autofluorescence imaging of environmental microplastic fragments composed of PET and PP.

Together, the fluorescence, SHG, and label-free datasets in Fig. 4.12 demonstrate that the dispersive-wave generator enables high-resolution two-photon excitation across a broad range of biological and non-biological samples. The consistent spatial detail observed in immunolabeled neurons, genetically encoded retinal fluorescence, crystalline protein structures, and synthetic polymer fragments highlights the compatibility of DW-based excitation with diverse contrast mechanisms and sample classes. These results extend the platforms applicability beyond deep-tissue neuroimaging and verifies its suitability for multimodal two-photon imaging.

4.5 Deep-Tissue 2PM Platform: Summary and Discussion

This chapter demonstrates a fiber-optic, wavelength-tunable two-photon excitation platform realizing the deep-tissue branch of the unified photonic imaging framework developed in this dissertation. Building on the theoretical foundations of nonlinear pulse propagation and noise transfer established in Chapter 2, and the low-noise fiber-optic subsystems introduced in Chapter 3, the presented system combines an energetic all-PM Yb-fiber laser with precisely engineered SCG and DW generation in PCFs to enable application-optimized excitation for deep-tissue two-photon brain imaging across diverse modalities.

The developed DW source provides sub-100 fs pulses with energies exceeding 6.7 nJ over a continuously tunable spectral range from 880 to 950 nm, achieving optical conversion efficiencies of up to 65 %. Comprehensive numerical simulations elucidate the physical mechanisms governing DW formation, spectral tunability, and noise transfer, enabling a predictive and reproducible experimental implementation. The resulting wavelength agility supports excitation-matched two-photon imaging across diverse fluorophores and neuronal markers, yielding high-resolution visualization of neuronal and vascular structures at substantial imaging depths. Imaging at 920 nm enabled detailed reconstruction of neuronal morphology in EGFP-labeled hippocampal tissue to depths approaching 600 µm, while excitation near 950 nm permitted clear resolution of individual neuronal nuclei in SO-labeled cerebellar tissue to depths of approximately 450 µm. Additional imaging in brain and corneal tissue, crystallized proteins, and polymers demonstrates robust, high-contrast structural imaging across biological and synthetic systems, verifying the platforms versatility and stability under realistic experimental conditions.

In the context of this dissertation, the DW-based deep-tissue two-photon imaging platform constitutes a concrete realization of a noise-resilient, spectrally agile fiber-optic excitation sys-

tem tailored to demanding biomedical imaging applications. In the following chapter, this unified photonic framework is extended toward chromatically multiplexed excitation, enabling multicolor and multi-target 2PM.

5 Multicolor Two-Photon Imaging Platform Enabled by Deterministic Spectral Engineering

The information content and functional versatility of 2PM platforms can be substantially expanded through spectrally multiplexed excitation, enabling the simultaneous visualization of multiple fluorophores or dynamic processes within a single specimen. This approach, subsequently referred to as *chromatically multiplexed two-photon microscopy* (CrM-2PM), has recently driven major biomedical research advancements. For instance, Rakhymzhan *et al.* visualized germinal center reactions in living lymph nodes using CrM-2PM with spectral unmixing [195], while Abdeladim *et al.* achieved subcellular-resolution, whole-brain imaging in Brainbow-labeled mice, enabling detailed mapping of neuronal connectivity [196].

Despite its transformative potential, realizing high-performance CrM-2PM remains technically demanding. Efficient multicolor excitation requires the simultaneous availability of spectrally distinct, ultrashort, and energetic pulses, each tuned to the absorption maxima of relevant fluorophores [32]. Three principal strategies have been pursued to achieve this goal: (i) employing multiple synchronized femtosecond lasers at different wavelengths [86,197], (ii) using nonlinear wavelength conversion to derive multiple colors from a single source [198,199], or (iii) generating broadband continua that cover several excitation bands [133,200,201]. Among these, fiber-based broadband sources offer distinct advantages in compactness, robustness, and cost-efficiency, key factors for turnkey and clinical systems.

While Ti:Sa-laser based parametric sources have long dominated multicolor excitation [88,202], YFLs have emerged as highly promising alternatives due to their stability, thermal efficiency, and compatibility with newly emerging yellow-shifted fluorophores such as yellow fluorescent protein (YFP) [130] and the recently developed calcium indicator jYCaMP6 [60]. Owing to their relatively narrow gain bandwidth (~1020-1080 nm), broadband YFL systems typically rely on nonlinear spectral broadening in PCFs to access multiple excitation bands [71,203]. Combined with the latest advances in ultra-low-noise and self-stabilized mode-locked fiber oscillators [73], this approach has enabled the first fully fiber-based CrM-2PM systems.

Several important proof-of-concept demonstrations highlight both the potential and the limitations of this approach. Li *et al.* realized multicolor CrM-2PM via Cherenkov and Raman gain processes in PCF [131], while Chou *et al.* [133] and Hsiao *et al.* [201] employed SPM and soliton dynamics to generate broadband continua enabling four-color excitation in Brainbow-labeled mouse brain tissue. However, such broadband continua typically exhibit wide spectral bandwidths (150-200 nm per channel), dispersing energy across wavelength regions rather than

concentrating it at specific excitation maxima. This results in reduced excitation efficiency, higher cross-talk, and increased risk of out-of-band phototoxicity [204,205]. For deep-tissue applications, the broad spectra further lead to temporal broadening and peak-power loss through tissue dispersion and scattering [206].

To address these limitations, recent research has focused on spectrally engineered nonlinear conversion in PCFs, exploiting controlled DW generation (see Section 4 or Ref. [207]) and tailored SPM [189,208] to produce tunable, spectrally concentrated outputs. Such approaches have already demonstrated high-performance single-channel 2PM excitation [209–212] and, more recently, dual-color excitation in auto-fluorescent plant tissue [132]. Nonetheless, these implementations have remained largely restricted to single-fluorophore excitation or simplified dual-color imaging outside of mammalian biomedical contexts.

The simultaneous generation of multiple, spectrally isolated, high-energy peaks matched to the excitation maxima of common fluorophores used in neuroscience and biomedical imaging has so far remained unexplored. Moreover, no previous study has systematically combined numerical modeling of nonlinear PCF dynamics with experimental realization to produce a fiber-based system capable of delivering multiple ultrashort, high-energy pulses optimized for efficient, low cross-talk CrM-2PM in complex, multi-labeled tissue.

In this chapter, we present the numerically designed and experimentally validated three-color wavelength conversion scheme developed for our ultrafast Yb-fiber laser platform. Building upon the low-noise and high-energy performance of the source introduced in Chapter 4, we simulate and realize controlled nonlinear broadening in PCF to achieve three spectrally distinct and energetically concentrated outputs centered at 940 nm, 1080 nm, and 1175 nm, closely aligned with the excitation bands of major biological fluorophores. The generated sub-115 fs pulses, each with 2.5-6 nJ of pulse energy, provide efficient three-color excitation without the need for multiple synchronized lasers or active wavelength tuning. We further demonstrate the application of this spectrally engineered output for multiplexed three-color two-photon imaging in triple-labeled mouse brain, kidney, and liver tissues, confirming the platform's capability to resolve complex biological structures across distinct fluorophore channels. This chapter thus integrates numerical design, nonlinear wavelength conversion, and multicolor imaging validation, establishing a robust and compact fiber-based architecture for next-generation CrM-2PM and related biomedical imaging modalities.

Parts of this chapter are based on results previously published by the author in the following preprint:

- M. Edelmann *et al*., "Multiplexed brain and visceral two-photon imaging using a simulation-guided ultrafast three-color fiber laser," *bioRxiv*, DOI: 10.1101/2025.06.19.660526 (2025).

All sections have been revised, expanded, and re-formatted to provide a unified presentation and additional discussion in the context of this dissertation.

5.1 Experimental Laser and Imaging Setup

As a first step, the experimental configuration of the three-color laser source and the integrated imaging system is presented. Figure 5.1 (a) shows the implemented wavelength-conversion setup, which builds upon the numerically optimized YFL introduced in chapter 4.1. The laser delivers a 30 MHz pulse train centered at 1028 nm, providing the input for nonlinear wavelength conversion in a PCF. The emerging broadband output is subsequently spectrally divided into three distinct bands using a series of dichroic mirrors (DM1-DM4) and bandpass filters (BPF2-BPF4), producing three energetic, temporally synchronized color channels centered at approximately 940 nm, 1080 nm, and 1175 nm. Each channel is individually collimated, compressed, and recombined using telescopes (T1-T3) and mirrors (M2-M4) to form the multiplexed multicolor excitation beam delivered to the microscope.

The multicolor two-photon imaging system, shown in Fig.5.1 (b), is based on a resonant-galvo scanning microscope (Thorlabs MPM-2PKIT) similar to the previous experiments, equipped with an 8 kHz resonant scanner and a 30 Hz galvo mirror to scan the FOV in the x-y plane. The multiplexed three-color beam is focused onto the sample using a 25× water-immersion objective (Olympus XLPLN25XWMP2, NA = 1.05, WD = 2 mm) and the resulting two-photon fluorescence signal is epi-collected through the same objective. For spectral separation and detection, the emitted fluorescence is sequentially split by a set of dichroic mirrors (DM5-DM7; cut-on wavelengths: 532 nm, 635 nm, 775 nm) and directed onto three GaAsP photomultiplier tubes (PMT2101, Thorlabs) optimized for a detection range of 300-720 nm with peak sensitivity at 550 nm. Additional bandpass filters (BPF5: 520 ± 12.5 nm, BPF6: 570 ± 16 nm, BPF7: 670 ± 12.5 nm) are positioned before each PMT to isolate the emission of Alexa Fluor 488, SYTOX Orange, and Alexa Fluor 647, respectively, minimizing spectral cross-talk between channels. Image acquisition and system control are performed via ThorImageLS software and an AlazarTech ATS9440 data acquisition card.

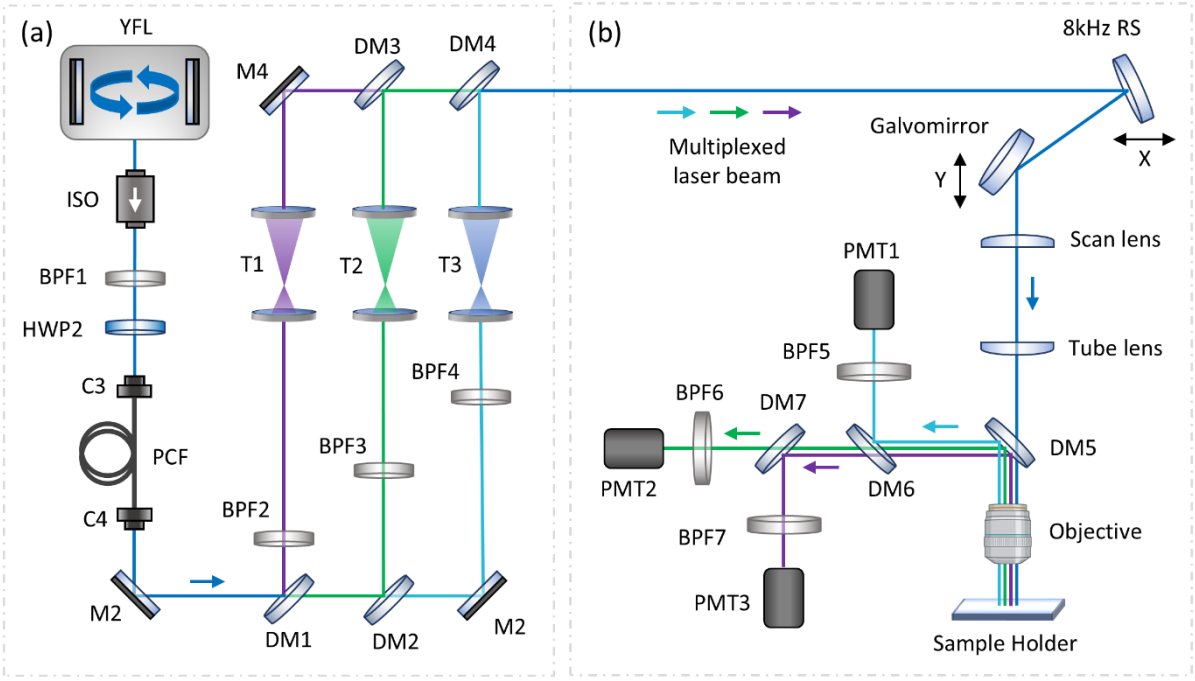

Figure 5.1: Overview of the three-color fiber-laser system and imaging setup. (a): Schematic of the nonlinear wavelength-conversion module driven by the high-power YFL. YFL: Ytterbium fiber laser, ISO: isolator, BPF: bandpass filter, HWP: half-wave plate, C: collimator, M: mirror, PCF: photonic crystal fiber, DM: dichroic mirror, T: telescope. (b) Experimental layout of the custom-built scanning microscope used for multiplexed three-color two-photon imaging. RS: resonant scanner, PMT: photomultiplier tube.

5.2 Numerical Design and Experimental Implementation

Building on the experimentally obtained ultrashort and energetic output pulses from the developed PCMA-based YFL driver (see Section 3.4), the subsequent numerical optimization focuses on broadband nonlinear spectral broadening in a PCF to achieve efficient multicolor pulse generation for CrM-2PM. The objective is to produce a supercontinuum featuring multiple, well-defined spectral peaks precisely aligned with the two-photon absorption bands of widely used fluorophores across the green to red spectral window. At the same time, the generated pulses must maintain sufficient peak power to drive strong two-photon excitation, requiring a clean temporal profile, sub-100 fs pulse duration, and adequate pulse energy per channel.

For this purpose, three target wavelength regions are identified around 950 nm, 1100 nm, and 1200 nm, which collectively cover a broad range of biologically relevant fluorophores while ensuring sufficient spectral separation to prevent channel cross-talk. The 950 nm band efficiently excites green-emitting fluorophores such as Alexa Fluor 488 and GFP, commonly used in GFP-transgenic mice for structural neural imaging without functional interference [213]. It also enables excitation of established calcium indicators including Fluo-4 and

jGCaMP6, supporting live-cell imaging of neuronal activity [81,214]. The 1100 nm region is well-suited for yellow-to-orange fluorophores such as YFP and SYTOX Orange, facilitating neuronal labeling and nuclear staining, as well as excitation of next-generation genetically encoded calcium indicators (GECIs) such as jYCaMP [60]. Finally, the 1200 nm spectral band is of growing significance for advanced functional imaging, overlapping with the two-photon absorption of red and far-red dyes including Alexa Fluor 647 and ATTO 647N, both essential for deep-tissue labeling and immunostaining [215]. Moreover, this spectral range coincides with the optimal two-photon excitation windows of recently developed far-red GECIs, such as FR-GECO1a and FR-GECO1c, which show peak brightness around 1110 nm and retain strong two-photon efficiency up to ~1200 nm [216]. It also supports high-speed voltage imaging using far-red genetically encoded voltage indicators (GEVIs) such as the rhodopsin-based Voltron2, which provides robust two-photon voltage-sensitive signals beyond 1100 nm, a range inaccessible to conventional Ti:Sa lasers [217].

To accurately reproduce the targeted spectral features and ensure precise control over the underlying nonlinear dynamics, the wavelength-conversion process in the PCF was modeled using the GNLSE-based numerical framework introduced in Chapter 2. As described there in great detail, the GNLSE accounts for the relevant dispersion and nonlinear effects governing SCG, including SPM, self-steepening, and SRS, with included higher-order dispersion terms. For efficient and controlled spectral broadening in the 900–1,200 nm range, the sub-50 fs, watt-level pulses from the PCMA were launched into a large-mode-area PCF with normal (positive) dispersion, which suppresses excessive nonlinear phase accumulation while promoting SPM-dominated spectral shaping with two symmetric side peaks as discussed in Section 2.3. The employed fiber (NKT Photonics PM-LMA-10) features a zero-dispersion wavelength near 1,300 nm (normal dispersion below), an effective mode-field diameter of $d_{eff} = 8.5\ \mu m$, a NA of 0.12 at 1,064 nm, and a nonlinear parameter of $\gamma = 3.5\ W^{-1}m^{-1}$. A complete set of simulation parameters is listed in Appendix Section 8.2.

Using the experimentally measured PCMA spectrum (see Fig.4.3) with an average power of 0.64 W (corresponding to a pulse energy of 21.8 nJ), the PCF output spectra were simulated for a range of pre-chirp values between -0.02 ps² and 0.02 ps². The resulting spectral evolution is summarized in the colormap of Fig.5.2 (a).

To identify the optimal conditions for efficient three-color generation, the integrated pulse energy within 50 nm spectral windows centered at 960 nm, 1080 nm, and 1175 nm was analyzed as a function of the applied pre-chirp, as shown in Fig.5.2 (b).

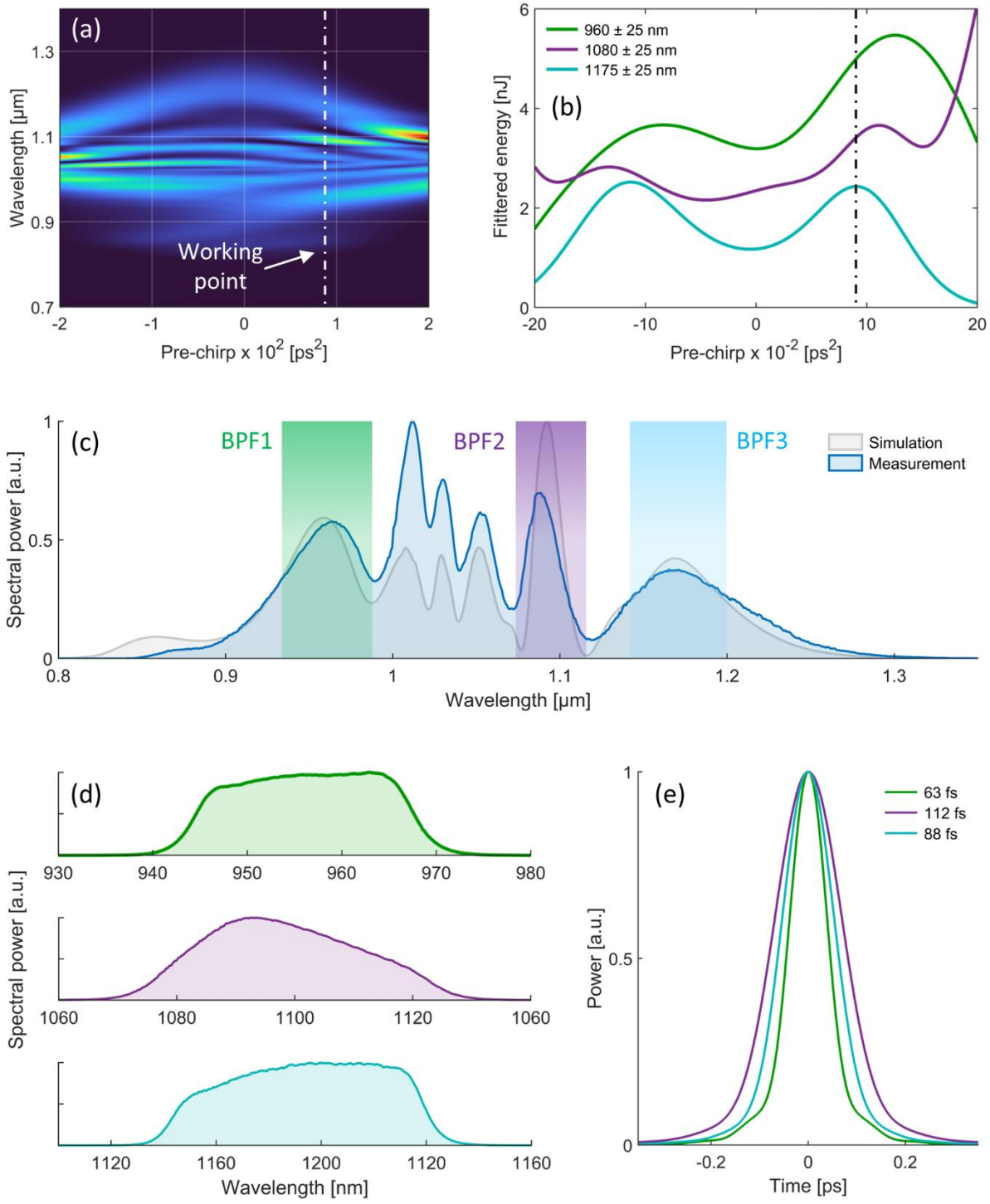

Figure 5.2: Numerical and experimental characterization of PCF-based three-color pulse generation. (a): Simulated output spectra after 20 mm of PCF for varying input pre-chirp values. (b) Corresponding pulse energies within 50 nm spectral windows centered at 960 nm, 1,080 nm, and 1,175 nm as a function, with indicated working point for balanced three-color generation. (c): Simulated spectrum at the working point compared to the measured spectrum with indicated BPF positions. (d): Measured output spectra after spectral filtering at 960 nm (green), 1080 nm (magenta), and 1175 nm (cyan). (e): Corresponding measured AC traces confirming ultrashort pulse durations (FWHM, assuming Gaussian pulse shape) of 63 fs (960 nm), 112 fs (1080 nm), and 88 fs (1175 nm).

A pre-chirp of approximately +0.09 ps² (corresponding to an input pulse duration of ~75 fs) provides the most balanced energy distribution across the three bands, yielding approximately 5.2 nJ at 960 nm, 3.5 nJ at 1080 nm, and 2.5 nJ at 1175 nm. The simulated output spectrum at this condition is shown in Fig.5.2 (c) alongside the experimentally measured spectrum obtained under equivalent parameters (0.64 W input power, ~66 fs pulse duration). In both cases, three well-defined peaks emerge at the target wavelengths, confirming excellent agreement between simulation and experiment.

Using appropriately selected dichroic mirrors in combination with the bandpass filters (BPFs) indicated in Fig.5.2 (c), i.e., 960 ± 25 nm (BPF1), 1080 ± 12.5 nm (BPF2), and 1175 ± 25 nm (BPF3), the three target spectral bands were separated according to the experimental layout shown in Fig.5.1. After accounting for the insertion losses of all optical components, including filters and telescopes, the measured pulse energies at the microscope input were 3.1 nJ at 960 nm, approximately 2.6 nJ at 1080 nm, and 2.8 nJ at 1175 nm. The corresponding filtered spectra are displayed in Fig.5.2 (d), while the autocorrelation traces in Fig.5.2 (e) confirm ultrashort pulse durations below 115 fs with clean temporal profiles across all three color-channels. This combination of high pulse energy, distinct spectral separation, and sub-115 fs pulse duration defines an optimal operating regime for efficient and versatile biomedical CrM-2PM applications.

5.3 Three-Color Two-Photon Imaging in Mouse Brain Tissue

To demonstrate the versatility of the simulation-guided fiber-laser platform for advanced biomedical imaging, three-color CrM-2PM was performed on triple-stained mouse hippocampal tissue. Neuronal cytoskeletons and astrocytes were visualized using antibodies against Microtubule-Associated Protein 2 (MAP2) and Glial Fibrillary Acidic Protein (GFAP), conjugated to Alexa Fluor 647 and Alexa Fluor 488, respectively, with efficient two-photon excitation at 1175 nm and 940 nm. MAP2 highlights the neuronal cytoskeleton, primarily labeling dendrites and axons, whereas GFAP selectively marks the intermediate filaments of astrocytic processes. A third imaging channel was introduced using the cell-impermeant nucleic acid stain SYTOX Orange (SO), which labels the nuclei of all cells within the tissue, including neurons, astrocytes, microglia, and endothelial cells, and is efficiently excited at 1080 nm via the central spectral lobe of the PCF-broadened output. The applied staining protocol was designed to enable comprehensive, high-resolution, and simultaneous visualization of neuronal (MAP2-positive), glial (GFAP-positive), and nuclear (SO-positive) components within a single imaging volume using the three-color output of the developed fiber-laser system. The ability to resolve these cellular

structures simultaneously provides an effective tool for neuroscientific studies requiring the correlated analysis of cellular morphology and interactions, such as investigations of neuro-glial coupling or the structural reorganization of hippocampal circuits in healthy and diseased brain states.

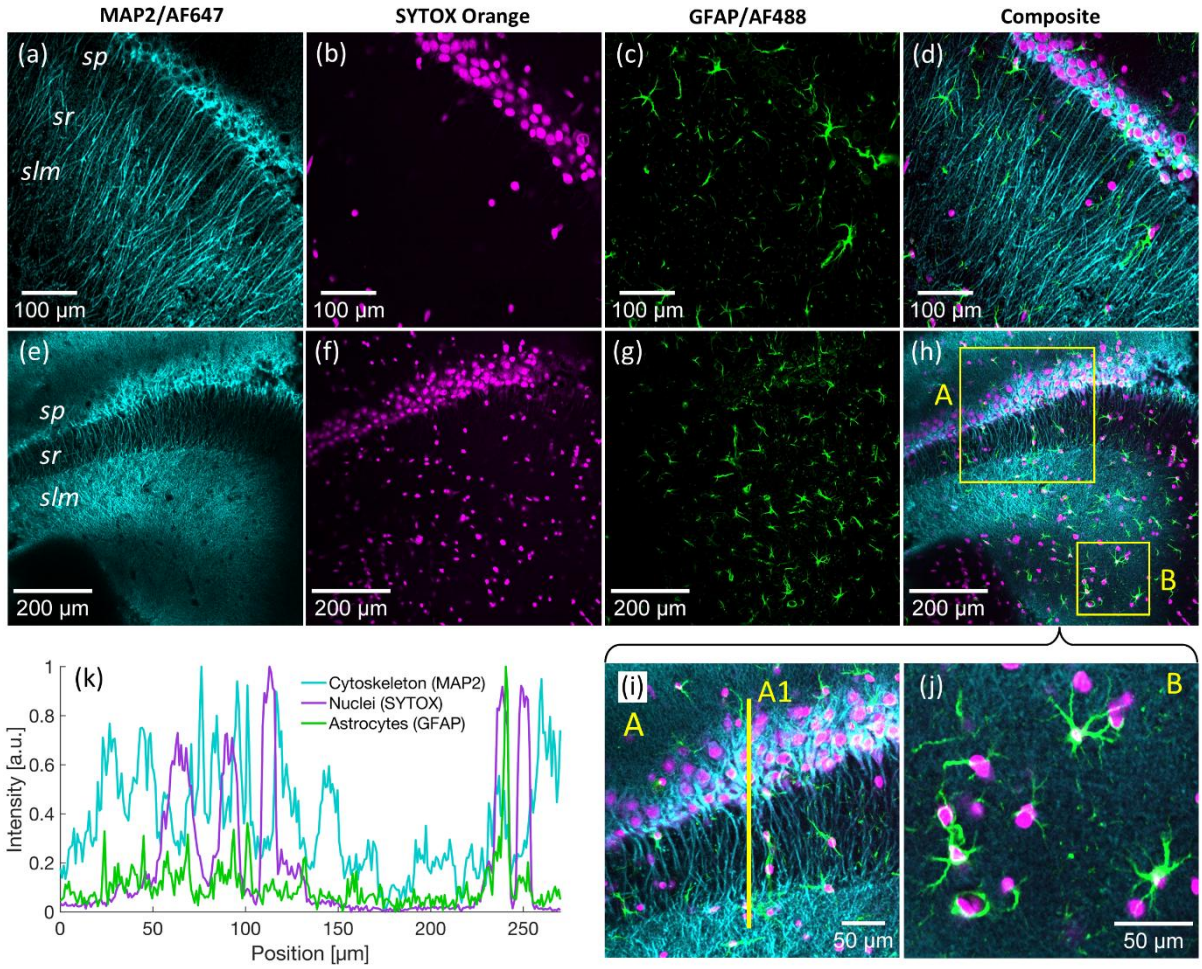

Figure 5.3: Multiplexed three-color two-photon imaging of the hippocampal region in triple-stained mouse brain tissue. (a-d): Single-channel fluorescence images of the hippocampal CA1 region showing AF647-labeled neuronal cytoskeletons (MAP2, cyan), SYTOX Orange-labeled nuclei (magenta), and AF488-labeled astrocytes (GFAP, green), together with the corresponding composite overlay. (e-h): Equivalent channel sequence acquired from the CA3 region, with highlighted regions of interest (ROIs A and B) marked in the composite image. (i): Magnified view of ROI A, illustrating the spatial arrangement and partial colocalization of astrocytes, neuronal nuclei, and MAP2-labeled dendritic processes. The yellow line (A1) indicates the position of the extracted fluorescence intensity profile. (j): Magnified view of ROI B, showing isolated astrocytes and neuronal nuclei within a less densely populated region. (k): Normalized fluorescence intensity profile along line A1, confirming well-separated and distinct signal distributions for all three fluorescent markers. *sp*, *sr*, and *slm* denote the *stratum pyramidale*, *stratum radiatum*, and *stratum lacunosum-moleculare*, respectively.

Imaging was performed in the CA1 region of the dorsal hippocampus, a structure critically involved in memory encoding, spatial navigation, and synaptic integration within the hippocampal network [218,219]. Details on the sample preparation and the animal handling are provided in the appendix, Section 8.3.2, of this dissertation. The optical power incident on the sample was maintained at 10 mW per color channel (corresponding to 0.33 nJ pulse energy) to ensure a high SNR and signal strength while minimizing photobleaching. Figures 5.3 (a-c) show the individual fluorescence channels recorded from the CA1 region, obtained by averaging three consecutive frames over a 751 × 751 µm² field of view (FOV) consisting of 818 × 818 pixels (0.918 µm/pixel). Figures 5.3 (e-g) present the corresponding channels acquired in a posterior CA1 region under identical imaging conditions within a 532 × 532 µm² FOV (580 × 580 pixels, 0.918 µm/pixel). The resulting composite images for both regions are shown in Figs.5.3 (d) and (h), respectively.

The displayed FOVs were extracted from the original image stacks of 940 × 940 µm² (1024 × 1024 pixels, 0.918 µm/pixel) and rescaled to 1024 × 1024 pixels for visualization using *ImageJ*. As illustrated, the combination of three-color laser excitation with the applied staining strategy enables clear and spectrally separated visualization of pyramidal neuronal cell bodies in the *stratum pyramidale* (sp) and their dendritic projections in the *stratum radiatum* (sr) (cyan). In addition, individual neuronal nuclei (magenta) and surrounding astrocytes (green) are distinctly resolved and spatially well separated within the imaged volumes.

In the composite image of the dorsal CA1 region shown in Fig.5.3 (h), two regions of interest (ROIs A and B) are highlighted and displayed in Figs.5.3 (i) and (j), respectively. ROI A corresponds to a 340 × 340 µm² sub-region (333 × 333 pixels, 0.918 µm/pixel) containing a densely packed pyramidal layer with strongly aligned neuronal somata, associated nuclei, and dendritic extensions. The surrounding astrocytes are clearly visualized between the neuronal structures, revealing their complementary spatial organization within the hippocampal architecture. ROI B, covering a less densely populated area (187 × 187 µm², 204 × 204 pixels, 0.918 µm/pixel), shows isolated astrocytes interspersed between sparsely distributed nuclei and neuronal fibers, highlighting the system's capability to resolve fine subcellular details and potentially also local interactions and dynamics across all three spectral channels.

To quantitatively evaluate the three-color imaging performance of the system, Fig.5.3 (k) shows the fluorescence intensity profile extracted along line A1 within ROI A (see Fig. 5.3 (i)). The profile reveals distinct spatial distributions corresponding to the three labeled structures: SYTOX Orange identifies densely packed neuronal soma as sharp peaks, MAP2 delineates sur-

rounding dendritic and axonal structures as broader intensity regions, and GFAP exhibits localized peaks adjacent to or between neuronal layers, consistent with the known spatial organization of astrocytes enveloping neuronal elements. The minimal overlap between channels and the high signal-to-background ratio confirm effective spectral separation, negligible cross-excitation, and robust target specificity, thereby validating the developed laser system's capability for simultaneous CrM-2PM imaging of multiple, spatially distinct cellular structures within complex brain tissue.

5.4 Three-Color Two-Photon Imaging in Mouse Kidney and Liver Tissue

To further demonstrate the versatility and broad applicability of the developed three-color fiber-laser system across different biological samples, three-color CrM-2PM was next applied to structurally labeled mouse liver and kidney tissues. The reference samples (FluoTissue, SunJin Lab) were mounted on prepared microchamber slides using the aqueous tissue-clearing agent RapiClear 1.52 (SunJin Lab) and stained with Alexa Fluor 488 and SYTOX Orange to label blood vessels and nuclei, respectively. In addition, anti-TUJ1 (anti-βIII-tubulin) antibodies conjugated with Alexa Fluor 647 were used to label neurons of the peripheral nervous system. Imaging was performed using the three-color fiber-laser system with an average optical power of ~10 mW per channel at the sample plane, ensuring strong two-photon fluorescence signals while avoiding photobleaching.

Figure 5.4 presents representative images of the triple-stained mouse liver and kidney tissue sections, acquired over a 940 × 940 μm² field of view (1024 × 1024 pixels at 0.918 μm/pixel) and averaged over three consecutive frames. In the liver tissue images shown in Figs.5.4 (a-d), individual fluorescence channels correspond to neuronal fibers (anti-TUJ1/AF647, cyan), nuclei (SYTOX Orange, magenta), and vasculature (AF488, green), with the merged composite in Fig.5.4 (d) illustrating the spatial organization of these structural components. Similarly, Figs.5.4 (e-h) show images of kidney tissue obtained using the same three-color excitation and detection scheme, with single-color channels presented in Figs.5.4 (e-g) and the combined composite image in Fig.5.4 (h).

Two magnified regions of interest (ROIs A and B) marked in Figs.5.4 (e) and (h) are shown in Figs.5.4 (i) and (j), respectively. ROI A, corresponding to a digitally enlarged 323 × 323 μm² field of view (352 × 352 pixels, 0.918 μm/pixel), reveals intricate nerve fiber networks, clearly demonstrating the ability of the system to resolve fine neuronal structures with high spatial fidelity. ROI B, shown as a digitally zoomed 330.5 × 330.5 μm² region (360 × 360 pixels, 0.918 μm/pixel), provides a detailed view of an individual glomerulus, where the spatial relationship

between vasculature, nuclei, and nerve fibers is distinctly visualized, highlighting the system's capacity for high-resolution, multi-channel imaging in densely structured tissue environments.

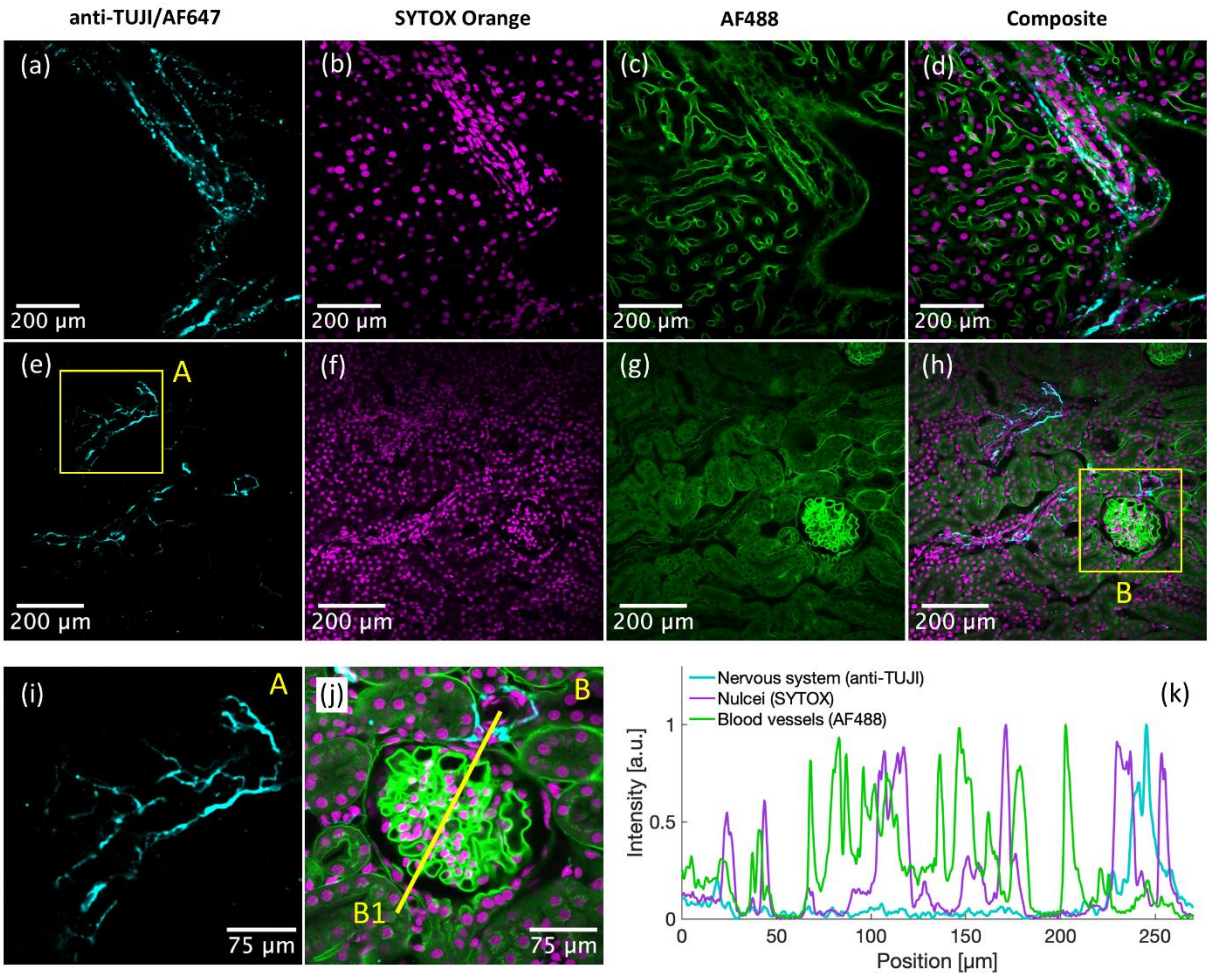

Figure 5.4: Multiplexed three-color two-photon imaging of triple-stained mouse liver and kidney tissues. (a-d): Single-channel fluorescence images of mouse liver tissue showing AF647-labeled peripheral nerve fibers (anti-TUJ1, cyan), SYTOX Orange–labeled nuclei (magenta), and AF488-labeled blood vessels (green), together with the corresponding composite overlay. (e-h): Equivalent channel sequence acquired from mouse kidney tissue, with marked regions of interest (ROIs A and B) in the anti-TUJ1 and composite images, respectively. (i): Magnified view of ROI A, illustrating the clear visualization of fine neuronal projections. (j): Magnified view of ROI B, highlighting an isolated glomerulus with spatially resolved vasculature, nuclei, and associated nerve fibers. The yellow line (B1) indicates the position of the extracted fluorescence intensity profile. (k): Normalized fluorescence intensity along line B1, demonstrating distinct and well-separated signal peaks for all three fluorophore channels.

To quantitatively analyze the spatial distribution of the labeled components, Fig.5.4 (k) shows the fluorescence intensity profile extracted along the yellow line B1 in Fig.5.4 (j), corresponding to ROI B. The profile reveals well-separated intensity peaks associated with the three fluorophore channels, analogous to the performance observed in the hippocampal imaging experiments. The minimal spectral overlap and high contrast confirm the system's excellent

spectral separation, sensitivity, and channel specificity, enabling clear differentiation of anatomical structures *in situ* across multiple tissue types.

In summary, this chapter presents the development and experimental validation of a compact, simulation-guided ultrafast fiber-laser system capable of efficient three-color two-photon excitation through tailored nonlinear spectral broadening in a PCF. By numerically engineering both the spectral shaping dynamics, three spectrally distinct, temporally synchronized, and energetically balanced ultrashort pulses were generated at 960 nm, 1080 nm, and 1175 nm, each providing pulse energies above 2.5 nJ and durations below 115 fs. These parameters are ideally suited for high-contrast, multichannel two-photon microscopy.

The resulting turnkey fiber-based laser platform enables simultaneous and spectrally isolated excitation of multiple fluorophores without requiring multiple laser sources, parametric conversion stages, or active wavelength tuning. Experimental demonstrations in triple-stained mouse brain, kidney, and liver tissues confirmed the system's capability to resolve neuronal, glial, vascular, and nuclear structures with high spatial resolution and minimal spectral crosstalk, underscoring its robustness and versatility.

Overall, the presented work establishes a powerful and scalable fiber-laser platform for multiplexed multicolor two-photon microscopy, offering a practical and cost-efficient alternative to traditional multi-laser or Ti:Sa-based solutions. Its demonstrated flexibility and imaging performance highlight its potential impact across a broad range of biomedical applications, including neuroscience, cancer research, and systems biology, marking an important step toward the widespread adoption of fiber-optic multicolor laser systems in advanced optical imaging.

5.5 Towards *in vivo* Alzheimer's drug screening in transgenic *C. Elegans*

To explore the applicability of the developed three-color fiber-laser system in living model organisms in the context of Alzheimer-related screening assays, preliminary in vivo two-photon imaging experiments were performed in transgenic *Caenorhabditis elegans* [220,221]. This work is embedded within an ongoing interdisciplinary seed-grant (PIER Seed Projects 2025) aimed at implementing a multicolor, high-throughput 2PM platform for quantifying the formation and dynamics of Alzheimer's disease-associated protein condensates *in vivo*.

Tau protein is a microtubule-associated protein that, under pathological conditions, undergoes liquid-liquid phase separation and subsequent aggregation into neurofibrillary tangles, representing a hallmark of Alzheimer's disease and strongly correlates with synaptic dysfunction,

neuronal loss, and cognitive decline [222–224]. Increasing evidence suggests that tau condensates form early in the disease cascade, prior to the appearance of aggregates, and may constitute a key intermediate state linking molecular-scale misfolding to cellular toxicity [225–227].

In this ongoing experiment, *C. elegans* strains are engineered to express human tau protein in defined neuronal populations, enabling direct visualization of these early condensation and aggregation processes within an intact organism [228]. To increase the information density and biological contextualization of these readouts, multicolor fluorescent labeling will be employed to map tau aggregates relative to additional protein markers that may undergo co-condensation, as well as to structural components such as the neuronal cytoskeleton or surrounding tissue morphology. Ideally, this should allow the aggregation state of tau to be traced over time in the context of local cellular architecture, potential interaction partners, and organism-wide physiological state. The developed multicolor 2PM platform is chosen for these studies due to its intrinsic optical sectioning capability, minimal out-of-focus fluorescence, and high imaging fidelity across the full spatial extent of the worm, all of which are essential for detecting and tracing small, spatially confined tau condensates at the earliest possible stages [32,57,204].

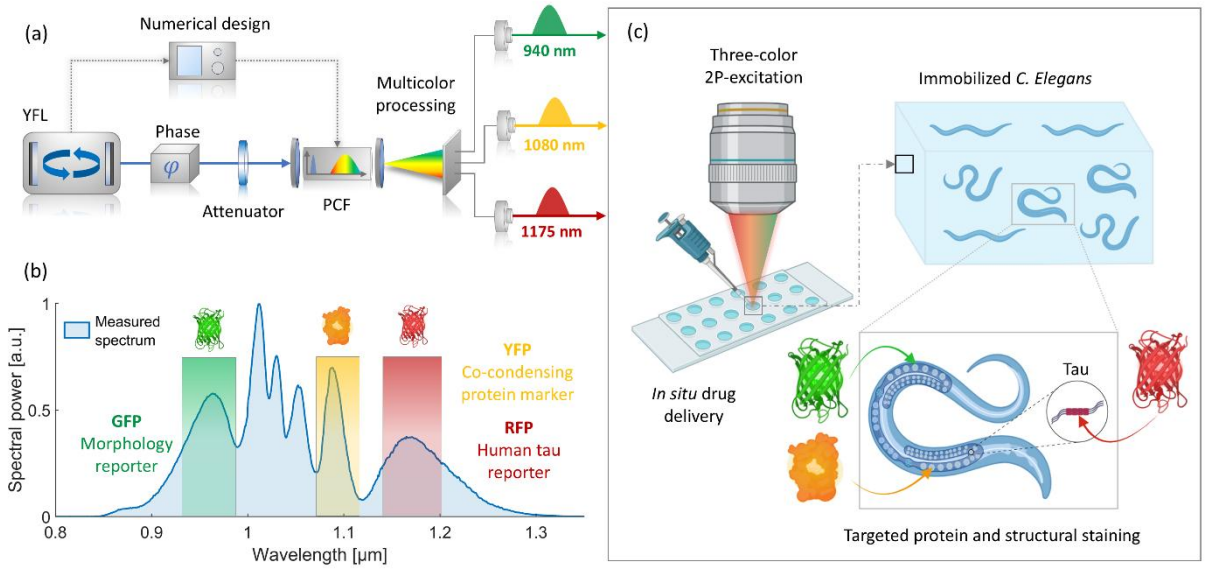

Figure 5.5: Schematic overview of the three-color excitation platform and its application to *in vivo C. elegans* imaging. (a): Three-color femtosecond pulse generation: a YFL is phase- and power-conditioned and spectrally broadened in a PCF, yielding synchronized excitation bands at 940, 1080, and 1175 nm as shown in Fig.5.2. (b): Measured output spectrum with representative excitation windows for GFP (morphology reporter), YFP (co-condensing protein marker), and RFP-tagged human tau. (c): Experimental concept for three-color two-photon imaging of immobilized *C. elegans*, enabling targeted protein and structural staining and supporting *in situ* drug delivery. The multicolor scheme permits simultaneous visualization of morphology, co-condensing proteins, and human tau condensates within the intact organism.

To illustrate the experimental workflow and underlying metrology, Fig.5.5 summarizes the complete three-color imaging strategy used for the preliminary *C. elegans* experiments. Figure 5.5 (a) outlines the routing and spectral separation of the three excitation bands generated by the fiber-laser system introduced in Chapter 5.1, highlighting their delivery into the microscope for simultaneous multicolor excitation at 940 nm, 1080 nm, and 1175 nm. The measured output spectrum together with representative excitation windows for GFP-based morphology reporters, YFP-labeled co-condensing proteins, and RFP-tagged human tau is shown in Fig.5.5 (b), illustrating the spectral assignment underlying the multiparametric fluorescence readout. The *in vivo* imaging workflow (Fig.5.5 (c)), includes the three-color two-photon excitation geometry, the chemical immobilization and targeted staining of transgenic *C. elegans*, and the optional *in situ* drug-delivery configuration for perturbation studies. Together, these elements provide a concise overview of the optical implementation, spectral targeting strategy, and biological context of the preliminary multicolor *C. elegans* imaging assay.

With this optical and biological framework established, preliminary *in vivo* imaging experiments in transgenic *C. elegans* were performed as initial step of the project to evaluate signal stability, multicolor excitation feasibility, and the robustness of GFP-based morphological tracking under native locomotion with excitation using the output band at 950 nm. Figure 5.6 summarizes the workflow and key locomotion-related metrics extracted from these datasets.

Figures 5.6 (a) and (b) show the extracted trajectories of a slow-moving and a fast-moving worm, respectively. Each trajectory represents the time-stamped centroid position (x_i, y_i) obtained from the fluorescence images, after segmentation of the worm body, skeletonization, and frame-to-frame selection of a stable tracking point under a maximum-jump constraint [229,230]. The positions were converted to physical units using a calibrated pixel size and FOV (1024x1024 pixels, 0.72 µm/pixel) and smoothed across a five-frame window. For visualization, each position is color-coded by its absolute time stamp, using the continuous 25-s colormap shown at the top of the figure. The slow worm shows a smooth, low-amplitude undulatory trajectory with limited net displacement (Fig.5.6 (a)), whereas the fast worm displays large and frequent movement with strong curvature and rapid accelerations (Fig.5.6 (b)).

The resulting cumulative path lengths are plotted in Fig.5.6 (c). The contrast between the two behavioral regimes is pronounced: over the 25-s recording, the slow worm travels only a few hundred micrometers, whereas the fast worm exceeds 2 mm of net path length, with a nearly linear increase in time. These distinct locomotor signatures demonstrate that the multicolor imaging platform and processing workflow can faithfully capture subtle kinematic differences, a prerequisite for quantitative phenotyping in the planned Alzheimer-related drug-

screening assays. Moreover, the same numerical framework readily extends to tracing the spatial evolution of fluorescently labeled protein aggregates, such as RFP- or YFP-tagged tau species, providing a unified analytical basis for both behavioral and molecular readouts.

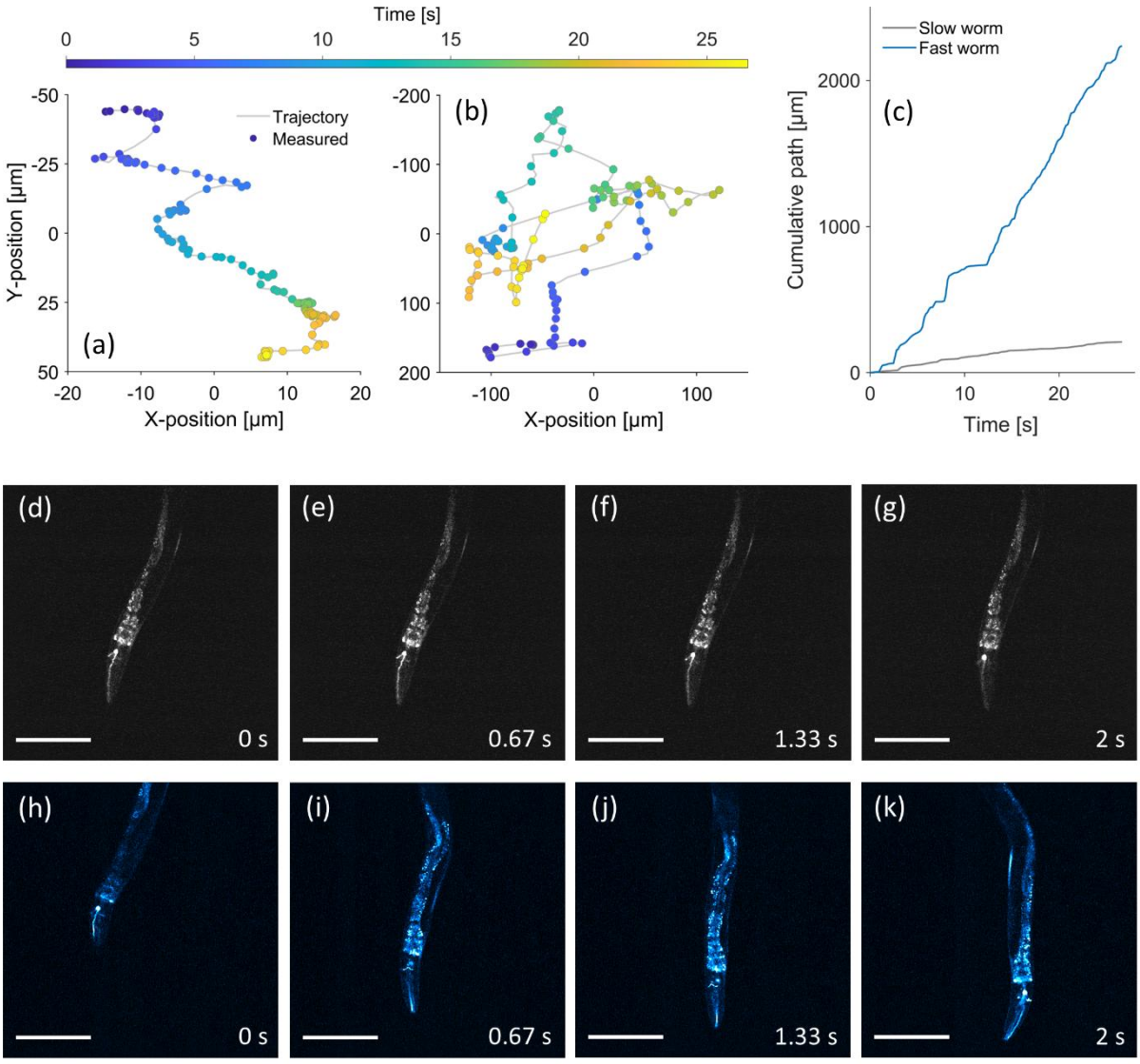

Figure 5.6: Quantitative locomotion tracking and time-resolved GFP imaging of slow and fast *C. elegans*. (a,b): Time-coded centroid trajectories of a slow (a) and fast (b) GFP-expressing worm extracted from two-photon image sequences. Positions were obtained by segmentation, skeletonization, and maximum-jump-constrained tracking, and are shown in physical units and color-coded by recording time (top bar). (c): Cumulative path length recorded over the full 25-s window, highlighting the pronounced difference in locomotor activity: the slow worm travels only a few hundred micrometers, whereas the fast worm exceeds 2 mm. (d-g): Four representative frames (1024x1024 pixels, 0.72 µm/pixel) of the slow worm over a 2-s interval, demonstrating stable morphological contrast and consistent body definition during movement. (h-k): Corresponding frames for the fast worm. Despite rapid displacement and posture changes, structural features remain well resolved, enabling robust tracking. Scale bars: 200 µm.

5.6 Multicolor 2PM Platform: Summary and Discussion

In summary, this chapter demonstrates a compact, simulation-guided ultrafast fiber-laser platform enabling efficient chromatically multiplexed two-photon microscopy through tailored nonlinear spectral broadening in photonic crystal fibers. Building on the low-noise, high-energy Yb-fiber laser foundation introduced in Chapter 4, controlled nonlinear dynamics were exploited to generate three spectrally distinct, temporally synchronized, and energetically balanced ultrashort pulse trains centered at 960 nm, 1080 nm, and 1175 nm. Each channel delivered pulse energies exceeding 2.5 nJ with pulse durations below 115 fs, meeting the stringent requirements for high-contrast multichannel two-photon excitation.

The resulting integrated 2PM platform enables simultaneous and spectrally isolated excitation of multiple fluorophores without the need for multiple synchronized laser sources, parametric conversion stages, or active wavelength tuning. Multicolor imaging experiments in triple-labeled mouse brain, kidney, and liver tissue confirmed robust excitation of neuronal, glial, vascular, and nuclear structures with minimal spectral cross-talk and high spatial resolution, validating the platform's suitability for complex, multi-labeled biological samples.

As a final pilot demonstration of *in vivo* compatibility, the platform was applied in preliminary two-photon imaging experiments in transgenic *Caenorhabditis elegans*. Here, GFP-based 2PM was used to validate signal stability under organismal motion and to establish quantitative tracking of organism-level dynamics, including locomotion behavior. While multicolor excitation *in vivo* remains ongoing work, these experiments primarily serve to verify the experimental robustness, motion tolerance, and analysis workflow required for future high-content *in vivo* assays combining chromatically multiplexed excitation with fluorescence-based readout of disease-relevant protein markers, including early aggregation and condensation processes associated with tau-related Alzheimer's disease models.

In the context of this dissertation, the three-color excitation platform constitutes a complementary realization of the unified photonic framework for advanced two-photon microscopy, extending the wavelength-agile deep-tissue excitation approach of Chapter 4 toward parallel, multi-target imaging at both tissue and whole-organism scales. Together, these results establish simulation-guided spectral engineering in photonic crystal fibers as a deterministic and scalable route to compact, low-noise multicolor excitation sources when driven by energetic, dispersion-engineered Yb-fiber lasers, directly addressing key performance requirements of advanced multiphoton microscopy.

6 Conclusion and Outlook

Ultrafast fiber lasers have evolved into highly capable platforms for nonlinear optics, advanced microscopy, and precision measurement, yet achieving simultaneous control over noise, spectral flexibility, and pulse energy to address complex biomedical imaging applications remains a central challenge in the field. This dissertation develops a cohesive photonic framework that addresses these requirements through a combination of theoretical modeling, fiber-laser engineering, nonlinear spectral design, and biological imaging validation. In doing so, this work advances the state-of-the-art of the underlying fiber-optic technologies across multiple performance dimensions, including intensity noise and timing stability, wavelength tunability, multicolor waveform generation, and nonlinear conversion efficiency, resulting in compact, robust, and highly versatile excitation sources for next-generation multiphoton microscopy.

A first major achievement lies in the development and advancement of environmentally stable, all-PM mode-locked oscillators and their integration with interferometric noise-suppression mechanisms. Through birefringence-engineered XPM reduction, phase-biased nonlinear interferometry, and optimized cavity dispersion, these systems achieve quantum-limited RIN across broad spectral regions, reduced timing jitter, and enhanced spectral purity, properties that are essential for ensuring coherence and reproducibility in downstream nonlinear processes. Together with energy-scalable amplifier architectures, these oscillators form a robust platform for high-power, low-noise femtosecond pulse generation.

Building on these foundations, the dissertation introduces several nonlinear spectral-engineering strategies that extend the accessible wavelength range far beyond the native Yb:fiber gain bandwidth. These include highly efficient dispersive-wave generation in PCFs, interferometric noise-reshaping for ultra-low-noise supercontinuum generation, and computationally guided multi-band spectral shaping for passively synchronized three-color excitation. The resulting systems deliver sub-100 fs pulses with nanojoule-level energies across widely tunable spectral bands, enabling tailored excitation of diverse fluorophores while maintaining low noise and compact, alignment-free operation.

The biological imaging demonstrations presented in Chapter 5 highlight the direct impact of these photonic technologies on the performance of advanced multiphoton microscopy. Deep-tissue two-photon imaging using dispersive-wave sources achieves high contrast and subcellular resolution at depths exceeding 600 µm, while multi-channel imaging using the three-color platform enables simultaneous visualization of neuronal structures, nuclei, and astrocytes with excellent spectral separation and minimal cross-talk. These results underscore the translational

potential of engineered fiber-laser sources for neuroscience, pathology, developmental biology, and other domains that require high-resolution imaging in complex or scattering media.

The photonic architectures developed in this dissertation open several promising directions for future research:

a) Deep-Tissue Functional Neuroimaging

The combination of ultra-low-noise Yb oscillators, the tunable DW generator, and the three-color conversion platform provides a foundation for next-generation deep-tissue two-photon imaging. Building on the demonstrated penetration depths in *ex vivo* tissue, future directions could include:

- *In vivo* cortical and hippocampal imaging between 950-1250 nm with reduced phototoxicity (enabled by low RIN and stable, energetic multi-color excitation)
- Large-volume population imaging in scattering brain regions using color-multiplexed excitation
- Fast functional mapping in deep layers (CA1, CA3, dentate gyrus) using optimized DW excitation at 880 - 950 nm
- Motion-robust deep imaging when combined with adaptive optics, resonant scanning, and pixel-clock synchronization

Together, these avenues exploit the stability, spectral matching, and multi-band pulse delivery established in this dissertation.

b) Functional and Hyperspectral Biomedical Two-Photon Microscopy

The three-color architecture, interferometric dual-color SHG source, and numerical spectral-design framework create new pathways for *functional*, *hyperspectral*, and *multi-channel* 2PM without the requirement for multiple, individually synchronized femtosecond laser systems. Future applications could include:

- Simultaneous functional imaging with multiple indicators (e.g., Ca^{2+} + glutamate + structural/morphological channels)
- Hyperspectral excitation sweeps for in vivo characterization of fluorescent protein dynamics
- Triple-band or phase-encoded functional imaging, using synchronized colors (940/1080/1175 nm)
- Spatially multiplexed functional imaging, where different tissue regions or cell-types are excited with different bands

c) Low-Noise Supercontinuum Platforms for Metrology and Coherent Imaging

The thesis introduced interferometric input conditioning for SCG and validated it through dual-color SQL-limited sources and a stochastic NLI+GNLSE model. This enables several future SCG-based technologies:

- Ultra-low noise SCG modules for coherent Raman, SRS, and multiphoton contrast
- Broadband frequency combs with reduced RIN and enhanced long-term performance
- Dual-comb spectroscopy using interferometrically stabilized SCG bands
- Ultra-stable white-light continua for coherent imaging in scattering tissue

These applications leverage one of the dissertation's key insights: temporal noise shaping via NLI-dynamics can directly influence octave-spanning RIN distributions.

d) Extension to Mid-IR and UV Spectral Regions

The stochastic GNLSE framework, dispersion-engineered DW design, and interferometric noise control established in this dissertation can be transferred to fluoride, chalcogenide, and hollow-core platforms. This could open new routes toward:

- Mid-IR label-free vibrational microscopy (CH stretch, amide bands, lipid contrast)
- Mid-IR supercontinuum sources for deep brain and pathology imaging
- UV multiphoton microscopy targeting intrinsic fluorophores (NADH, FAD, collagen, elastin)
- UV-VIS multi-color sources coupled to genetically encoded metabolic sensors
- **Hybrid mid-IR / NIR excitation for combined structural and chemical contrast.**

These directions extend the spectral reach of the fiber-based architectures developed here far beyond the gain bandwidths of available laser materials.

Overall, this dissertation establishes a unified and experimentally validated photonic toolbox that combines ultrafast fiber-laser engineering, nonlinear spectral control, and advanced imaging applications. The demonstrated performance and versatility highlight strong potential for further technological advancement and broad scientific impact across ultrafast optics, biophotonics, neuroscience, and precision measurement.

7 References

1. L. Fenno, O. Yizhar, and K. Deisseroth, "The Development and Application of Optogenetics," Annu. Rev. Neurosci. **34**, 389–412 (2011).
2. N. G. Horton, K. Wang, D. Kobat, C. G. Clark, F. W. Wise, C. B. Schaffer, and C. Xu, "In vivo three-photon microscopy of subcortical structures within an intact mouse brain," Nature Photon **7**, 205–209 (2013).
3. E. H. K. Stelzer, "Light-sheet fluorescence microscopy for quantitative biology," Nat Methods **12**, 23–26 (2015).
4. E. Moen, D. Bannon, T. Kudo, W. Graf, M. Covert, and D. Van Valen, "Deep learning for cellular image analysis," Nat Methods **16**, 1233–1246 (2019).
5. J. Jumper, R. Evans, A. Pritzel, T. Green, M. Figurnov, O. Ronneberger, K. Tunyasuvunakool, R. Bates, A. Žídek, A. Potapenko, A. Bridgland, C. Meyer, S. A. A. Kohl, A. J. Ballard, A. Cowie, B. Romera-Paredes, S. Nikolov, R. Jain, J. Adler, T. Back, S. Petersen, D. Reiman, E. Clancy, M. Zielinski, M. Steinegger, M. Pacholska, T. Berghammer, S. Bodenstein, D. Silver, O. Vinyals, A. W. Senior, K. Kavukcuoglu, P. Kohli, and D. Hassabis, "Highly accurate protein structure prediction with AlphaFold," Nature **596**, 583–589 (2021).
6. H. Wang, Y. Rivenson, Y. Jin, Z. Wei, R. Gao, H. Günaydın, L. A. Bentolila, C. Kural, and A. Ozcan, "Deep learning enables cross-modality super-resolution in fluorescence microscopy," Nat Methods **16**, 103–110 (2019).
7. M. Chalfie, Y. Tu, G. Euskirchen, W. W. Ward, and D. C. Prasher, "Green Fluorescent Protein as a Marker for Gene Expression," Science **263**, 802–805 (1994).
8. M. Jinek, K. Chylinski, I. Fonfara, M. Hauer, J. A. Doudna, and E. Charpentier, "A Programmable Dual-RNA–Guided DNA Endonuclease in Adaptive Bacterial Immunity," Science **337**, 816–821 (2012).
9. A. Mortazavi, B. A. Williams, K. McCue, L. Schaeffer, and B. Wold, "Mapping and quantifying mammalian transcriptomes by RNA-Seq," Nat Methods **5**, 621–628 (2008).
10. A. Rossi, K. Berger, H. Chen, D. Leslie, R. B. Mailman, and X. Huang, "Projection of the prevalence of Parkinson's disease in the coming decades: Revisited," Movement Disorders **33**, 156–159 (2018).
11. M. Prince, R. Bryce, E. Albanese, A. Wimo, W. Ribeiro, and C. P. Ferri, "The global prevalence of dementia: A systematic review and metaanalysis," Alzheimer's & Dementia **9**, 63 (2013).
12. R. Brookmeyer, E. Johnson, K. Ziegler-Graham, and H. M. Arrighi, "Forecasting the global burden of Alzheimer's disease," Alzheimer's & Dementia **3**, 186–191 (2007).
13. F. Bray, M. Laversanne, H. Sung, J. Ferlay, R. L. Siegel, I. Soerjomataram, and A. Jemal, "Global cancer statistics 2022: GLOBOCAN estimates of incidence and mortality worldwide for 36 cancers in 185 countries," CA A Cancer J Clinicians **74**, 229–263 (2024).
14. W. R. Zipfel, R. M. Williams, and W. W. Webb, "Nonlinear magic: multiphoton microscopy in the biosciences," Nat Biotechnol **21**, 1369–1377 (2003).
15. T. L. Whiteside, "The tumor microenvironment and its role in promoting tumor growth," Oncogene **27**, 5904–5912 (2008).
16. P. Beard, "Biomedical photoacoustic imaging," Interface Focus. **1**, 602–631 (2011).
17. R. Weissleder and M. J. Pittet, "Imaging in the era of molecular oncology," Nature **452**, 580–589 (2008).
18. J. G. Fujimoto, C. Pitris, S. A. Boppart, and M. E. Brezinski, "Optical Coherence Tomography: An Emerging Technology for Biomedical Imaging and Optical Biopsy," Neoplasia **2**, 9–25 (2000).
19. S. W. Hell and J. Wichmann, "Breaking the diffraction resolution limit by stimulated emission: stimulated-emission-depletion fluorescence microscopy," Opt. Lett. **19**, 780 (1994).

20. W. Kühlbrandt, "The Resolution Revolution," Science **343**, 1443–1444 (2014).
21. O. Shimomura, F. H. Johnson, and Y. Saiga, "Extraction, Purification and Properties of Aequorin, a Bioluminescent Protein from the Luminous Hydromedusan, *Aequorea*," J. Cell. Comp. Physiol. **59**, 223–239 (1962).
22. R. Y. Tsien, "THE GREEN FLUORESCENT PROTEIN," Annu. Rev. Biochem. **67**, 509–544 (1998).
23. J. C. Gore, "Principles and practice of functional MRI of the human brain," J. Clin. Invest. **112**, 4–9 (2003).
24. D. Huang, E. A. Swanson, C. P. Lin, J. S. Schuman, W. G. Stinson, W. Chang, M. R. Hee, T. Flotte, K. Gregory, C. A. Puliafito, and J. G. Fujimoto, "Optical Coherence Tomography," Science **254**, 1178–1181 (1991).
25. J. W. Lichtman and J.-A. Conchello, "Fluorescence microscopy," Nat Methods **2**, 910–919 (2005).
26. Q. Pian, C. Wang, X. Chen, J. Liang, L. Zhao, G. Wang, and X. Intes, "Multimodal Biomedical Optical Imaging Review: Towards Comprehensive Investigation of Biological Tissues," CMI **3**, 72–87 (2015).
27. D. Razansky, J. Klohs, and R. Ni, "Multi-scale optoacoustic molecular imaging of brain diseases," Eur J Nucl Med Mol Imaging **48**, 4152–4170 (2021).
28. K. Svoboda and R. Yasuda, "Principles of Two-Photon Excitation Microscopy and Its Applications to Neuroscience," Neuron **50**, 823–839 (2006).
29. J. M. Squirrell, D. L. Wokosin, J. G. White, and B. D. Bavister, "Long-term two-photon fluorescence imaging of mammalian embryos without compromising viability," Nat Biotechnol **17**, 763–767 (1999).
30. S. W. Perry, R. M. Burke, and E. B. Brown, "Two-Photon and Second Harmonic Microscopy in Clinical and Translational Cancer Research," Ann Biomed Eng **40**, 277–291 (2012).
31. M. Göppert-Mayer, "Über Elementarakte mit zwei Quantensprüngen," Annalen der Physik **401**, 273–294 (1931).
32. F. Helmchen and W. Denk, "Deep tissue two-photon microscopy," Nat Methods **2**, 932–940 (2005).
33. S. L. Jacques, "Optical properties of biological tissues: a review," Phys. Med. Biol. **58**, R37–R61 (2013).
34. A. M. Smith, M. C. Mancini, and S. Nie, "Second window for in vivo imaging," Nature Nanotech **4**, 710–711 (2009).
35. M. Li, F. Liu, H. Jiang, T. S. Lee, and S. Tang, "Long-Term Two-Photon Imaging in Awake Macaque Monkey," Neuron **93**, 1049-1057.e3 (2017).
36. C. Stosiek, O. Garaschuk, K. Holthoff, and A. Konnerth, "*In vivo* two-photon calcium imaging of neuronal networks," Proc. Natl. Acad. Sci. U.S.A. **100**, 7319–7324 (2003).
37. J. B. Pawley, ed., *Handbook Of Biological Confocal Microscopy* (Springer US, 2006).
38. P. Theer and W. Denk, "On the fundamental imaging-depth limit in two-photon microscopy," J. Opt. Soc. Am. A **23**, 3139 (2006).
39. D. Débarre, W. Supatto, A.-M. Pena, A. Fabre, T. Tordjmann, L. Combettes, M.-C. Schanne-Klein, and E. Beaurepaire, "Imaging lipid bodies in cells and tissues using third-harmonic generation microscopy," Nat Methods **3**, 47–53 (2006).
40. P. J. Campagnola and C. -Y. Dong, "Second harmonic generation microscopy: principles and applications to disease diagnosis," Laser & Photonics Reviews **5**, 13–26 (2011).
41. X. Chen, O. Nadiarynkh, S. Plotnikov, and P. J. Campagnola, "Second harmonic generation microscopy for quantitative analysis of collagen fibrillar structure," Nat Protoc **7**, 654–669 (2012).
42. N. T. Shaked, S. A. Boppart, L. V. Wang, and J. Popp, "Label-free biomedical optical imaging," Nat. Photon. **17**, 1031–1041 (2023).

43. R. Prakash, O. Yizhar, B. Grewe, C. Ramakrishnan, N. Wang, I. Goshen, A. M. Packer, D. S. Peterka, R. Yuste, M. J. Schnitzer, and K. Deisseroth, "Two-photon optogenetic toolbox for fast inhibition, excitation and bistable modulation," Nat Methods **9**, 1171–1179 (2012).
44. S. Weisenburger and A. Vaziri, "A Guide to Emerging Technologies for Large-Scale and Whole-Brain Optical Imaging of Neuronal Activity," Annu. Rev. Neurosci. **41**, 431–452 (2018).
45. T. Imamura, T. Saitou, and R. Kawakami, "In vivo optical imaging of cancer cell function and tumor microenvironment," Cancer Science **109**, 912–918 (2018).
46. K. McDole, Y. Xiong, P. A. Iglesias, and Y. Zheng, "Lineage mapping the pre-implantation mouse embryo by two-photon microscopy, new insights into the segregation of cell fates," Developmental Biology **355**, 239–249 (2011).
47. M. Drobizhev, N. S. Makarov, S. E. Tillo, T. E. Hughes, and A. Rebane, "Two-photon absorption properties of fluorescent proteins," Nat Methods **8**, 393–399 (2011).
48. M. Yildirim, H. Sugihara, P. T. C. So, and M. Sur, "Functional imaging of visual cortical layers and subplate in awake mice with optimized three-photon microscopy," Nat Commun **10**, 177 (2019).
49. T. Wang and C. Xu, "Three-photon neuronal imaging in deep mouse brain," Optica **7**, 947 (2020).
50. T. H. Maiman, "Stimulated Optical Radiation in Ruby," Nature **187**, 493–494 (1960).
51. A. J. DeMaria, C. M. Ferrar, and G. E. Danielson, "MODE LOCKING OF A Nd3+-DOPED GLASS LASER," Applied Physics Letters **8**, 22–24 (1966).
52. W. Denk, J. H. Strickler, and W. W. Webb, "Two-Photon Laser Scanning Fluorescence Microscopy," Science **248**, 73–76 (1990).
53. T. W. Hänsch, "Nobel Lecture: Passion for precision," Rev. Mod. Phys. **78**, 1297–1309 (2006).
54. A. L'Huillier, "Nobel Lecture: The route to attosecond pulses," Rev. Mod. Phys. **96**, 030503 (2024).
55. F. Krausz and M. Ivanov, "Attosecond physics," Rev. Mod. Phys. **81**, 163–234 (2009).
56. M. Rubart, "Two-Photon Microscopy of Cells and Tissue," Circulation Research **95**, 1154–1166 (2004).
57. P. T. C. So, C. Y. Dong, B. R. Masters, and K. M. Berland, "Two-Photon Excitation Fluorescence Microscopy," Annu. Rev. Biomed. Eng. **2**, 399–429 (2000).
58. C. Xu and F. W. Wise, "Recent advances in fibre lasers for nonlinear microscopy," Nature Photon **7**, 875–882 (2013).
59. R. Dalangin, B. Z. Jia, Y. Qi, A. Aggarwal, K. Sakoi, M. Drobizhev, R. S. Molina, R. Patel, A. S. Abdelfattah, J. Zheng, D. Reep, J. P. Hasseman, The GENIE Project Team, G. Tsegaye, A. Tsang, G. C. Turner, Y. Zhao, J. Wu, K. Podgorski, A. G. Tebo, E. R. Schreiter, T. E. Hughes, T. Terai, M.-E. Paquet, S. G. Megason, A. E. Cohen, Y. Shen, and R. E. Campbell, "Far-red fluorescent genetically encoded calcium ion indicators," Nat Commun **16**, 3318 (2025).
60. M. A. Mohr, D. Bushey, A. Aggarwal, J. S. Marvin, J. J. Kim, E. J. Marquez, Y. Liang, R. Patel, J. J. Macklin, C.-Y. Lee, A. Tsang, G. Tsegaye, A. M. Ahrens, J. L. Chen, D. S. Kim, A. M. Wong, L. L. Looger, E. R. Schreiter, and K. Podgorski, "jYCaMP: an optimized calcium indicator for two-photon imaging at fiber laser wavelengths," Nat Methods **17**, 694–697 (2020).
61. F. Wise, "Lasers for Nonlinear Microscopy," Cold Spring Harb Protoc **2013**, pdb.top073551 (2013).
62. B. C. Wilson, M. Jermyn, and F. Leblond, "Challenges and opportunities in clinical translation of biomedical optical spectroscopy and imaging," J. Biomed. Opt. **23**, 1 (2018).

63. K. König, H. G. Breunig, A. Batista, A. Schindele, M. Zieger, and M. Kaatz, "Translation of two-photon microscopy to the clinic: multimodal multiphoton CARS tomography of in vivo human skin," J. Biomed. Opt. **25**, 1 (2020).
64. P.-J. Treacy, A. Khosla, N. Kyprianou, U. G. Falagario, N. Tsavaras, P. Wiklund, A. K. Tewari, and M. Durand, "Value of multiphoton microscopy in uro-oncology: a narrative review," Transl Androl Urol **12**, 508–518 (2023).
65. J. Limpert, F. Roser, T. Schreiber, and A. Tunnermann, "High-power ultrafast fiber laser systems," IEEE J. Select. Topics Quantum Electron. **12**, 233–244 (2006).
66. W. Shi, Q. Fang, X. Zhu, R. A. Norwood, and N. Peyghambarian, "Fiber lasers and their applications [Invited]," Appl. Opt. **53**, 6554 (2014).
67. G. Chang and Z. Wei, "Ultrafast Fiber Lasers: An Expanding Versatile Toolbox," iScience **23**, 101101 (2020).
68. M. N. Zervas and C. A. Codemard, "High Power Fiber Lasers: A Review," IEEE J. Select. Topics Quantum Electron. **20**, 219–241 (2014).
69. G. P. Agrawal, *Nonlinear Fiber Optics*, 5th ed (Academic Press, 2013).
70. W. J. Wadsworth, A. Ortigosa-Blanch, J. C. Knight, T. A. Birks, T.-P. M. Man, and P. St. J. Russell, "Supercontinuum generation in photonic crystal fibers and optical fiber tapers: a novel light source," J. Opt. Soc. Am. B **19**, 2148 (2002).
71. J. M. Dudley, G. Genty, and S. Coen, "Supercontinuum generation in photonic crystal fiber," Rev. Mod. Phys. **78**, 1135–1184 (2006).
72. T. Sylvestre, E. Genier, A. N. Ghosh, P. Bowen, G. Genty, J. Troles, A. Mussot, A. C. Peacock, M. Klimczak, A. M. Heidt, J. C. Travers, O. Bang, and J. M. Dudley, "Recent advances in supercontinuum generation in specialty optical fibers [Invited]," J. Opt. Soc. Am. B **38**, F90 (2021).
73. J. Kim and Y. Song, "Ultralow-noise mode-locked fiber lasers and frequency combs: principles, status, and applications," Adv. Opt. Photon. **8**, 465 (2016).
74. R. M. Shelby, M. D. Levenson, D. F. Walls, A. Aspect, and G. J. Milburn, "Generation of squeezed states of light with a fiber-optic ring interferometer," Phys. Rev. A **33**, 4008–4025 (1986).
75. S. Schmitt, J. Ficker, M. Wolff, F. König, A. Sizmann, and G. Leuchs, "Photon-Number Squeezed Solitons from an Asymmetric Fiber-Optic Sagnac Interferometer," Phys. Rev. Lett. **81**, 2446–2449 (1998).
76. M. E. Marhic, *Fiber Optical Parametric Amplifiers, Oscillators and Related Devices*, 1st ed. (Cambridge University Press, 2007).
77. R. R. Sims, I. Bendifallah, C. Grimm, A. S. M. Lafirdeen, S. Domínguez, C. Y. Chan, X. Lu, B. C. Forget, F. St-Pierre, E. Papagiakoumou, and V. Emiliani, "Scanless two-photon voltage imaging," Nat Commun **15**, 5095 (2024).
78. F. Phil Brooks, H. C. Davis, J. D. Wong-Campos, and A. E. Cohen, "Optical constraints on two-photon voltage imaging," Neurophoton. **11**, (2024).
79. J. Platisa, X. Ye, A. M. Ahrens, C. Liu, I. A. Chen, I. G. Davison, L. Tian, V. A. Pieribone, and J. L. Chen, "High-speed low-light in vivo two-photon voltage imaging of large neuronal populations," Nat Methods **20**, 1095–1103 (2023).
80. K. Ota, Y. Oisi, T. Suzuki, M. Ikeda, Y. Ito, T. Ito, H. Uwamori, K. Kobayashi, M. Kobayashi, M. Odagawa, C. Matsubara, Y. Kuroiwa, M. Horikoshi, J. Matsushita, H. Hioki, M. Ohkura, J. Nakai, M. Oizumi, A. Miyawaki, T. Aonishi, T. Ode, and M. Murayama, "Fast, cell-resolution, contiguous-wide two-photon imaging to reveal functional network architectures across multi-modal cortical areas," Neuron **109**, 1810-1824.e9 (2021).
81. C. Grienberger, A. Giovannucci, W. Zeiger, and C. Portera-Cailliau, "Two-photon calcium imaging of neuronal activity," Nat Rev Methods Primers **2**, 67 (2022).

82. R. Wu, C. Zhao, S. Qiu, Y. Zhu, L. Zhang, Q. Fu, Y. Hu, D. Wu, F. Yu, F. Zhou, H. Huang, Y. Zhang, X. Wang, A. Wang, and H. Cheng, "A versatile miniature two-photon microscope enabling multicolor deep-brain imaging," Nat Methods **22**, 1935–1943 (2025).
83. W. Zong, R. Wu, S. Chen, J. Wu, H. Wang, Z. Zhao, G. Chen, R. Tu, D. Wu, Y. Hu, Y. Xu, Y. Wang, Z. Duan, H. Wu, Y. Zhang, J. Zhang, A. Wang, L. Chen, and H. Cheng, "Miniature two-photon microscopy for enlarged field-of-view, multi-plane and long-term brain imaging," Nat Methods **18**, 46–49 (2021).
84. W. Zong, H. A. Obenhaus, E. R. Skytøen, H. Eneqvist, N. L. De Jong, R. Vale, M. R. Jorge, M.-B. Moser, and E. I. Moser, "Large-scale two-photon calcium imaging in freely moving mice," Cell **185**, 1240-1256.e30 (2022).
85. M. Fişek, D. Herrmann, A. Egea-Weiss, M. Cloves, L. Bauer, T.-Y. Lee, L. E. Russell, and M. Häusser, "Cortico-cortical feedback engages active dendrites in visual cortex," Nature **617**, 769–776 (2023).
86. N. L. Pettit, X. C. Yuan, and C. D. Harvey, "Hippocampal place codes are gated by behavioral engagement," Nat Neurosci **25**, 561–566 (2022).
87. M. Clough, I. A. Chen, S.-W. Park, A. M. Ahrens, J. N. Stirman, S. L. Smith, and J. L. Chen, "Flexible simultaneous mesoscale two-photon imaging of neural activity at high speeds," Nat Commun **12**, 6638 (2021).
88. P. Mahou, M. Zimmerley, K. Loulier, K. S. Matho, G. Labroille, X. Morin, W. Supatto, J. Livet, D. Débarre, and E. Beaurepaire, "Multicolor two-photon tissue imaging by wavelength mixing," Nat Methods **9**, 815–818 (2012).
89. W. Yang, L. Carrillo-Reid, Y. Bando, D. S. Peterka, and R. Yuste, "Simultaneous two-photon imaging and two-photon optogenetics of cortical circuits in three dimensions," eLife **7**, e32671 (2018).
90. D. R. Hochbaum, Y. Zhao, S. L. Farhi, N. Klapoetke, C. A. Werley, V. Kapoor, P. Zou, J. M. Kralj, D. Maclaurin, N. Smedemark-Margulies, J. L. Saulnier, G. L. Boulting, C. Straub, Y. K. Cho, M. Melkonian, G. K.-S. Wong, D. J. Harrison, V. N. Murthy, B. L. Sabatini, E. S. Boyden, R. E. Campbell, and A. E. Cohen, "All-optical electrophysiology in mammalian neurons using engineered microbial rhodopsins," Nat Methods **11**, 825–833 (2014).
91. W. T. Silfvast, *Laser Fundamentals*, 2nd ed. (Cambridge University Press, 2004).
92. U. Keller, *Ultrafast Lasers: A Comprehensive Introduction to Fundamental Principles with Practical Applications*, Graduate Texts in Physics (Springer International Publishing, 2021).
93. U. Keller, K. J. Weingarten, F. X. Kartner, D. Kopf, B. Braun, I. D. Jung, R. Fluck, C. Honninger, N. Matuschek, and J. Aus Der Au, "Semiconductor saturable absorber mirrors (SESAM's) for femtosecond to nanosecond pulse generation in solid-state lasers," IEEE J. Select. Topics Quantum Electron. **2**, 435–453 (1996).
94. A. Dienes, "Mode-locked CW dye lasers," Opto-electronics **6**, 99–113 (1974).
95. T. Brabec, Ch. Spielmann, P. F. Curley, and F. Krausz, "Kerr lens mode locking," Opt. Lett. **17**, 1292 (1992).
96. W. Hänsel, H. Hoogland, M. Giunta, S. Schmid, T. Steinmetz, R. Doubek, P. Mayer, S. Dobner, C. Cleff, M. Fischer, and R. Holzwarth, "All polarization-maintaining fiber laser architecture for robust femtosecond pulse generation," Appl. Phys. B **123**, 41 (2017).
97. H. A. Haus and A. Mecozzi, "Noise of mode-locked lasers," IEEE J. Quantum Electron. **29**, 983–996 (1993).
98. R. Paschotta, "Noise of mode-locked lasers (Part I): numerical model," Appl Phys B **79**, 153–162 (2004).
99. C. H. Henry and R. F. Kazarinov, "Quantum noise in photonics," Rev. Mod. Phys. **68**, 801–853 (1996).
100. R. Paschotta, "Noise of mode-locked lasers (Part II): timing jitter and other fluctuations," Appl Phys B **79**, 163–173 (2004).

101. N. R. Newbury and W. C. Swann, "Low-noise fiber-laser frequency combs (Invited)," J. Opt. Soc. Am. B **24**, 1756 (2007).
102. S. Koke, C. Grebing, H. Frei, A. Anderson, A. Assion, and G. Steinmeyer, "Direct frequency comb synthesis with arbitrary offset and shot-noise-limited phase noise," Nature Photon **4**, 462–465 (2010).
103. K. Jung and J. Kim, "Subfemtosecond synchronization of microwave oscillators with mode-locked Er-fiber lasers," Opt. Lett. **37**, 2958 (2012).
104. M. Xin, K. Şafak, M. Y. Peng, A. Kalaydzhyan, W.-T. Wang, O. D. Mücke, and F. X. Kärtner, "Attosecond precision multi-kilometer laser-microwave network," Light Sci Appl **6**, e16187–e16187 (2016).
105. A. Hasegawa and F. Tappert, "Transmission of stationary nonlinear optical pulses in dispersive dielectric fibers. I. Anomalous dispersion," Applied Physics Letters **23**, 142–144 (1973).
106. A. Hasegawa and F. Tappert, "Transmission of stationary nonlinear optical pulses in dispersive dielectric fibers. II. Normal dispersion," Applied Physics Letters **23**, 171–172 (1973).
107. A. M. Weiner, *Ultrafast Optics*, Wiley Series in Pure and Applied Optics (Wiley, 2009).
108. T. Schreiber, B. Ortaç, J. Limpert, and A. Tünnermann, "On the study of pulse evolution in ultra-short pulse mode-locked fiber lasers by numerical simulations," Opt. Express **15**, 8252 (2007).
109. R. Paschotta, J. Nilsson, A. C. Tropper, and D. C. Hanna, "Ytterbium-doped fiber amplifiers," IEEE J. Quantum Electron. **33**, 1049–1056 (1997).
110. C. R. Giles and E. Desurvire, "Modeling erbium-doped fiber amplifiers," J. Lightwave Technol. **9**, 271–283 (1991).
111. M. Edelmann, Y. Hua, M. Pergament, and F. X. Kärtner, "Performance enhancement via XPM suppression of a linear all-PM mode-locked fiber oscillator," Opt. Lett. **49**, 1237 (2024).
112. M. Edelmann, Y. Hua, K. Şafak, Y. E. Sharkawy, M. Pergament, and F. X. Kärtner, "Optimized Noise and Stability Regimes in XPM-Suppressed All-PM Linear Mode-Locked Fiber Lasers," J. Lightwave Technol. **43**, 8378–8385 (2025).
113. F. DeMartini, C. H. Townes, T. K. Gustafson, and P. L. Kelley, "Self-Steepening of Light Pulses," Phys. Rev. **164**, 312–323 (1967).
114. S. J. Carter, "Quantum theory of nonlinear fiber optics: Phase-space representations," Phys. Rev. A **51**, 3274–3301 (1995).
115. B. Sierro, P. Hänzi, D. Spangenberg, A. Rampur, and A. M. Heidt, "Reducing the noise of fiber supercontinuum sources to its limits by exploiting cascaded soliton and wave breaking nonlinear dynamics," Optica **9**, 352 (2022).
116. K. L. Corwin, N. R. Newbury, J. M. Dudley, S. Coen, S. A. Diddams, K. Weber, and R. S. Windeler, "Fundamental Noise Limitations to Supercontinuum Generation in Microstructure Fiber," Phys. Rev. Lett. **90**, 113904 (2003).
117. B. Wetzel, A. Stefani, L. Larger, P. A. Lacourt, J. M. Merolla, T. Sylvestre, A. Kudlinski, A. Mussot, G. Genty, F. Dias, and J. M. Dudley, "Real-time full bandwidth measurement of spectral noise in supercontinuum generation," Sci Rep **2**, 882 (2012).
118. A. Rampur, D.-M. Spangenberg, B. Sierro, P. Hänzi, M. Klimczak, and A. M. Heidt, "Perspective on the next generation of ultra-low noise fiber supercontinuum sources and their emerging applications in spectroscopy, imaging, and ultrafast photonics," Applied Physics Letters **118**, 240504 (2021).
119. B. R. Masters and T. C. S. Peter, eds., *Handbook of Biomedical Nonlinear Optical Microscopy* (Oxford University PressNew York, NY, 1998).

120. F. Bestvater, E. Spiess, G. Stobrawa, M. Hacker, T. Feurer, T. Porwol, U. Berchner-Pfannschmidt, C. Wotzlaw, and H. Acker, "Two-photon fluorescence absorption and emission spectra of dyes relevant for cell imaging," Journal of Microscopy **208**, 108–115 (2002).
121. J. Mütze, V. Iyer, J. J. Macklin, J. Colonell, B. Karsh, Z. Petrášek, P. Schwille, L. L. Looger, L. D. Lavis, and T. D. Harris, "Excitation Spectra and Brightness Optimization of Two-Photon Excited Probes," Biophysical Journal **102**, 934–944 (2012).
122. R. W. Boyd, *Nonlinear Optics*, Fourth edition (Elsevier, AP Academic Press, 2020).
123. R. W. Cole, T. Jinadasa, and C. M. Brown, "Measuring and interpreting point spread functions to determine confocal microscope resolution and ensure quality control," Nat Protoc **6**, 1929–1941 (2011).
124. A. Diaspro, G. J. Brakenhoff, and L. Bagatolli, eds., *Confocal and Two-Photon Microscopy: Foundations, Applications, and Advances* (Wiley-Liss, 2002).
125. M. Xin, K. Şafak, and F. X. Kärtner, "Ultra-precise timing and synchronization for large-scale scientific instruments," Optica **5**, 1564 (2018).
126. X. Xie, R. Bouchand, D. Nicolodi, M. Giunta, W. Hänsel, M. Lezius, A. Joshi, S. Datta, C. Alexandre, M. Lours, P.-A. Tremblin, G. Santarelli, R. Holzwarth, and Y. Le Coq, "Photonic microwave signals with zeptosecond-level absolute timing noise," Nature Photon **11**, 44–47 (2017).
127. B. R. Washburn, S. A. Diddams, N. R. Newbury, J. W. Nicholson, M. F. Yan, and C. G. Jørgensen, "Phase-locked, erbium-fiber-laser-based frequency comb in the near infrared," Opt. Lett. **29**, 250 (2004).
128. N. Davoudzadeh, G. Ducourthial, and B. Q. Spring, "Custom fabrication and mode-locked operation of a femtosecond fiber laser for multiphoton microscopy," Sci Rep **9**, 4233 (2019).
129. S. Fan, S. Wang, C. Yang, F. Wise, and L. Kong, "Advances of Mode-Locking Fiber Lasers in Neural Imaging," Advanced Optical Materials **11**, 2202945 (2023).
130. E. P. Perillo, J. E. McCracken, D. C. Fernée, J. R. Goldak, F. A. Medina, D. R. Miller, H.-C. Yeh, and A. K. Dunn, "Deep in vivo two-photon microscopy with a low cost custom built mode-locked 1060 nm fiber laser," Biomed. Opt. Express **7**, 324 (2016).
131. K.-C. Li, L. L. H. Huang, J.-H. Liang, and M.-C. Chan, "Simple approach to three-color two-photon microscopy by a fiber-optic wavelength convertor," Biomed. Opt. Express **7**, 4803 (2016).
132. L.-T. Chou, Y.-C. Liu, D.-L. Zhong, W.-Z. Lin, H.-H. Hung, C.-J. Chan, Z.-P. Chen, and S.-H. Chia, "Low noise, self-phase-modulation-enabled femtosecond fiber sources tunable in 740-1236 nm for wide two-photon fluorescence microscopy applications," Biomed. Opt. Express **12**, 2888 (2021).
133. L.-T. Chou, S.-H. Wu, H.-H. Hung, W.-Z. Lin, Z.-P. Chen, A. A. Ivanov, and S.-H. Chia, "Compact multicolor two-photon fluorescence microscopy enabled by tailorable continuum generation from self-phase modulation and dispersive wave generation," Opt. Express **30**, 40315 (2022).
134. J. Noda, K. Okamoto, and Y. Sasaki, "Polarization-maintaining fibers and their applications," J. Lightwave Technol. **4**, 1071–1089 (1986).
135. X. Liu, F. Ye, Y. Luo, H. Fu, and Q. Li, "Ultrafast Polarization-Maintaining Fiber Lasers: Design, Fabrication, Performance, and Applications," Laser & Photonics Reviews **19**, 2400927 (2025).
136. Y. Wang and M. Wang, "Research Progress on All-Polarization-Maintaining Mode-Locked Fiber Lasers," Photonics **12**, 366 (2025).
137. S. Y. Ryu, K.-S. Kim, J. Kim, and S. Kim, "Degradation of optical properties of a film-type single-wall carbon nanotubes saturable absorber (SWNT-SA) with an Er-doped all-fiber laser," Opt. Express **20**, 12966 (2012).

138. M. Haiml, R. Grange, and U. Keller, "Optical characterization of semiconductor saturable absorbers," Appl. Phys. B **79**, 331–339 (2004).
139. S. M. Kobtsev and S. V. Smirnov, "Fiber lasers mode-locked due to nonlinear polarization evolution: Golden mean of cavity length," Laser Phys. **21**, 272–276 (2011).
140. N. J. Doran and D. Wood, "Nonlinear-optical loop mirror," Opt. Lett. **13**, 56 (1988).
141. M. E. Fermann, F. Haberl, M. Hofer, and H. Hochreiter, "Nonlinear amplifying loop mirror," Opt. Lett. **15**, 752 (1990).
142. X. Liu, Q. Li, D. Pan, F. Ye, B. Malomed, and H. Y. Fu, "A Robust and Novel Linear Fiber Laser Mode-locked by Nonlinear Polarization Evolution in All-polarization-maintaining Fibers," J. Lightwave Technol. 1–1 (2021).
143. X. Liu, F. Ye, M. Zhao, B. A. Malomed, H. Y. Fu, and Q. Li, "All-Polarization-Maintaining Linear Cavity Fiber Lasers Mode-Locked by Nonlinear Polarization Evolution in Stretched Pulse Regime," J. Lightwave Technol. **41**, 5107–5115 (2023).
144. M. Edelmann, Y. Hua, G. Kulcsar, and F. X. Kärtner, "All-polarization-maintaining divided pulse fiber oscillator mode-locked with the optical Kerr effect," Opt. Lett. **46**, 6083 (2021).
145. M. Edelmann, M. M. Sedigheh, Y. Hua, E. C. Vargas, M. Pergament, and F. X. Kärtner, "Large-mode-area soliton fiber oscillator mode-locked using NPE in an all-PM self-stabilized interferometer," Appl. Opt. **62**, 1672 (2023).
146. J. Wang, B. Wen, X. Chen, H. Zhang, X. Chen, P. Yan, and H. Zhang, "All-polarization-maintaining Ho-doped fiber oscillator mode-locked with nonlinear polarization evolution," Opt. Lett. **49**, 133 (2024).
147. A. S. Mayer, W. Grosinger, J. Fellinger, G. Winkler, L. W. Perner, S. Droste, S. H. Salman, C. Li, C. M. Heyl, I. Hartl, and O. H. Heckl, "Flexible all-PM NALM Yb:fiber laser design for frequency comb applications: operation regimes and their noise properties," Opt. Express **28**, 18946 (2020).
148. F. L. Pedrotti, L. M. Pedrotti, and L. S. Pedrotti, *Introduction to Optics*, 3rd ed (Cambridge university press, 2018).
149. K. Tamura, E. P. Ippen, and H. A. Haus, "Pulse dynamics in stretched-pulse fiber lasers," Applied Physics Letters **67**, 158–160 (1995).
150. Y. Song, X. Shi, C. Wu, D. Tang, and H. Zhang, "Recent progress of study on optical solitons in fiber lasers," Applied Physics Reviews **6**, 021313 (2019).
151. F. Ö. Ilday, J. R. Buckley, W. G. Clark, and F. W. Wise, "Self-Similar Evolution of Parabolic Pulses in a Laser," Phys. Rev. Lett. **92**, 213902 (2004).
152. J. Kim, J. Chen, Z. Zhang, F. N. C. Wong, F. X. Kärtner, F. Loehl, and H. Schlarb, "Long-term femtosecond timing link stabilization using a single-crystal balanced cross correlator," Opt. Lett. **32**, 1044 (2007).
153. Hyoji Kim, Peng Qin, Youjian Song, Heewon Yang, Junho Shin, Chur Kim, Kwangyun Jung, Chingyue Wang, and Jungwon Kim, "Sub-20-Attosecond Timing Jitter Mode-Locked Fiber Lasers," IEEE J. Select. Topics Quantum Electron. **20**, 260–267 (2014).
154. R. Hui, Y. Wang, K. Demarest, and C. Allen, "Frequency response of cross-phase modulation in multispan WDM optical fiber systems," IEEE Photon. Technol. Lett. **10**, 1271–1273 (1998).
155. B. R. Washburn, W. C. Swann, and N. R. Newbury, "Response dynamics of the frequency comb output from a femtosecond fiber laser," Opt. Express **13**, 10622 (2005).
156. S. Namiki and H. A. Haus, "Noise of the stretched pulse fiber laser. I. Theory," IEEE J. Quantum Electron. **33**, 649–659 (1997).
157. R. Paschotta, "Timing jitter and phase noise of mode-locked fiber lasers," Opt. Express **18**, 5041 (2010).

158. S. Xiong, D. Luo, Y. Liu, W. Wang, Z. Deng, Z. Tang, G. Xie, L. Zhou, Z. Zuo, C. Gu, and W. Li, "Investigation of stable pulse mode-locking regimes in a NALM figure-9 Er-doped fiber laser," Opt. Express **31**, 514 (2023).
159. P. Tchofo Dinda, A. Malfondet, P. Grelu, G. Millot, and A. Kamagate, "Strategies for accessing the multipulse regime of mode-locked fiber lasers," Phys. Rev. A **107**, 033513 (2023).
160. Wei Zhao, Xiaohong Hu, and Yishan Wang, "Femtosecond-Pulse Fiber Based Amplification Techniques and Their Applications," IEEE J. Select. Topics Quantum Electron. **20**, 512–524 (2014).
161. A. Chong, W. H. Renninger, and F. W. Wise, "All-normal-dispersion femtosecond fiber laser with pulse energy above 20nJ," Opt. Lett. **32**, 2408 (2007).
162. S. K. Turitsyn, B. G. Bale, and M. P. Fedoruk, "Dispersion-managed solitons in fibre systems and lasers," Physics Reports **521**, 135–203 (2012).
163. E. S. Lamb, L. G. Wright, and F. W. Wise, "Divided-pulse lasers," Opt. Lett. **39**, 2775 (2014).
164. W. Liu, H. Shi, J. Cui, C. Xie, Y. Song, C. Wang, and M. Hu, "Single-polarization large-mode-area fiber laser mode-locked with a nonlinear amplifying loop mirror," Opt. Lett. **43**, 2848 (2018).
165. H. A. Haus, "Mode-locking of lasers," IEEE J. Select. Topics Quantum Electron. **6**, 1173–1185 (2000).
166. F. X. Kartner, I. D. Jung, and U. Keller, "Soliton mode-locking with saturable absorbers," IEEE J. Select. Topics Quantum Electron. **2**, 540–556 (1996).
167. M. Edelmann, Y. Hua, K. Şafak, and F. X. Kärtner, "Intrinsic amplitude-noise suppression in fiber lasers mode-locked with nonlinear amplifying loop mirrors," Opt. Lett. **46**, 1752 (2021).
168. X. Zeng, S. Cui, J. Qian, X. Cheng, J. Dong, J. Zhou, Z. Xu, and Y. Feng, "10 W low-noise green laser generation by the single-pass frequency doubling of a single-frequency fiber amplifier," Laser Phys. **30**, 075001 (2020).
169. R. Collin, T. Chartier, and P. Besnard, "Numerical investigation of relative intensity noise in frequency-doubled multimode fiber lasers," Optics Communications **485**, 126724 (2021).
170. M. Tawfieq, A. K. Hansen, O. B. Jensen, D. Marti, B. Sumpf, and P. E. Andersen, "Intensity Noise Transfer Through a Diode-Pumped Titanium Sapphire Laser System," IEEE J. Quantum Electron. **54**, 1–9 (2018).
171. S. Rao D. S., M. Jensen, L. Grüner-Nielsen, J. T. Olsen, P. Heiduschka, B. Kemper, J. Schnekenburger, M. Glud, M. Mogensen, N. M. Israelsen, and O. Bang, "Shot-noise limited, supercontinuum-based optical coherence tomography," Light Sci Appl **10**, 133 (2021).
172. C. A. Casacio, L. S. Madsen, A. Terrasson, M. Waleed, K. Barnscheidt, B. Hage, M. A. Taylor, and W. P. Bowen, "Quantum-enhanced nonlinear microscopy," Nature **594**, 201–206 (2021).
173. M. Endo, T. D. Shoji, and T. R. Schibli, "Ultralow Noise Optical Frequency Combs," IEEE J. Select. Topics Quantum Electron. **24**, 1–13 (2018).
174. K. J. Kaltenecker, S. Rao D. S., M. Rasmussen, H. B. Lassen, E. J. R. Kelleher, E. Krauss, B. Hecht, N. A. Mortensen, L. Grüner-Nielsen, C. Markos, O. Bang, N. Stenger, and P. U. Jepsen, "Near-infrared nanospectroscopy using a low-noise supercontinuum source," APL Photonics **6**, 066106 (2021).
175. G. Cirmi, R. E. Mainz, M. A. Silva-Toledo, F. Scheiba, H. Çankaya, M. Kubullek, G. M. Rossi, and F. X. Kärtner, "Optical Waveform Synthesis and Its Applications," Laser & Photonics Reviews **17**, 2200588 (2023).

176. Q. Huang, M. A. Cohen, F. C. Alsina, G. Devlin, A. Garrett, J. McKey, P. Havlik, N. Rakhilin, E. Wang, K. Xiang, P. Mathews, L. Wang, C. Bock, V. Ruthig, Y. Wang, M. Negrete, C. W. Wong, P. K. L. Murthy, S. Zhang, A. R. Daniel, D. G. Kirsch, Y. Kang, B. Capel, A. Asokan, D. L. Silver, R. Jaenisch, and X. Shen, "Intravital imaging of mouse embryos," Science **368**, 181–186 (2020).
177. G. Alzeeb, M. Dubreuil, D. Arzur, S. Rivet, L. Corcos, Y. L. Grand, and C. Le Jossic-Corcos, "Gastric cancer multicellular spheroid analysis by two-photon microscopy," Biomed. Opt. Express **13**, 3120 (2022).
178. C. Ricard, E. D. Arroyo, C. X. He, C. Portera-Cailliau, G. Lepousez, M. Canepari, and D. Fiole, "Two-photon probes for in vivo multicolor microscopy of the structure and signals of brain cells," Brain Struct Funct **223**, 3011–3043 (2018).
179. J. Li, X. Wu, Y. Fu, H. Nie, and Z. Tang, "Two-photon microscopy: application advantages and latest progress for *in vivo* imaging of neurons and blood vessels after ischemic stroke," Reviews in the Neurosciences **34**, 559–572 (2023).
180. J. Grutzendler and W.-B. Gan, "Two-photon imaging of synaptic plasticity and pathology in the living mouse brain," NeuroRX **3**, 489–496 (2006).
181. W. Zong, R. Wu, M. Li, Y. Hu, Y. Li, J. Li, H. Rong, H. Wu, Y. Xu, Y. Lu, H. Jia, M. Fan, Z. Zhou, Y. Zhang, A. Wang, L. Chen, and H. Cheng, "Fast high-resolution miniature two-photon microscopy for brain imaging in freely behaving mice," Nat Methods **14**, 713–719 (2017).
182. J. C. Jung, A. D. Mehta, E. Aksay, R. Stepnoski, and M. J. Schnitzer, "In Vivo Mammalian Brain Imaging Using One- and Two-Photon Fluorescence Microendoscopy," Journal of Neurophysiology **92**, 3121–3133 (2004).
183. H. Dana, T.-W. Chen, A. Hu, B. C. Shields, C. Guo, L. L. Looger, D. S. Kim, and K. Svoboda, "Thy1-GCaMP6 Transgenic Mice for Neuronal Population Imaging In Vivo," PLoS ONE **9**, e108697 (2014).
184. N. A. Steinmetz, C. Buetfering, J. Lecoq, C. R. Lee, A. J. Peters, E. A. K. Jacobs, P. Coen, D. R. Ollerenshaw, M. T. Valley, S. E. J. De Vries, M. Garrett, J. Zhuang, P. A. Groblewski, S. Manavi, J. Miles, C. White, E. Lee, F. Griffin, J. D. Larkin, K. Roll, S. Cross, T. V. Nguyen, R. Larsen, J. Pendergraft, T. Daigle, B. Tasic, C. L. Thompson, J. Waters, S. Olsen, D. J. Margolis, H. Zeng, M. Hausser, M. Carandini, and K. D. Harris, "Aberrant Cortical Activity in Multiple GCaMP6-Expressing Transgenic Mouse Lines," eNeuro **4**, ENEURO.0207-17.2017 (2017).
185. J. Cichon, J. Magrané, E. Shtridler, C. Chen, L. Sun, G. Yang, and W.-B. Gan, "Imaging neuronal activity in the central and peripheral nervous systems using new Thy1.2-GCaMP6 transgenic mouse lines," Journal of Neuroscience Methods **334**, 108535 (2020).
186. Z. Shen, Z. Lu, P. Y. Chhatbar, P. O'Herron, and P. Kara, "An artery-specific fluorescent dye for studying neurovascular coupling," Nat Methods **9**, 273–276 (2012).
187. H. Jia, N. L. Rochefort, X. Chen, and A. Konnerth, "In vivo two-photon imaging of sensory-evoked dendritic calcium signals in cortical neurons," Nat Protoc **6**, 28–35 (2011).
188. K. E. Fenton, N. L. Martirosyan, M. G. Abdelwahab, S. W. Coons, M. C. Preul, and A. C. Scheck, "In vivo visualization of GL261-luc2 mouse glioma cells by use of Alexa Fluor–labeled TRP-2 antibodies," FOC **36**, E12 (2014).
189. W. Liu, C. Li, Z. Zhang, F. X. Kärtner, and G. Chang, "Self-phase modulation enabled, wavelength-tunable ultrafast fiber laser sources: an energy scalable approach," Opt. Express **24**, 15328 (2016).
190. H.-Y. Chung, W. Liu, Q. Cao, L. Song, F. X. Kärtner, and G. Chang, "Megawatt peak power tunable femtosecond source based on self-phase modulation enabled spectral selection," Opt. Express **26**, 3684 (2018).

191. F. Niu, J. Li, W. Yang, Z. Zhang, and A. Wang, "Fiber-Based High-Energy Femtosecond Pulses Tunable From 920 to 1030 nm for Two-Photon Microscopy," IEEE Photon. Technol. Lett. **30**, 1479–1482 (2018).
192. I. Cristiani, R. Tediosi, L. Tartara, and V. Degiorgio, "Dispersive wave generation by solitons in microstructured optical fibers," Opt. Express **12**, 124 (2004).
193. A. V. Husakou and J. Herrmann, "Supercontinuum generation, four-wave mixing, and fission of higher-order solitons in photonic-crystal fibers," J. Opt. Soc. Am. B **19**, 2171 (2002).
194. M. Manto, J. D. Schmahmann, F. Rossi, D. L. Gruol, and N. Koibuchi, eds., *Handbook of the Cerebellum and Cerebellar Disorders* (Springer Netherlands, 2013).
195. A. Rakhymzhan, R. Leben, H. Zimmermann, R. Günther, P. Mex, D. Reismann, C. Ulbricht, A. Acs, A. U. Brandt, R. L. Lindquist, T. H. Winkler, A. E. Hauser, and R. A. Niesner, "Synergistic Strategy for Multicolor Two-photon Microscopy: Application to the Analysis of Germinal Center Reactions In Vivo," Sci Rep **7**, 7101 (2017).
196. L. Abdeladim, K. S. Matho, S. Clavreul, P. Mahou, J.-M. Sintes, X. Solinas, I. Arganda-Carreras, S. G. Turney, J. W. Lichtman, A. Chessel, A.-P. Bemelmans, K. Loulier, W. Supatto, J. Livet, and E. Beaurepaire, "Multicolor multiscale brain imaging with chromatic multiphoton serial microscopy," Nat Commun **10**, 1662 (2019).
197. J. Herz, V. Siffrin, A. E. Hauser, A. U. Brandt, T. Leuenberger, H. Radbruch, F. Zipp, and R. A. Niesner, "Expanding Two-Photon Intravital Microscopy to the Infrared by Means of Optical Parametric Oscillator," Biophysical Journal **98**, 715–723 (2010).
198. K. Wang, T.-M. Liu, J. Wu, N. G. Horton, C. P. Lin, and C. Xu, "Three-color femtosecond source for simultaneous excitation of three fluorescent proteins in two-photon fluorescence microscopy," Biomed. Opt. Express **3**, 1972 (2012).
199. K. Guesmi, L. Abdeladim, S. Tozer, P. Mahou, T. Kumamoto, K. Jurkus, P. Rigaud, K. Loulier, N. Dray, P. Georges, M. Hanna, J. Livet, W. Supatto, E. Beaurepaire, and F. Druon, "Dual-color deep-tissue three-photon microscopy with a multiband infrared laser," Light Sci Appl **7**, 12 (2018).
200. R. S. Pillai, C. Boudoux, G. Labroille, N. Olivier, I. Veilleux, E. Farge, M. Joffre, and E. Beaurepaire, "Multiplexed two-photon microscopy of dynamic biological samples with shaped broadband pulses," Opt. Express **17**, 12741 (2009).
201. Y.-T. Hsiao, Y.-F. Huang, B. J. Borah, S.-K. Chen, and C.-K. Sun, "Single-laser-based simultaneous four-wavelength excitation source for femtosecond two-photon fluorescence microscopy," Biomed. Opt. Express **12**, 4661 (2021).
202. M. H. Brenner, D. Cai, J. A. Swanson, and J. P. Ogilvie, "Two-photon imaging of multiple fluorescent proteins by phase-shaping and linear unmixing with a single broadband laser," Opt. Express **21**, 17256 (2013).
203. P. Russell, "Photonic Crystal Fibers," Science **299**, 358–362 (2003).
204. P. Luu, S. E. Fraser, and F. Schneider, "More than double the fun with two-photon excitation microscopy," Commun Biol **7**, 364 (2024).
205. I. Pastirk, J. M. D. Cruz, K. A. Walowicz, V. V. Lozovoy, and M. Dantus, "Selective two-photon microscopy with shaped femtosecond pulses," Opt. Express **11**, 1695 (2003).
206. X. Liang, W. Hu, and L. Fu, "Pulse compression in two-photon excitation fluorescence microscopy," Opt. Express **18**, 14893 (2010).
207. M. Edelmann, A. Matamoros-Angles, M. Shafiq, M. Pergament, M. Glatzel, and F. X. Kärtner, "Deep-tissue two-photon brain imaging enabled by a tunable fiber-optic dispersive wave generator," Sci Rep **15**, 24404 (2025).
208. G. Zhou, Q. Cao, F. X. Kärtner, and G. Chang, "Energy scalable, offset-free ultrafast mid-infrared source harnessing self-phase-modulation-enabled spectral selection," Opt. Lett. **43**, 2953 (2018).

209. W. Liu, S.-H. Chia, H.-Y. Chung, R. Greinert, F. X. Kärtner, and G. Chang, "Energetic ultrafast fiber laser sources tunable in 1030–1215 nm for deep tissue multi-photon microscopy," Opt. Express **25**, 6822 (2017).
210. H.-Y. Chung, R. Greinert, F. X. Kärtner, and G. Chang, "Multimodal imaging platform for optical virtual skin biopsy enabled by a fiber-based two-color ultrafast laser source," Biomed. Opt. Express **10**, 514 (2019).
211. J. R. Unruh, E. S. Price, R. G. Molla, L. Stehno-Bittel, C. K. Johnson, and R. Hui, "Two-photon microscopy with wavelength switchable fiber laser excitation," Opt. Express **14**, 9825 (2006).
212. Y. Liu, H. Tu, W. A. Benalcazar, E. J. Chaney, and S. A. Boppart, "Multimodal Nonlinear Microscopy by Shaping a Fiber Supercontinuum From 900 to 1160 nm," IEEE J. Select. Topics Quantum Electron. **18**, 1209–1214 (2012).
213. W. Wei, J. Elstrott, and M. B. Feller, "Two-photon targeted recording of GFP-expressing neurons for light responses and live-cell imaging in the mouse retina," Nat Protoc **5**, 1347–1352 (2010).
214. C. Grienberger and A. Konnerth, "Imaging Calcium in Neurons," Neuron **73**, 862–885 (2012).
215. R. T. Lang and B. Q. Spring, "Two-photon peak molecular brightness spectra reveal long-wavelength enhancements of multiplexed imaging depth and photostability," Biomed. Opt. Express **12**, 5909 (2021).
216. R. Dalangin, B. Z. Jia, Y. Qi, A. Aggarwal, K. Sakoi, M. Drobizhev, R. S. Molina, R. Patel, A. S. Abdelfattah, J. Zheng, D. Reep, J. P. Hasseman, The GENIE Project Team, G. Tsegaye, A. Tsang, G. C. Turner, Y. Zhao, J. Wu, K. Podgorski, A. G. Tebo, E. R. Schreiter, T. E. Hughes, T. Terai, M.-E. Paquet, S. G. Megason, A. E. Cohen, Y. Shen, and R. E. Campbell, "Far-red fluorescent genetically encoded calcium ion indicators," Nat Commun **16**, 3318 (2025).
217. A. S. Abdelfattah, J. Zheng, A. Singh, Y.-C. Huang, D. Reep, G. Tsegaye, A. Tsang, B. J. Arthur, M. Rehorova, C. V. L. Olson, Y. Shuai, L. Zhang, T.-M. Fu, D. E. Milkie, M. V. Moya, T. D. Weber, A. L. Lemire, C. A. Baker, N. Falco, Q. Zheng, J. B. Grimm, M. C. Yip, D. Walpita, M. Chase, L. Campagnola, G. J. Murphy, A. M. Wong, C. R. Forest, J. Mertz, M. N. Economo, G. C. Turner, M. Koyama, B.-J. Lin, E. Betzig, O. Novak, L. D. Lavis, K. Svoboda, W. Korff, T.-W. Chen, E. R. Schreiter, J. P. Hasseman, and I. Kolb, "Sensitivity optimization of a rhodopsin-based fluorescent voltage indicator," Neuron **111**, 1547-1563.e9 (2023).
218. C. Dong, A. D. Madar, and M. E. J. Sheffield, "Distinct place cell dynamics in CA1 and CA3 encode experience in new environments," Nat Commun **12**, 2977 (2021).
219. P. E. Gilbert and A. M. Brushfield, "The role of the CA3 hippocampal subregion in spatial memory: A process oriented behavioral assessment," Progress in Neuro-Psychopharmacology and Biological Psychiatry **33**, 774–781 (2009).
220. C. D. Link, "Expression of human beta-amyloid peptide in transgenic Caenorhabditis elegans.," Proc. Natl. Acad. Sci. U.S.A. **92**, 9368–9372 (1995).
221. M. Markaki and N. Tavernarakis, "Caenorhabditis elegans as a model system for human diseases," Current Opinion in Biotechnology **63**, 118–125 (2020).
222. M. Kolarova, F. García-Sierra, A. Bartos, J. Ricny, and D. Ripova, "Structure and Pathology of Tau Protein in Alzheimer Disease," International Journal of Alzheimer's Disease **2012**, 1–13 (2012).
223. S. Wegmann, B. Eftekharzadeh, K. Tepper, K. M. Zoltowska, R. E. Bennett, S. Dujardin, P. R. Laskowski, D. MacKenzie, T. Kamath, C. Commins, C. Vanderburg, A. D. Roe, Z. Fan, A. M. Molliex, A. Hernandez-Vega, D. Muller, A. A. Hyman, E. Mandelkow, J. P. Taylor, and B. T. Hyman, "Tau protein liquid–liquid phase separation can initiate tau aggregation," The EMBO Journal **37**, e98049 (2018).

224. M. Jouanne, S. Rault, and A.-S. Voisin-Chiret, "Tau protein aggregation in Alzheimer's disease: An attractive target for the development of novel therapeutic agents," European Journal of Medicinal Chemistry **139**, 153–167 (2017).
225. S. Boyko, X. Qi, T.-H. Chen, K. Surewicz, and W. K. Surewicz, "Liquid–liquid phase separation of tau protein: The crucial role of electrostatic interactions," Journal of Biological Chemistry **294**, 11054–11059 (2019).
226. S. K. Rai, A. Savastano, P. Singh, S. Mukhopadhyay, and M. Zweckstetter, "Liquid–liquid phase separation of tau: From molecular biophysics to physiology and disease," Protein Science **30**, 1294–1314 (2021).
227. J. Wen, L. Hong, G. Krainer, Q.-Q. Yao, T. P. J. Knowles, S. Wu, and S. Perrett, "Conformational Expansion of Tau in Condensates Promotes Irreversible Aggregation," J. Am. Chem. Soc. **143**, 13056–13064 (2021).
228. B. C. Kraemer, B. Zhang, J. B. Leverenz, J. H. Thomas, J. Q. Trojanowski, and G. D. Schellenberg, "Neurodegeneration and defective neurotransmission in a *Caenorhabditis elegans* model of tauopathy," Proc. Natl. Acad. Sci. U.S.A. **100**, 9980–9985 (2003).
229. E. Yemini, T. Jucikas, L. J. Grundy, A. E. X. Brown, and W. R. Schafer, "A database of Caenorhabditis elegans behavioral phenotypes," Nat Methods **10**, 877–879 (2013).
230. D. Ramot, B. E. Johnson, T. L. Berry, L. Carnell, and M. B. Goodman, "The Parallel Worm Tracker: A Platform for Measuring Average Speed and Drug-Induced Paralysis in Nematodes," PLoS ONE **3**, e2208 (2008).

8 Appendix

8.1 Simulation Parameter for PCMA Simulations

Parameter	Symbol	Value
Input Pulse (Measured from YDF):		
Pulse energy	E_0	Variable as shown in Fig. 2 (a) and (b)
Repetition rate	f_{rep}	30 MHz
Group-delay dispersion (Pre-chirp)	GDD_0	Variable as shown in Fig. 2 (a) and (b)
Center wavelength	λ_c	1050 nm
Spectral bandwidth (FWHM)	$\Delta\lambda$	~30 nm
PCMA Parameters:		
Passive fiber length at C1	L_{p1}	0.8 m
Passive fiber length at C2	L_{p2}	0.5 m
Gain fiber length	L_g	1.1 m
Mode-field diameter	MFD	10.5 µm @ 1060 nm (both gain and passive fiber)
Nonlinear refractive index	n_2	$2.6 * 10^{-20}$ m^2/W
Group-velocity dispersion	β_2	23 fs^2/mm
Third-order dispersion	β_3	46 fs^2/mm
Doping concentration	-	$1.1 * 10^8$ µm^{-3}
Cross-sections	-	R. Paschotta, et al, IEEE Journal of quantum electronics, Vol.33, p 1049 (1997).
Pump loss	-	Y. Hua, et al., Opt. Express 26, 6427-6438 (2018).
Grating compressor		
Angle of incidence	-	31.3°
Line density	-	1000 lines/mm
Grating distance	d_g	Variable to optimize Strehl-ratio
Bandpass filter		
Center wavelength	$\lambda_{c,BPF}$	1048 nm
Spectral bandwidth (FWHM)	$\Delta\lambda_{BPF}$	60 nm
Super-Gaussian order	-	4

8.2 Simulation Parameter for Multicolor Wavelength Conversion

Parameter	Symbol	Value
Input Pulse (Measured from filtered PCMA output):		
Pulse energy	E_0	21.8 nJ
Repetition rate	f_{rep}	30 MHz
Temporal FWHM	Δt	62 fs
Group-delay dispersion (pre-chirp)	GDD_0	$9 * 10^2$ fs^2

Third order dispersion	TOD_0	$-0.6 * 10^4$ fs^3
Center wavelength	λ_c	1048 nm
Spectral bandwidth (FWHM)	$\Delta\lambda$	~50 nm
PCF Parameters		
Mode field diameter	d_{eff}	8.5 µm @ λ_c
Fiber length	L_{PCF}	20 mm
Nonlinear refractive index	n_2	$33.8 * 10^{-20}$ m^2/W
Dispersion profile	-	Imported from datasheet (NKT, PM-LMA-10)
Numerical aperture	NA	0.12 @ 1064 nm
Zero dispersion wavelength	λ_{zdw}	1300 nm

8.3 Imaging Methods: Animals and Sample Preparation

8.3.1 Deep-Tissue Imaging with Tunable DW-Generator

Animal Handling: The mouse model is an adult wild-type C57BL/6 J male mouse (~ 6 months old, P180–P210) with ubiquitous EGFP expression. No experiments with living animals were performed. The animal breeding and euthanasia to obtain the tissue were approved by the ethical research committees of respective national/local authorities: Freie und Hansestadt Hamburg, Behörde für Gesundheit und Verbraucherschutz, Hamburg, Germany (ORG1108). Sampling was performed following the protocols and guidelines of the Ethical Committee and the directives of the European Union Council 86/609 and 2010/63.

Sample Preparation: The brain of the EGFP mouse model was quickly extracted from the skull and fixed with 4% paraformaldehyde for 24 h in the fridge. The following day, the tissue was washed with phosphate buffer 1 M three times. Subsequently, the brain was sliced coronally (~ 2 mm thick) with a scalpel, and then, under the microscope the hippocampus area was separated and mounted in a compartment of a glass-bottom µ-slide microscopy chamber (Ibidi, #80427-90) using Fluoromount (Invitrogen, #00-4958-02). Imaging was performed through the ~ 0.5 mm thin undersurface of the slide, to enable the insertion of a purified water droplet between the sample and the water immersion objective.

8.3.2 Multiplexed Three-Color Imaging

Animal Handling: The mouse model used for the brain imaging is an adult wild-type C57BL/6J male mouse (~6 months old, P180–P210). No experiments with living animals were performed. The animal breeding and euthanasia to obtain the tissue were approved by the ethical research committees of respective national/local authorities: *Freie und Hansestadt Ham-*

burg, Behörde für Gesundheit und Verbraucherschutz, Hamburg, Germany (ORG1108). Sampling was performed following the protocols and guidelines of the Ethical Committee and the directives of the European Union Council 86/609 and 2010/63.

Sample Preparation: The brain of the adult mouse model was quickly extracted from the skull and fixed with 4% paraformaldehyde for 24h in the fridge. The following day, the tissue was washed with 1 M phosphate buffer (PBS) three times. Subsequently, the brain was sliced coronally (~2 mm thick) with a scalpel, and then, under the microscope the hippocampus area was separated and placed in a compartment of a glass-bottom µ-slide microscopy chamber (Ibidi, #80427-90). Then, the tissues were impermeabilized with 0.2% Triton (in PBS) for 1h. Afterward, after 2 washes with PBS, the primary antibodies were applied in PBS for 4 days at 4°C (shaking smoothly): MAP-2 (1:300, #188002, Synaptic Systems) and (1:300, #173011, Synaptic Systems). Then, after two long PBS washes, the secondary antibodies were applied in PBS (+ 10 % Goat Serum) for 3 days: Alexa anti-Rabbit 488 (1:300, #A21202 Invitrogen) and Alexa anti-Mouse 647 (1:300, #A21443 Invitrogen). The nuclei dye SYTOX Orange (1:10,000, #S11368, Thermo Fisher) was applied together with the secondary antibodies. Finally, 3 washes with PBs were applied, and the sample was mounted using Fluoromount (Invitrogen, #00-4958-02). Imaging was performed through the ~0.5 mm thin undersurface of the slide, to enable the insertion of a purified water droplet between the sample and the water immersion objective.

8.4 Simulation parameters for Interferometric SCG

Parameter	Symbol	Value
Input Pulse and Noise Parameters		
Pulse shape	-	Sech (transform-limited)
Pulse energy	E_0	40 nJ
Center wavelength	λ_c	1050 nm
Temporal FWHM	Δt	80 fs
Number of realizations	N	500
Technical RIN (std)	σ_{RIN}	0.3% of the mean pulse energy
Quantum noise model	-	One-photon-per-mode (Section 2.3)
PCF Parameters		
Mode field diameter	d_{eff}	8.5 µm @ λ_c
Fiber length	L_{PCF}	50 mm
Nonlinear refractive index	n_2	$33.8 * 10^{-20}$ m^2/W
Dispersion profile	-	Imported from datasheet (NKT, PM-LMA-10)
Numerical aperture	NA	0.12 @ 1064 nm
Zero dispersion wavelength	λ_{zdw}	1300 nm